DOCTOR OF PHILOSOPHY

A qualitative and quantitative investigation of the functional morphology of the juvenile scapula

O'Malley, Andrew Stephen

Award date:
2013

DOCTOR OF PHILOSOPHY

A qualitative and quantitative investigation of the functional morphology of the juvenile scapula

Andrew Stephen O'Malley

2013

University of Dundee

A QUALITATIVE AND QUANTITATIVE INVESTIGATION OF THE FUNCTIONAL MORPHOLOGY OF THE JUVENILE SCAPULA

ANDREW STEPHEN O'MALLEY

PhD in Anatomy & Human Identification
University of Dundee
June 2013

Table of Contents

List of Tables

List of Figures

List of Abbreviations

BV/TV	**Bone Volume/Total Volume (i.e. bone volume fraction)**
CLUT	**Colour Look-Up Table**
CT	**Computed Tomography**
DA	**Degree of Anisotropy**
MPR	**Multi-Planar Reconstruction**
ROI	**Region of Interest**
SMI	**Structural Model Index**
Tb.N	**Trabecular Number**
Tb.Sp	**Trabecular Separation**
Tb.Th	**Trabecular Thickness**
VOI	**Volume of Interest**

Acknowledgements

My thanks go to my supervisors Professor Sue Black and Professor Roger Soames, who have encouraged and supported me during this project. They have always provided me with advice and opportunity, and I am particularly thankful for their role in the inception and design of the Greenhouse programme, which has funded this investigation and enabled me to teach gross anatomy alongside my research.

I also owe a great deal of gratitude to Dr Craig Cunningham for the insight and support he has continually offered at every stage of this project; he has been an invaluable source of knowledge and inspiration, and a pleasure to work and study with.

I would also like to acknowledge the following people of their help:

Professor Michael Fagan and Ms Sue Taft, Centre for Medical and Engineering Technology, University of Hull, for their collaborative assistance and the provision of micro-computed tomography facilities.

Ms Margaret Low for her expertise and time, which she kindly offered during the collection of radiographs.

I would also acknowledge all the staff and research students in the Centre for Anatomy and Human Identification; working with a group of such professional, intelligent and creative people has helped make this process enjoyable and fulfilling.

I would like to thank my family, close friends and partner, Jennifer, who have always provided support and encouragement throughout my studies. Their belief, pride and encouragement have made a significant contribution to my ability to complete this work.

Declaration

The candidate, Andrew Stephen O'Malley, is the author of the thesis. Unless otherwise stated all references cited have been consulted by the candidate. The work, of which the thesis is a record, was completed by the candidate, and has not been previously accepted for a higher degree or qualification at this or any other university or other institution of learning.

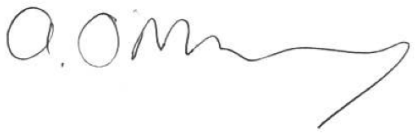

Andrew O'Malley

I certify that the candidate, Andrew Stephen O'Malley, has conducted 3.5 years of research under my supervision. He has fulfilled the conditions of Ordinance 39 and is qualified to submit the accompanying thesis in application for the degree of Doctor of Philosophy.

Professor Sue Black

Professor Roger Soames

Copyright

Summary

This thesis presents a radiographic description of developmental morphology of the human scapula and a comprehensive morphological description of trabecular bone in the perinatal scapula. While the aim was originally to describe the changing trabecular morphology in the developing scapula, considerable thought has gone into the design, advancement and validity of the methodologies presented in this thesis. The work of previous studies has been considered and improved upon to take into account recent advances in software and hardware. Specifically, the introduction of MPR to the methodology has resulted in a more efficient and reliable technique that could allow future researchers to examine larger datasets in shorter periods of time. Additional anthropometric data were also gathered on the perinatal scapula, which was used to assist in the design of the multiplanar stereoscopic analysis. User error associated with threshold definition and VOI placement was also investigated and found to be negligible.

With respect to development of the juvenile scapula, three distinct developmental phases, comprising eight separate groups, were identified from the radiographic study and anthropometric review study: pre-reboot (<0.5y), reboot (0.5-3y) and post-reboot (>3y). A clear pattern of regional organisation was visible at the earliest stages of development, echoing the findings of previous studies. It was suggested that the reboot phase represents a developmental period in which the scapula undergoes functional change under a two-tier mechanism, which influences its overall development.

On one level the scapula appears constrained by a rigid template that controls macro-morphology in preparation for phylogenetically anticipated demands, which may, or may not, materialise; on a second tier is the adaptive micro-architecture that initially compliments the phylogenetic template, but retains the flexibility to respond to shifting ontogenetic demands.

The trabecular architecture of the pre-reboot specimens was subsequently analysed in quantitative detail. A progressive radiating pattern, which originated from the approximate location of the primary ossification centre, was identified; it is suggested that a combination of radiating growth and internal vascular distribution are significant contributors to this pattern.

This thesis provides a detailed account of the developmental morphology of the human scapula and contributes new elements to the evolving methodologies used in this field. The findings of this study also lay the foundation for further investigation of the radiating pattern of ossification and the potential for micro-architecture in developing bone to adapt to ontogenetic demands despite gross morphology that is phylogenetically constrained.

Chapter 1: Introduction

1.1. Outline of thesis

This project will investigate the internal architecture and gross morphology of the human scapula. Developmental changes to this architecture will receive particular attention, and the configuration of the perinatal scapula will be described in detail.

Bone modelling and remodelling is not only the core of the mechanisms involved in bone growth and repair, but is also central to bone's ability to adapt to the changing stresses to which it is subjected. The concept of bone's ability to react to varying biomechanical stresses has been studied in depth, and was first described by Julius Wolff in 1892:

"Every change in the function of bone is followed by certain changes in the internal architecture and external conformation in accordance with the mathematical laws" – Julius Wolff, 1892.

Although the "mathematical laws" that Wolff described are often disregarded due to the dynamic nature of bone, the general concept of 'form follows function' is still fundamental to the study of skeletal morphology.

In its simplest form, Wolff's law can be used to explain almost any variation in the morphology of healthy human bone. For example:

- Increased bone density is seen in athletes of some sports (such as weight lifting) due to the increased load being imposed on the bone.
- Asymmetrical adaptation is also seen in athletes who use one side of their body more than the other; the unilateral increase in muscle mass in tennis players' upper limbs results in the bones of one arm becoming more robust. This emphasises the role of local biomechanical stresses in bone adaptation,

rather than indicating that some kind of systemic influence is the main contributing factor.

- Conversely, less load transfer through a bone will result in a decrease in its density. This is seen in astronauts where bone is reabsorbed due to the lack of weight transference, which often results in fractures upon their return to Earth.

In these respects, adaptive bone remodelling in scapulae has been studied in some detail, but there are areas which have been considered little in the literature: for example, the internal configuration of scapulae during the fetal, neonatal and subsequent juvenile periods has received little consideration. Such a lack of advancement in this area is due to a combination of logistical (i.e. the rarity of juvenile material, its fragility and its irreplaceable nature) and technical constraints (i.e. the technology used to study specimens in sufficient detail causes irreversible damage). Recent technical advances in micro-computed tomography (micro-CT) and computing power, and the availability of juvenile remains from the Scheuer Collection, allow the non-destructive investigation of juvenile bone.

This investigation will present a radiographic description of the developmental morphology of the human scapula and a comprehensive morphological description of trabecular bone in the perinatal scapula. Additional work will be carried out into the design, advancement and validity of existing methodologies in this field.

Further research into the functional development of the scapula could contribute to current knowledge of bone modelling and remodelling in the juvenile, and could reveal more about the growth and development of the scapula specifically, and its capacity to adapt to changing stresses. Practically, research into this area has the potential to shed light on the evolutionary history of the pectoral girdle (specifically in relation to the upper limb's modified role in the biped), as well as potential use in the forensic arena (as a technique for age estimation), and may also have clinical significance in the field of paediatric orthopaedics.

1.2. Objectives

The objectives of this thesis are to describe the changing trabecular morphology in the developing scapula by employing established and novel techniques. The complex shape of the scapula will require that previously established methodologies be modified for use on this unique bone; an additional objective of this study is the design and assessment of such techniques. The final objective of this study is to describe the development of the juvenile scapula in context and discuss potential influencing factors. Specific objective are listed below and summarised in Figure 1.1:

- To use established **radiographic techniques**[1] to document the morphology of the human scapula from early stages of development through to skeletal maturity.
    - Use this radiographic data to qualitatively describe the growth and development of the human scapula.
    - Consider what factors may influence growth and development.
- To design a robust technique of defining volumes of interest (VOIs) in the perinatal scapula.
    - Employ **anthropometric techniques**[2] to assist in the reliable and repeatable VOI definition.
    - Quantify how **user-error**[3] influences VOI placement and analysis.
- To describe quantitatively the trabecular architecture, using **micro-computed tomography**[4] (micro-CT), of the perinatal scapula.

---

[1] See 0

Radiographic Study
[2] See Chapter 4: Anthropometric Study
[3] See Chapter 5: Stereoscopic Error Study
[4] See Chapter 6: Stereoscopic Study

- To discuss the quantitative and qualitative data in terms of growth, development, structure and function.

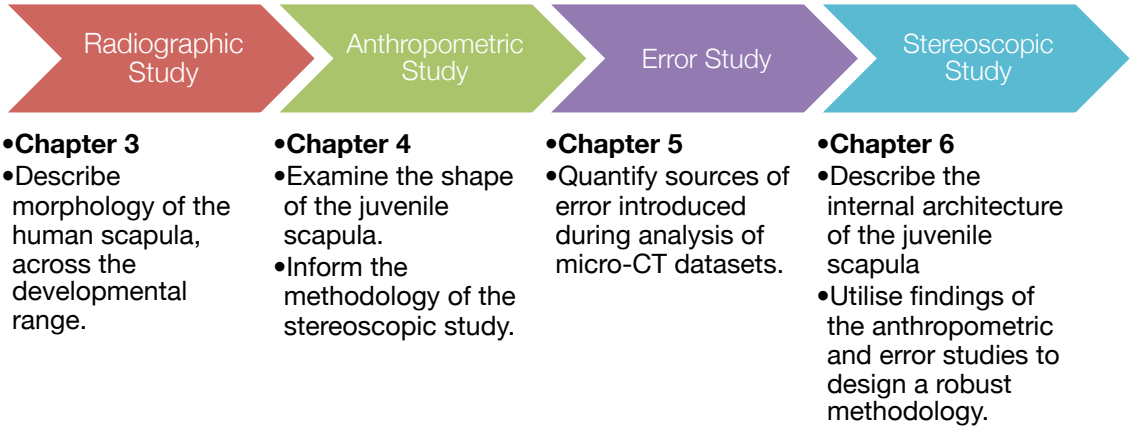

Figure 1.1: Study Aims

1.3. The Scheuer Collection

This investigation utilised material from the Scheuer Collection, which is an active repository of juvenile skeletal remains. The assemblage contains material from over 150 individuals and is located within the Centre of Anatomy and Human Identification, University of Dundee. The specimens of the Scheuer Collection are of archeological, forensic and historical anatomical origin. The specimens that comprise the collection are either the complete or partial skeletons of individuals, or single isolated bones. While the Collection contains material in various conditions, only specimens in a good or undamaged condition were used in this study; specimens that exhibited extensive damage or possible signs of pathology or trauma were excluded.

While some of the material is of documented provenance the majority of individuals are assigned age and sex based on analysis of the dentition, or via anthropometric and morphological assessment of isolated specimens. This should be considered while interpreting the results of this investigation, as should the possibility that the individuals' cause of death or associated morbidity could impact on the structure and function of the material being analysed.

Chapter 2: Review of Literature

Understanding the structure and origin of the scapula, and the pectoral girdle as a whole, is crucial in understanding how its tissues behave. This chapter will describe the anatomy of the region at various stages of development and the evolutionary origin of the girdles.

2.1. Adult Anatomy

The Pectoral Girdle

The human pectoral girdle represents the only skeletal communication between the upper limb and the torso. Skeletal tissues present in the pectoral girdle include the scapula, which articulates with the humerus laterally at the shoulder joint, and the clavicle, which articulates with the scapula laterally and the manubrium of the sternum medially. These bones work together to provide a broad site for muscle attachment, in the case of the scapula, and to lateralise the upper limb, in the case of the clavicle, thus liberating the upper limb for a large range of highly specific prehensile and manipulative movements (Scheuer and Black, 2000).

The movements at the pectoral girdle all contribute to the ultimate function of the human upper limb: positioning of the hand. While the functions of the lower limb include locomotion and support, bipedalism has essentially freed the upper limb from locomotive responsibilities and allowed its extremity, the hand, to explore and manipulate the surrounding environment. The shoulder joint is best described as a synovial ball-and-socket joint between the glenoid fossa of the scapula and the head of the humerus. This glenohumeral joint is capable of a large range of movements.

In addition to the glenohumeral joint itself, the ‘floating’ nature of the scapula also contributes to greater degrees of freedom (Drake et al., 2005). The pectoral girdle only articulates with the axial skeleton via the clavicle at the manubriosternal joint, while the scapula has no skeletal articulations with the trunk. This arrangement allows the

scapula to move freely relative to the torso, and permits protraction, retraction, rotation, elevation and depression of the scapula. These movements change the position of the glenohumeral joint and assist to enhance its range of movements.

The pectoral region also acts as a conduit for vascular, lymphatic and neural structures to travel between proximal and distal locations. These structures are crucial in allowing arterial supply, venous and lymphatic drainage, and innervation of the upper limb, and are essential in allowing the upper limb to function normally.

Movements at the pectoral girdle

Movements of the arm at the glenohumeral joint include flexion, extension, abduction, adduction, medial (internal) rotation, lateral (external) rotation and circumduction (Figure 2.1).. Flexion of the arm at the glenohumeral joint is opposed by extension, abduction is opposed by adduction, and medial rotation is opposed by lateral rotation.

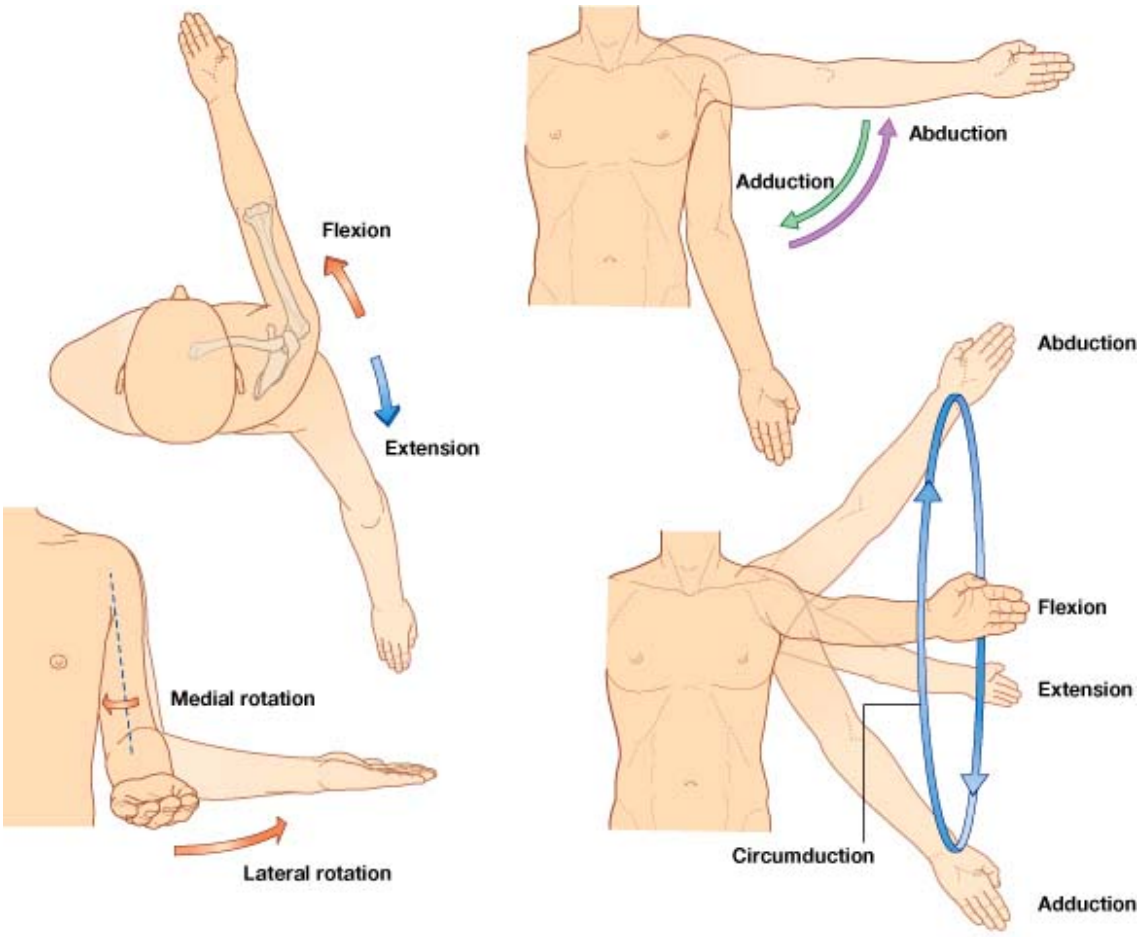

Figure 2.1: Movements of the arm at the glenohumeral joint. (Drake et al., 2005)

In addition to movements of the arm, the scapula itself can be repositioned by the muscles that surround it (Figure 2.2). The muscles that affect these movements will be discussed later in this section.

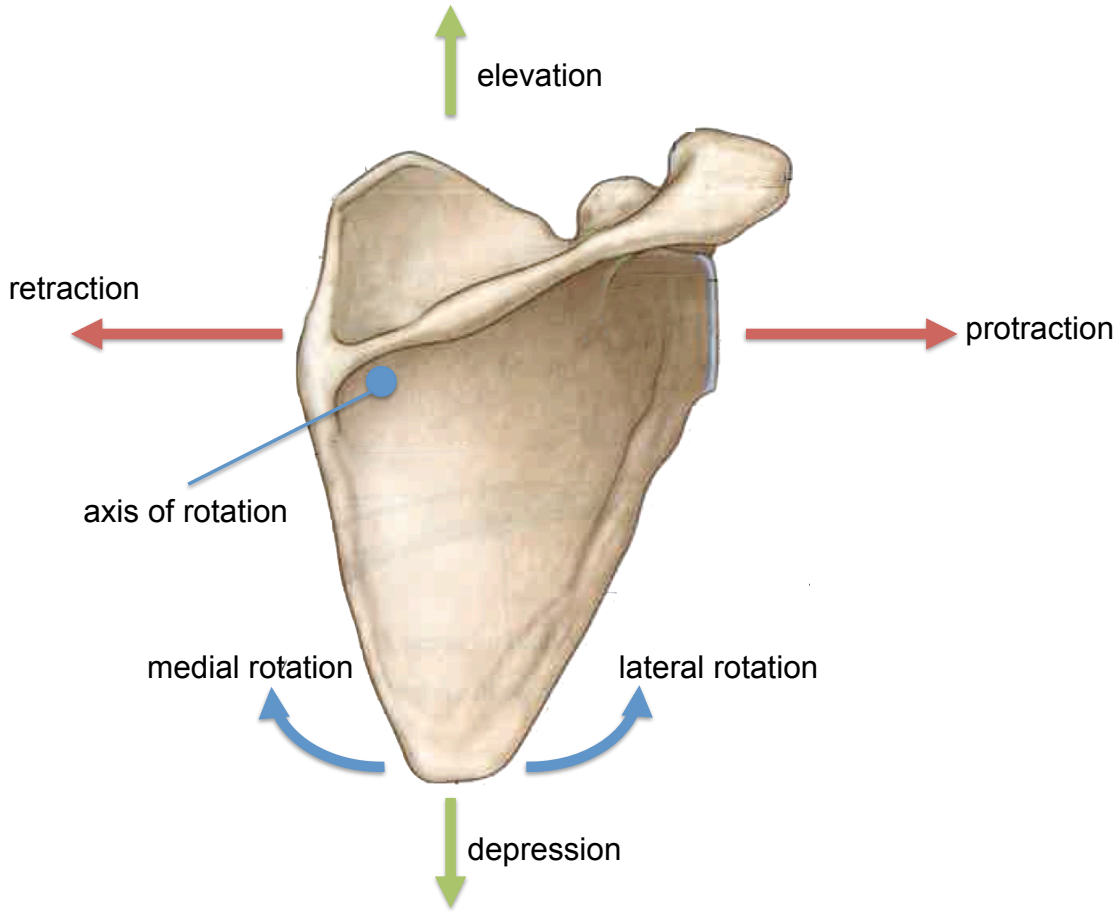

Figure 2.2: Movements of the scapula. (Drake et al., 2005)

Protraction and retraction are opposing movements that refer to the position of the scapula relative to the vertebral column. Retraction can be thought of as adduction of the scapula, as it moves towards the midline. Since the scapula slides across the curvature of the chest wall, retraction also involves the scapula moving posteriorly and medially towards the column.

Conversely, protraction occurs as the scapula moves away from the vertebral column and can be thought of as abduction of the scapula, as it moves away from the midline while maintaining contact with the posterior chest.

Elevation and depression are two additional opposing movements that refer to the movement of the scapula along its long axis. Superior deviation of the scapula, such as ‘shoulder-shrugging’, is referred to as elevation, while inferior deviation is referred to as depression.

Osteology

Information in this section is sourced from standard anatomical texts, such as Gray’s Anatomy for Students (Drake et al., 2005), Developmental Juvenile Osteology (Scheuer and Black, 2000) and Anatomy and Human Movement (Palastanga et al., 2007).

The Clavicle

The clavicle articulates medially with the manubrium of the sternum, and laterally with the acromion process of the scapula. In the adult, it lies horizontally at the root of the neck with the medial end positioned anteriorly, and the lateral end occupying a more posterior position. In order for the clavicle to adopt this position, it has a characteristic ‘S’-shape, which is anteriorly concave in the lateral third and anteriorly convex in the medial two-thirds.

This positioning allows the clavicle to fulfil three basic functions:

1. To act as a site of attachment for muscles associated with the upper limb and may assist in respiration
2. To act as a strut, with the aim of:
    a. Holding the glenohumeral joint in a lateral position
    b. Transmitting stresses between the upper limb and the axial skeleton
3. Protection of deeper neurovascular tissues

The superior and inferior surfaces of the clavicle facilitate the majority of muscle attachments. While considering attachments at the medial and lateral extremities, it is useful to bear in mind the overall orientation of the clavicle and its double curvature.

Sites of muscle attachment are easily identified on the superior surface; due to the largely smooth appearance of the surface, rougher areas towards the medial and lateral extremities are clear indications of attachment sites. Trapezius (posteriorly) and deltoid (anteriorly) attach at the lateral end, while sternocleidomastoid (posteriorly) and pectoralis major (anteriorly) attach to the medial end.

Subclavius and sternohyoid attach to the inferior surface of the clavicle; the attachment site for subclavius can be observed, while the latter rarely leaves an impression on the bone.

In addition to muscle attachments, the inferior surface of the clavicle also has ligamentous attachments. At the medial extremity, a large rough area is for the attachment of the costoclavicular ligament, which holds the medial end of the clavicle to the anterior end of the first rib and its associated costal cartilage.

The conoid tubercle on the lateral end of the clavicle is another feature of its inferior surface and is the attachment of the conoid part of the coracoclavicular ligament, which also attaches to the coracoid process of the scapula. The coracoclavicular ligament also has a trapezoid part, which attaches the trapezoid ridge of the inferior surface of the lateral clavicle to the coracoid process. Together these parts of the coracoclavicular ligament act to stabilise the acromioclavicular joint, which is a potential weak link in the pectoral complex.

Invasion of the nutrient vessels also occurs on the inferior surface of the clavicle, and in dry specimens a nutrient foramen is usually visible at the point of maximum concavity.

The Scapula

Together with the clavicle, the scapula completes the pectoral girdle. It articulates with the upper limb at the glenohumeral joint and facilities its full range of movements. The acromion of the scapula articulates with the lateral, more posterior, extremity of the clavicle at the acromioclavicular joint. Although this joint is synovial in nature, movement here is highly restricted due to the nature of the ligaments that stabilise the joint (Palastanga et al., 2007). The functional role of this complex is to permit limited controlled movement, while holding the pectoral girdle in a stable lateral position.

As previously described, the scapula does not articulate directly with the axial skeleton and essentially ‘floats’ in large volumes of muscle (Culham and Peat, 1993). This allows the scapula to dynamically re-orientate itself to allow an increased range of movement at the upper limb.

The adult scapula can be thought of as a single blade, with additional components emerging at various locations (Figure 2.3). The blade itself is comprised of the infra- and supra-spinous fossee on the dorsal surface and the subscapular fossa on the ventral surface and is concave ventrally as it accommodates the curvature of the posterior wall of the chest. The supra- and infra-spinous fossae are separated by a dorsal projection: the spinous process. This dorsal projection is angled cranially, and extends in a lateral direction. The lateral terminus of this feature is the acromion process, which articulates with the lateral extremity of the clavicle. The meeting of the spinous process with the fossae is referred to as the base. The most medial point on the base is referred to the root of the spine, and the most lateral point corresponds to the spinoglenoid notch.

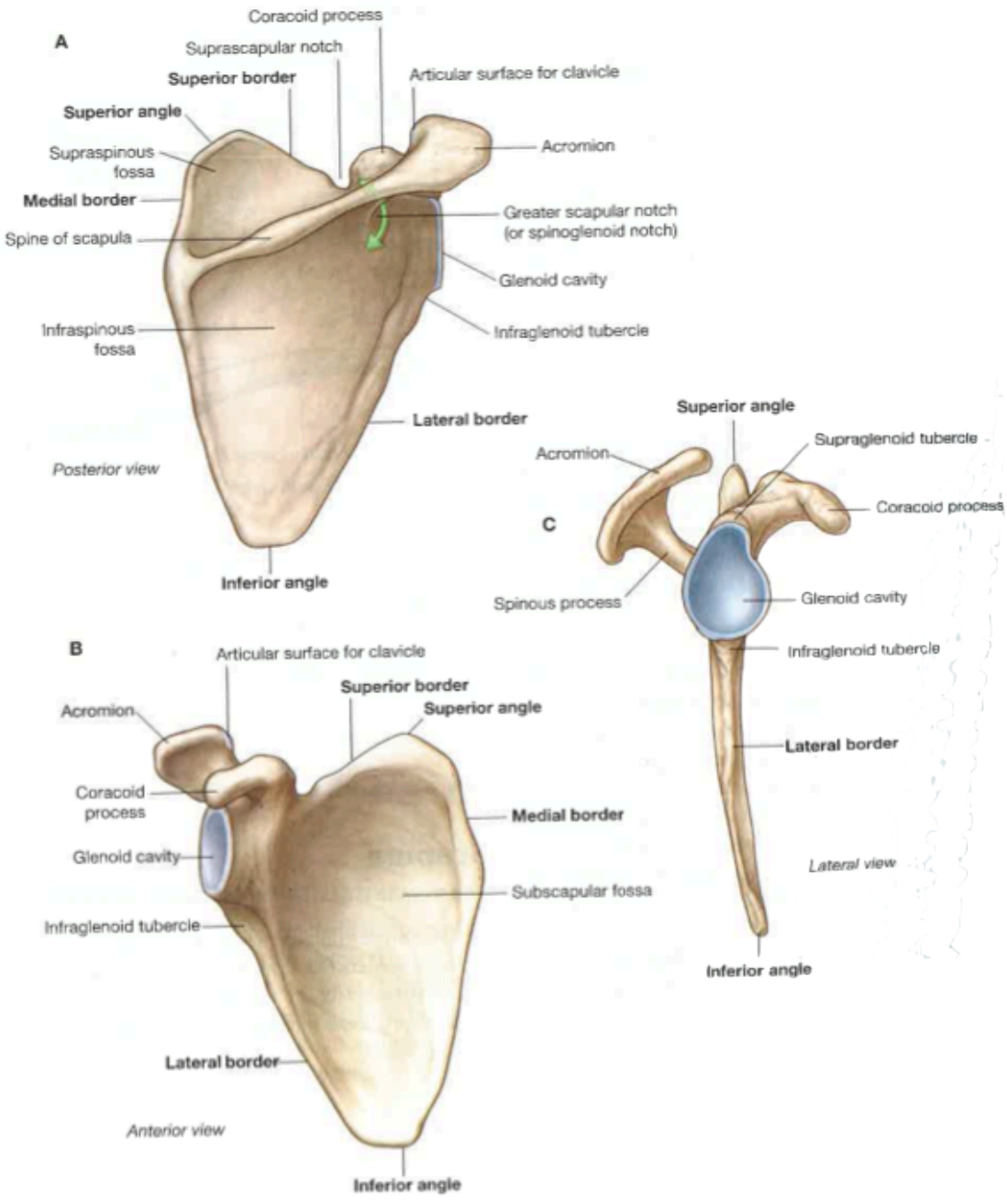

Figure 2.3: Osteological features of the adult human scapula.
A: Dorsal view; B: Ventral view; C: Lateral view. (Drake et al., 2005)

The infraspinous fossa can be thought of as an inverted triangle; the three sides of the infraspinous fossa are:

1. The lateral border of the scapula
2. The portion of the medial border inferior to the root of the spinous process
3. The base of the spinous process superiorly

The lateral and medial borders meet at the inferior angle, and the inferior portion of the medial border and the base of the spine intersect at the most medial point on the scapula.

The supraspinous fossa can also be thought of as a triangle; its three sides being:

1. The base of the spinous process
2. The portion of the medial border superior to the root of the spinous process
3. The superior border

The superior border and the superior portion of the medial border meet at the superior angle. As with the infraspinous fossa, the superior portion of the medial border and the base of the spine also intersect at the most medial point on the scapula.

Continuing with the geometric theme, it is also possible to liken the spinous process to a triangle, albeit in a different plane.

In addition to the spinous process, acromion process and the fossae, the glenoid fossa is situated at the lateral extremity of the scapula. It articulates with the head of the humerus at the glenohumeral joint. As is typical of synovial joints, the articular surface of the glenoid is covered with a layer of hyaline cartilage.

The glenoid fossa has a small surface area in comparison to the humeral head, despite the articular surface being enlarged by a modest cartilaginous glenoid labrum. This discrepancy in the size of the congruent joint surfaces is a result of the requirement for an increased range of movement. Conversely, the acetabulum of the ilium is relatively larger than the glenoid while permitting a reduced range of movement.

There are several sites around the glenoid region that serve as attachment sites for some muscles of the upper limb. The long head of biceps brachii attaches to the supraglenoid tubercle, which is situated immediately superior to the glenoid fossa. The long head of triceps brachii attaches to the infraglenoid tubercle, which is located

immediately inferior to the glenoid fossa at the superior extremity of the lateral border of the scapula.

Protruding in an initially superior, then lateral, direction from the superior aspect of the glenoid region is the coracoid process, which serves as an attachment site for the short head of biceps brachii, coracobrachialis and pectoralis major. Despite its deep position, this structure can be palpated in lean individuals.

The Proximal Humerus

The proximal extremity of the humerus comprises the articular head, the anatomical neck, the greater and lesser tubercles, the surgical neck and the superior portion of the shaft.

The head of the humerus contributes the distal side of the glenohumeral joint, and is easily recognisable by its hemispherical shape. As in the glenoid, the articular surface of the head is covered with a layer of hyaline cartilage.

The anatomical neck of the humerus is a short constriction immediately distal to the head. It is positioned obliquely, relative to the long axis of the humerus, and separates the head (superomedially) and the tubercles (superolaterally and inferomedially).

The greater and lesser tubercles offer attachment sites for the four rotator cuff muscles: supraspinatus, infraspinatus, subscapularis and teres minor. Both tubercles are oriented anteriorly, with the lesser tubercle being medial to the greater tubercle with the intertubercular sulcus separating the two. This sulcus houses the passage of the long head of the biceps brachii muscle.

Additional muscles (deltoid, pectoralis major and minor, teres major and latissimus dorsi), which are not part of the rotator cuff group, also cross the glenohumeral joint and insert onto the superior portion of the shaft. The deltoid tuberosity is perhaps the most obvious muscular attachment site, and is situated on the lateral aspect of the humerus.

Musculature

The muscles of the pectoral girdle act primarily to position the hand in space. Additionally, the fixation of the distal attachment of some of these muscles, particularly pectoralis major, can assist in respiration during exertion. Information in this section is sourced from standard anatomical texts, such as Gray's Anatomy for Students (Drake et al., 2005), Developmental Juvenile Osteology (Scheuer and Black, 2000) and Anatomy and Human Movement (Palastanga et al., 2007).

The muscles that attach to the pectoral girdle can be divided into four general groups (Lewis, n.d.)(Table 2.1).

Muscles connecting the upper extremity to the vertebral column	Muscles connecting the upper extremity to the anterior and lateral thoracic wall	Muscles of the shoulder	Muscles of the arm
Trapezius	Pectoralis major	Deltoid	Coracobrachialis
Rhomboid major	Pectoralis minor	Teres major	Triceps brachii
Rhomboid minor	Subclavius	Teres minor	Biceps brachii
Levator scapulae	Serratus anterior	Supraspinatus	
Latissimus dorsi		Infraspinatus	
		Subscapularis	

Table 2.1: Muscles of the pectoral girdle, arranged into four general groups.

Muscles connecting the upper extremity to the vertebral column

These muscles all attach to the scapula, and one (latissimus dorsi) also has attachments to the humerus as well as the pectoral girdle. Together, they act to position the scapula on the posterior chest wall. Latissimus dorsi contributes little to this arrangement however, and is most effective in extending the upper limb at the glenohumeral joint. A summary of these muscles can be found in Table 2.2.

Trapezius attaches superiorly from the superior nuchal line and external occipital protuberance of the occipital bone and the nuchal ligament. Inferiorly, it attaches to the spinous processes of vertebrae C7 to T1, and the associated supraspinous ligaments. Trapezius inserts laterally on the superior edge of the spinous process and

acromion of the scapula, and the lateral third of the clavicle. These attachments result in a triangular shape when considered unilaterally, or a trapezium when considered bilaterally. Different fibres within trapezius act to elevate, rotate, retract and depress the scapula.

Retraction (pulling the scapula towards the vertebral column) is brought about by the contraction of middle fibres of trapezius aided by contraction of the superior and inferior fibres. The superior fibres of trapezius elevate the scapula, producing the movement commonly described as ‘shoulder shrugging’, and also maintain the position of the scapula during lifting. The inferior fibres exert a downward pull upon contraction, which lowers the position of the scapula. It is important to bear in mind that these portions of the muscle do not act in isolation, and combinations of contractions of different parts of trapezius will result in re-positioning of the scapula that will facilitate increased ranges of movement at the glenohumeral joint.

Rhomboid major and minor are traditionally considered distinct muscles, but are often continuous with each other and distinguishable only by their attachment sites. Rhomboid major, the larger of the two, occupies a more inferior position and spans between the dorsal edge of the medial border of the scapula (between the root of the spine and inferior angle) and the spinous processes of T2-T5 (and the associated portion of the supraspinous ligament). Rhomboid minor attaches to the dorsal surface of the medial border of the scapula, at the root of the spinous process, laterally and the spinous processes of C7 and T1 (and the supraspinous ligament between them) medially. They both lie deep to trapezius and latissimus dorsi and superficial to the long postural muscles of the back. As with the medial portion of trapezius, the rhomboids act to retract the scapula.

Muscle	Origin	Insertion	Innervation	Action
Trapezius	Superior nuchal line, external occipital protuberance, ligamentum nuchae, spinous processes of C7-T1.	Superior edge of the spine and acromion of the scapula, dorsal edge of the lateral third of the clavicle.	Spinal division of CN XI.	Elevates, depresses, laterally rotates and retracts scapula.
Rhomboid major	Spinous processes and supraspinous ligaments of T2-T5.	Dorsal surface of the medial border of the scapula, between the root of the spine to the inferior angle.	Dorsal scapular nerve	Elevates and retracts the scapula.
Rhomboid minor	Inferior portion of the ligamenum nuchae, and spinous processes of C7-T1.	Dorsal surface of the medial border of the scapula, at the root of the spine.	Dorsal scapular nerve	Elevates and retracts the scapula
Levator scapulae	Transverse processes of C1-C4.	Dorsal surface of the medial border of the scapula, between the root of the spine and the superior angle.	Dorsal rami of spinal nerves C3+4	Elevates the scapula
Latissimus dorsi	Spinous processes and interspinous ligaments of T6-T12, spinous processes of lumbar vertebrae (via thoracolumbar fascia), ribs 8-12, iliac crest.	Floor of intertubercular sulcus of the humerus, and dorsal surface of the inferior angle of the scapula.	Thoracodorsal nerve (C6-8)	Adduction, medial rotation and extension of the arm at the glenohumeral joint, concurrent anchoring of the scapula.

Table 2.2: Summary of muscles that connect the upper extremity to the vertebral column.

Levator scapulae occupies the same tissue plane as the rhomboids, but ascends superiorly into the neck. It inserts laterally to the dorsal edge of the medial border of the scapula above the root of the spine. It originates medially from the transverse processes of C1-4 via tendinous attachments. Along with the superior fibres of trapezius, levator scapulae elevates the scapula and offers resistance to the effects of gravity and active lifting. It can also assist in retraction, and resists medial rotation, of the scapula.

Latissimus dorsi is included here for completeness since it includes a small attachment around the inferior angle of the scapula. The majority of the functionality of this muscle relates to the upper limb, with minimal influence on the scapula. Latissimus dorsi assists in anchoring the scapula to the chest wall during movements of the upper limb.

Muscles connecting the upper extremity to the anterior and lateral thoracic wall

The muscles that connect the upper extremity to the anterior and lateral chest walls include pectoralis major and minor, subclavius and serratus anterior. **Pectoralis major** and **subclavius** are included here for completeness, but they have no attachments to the scapula and will not be considered in detail. A summary of this group of muscles can be found in Table 2.3.

Muscle	Origin	Insertion	Innervation	Action
Pectoralis major	External surface of medial half of the clavicle (clavicular head); anterior surface of sternum and neighboring costal cartilages (sternal head).	Lateral lip of the intertubercular sulcus of humerus.	Medial and lateral pectoral nerves (C5-T1).	Flexion, medial rotation and adduction at glenohumeral joint.
Pectoralis minor	External surface of ribs 3-5.	Coracoid process of the scapula.	Medial pectoral nerve (C6-8).	Protraction of the scapula.
Subclavius	Sternal end of rib 1.	Inferior surface of the clavicle.	Nerve to subclavius (C5+6).	Stabilization of the clavicle.
Serratus anterior	Lateral edges of ribs 1-9.	Ventral surface of the medial border of the scapula.	Long thoracic nerve (C5-7).	Protraction and lateral rotation of the scapula.

Table 2.3: Summary of muscles that connect the upper extremity to the anterior and lateral chest wall.

Pectoralis minor is a flat triangular muscle with a broad inferior origin along the external surface of ribs 3-5, immediately lateral to the costochondral junctions. The muscle inserts superiorly to the ventral surface of the coracoid process. Contraction of this muscle results in the scapula being pulled anteriorly and superiorly. Additionally, pectoralis minor can also assist in respiration if the pectoral girdle is fixed (by leaning over and bracing the hands against the thighs, for example).

Serratus anterior, named due to its jagged medial attachments, exists in a plane between the scapula and the chest wall. It inserts on the ventral (deep) aspect of the medial border of the scapula and extends anteriorly under the scapula to the external surfaces of the upper nine ribs in the midaxilliary line.

Serratus anterior acts to protract the pectoral girdle and stabilizes the scapula during flexion of the upper limb. Paralysis of this muscle causes ‘winging’ of the scapula, often due to damage of the long thoracic nerve. Common clinical scenarios that result in damage to the long thoracic nerve include stab wounds to the lateral chest wall or iatrogenic damage to the nerve during mastectomy.

Muscles of the shoulder

The muscles of the shoulder originate proximally from the bones of the pectoral girdle (chiefly the scapula) and insert distally on the humerus. This muscle group includes the rotator cuff muscles (supraspinatus, infraspinatus, subscapularis and teres minor), teres major and deltoid. A summary of this group of muscles can be found in Table 2.4.

Muscle	Origin	Insertion	Innervation	Action
Detoid	Anterior border of lateral third of the clavicle (anterior fibres); Tip of the acromion process of the scapula (middle fibres); Inferior edge of the lateral half of the spine of the scapula (posterior fibres).	Deltoid tuberosity of the humerus	Axillary nerve (C5+6)	Abduction of the arm (beyond 20°). Posterior fibres can assist in flexion; anterior fibres assist in extension.
Teres major	Inferior third of the posterior surface of the lateral border of the scapula.	Medial lip of the intertubercular groove of the humerus.	Inferior scapular nerve (C6+7)	Adduction and medial rotation of the humerus.
Subscapularis	Subscapular fossa via tendinous intersections	Lesser tubercle of the humerus.	Superior and inferior subscapular nerves (C5-7)	Medial rotation at the glenohumeral joint.
Supraspinatus	Supraspinous fossa	Superior facet of the greater tubercle of the humerus.	Suprascapular nerve (C5+6)	Abduction of the arm (initial 20°).
Infraspinatus	Infraspinous fossa via tendinous intersections	Middle facet of the greater tubercle of the humerus.	Suprascapular nerve (C5+6)	Lateral rotation of the arm.
Teres minor	Superior two-thirds of the posterior surface of the lateral border of the scapula.	Inferior facet of the greater tubercle of the humerus.	Axillary nerve (C5+6)	Adduction and lateral rotation of the humerus.

Table 2.4: A summary of the muscles of the shoulder.

Deltoid is a thick muscle that contributes to the external rounded appearance of the shoulder. Named due to its similarity to the fourth letter of the Greek alphabet (delta, Δ), deltoid appears triangular when observed from the lateral aspect. It has three distinct parts (anterior, middle and posterior) that are distinguishable by their proximal attachments; all parts combine to insert distally to the deltoid tuberosity of the humerus, and work together to abduct the arm at the glenohumeral joint with the initial assistance of supraspinatus.

The anterior and posterior groups of fibres can also act in isolation to produce additional movements. The anterior fibres originate from the anterior border of the lateral third of the clavicle, and can act to flex and medially rotate the upper limb at the shoulder joint. The posterior fibres originate from the dorsal edge of the lateral third of the spine of the scapula, and act to counteract the medial rotation that occurs during adduction of the arm caused by the contraction of latissimus dorsi, pectoralis major and the anterior deltoid. The posterior fibres also assist in lateral rotation and extension at the shoulder joint.

Teres major originates on the dorsal side of the inferior third of the lateral border of the scapula, and inserts onto the medial lip of the intertubercular groove of the humerus. Teres major acts to extend and medially rotate the arm at the glenohumeral joint, and works with latissimus dorsi and pectoralis major to pull the torso upwards when the upper limbs are fixed.

The remaining muscles in this group are referred to as the rotator cuff muscles: supraspinatus, infraspinatus, subscapularis and teres minor. They all originate on the scapula and insert on the tubercles of the humerus, and act to assist movement and stabilize the glenohumeral joint.

Supraspinatus originates from the supraspinous fossa on the dorsal surface of the scapula and inserts into the upper facet on the greater tubercle. The muscle passes between the coracoid and acromion processes deep to the coracoacromial ligament, and superior to the glenohumeral joint. The muscle acts to abduct the arm at the glenohumeral joint to approximately 20° before deltoid takes over.

Infraspinatus originates from the infraspinous fossa, on the dorsal surface of the scapula, via tendinous intersections that package the muscle fibres into bundles. Evidence of the attachments of these intersections can be seen onto the scapula as oblique ridges visible on the blade. Infraspinatus inserts on the middle facet of the

greater tubercle of the humerus, and acts to laterally rotate the arm at the glenohumeral joint.

Subscapularis originates from the subscapular fossa, on the ventral surface of the scapula. It inserts onto the anteriorly oriented lesser tubercle of the humerus, and, as a result, acts to medially rotate the arm at the glenohumeral joint.

Teres minor originates from the upper two-thirds of the dorsal surface of the lateral border of the scapula, and inserts onto the inferior facet of the greater tubercle of the humerus. Teres minor acts to laterally rotate the arm at the glenohumeral joint, but can also assist in adduction of the arm.

Muscles of the arm

The muscles of the arm that cross the glenohumeral joint include coracobrachialis, biceps brachii and triceps brachii. They all originate proximally from lateral features of the scapula and insert distal to the glenohumeral joint. A summary of this group of muscles can be found in Table 2.5.

Coracobrachialis originates from the coracoid process of the scapula and inserts on the medial side of the mid-shaft of the humerus. It assists in adduction of the arm at the glenohumeral joint.

Muscle	Origin	Insertion	Innervation	Action
Coraco-brachialis	Tip of the coracoid process	Medial side of the mid-shaft of the humerus	Musculo-cutaneous nerve (C5+6)	Flexion of the arm at the glenohumeral joint
Biceps brachii	Supraglenoid tubercle of the scapula (long head) and tip of the coracoid process of the scapula (short head)	Radial tuberosity	Musculo-cutaneous nerve (C5+6)	Flexion of the arm at the glenohumeral joint,
[long head of] triceps brachii	Infraglenoid tubercle of the scapula	Olecranon process of the ulna	Radioal nerve (C6-8)	Extension at the elbow, extension and adduction at the glenohumeral joint.

Table 2.5: Muscles of the arm that have actions at the glenohumeral joint.

Biceps brachii originates from the pectoral girdle from two tendinous heads; the long head exists within the glenohumeral joint surrounded by a synovial sheath and runs in the intertuberclar groove to attach to the supraglenoid tubercle of the scapula. The short head originates with coracobrachialis from a shared tendon on the coracoid process of the scapula. The two heads unite to form a single belly in the anterior arm. This belly has to distal attachments: one tendon that inserts on the radial tuberosity and an aponeurosis that deviates medially to blend with the deep fascia of the forearm.

Biceps brachii crosses both the shoulder and the elbow joints, and as a result produces movements at both. It is a powerful flexor of the arm at the glenohumeral joint, and also acts to supinate the forearm due to its distal aponeurosis that attaches on the medial aspect of the forearm.

Triceps brachii inserts distally on the olecranon process of the ulna, and has three proximal origins. The medial and lateral heads both originate from the humerus, and have no interactions with the pectoral girdle; they will not be considered here. The long head originates as a tendon from the infraglenoid tubercle. By acting in unison, the three heads of triceps brachii produce extension at the elbow joint. Additionally, the long head produces extension of the arm at the glenohumeral joint when deployed in isolation.

Summary of muscular attachment sites of the scapula

Figure 2.4 graphically shows the scapular attachment sites of the muscles of the pectoral girdle, while Table 2.6 summarises the actions of these muscles.

Affected structure	**Movement**	**Muscles**
Scapula	Protraction	Serratus anterior, pectoralis minor
	Retraction	Rhomboid major and minor, trapezius
	Elevation	Superior fibres of trapezius, levator scapulae
	Depression	Pectoralis minor, inferior fibres of trapezius
	Lateral Rotation	Trapezius, serratus anterior
	Medial Rotation	Rhomboid major and minor, levator scapulae, pectoralis minor
Arm	Abduction	Supraspinatus, deltoid
	Adduction	Coracobrachialis, latissimus dorsi, teres major, pectoralis major
	Flexion	Anterior fibres of deltoid, coracobrachialis, long head of biceps brachii, pectoralis major
	Extension	Latissimus dorsi, teres major, posterior fibres of deltoid, long head of triceps brachii
	Lateral Rotation	Teres minor, infraspinatus, posterior fibres of deltoid
	Medial Rotation	Subscapularis, teres major, latissimus dorsi, pectoralis major, anterior fibres of deltoid

Table 2.6: Summary of movements at the pectoral girdle.

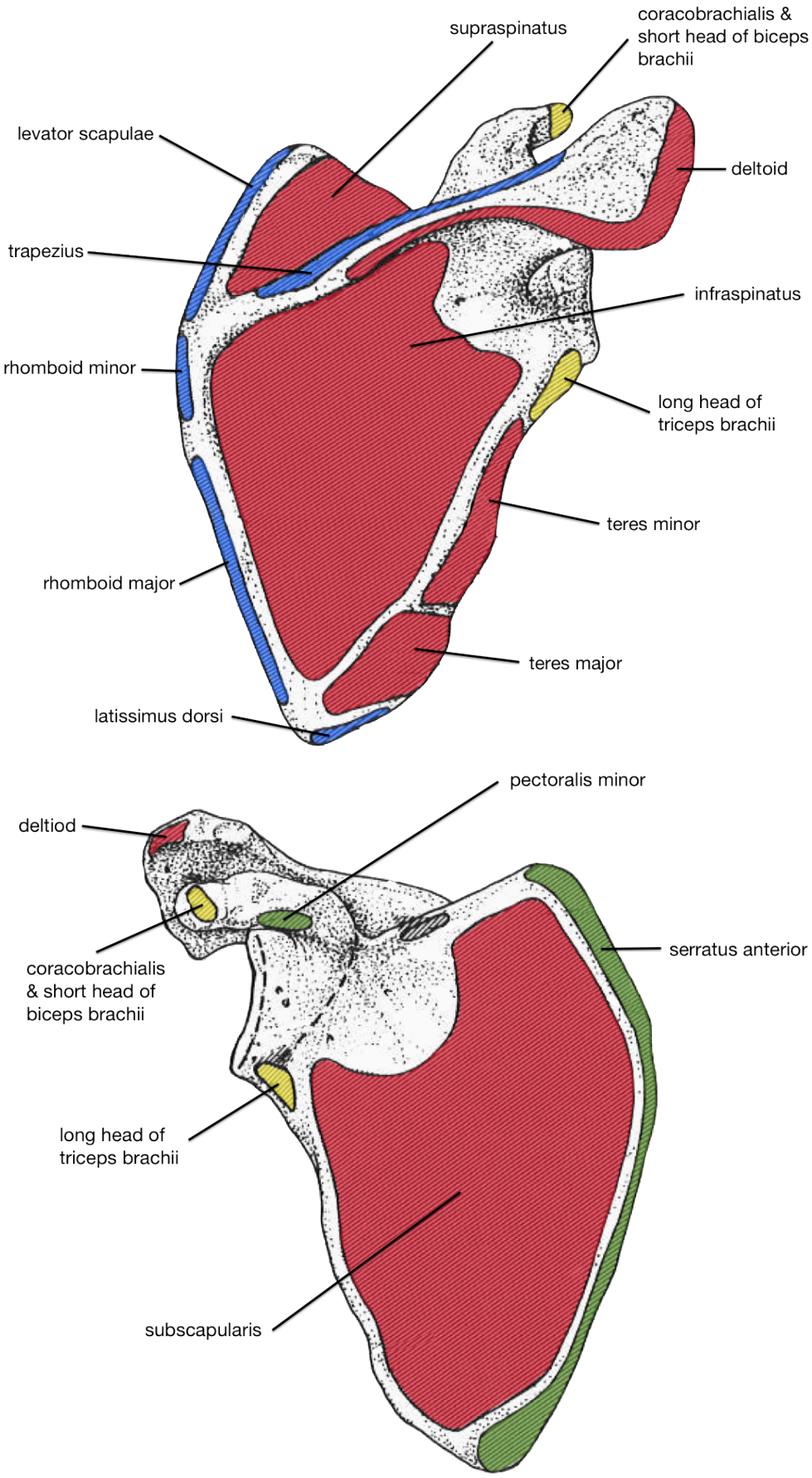

Figure 2.4: Muscle attachment sites of the right adult scapula. Colours refer to the four groups outlined in Table 2.1. Blue = muscles connecting the upper extremity to the vertebral column; Green = muscles connecting the upper extremity to the chest wall; Red = muscles of the shoulder; Yellow = muscles of the arm. (Adapted from Scheuer and Black, 2000)

Vasculature & Lymphatics

The region of the pectoral girdle, specifically the axilla, acts as a conduit between the thorax and the upper limb for vasculature, lymphatics and nerves. The tissues of the pectoral girdle take their blood supply from the large vascular structures that ultimately supply the entire upper limb.

The subclavian artery arises from the brachiocephalic trunk on the right side and the arch of the aorta on the left. The subclavian artery exits the chest superior to the first rib and inferior to the clavicle. The artery passes posterior to the scalenus anterior muscle, which attaches to the scalene tubercle on the superior surface of the first rib, and begins to passes inferolaterally. At this point it makes contact with the first rib and contributes to an impression on the superior surface of the bone. As the artery passes next to the lateral border of the first rib it is renamed as the axillary artery and continues to travel inferiorly deep to pectoralis minor. The axillary artery continues into the arm and becomes the brachial artery at the inferior border of teres major.

Various branches leave this artery as it travels through the pectoral region. These branches supply the tissues of the girdle and contribute to the scapular anastomosis that supplies the bone. The subclavian artery is divided into three sections:

1. Proximal to the medial border of scalenus anterior
2. Deep to scalenus anterior
3. Distal to the lateral border of scalenus anterior

The first section of the subclavian artery gives rise to three arteries: the vertebral artery, internal thoracic artery and the thyrocervical trunk. Of these three branches, only the thyrocervical trunk contributes to the vascular supply of the pectoral girdle: the thyrocervical trunk further divides into the inferior thyroid, suprascapular and transverse cervical arteries.

The second section of the subclavian artery gives rise to the costocervical trunk, which further divides into the deep cervical and superior intercostal arteries.

The third section of the subclavian artery usually gives rise to the dorsal scapular artery. However, in approximately one third of cases, the dorsal scapular artery may arise as a deep branch of the transverse cervical artery.

Of these branches, the suprascapular branch of the thyrocervical trunk and the dorsal scapular artery (either from the thyrocervical trunk, or directly from the subclavian artery) contribute to the anastomosis of vessels that supply the scapula. The anastomosis also ensures that the upper limb is supplied despite movements, or potential damage, at the glenohumeral joint.

The axillary artery, which is the continuation of the subclavian artery, also gives various branches. The axillary artery is also divided into three parts:

1. Proximal to pectoralis minor
2. Posterior to pectoralis minor
3. Distal to pectoralis minor

The superior thoracic artery branches from the first part of the axillary artery.

The thoraco-acromial and lateral thoracic arteries arise from the second part of the axillary artery.

The subscapular artery arises from the third part of the axillary artery and branches into the circumflex scapular artery and the thoracodorsal artery. The anterior and posterior circumflex humeral arteries also arise from the third part of the axillary artery.

2.2. Developmental Anatomy

Early Development

Lateral plate mesoderm opposite somites 8-10 (future vertebrae C5 – C7) give rise to the upper limb buds at the beginning of week 5 of fetal development (Huang et al., 2000; Scheuer and Black, 2000). Mesenchyme then begins to condense within the bud and a scapular precursor is recognisable by the 37th day (Gardner and Gray, 1953a; Moore and Persaud, 1998). Lewis (1901 in Gardner and Gray, 1953b) found the scapula consisted entirely of mesenchyme at 37 days and precartilage at 38 days.

Despite this generally accepted account, recent gene studies have shown that the pectoral girdle may have additional origins. It is thought that while the posterior neck region and shoulder girdle are derived from mesenchyme, neural crest cells may give rise to the 'anterior lining' of the shoulder girdle (Matsuoka et al., 2005).

The theory of complex scapular origin is further advanced by Huang et al (2000) who showed that in avian species, only the scapular head and neck are lateral plate mesoderm derived, whereas the blade of the scapula is derived from somites (specifically the dermomyotome).

Local organisation of the scapula is regulated by a series of genes:

- *Hox* genes are believed to organise the lateral plate component of the scapula (the head and neck), although the molecular mechanism of morphogenesis remains uncertain (Aubin et al., 1998; Moore and Persaud, 1998; Huang et al., 2000; Kuijper et al., 2005).
- The scapular 'blade', derived from somitic dermomyotome, has been shown to be very strictly regulated by the *Pax1* gene; cells of the scapular blade are organised craniocaudally in the same order as the somites from which they are derived (Bialek et al., 2000; Huang et al., 2000; Kuijper et al., 2005; Huang et al., 2006). Furthermore, the *Pax1* gene has been shown to be controlled by *kkt*,

mutation of which causes absence of the acromion process (Bialek et al., 2000).

- *Tbx15* null mutant mice have been shown to display complete absence of the centre region of the blade (Kuijper et al., 2005; Singh et al., 2005; Huang et al., 2006).

Chondrification

During Week 6, as the limb buds develop, the mesenchymal condensations undergo chondrification to form hyaline cartilage bone precursors (Gardner and Gray, 1953a; Scheuer and Black, 2000). These anlage migrate caudally to distance themselves from their cervical origins so that by day 44 they lie opposite the first rib, by day 48 they have reached the fifth rib and by day 52 the lower angle has reached the fifth intercostal space (Gardner and Gray, 1953a; Moore and Persaud, 1998; Scheuer and Black, 2000).

Following the craniocaudal gradient of development, chondrification of the humeral anlage is reported to occur later than scapular chondrification (Gardner and Gray, 1953a; Moore and Persaud, 1998).

Cavitation of the shoulder joint begins in week 7, during which time no scapular spine is present. By the end of this week (approximately day 49) the spine of the scapula becomes visible, and the glenoid deepens as the labrum begins to form with the glenoid region becoming increasingly concave during week 8. Cavitation of the shoulder joint is completed by week 10 (Gardner and Gray, 1953a; Scheuer and Black, 2000).

At this stage of development, the scapula does not display its classic ventral concavity. This is due to the lack of a distinct supraspinous fossa. However, as the supraspinous muscle mass increases, perichondral ossification of the supraspinous fossa is triggered. This results in two nonparallel fossae either side of the spine (one

caudal, one cranial), producing a concave ventral surface, with the apex of the concavity corresponding to the underside of the spine (Scheuer and Black, 2000).

Ossification

Ossification of the scapula commences in week 8 of uterine life around the ventral aspect of the surgical neck. It is reported that this ossification is perichondral in nature despite no muscle activity is present at this location to initiate this change (Scheuer and Black, 2000); alternative theories have been presented to account for the initiation of perichondral ossification in the absence of muscle activity:

One such theory suggests that there may be a neurogenic influence on perichondral ossification: Laurenson (1964) showed that primary ossification of the ilium is initially perichondral and begins around the greater sciatic notch, and perhaps crucially the location of the sciatic nerve. Laurenson (1964) also compares this mode of ossification to the perichondral ossification seen in the clavicle (and its proximity to the brachial plexus) and the ribs, and claims perichondral bone formation has a developmentally protective role for immediate neurological tissues.

This neurogenic theory can also be applied to the scapula. As previously mentioned, the supraspinous fossa is not well developed at this stage, and the observed primary ossification site of the scapula (at the ventral aspect of the surgical neck) corresponds closely to the location of the suprascapular nerve as it relates to the bone's superior border.

Despite the theory of neurogenic perichondral ossification seeming plausible, it is perhaps more accurately described as a hypothesis, since it is unproven and based on a single paper. Laurenson (1964) attributes primary ossification of the ilium to neurogenic influence with little verification, and does not consider alternative triggers. For example, in each of the locations Laurenson uses to illustrate his neurogenic theory (ilium, clavicle and ribs), the proximity of the vascular channels is ignored. Although the reasons are unclear, Laurenson attributes perichondral ossification to

nearby nerves, and discounts the potential role of the vascular structures they invariably accompany – in the case of the scapula, the suprascapular artery, which lies closer to the ossification centre than the suprascapular nerve.

Although the idea of neurogenic initiation of perichondral ossification is a tenable hypothesis, the fact remains that the initial perichondral ossification of the ilium is observed but not fully understood; and more relevant to this thesis, it is neither observed nor understood in the scapula.

In addition to the poorly understood nature of the scapula's suspected perichondral ossification, descriptions of the subsequent (and often simultaneous) endochondral ossification occurring in the rest of the scapula are equally sparse.

Scheuer and Black (2000) observed the largest nutrient foramen for the scapula on the lateral aspect of the supraspinous fossa where it meets the ventral aspect of the spine. This is thought to be the site of endochondral ossification – triggered by invasion of the suprascapular artery. This view was shared by Ogden and Phillips (1983), who also offered the only complete theory of scapular ossification.

Ogden and Phillips stated that scapular endochondral ossification begins at the lateral aspect of the supraspinous fossa, and extends bidirectionally to the proximal (vertebral) and distal (glenoid) borders (Figure 2.5).

However, Ogden and Phillips' ossification model is not based solely on endochondral ossification. They also suggested that intramembranous (IM) ossification takes place in the supraspinous and infraspinous fossae (Figure 2.5). The IM ossification they refer to was not considered to be initial perichondral ossification per se, but dermal ossification as seen in the flat bones of the cranium.

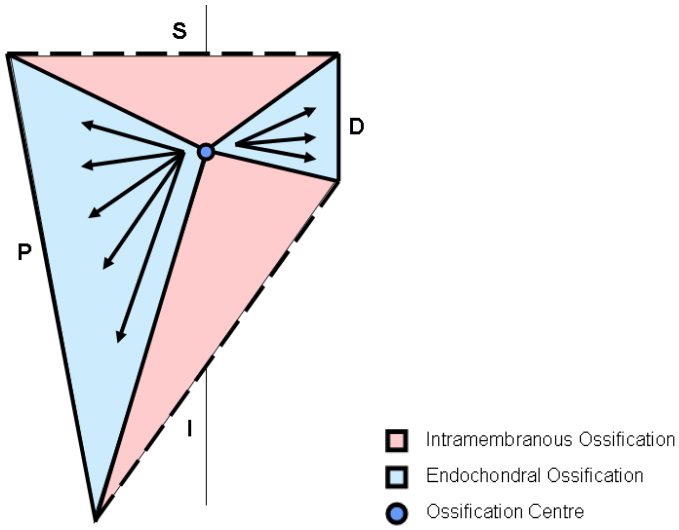

Figure 2.5: The Ogden & Phillips model of scapular ossification.
(Adapted from Ogden and Phillips, 1983)

The authors of this theory argue that the thick areas of the scapula (spine, glenoid and medial border) were formed endochondrally, and the thinner fossae, formed intramembranously. Although this model seems to have some logic on first impression, it does not hold up to more detailed scrutiny.

The argument for the involvement of endochondral ossification is sound:

- The presence of the nutrient foramen is consistent with endochondral ossification, such as the long bones, and crucially the ilium.
- The scapula's homology with the ilium is relevant when considering scapular ossification. Laurenson (1964) has shown that the ilium initially ossifies perichondrally, before endochondral ossification completes its development.
- The evolutionary origin of the girdles would suggest endochondral development.
- The presence of epiphyses is unique to endochondral bones. Ogden and Phillips (1983) argue that scapular endochondral ossification is simply a "structural modification of longitudinal bone growth". This idea seems plausible when considering their observations of endochondral scapular ossification in marine mammals, whose trabecular remodelling is minimal. In

the scapulae of developing fin whales, for example, trabecular bone retains its longitudinal orientation and shows a “progressive, constant addition to each elongating column once it is formed” (Ogden and Phillips, 1983).

- The existence of cartilaginous anlagen has been frequently observed (Gardner and Gray, 1953; Huang et al, 2000; Ogden and Phillips, 1983; O’Rahilly and Gardner, 1972; Scheuer and Black, 2000).

However, the argument for the presence of dermal IM ossification is less compelling. Much of Ogden and Phillips’ (1983) justification for the presence of dermal IM ossification was based on the argument that typical endochondral ossification did not explain the morphology of the fossae.

The absence of epiphyses on the superior and inferior borders does not mean endochondral ossification could not have occurred, particularly when applying the modified long bone growth model. Just as the absence of superior and inferior epiphyses does not eliminate endochondral ossification, it by no means confirms the presence of dermal IM ossification.

The supposition that ‘thin’ fossae undergo dermal IM ossification and ‘thick’ buttresses are endochondrally ossified may be flawed and considers only adult morphology. Upon examination of perinatal scapulae, it becomes clear that at birth the fossae are not thin; they are in fact just as thick as the buttresses (Figure 2.6).

There is no evidence to suggest that the thickness of bone in either the juvenile or the adult can be used as a means of retrospectively determining its mode of ossification. Furthermore, if there were evidence to suggest that dermal IM bone is thin (and endochondral bone morphologically thick) it would directly contradict well-understood ossification patterns elsewhere in the body. For example: dermal bones, such as the frontal bone and the squamous part of the occipital bone, could not be described as thin; similarly, the blade of the ilium is frequently thin in its centre, despite its endochondral origins.

In the scapula this supposition causes further problems. The lateral border (supposedly dermal) is thicker than the medial (supposedly endochondral) border.

Considering the evolutionary history of dermal bone as a protective and defensive structure, it seems illogical and juxtaposed to assume that dermal bone is traditionally thin in the adult scapula.

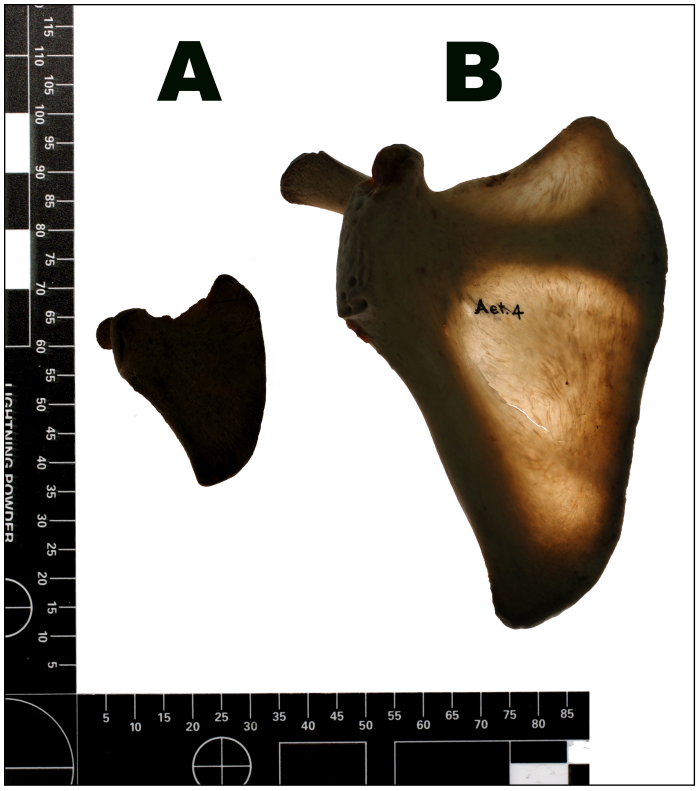

Figure 2.6: A backlit perinatal scapula (A) alongside a backlit scapula of a four year old (B)

Other bones that are part dermal, part endochondral (e.g. temporal, occipital) develop separately, before eventually fusing after substantial independent ossification. This is certainly not seen in the scapula, which seems to develop as a single entity.

Put simply, the Ogden and Phillips (1983) theory of scapular development is based on final adult morphology, rather than actual developmental observations.

Examination of juvenile scapulae from the Scheuer Collection clearly shows that it develops as one relatively thick bone with internal trabecular structures. It is also clear that the bone thins in the regions of the fossae as the bone matures (Figure 2.7). The

fossae of neonatal scapulae are relatively thicker in real terms than the fossae of adult scapulae. This further discredits the reasoning that dermal IM ossification occurred *in utero* due to the presence of thin fossae in the adult.

Figure 2.7: A series of backlit scapulae in order of ascending skeletal age. 5 months (left); 4 years (middle); 12 years (right).

Despite rejecting dermal IM ossification, the role of perichondral IM or endochondral ossification of the scapula is still plausible. The presence of a cartilaginous anlagen (Gardner and Gray, 1953a; O'Rahilly and Gardner, 1972; Ogden and Phillips, 1983; Huang et al., 2000; Scheuer and Black, 2000), as well as documented perichondral ossification in the homologous ilium (Laurenson, 1964), seems to favour these as alternative modes of ossification. This conventional dual mode of ossification has been alluded to in the literature (Huang et al., 2000; Scheuer and Black, 2000; Sánchez-Villagra and Maier, 2006). Not only does initial perichondral and subsequent endochondral ossification correspond with the situation in the ilium, the absence of dermal IM ossification in the scapula also favours the theory that the scapula develops as a modified long bone (Ogden and Phillips, 1983).

2.3. Evolutionary Context

When considering development of the juvenile human scapula it is prudent to consider its evolutionary roots. By exploring the evolutionary origin of the scapula the rudimentary fundamental principles that govern its development can be explored. The relevance of comparative studies of the scapula is highlighted by Oxnard (1968) who has shown that the gross anatomy of the scapula is functionally very similar across a wide range of species, indicating that an ancient genetic origin which may restrict significant morphological variation.

Ancient Origin of the Limbs & Girdles

In an evolutionary context, the girdle and limb elements constituting the appendicular skeleton belong to the general somatic system of endoskeletal structures, most likely from the fins of crossopterygian fishes (Romer and Parsons, 1977; Weichert and Presh, 1975).

Anterior pectoral appendages are situated just behind the gills in fish, or at the border of the neck and chest region in land vertebrates. Although the theory of cervical origin has its roots in comparative studies, recent findings of genetic studies add new weight to this school of thought (Aubin et al., 1998; Bialek et al., 2000; Matsuoka et al., 2005). Typically, the posterior pelvic appendages are found just anterior to the cloaca or anus (Romer and Parsons, 1977).

As tetrapods we tend to think of paired limbs as actively propulsive structures, but this was not their initial function (Romer and Parsons, 1977). It is believed that appendages (both paired and unpaired) evolved in response to unwanted deviation during aquatic locomotion – i.e. roll, pitch and yaw (Wake, 1992)(Figure 2.8).

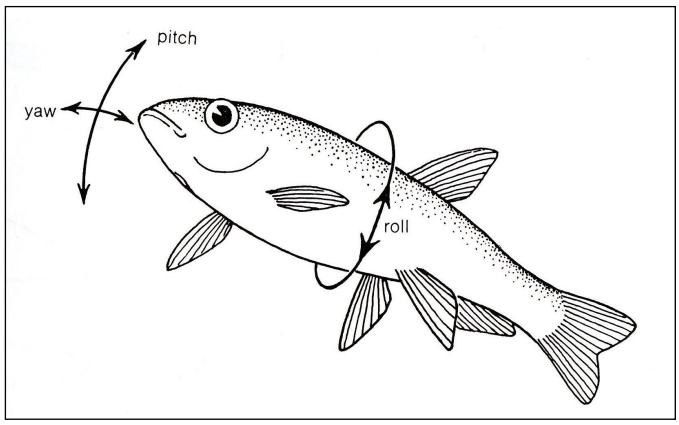

Figure 2.8: Unwanted movement deviations that the fin fold extensions oppose. (Wake, 1992)

The evolution of such appendages began with the appearance of lateral and median fin folds. The majority of the fin folds regressed, leaving behind isolated fins (Figure 2.9). The remaining fins were either paired or unpaired:

- Unpaired fins persist on the midline as remnants of either the median fin fold, or the midline-fused lateral fin folds.
- Paired fins remain as bilateral structures, in both the pectoral and pelvic regions. It is these paired lateral fins that are believed to be the precursors of the (endochondral) girdles and limbs (Wake, 1992).

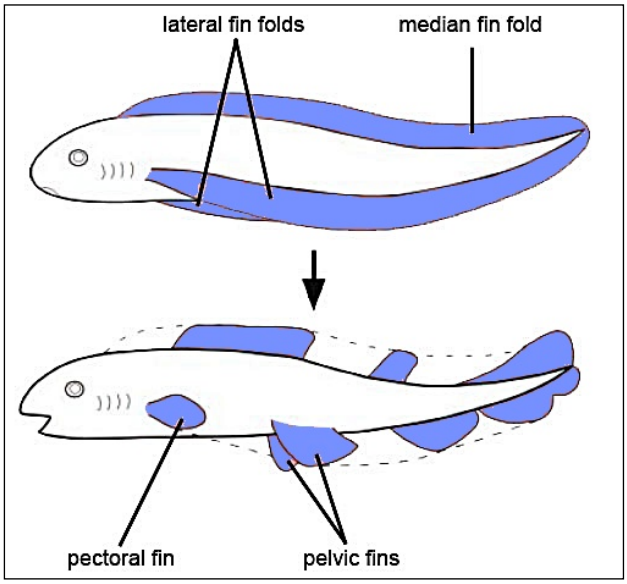

Figure 2.9: Regression of lateral fin folds into paired fins, which are precursors to the limbs, pelvic girdle and the (endochondral) pectoral girdle. (Adapted from Tamura et al., 2001).

It is most likely that the girdles formed **after** the paired fins as a consequence of increased locomotor function. As more stresses and strains were placed on the fins, they required internal bracing mechanism to remain useful (Graham, 2005). Without such bracing, the fins would presumably have no influence on the body they were attempting to stabilise, and would move freely without effect.

Initially, the formation of the pectoral girdle would have been opportunistic in nature, as the pectoral fins gained internal bracing from the existing dermal thoracic (and cranial) armour. However, the absence of dermal armour in the pelvic region combined with reduction in thoracic dermal armour as the fish became more mobile, would create the need for a 'custom built' endochondral girdle (Wake, 1992).

The endochondral girdles had their origins in the same general somatic skeletal structures as the fins themselves, specifically the pterygiophores. Each pterygiophore, consisting of radial and basal components, exists within the fins as internal strut-like supports. The girdles seem to have derived from the basal pterygiophores which enlarged and extended medially, eventually coming into contact with each other on the midline with each other (Figure 2.10), and providing a central endochondral structure to act as an anchor for the limbs (Wake, 1992).

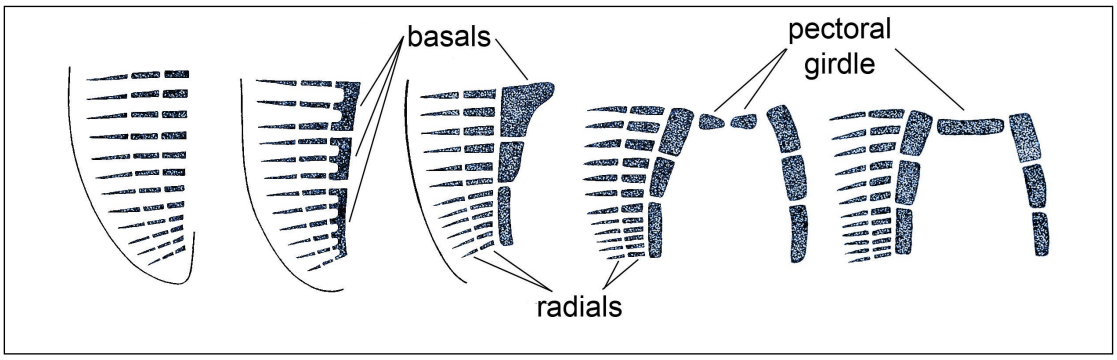

Figure 2.10: Morphological sequence showing the formation of the endochondral component of the limb girdles from basal pterygiophores. (Adapted from Wake, 1992)

While bearing in mind the ancient origin of the endochondral and dermal components of the girdles it is their subsequent evolution that is particularly relevant in the context of this thesis. An understanding of the evolutionary history of the girdles is useful both when observing the declining role of dermal bone in the pectoral girdle, and when considering the homology of the scapula and the ilium.

Evolution of the Pectoral Girdle

The general evolution of the pectoral girdle is most succinctly described as a progressive reduction in dermal bones, and a progressive proliferation of endochondral bones.

Despite dermal bone's wide spread reduction, it is still present to some extent in all tetrapods (Wake, 1992). As previously stated, the dermal component of the girdle would have derived from the dermal armour that would have covered the majority of the anterior part of the fish body (Romer and Parsons, 1977). In the early lobe-finned fish, the main dermal girdle component was the cleithrum, which articulated with several other components of the dermal girdle (clavicle, anocleithrum, supracleithrum), which in turn articulated with the dermal thoracic armour and indeed the skull via the post-temporal bone (Figure 2.11A). At this stage in evolution, the endochondral girdle was in its infancy and comprised only of a small scapulocoracoid bone, which articulated with the limb distally and cleithrum medially (Romer and Parsons, 1977).

The advent of digits in *Acanthostega* (the first true tetrapod capable of movement on land) caused the girdle to adapt to a more active role, thus leading to a reduction in dermal elements and expansion of the scapulocoracoid (Figure 2.11B) (Vickaryous and Hall, 2006). Presumably musculature was becoming well developed, since the girdle became independent from the skull at this time.

Further reduction of the dermal girdle, particularly the cleithrum, and the partitioning of the scapulocoracoid into a dorsal scapula and a vental coracoid are seen in

Seymouria (the first tetrapod to adapt to life on land), with the glenoid now involving two distinct endochondral bones (Figure 2.11C) (Vickaryous and Hall, 2006).

In basal amniotes (including reptiles) the coracoid bone undergoes another partitioning, into a procoracoid cranially and a metacoracoid caudally, each contributing to the glenoid (Figure 2.11D,E). As amniotes evolved further, the procoracoid began to relinquish its involvement with the glenoid (Figure 2.11F). In modern mammals only the monotremes retain three distinct endochondral elements (Figure 2.11G), with the procoracoid still playing no role in the glenoid. The monotreme pectoral girdle continues the pattern of reducing dermal bones, as the cleithrum fails to ossify. In therians, dermal involvement in the girdle has become reduced to only the clavicle (Figure 2.11H); the more modern metacoracoid becomes the coracoid process (McGonnell, 2001; Vickaryous and Hall, 2006), while the fate of the more ancient procoracoid is not well understood.

In summary, it is useful to consider that the dermal girdle component adopts the role of a stabiliser, while the endochondral girdle provides support for an active, mechanical and propulsive limb. The decreased dermal contribution and increased endochondral contribution reflects the changing role of the limb itself – from a passive stabiliser to an active propeller. A similar process is involved in the pelvic girdle, but with the total absence of dermal influence.

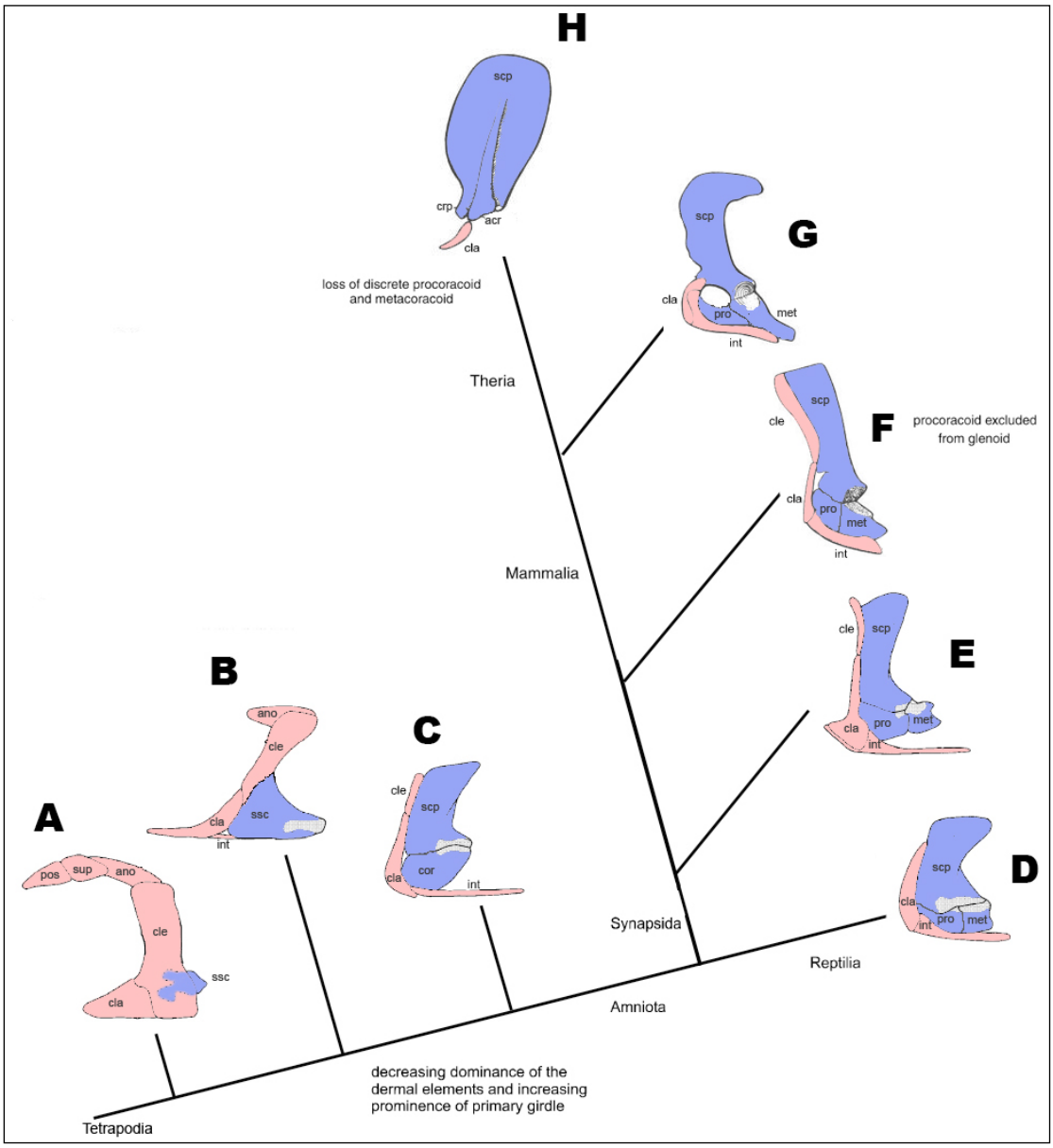

Figure 2.11: Functional cladogram showing evolution of the pectoral girdle.
acr (acromion); ano (anocleithrum); cla (clavicle); cle (cleithrum); cor (coracoid); crp (coracoid process); int (interclavicle); met (metacoracoid); pos (post-temporal); pro (procoracoid); scp (scapula); scc (scapulocoracoid); sup (supracleitrum).
A=Eusthenopteron; B=Acanthostega; C=Seymouria; D=Captorhinus; E=Dimetrodon; F=Dicynodont (kannemeyeria); G=Monotreme (duckbill); H=Didelphys (opossum)
Dermal bones in pink – Endochondral bones in blue – Glenoid in grey
(Adapted from Romer, 1956; Romer and Parsons, 1977; Vickaryous and Hall, 2006)

Evolution of the Pelvic Girdle

As with the endochondral pectoral girdle, the pelvic girdle originated from the basal pterygiophores of the pelvic fins, in a process similar to the pectoral girdle (Figure 2.10) (Wake, 1992).

In the lobe finned fish (e.g. Sarcopterygians, Rhizodonts, *Eusthenopteron*) the primitive pelvic girdle consisted of an endoskeletal bar embedded in the ventral body wall musculature (Figure 2.12A). An unossified symphysis and acetabulum have been observed, with pubic and iliac processes, but without visible traces of boundaries between three discrete bones. No sacral attachment is present, presumably because the fin exists in a largely passive capacity as a stabiliser (Coates et al., 2002).

In *Acanthostega* (Figure 2.12B) the pelvis is much larger, and the iliac region articulates with the axial skeleton via a sacral rib. Both these observations are most likely attributable to the amphibian's occasional terrestrial locomotion, as opposed to passive stabilisation. As in the lobe-finned fish, a broad ischial plate has been observed and the two innominates are united by an ischiopubic symphysis. Also, in *Acanthostega* there are no traces of sutures indicating the limits of the pubis, ischium and ilium (Coates et al., 2002).

In *Seymouria* (Figure 2.12C), the pelvis displays obvious buttressing above the acetabulum as well as visible sutures between the pubis, ischium and ilium (Coates et al., 2002). It is interesting to consider that *Seymouria* was the first "truly terrestrial" tetrapod (Berman et al., 2000), and shows signs of buttressing. Edwards (1989) has shown that the limbs, and girdles, evolved as underwater locomotive structures rather than for locomotion on dry land. Bearing this in mind, it becomes clear that the transition from aquatic locomotion to terrestrial locomotion (as seen in *Seymouria*) resulted in major biomechanical and morphological changes.

In reptiles (Figure 2.12D), the blade of the ilium increases in surface area to accommodate more extensive limb muscles on the outer surface, and for the attachment medially of more sacral ribs (Romer, 1956).

Mammal and mammal-like reptile pelves (Figure 2.12E,F,G,H) undergo significant rotation; the ilium, which grew mainly caudally and dorsally in more primitive species, comes to extend ventrally as it articulates with the sacrum. Conversely, the pubis and ischium move posteriorly so that the flat plate of the girdle hardly extends to the acetabulum (Romer and Parsons, 1977).

Romer and Parsons (1977) observe:

The mammalian ilium is primitively a rather slender rod, triangular in section; however in heavy-bodied ungulates or bipeds there are powerful gluteal muscles running from ilium to femur this bone may be much expanded.

As with *Seymouria's* girdle adaptation to life on land, this also shows the girdles' ability to adapt morphologically to 'extreme' functional changes.

Finally, unique to monotremes and marsupials (Figure 2.12G,H), there is a pair of "marsupial bones" (prepubes). These extend cranially from the pubes and are thought to support the body wall or play a role in providing structural integrity to their pouch (Romer and Parsons, 1977).

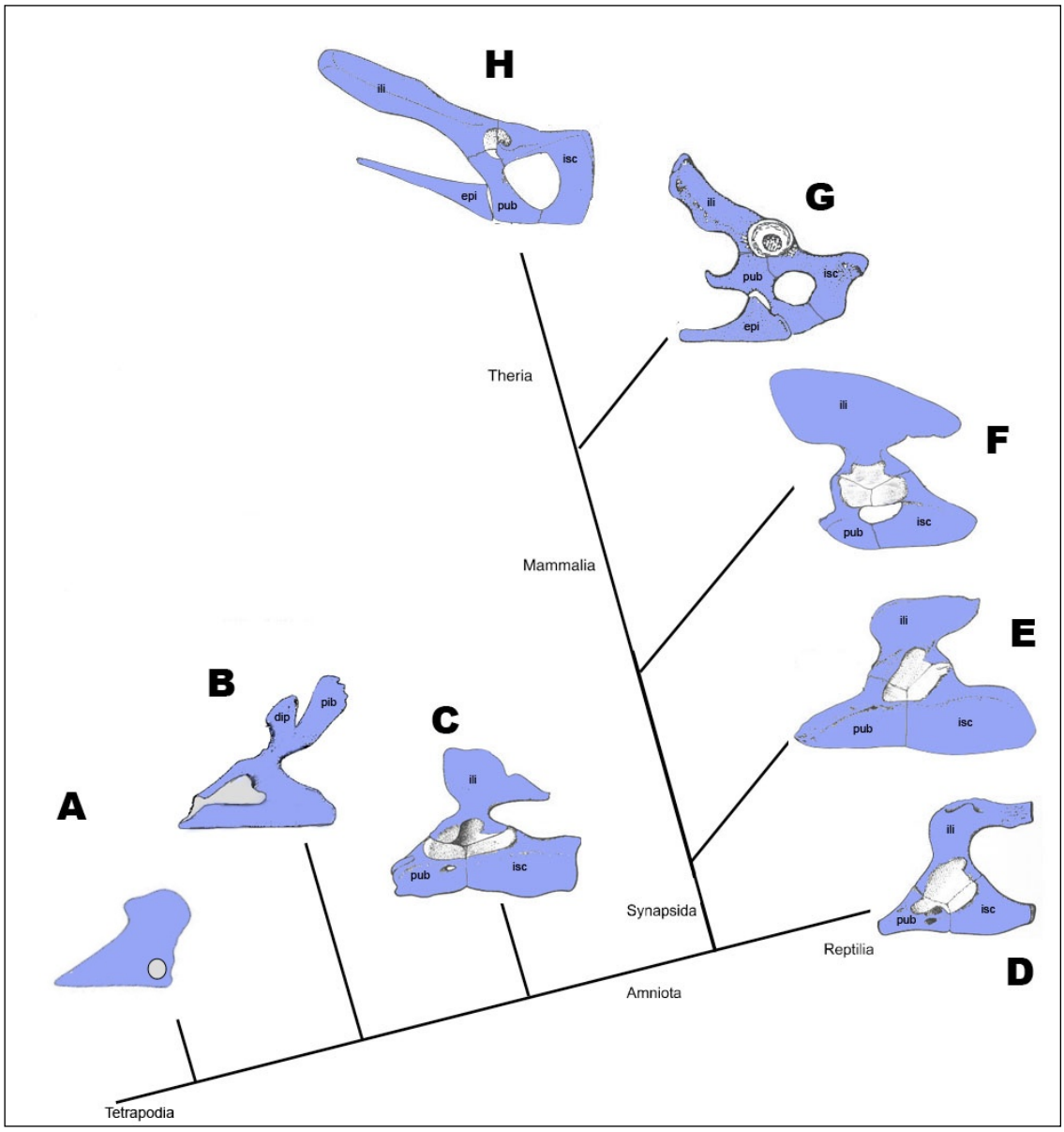

Figure 2.12: Functional cladogram showing evolution of the pelvic girdle.
dip (dorsal iliac process); epi (epipubis); ili (ilium); isc (ischium); pib (posterior iliac blade); pub (pubis)
A=Eusthenopteron; B=Acanthostega; C=Seymouria; D=Limnoscelis; E=Dimetrodon; F=Cynodont (cynognathus); G=Monotreme (duckbill); H=Didelphys (opossum)
Note all bones are endochondral (blue) – Acetabulum in grey
(Adapted from Romer, 1956; Romer and Parsons, 1977; Wake, 1992; Li and Luo, 2006)

Pectoral-Pelvic Homology

Homology of the hind- and fore- limbs (and their girdles) polarises evolutionary biologists. Charles Darwin made this statement in his ubiquitous *Origin of the Species*:

The anterior and posterior limbs in each member of the vertebrate and articulate classes are plainly homologous.

However, some modern comparative anatomists disagree. Romer and Parsons (1977) state:

Theories that pectoral and pelvic girdles are comparable, bone for bone, are purely fanciful.

Despite contrasting opinions, morphological similarities between the primitive limbs and girdles are visible, although the bone-for-bone homology is less clear (Figure 2.13, Figure 2.14).

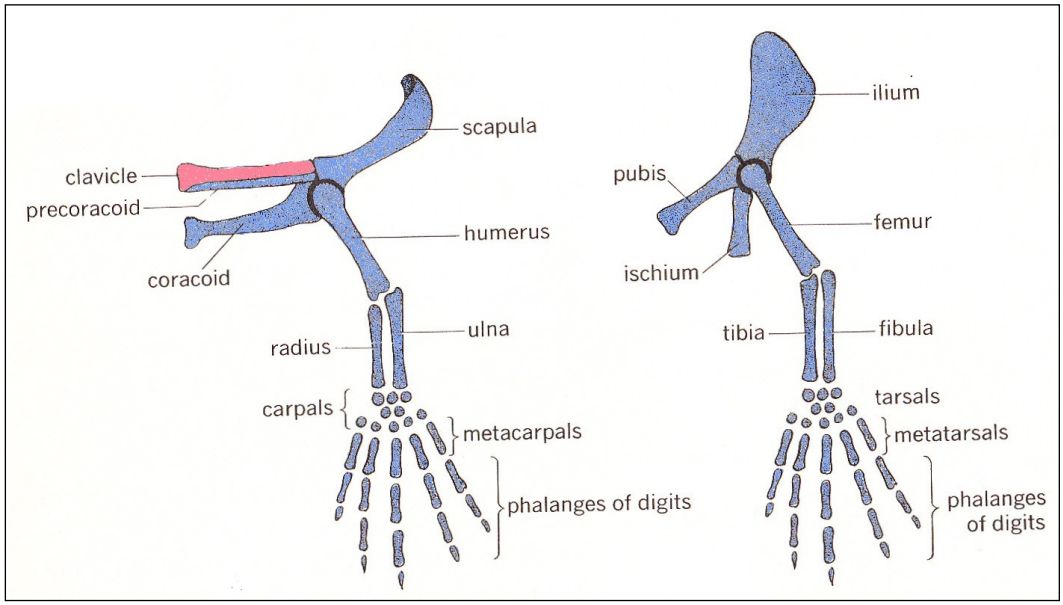

Figure 2.13: Comparison of the hind- and fore- limbs of generic tetrapods.
Left – forelimb; Right – hindlimb
(Adapted from Weichert and Presh, 1975)

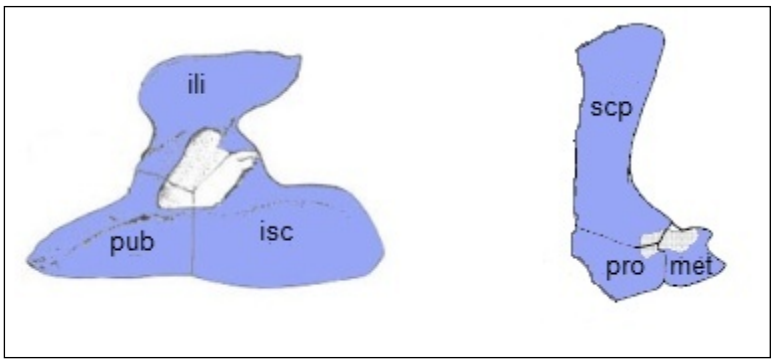

Figure 2.14: Comparisons of the girdles of *Dimetrodon*.
ili (ilium); isc (ischium); met (metacoracoid); pro (procoracoid); pub (pubis); scp (scapula)
Left – pelvic girdle; Right – pectoral girdle
(Adapted from Romer and Parsons, 1977; Vickaryous and Hall, 2006)

Apologists of limb homology theory would argue that the presence of three endochondral bones, each occupying comparative roles within the primitive girdle, and each deriving from basal pterygiophores in response to an active limb, is evidence of homology. However, antagonists of the theory would argue that there are significant differences: the absence of a dermal component in the primitive pelvic girdle raises questions, as do the apparent differences in genetic factors influencing configuration of the two regions.

When comparing the fore- and hind- limb girdles of basal amniotes, and even monotremes, it is possible to compare the ilium to the scapula, the pubis to the procoracoid, and the ischium to the metacoracoid. However, when trying to extrapolate this theory to include modern mammals, the deletion or modification of the metacoracoid and procoracoid causes problems. In modern mammals, humans included, it becomes almost impossible to equate the bones of the innominate to the bones of the pectoral girdle.

Despite confusion surrounding the metacoracoid and procoracoid, it seems that the scapula of primitive animals persists as the majority (perhaps all) of the human scapula. If this is the case, the scapula may well be homologous to the ilium – both in terms of its role in the primitive girdle, and its mode of ossification and development. In modern humans, its role has certainly changed since quadrupedalism, but it is

highly unlikely that this previously endochondral bone would betray 300 million years of evolution by adopting the even more ancient dermal IM ossification.

This becomes a crucial point when considering theories of development of the modern human scapula; particularly those which attempt to reintroduce dermal IM ossification to the development of the scapular blade (Ogden and Phillips, 1983).

2.4. Morphological Studies

Although the methodology employed in this thesis is largely novel, a series of similar studies have previously been conducted on the juvenile ilium:

In a radiographic study of thirty human fetal and neonatal ilia, Cunningham and Black (2009b) investigated the early patterns in trabecular bone arrangement prior to the influences of direct weight-bearing locomotion. They identified well-defined patterns of internal organization that corresponded with regions that have been attributed directly to forces associated with bipedal locomotion (Thomason, 1985; Carter et al., 1989; Rook et al., 1999; Fajardo and M ller, 2001; Ryan and Ketcham, 2002; Ryan and Krovitz, 2006). Their study postulated that patterns previously attributed to weight-bearing locomotive responses are present in the earliest stages of the development, perhaps indicating a predetermined template upon which locomotive influences may be subsequently superimposed and reinforced. Cunningham and Black alternatively suggest that this early pattern may mimic the adult form due to the effects of in-utero limb movement.

In a supplementary study, Cunningham and Black (2009a) report the findings of an analysis of micro-CT scans from 28 neonatal ilia, specifically the structural metrics bone volume fraction (BV/TV), trabecular thickness (Tb.Th), trabecular spacing (Tb.Sp) and trabecular number (Tb.N). They found that the previously reported rudimentary scaffold of the neonatal ilium could quantified in the trabecular bone, and suggested

that it could be attributable to other non-weight bearing anatomical interactions or even to a predetermined genetic blueprint.

Cunningham and Black (2009c) also conduced a study of the configuration of compact bone in the gluteal and pelvic iliac shells in thirty human neonatal ilia using micro-CT. Their analysis revealed a distinctive patterning consistent with the expected bone distribution achieved through early bone modelling and remodeling; i.e. thin cortices at the growing periphery of the bone, and thick cortices at the central ‘mature’ regions. They again point out the significance of evident remodeling in the earliest stages of pelvic development prior to the introduction of locomotive influences.

Chapter 3: Radiographic Study

Prior to undertaking analysis of trabecular organisation in the perinatal cohort, a qualitative study was carried out. The aim of this study was to describe general radiographic patterns both within the perinatal cohort and in subsequent developmental groups. The findings from this study were used to consider ontogenetic changes, and also assisted in the design of the subsequent quantitative study (Figure 1.1).

This initial study follows established techniques (Cunningham and Black, 2009b) to document patterns in the internal structures of developing bone. The findings of this study will be compared to the results of similar studies in the literature, specifically Cunningham and Black (2009b).

3.1. Materials & Methods

Specimens selected for the radiographic study (Table 3.1) were radiographed at Ninewells Hospital Dundee using a Multix Tube & Table (Siemens) radiographic system and digital detector plates with the assistance of an experienced clinical radiographer, at 55kV and 1.8mAs. The resulting digital radiographs were produced as 4.2 megapixel (1768x2368) TIFF format images and transferred to the University of Dundee via compact disks and transferred to a secure server upon arrival.

Age		***n***
Juvenile	Fetal (<0y)	3
	Perinatal (~0y)	16
	Infant (0-1y)	4
	Childhood (1-10y)	24
	Adolescence (>10y)	28
Adult		8
Total		**83**

Table 3.1: Specimens used in the qualitative radiographic study.

The images were opened in Adobe Photoshop CS3 v10.0 and converted from grayscale 8 bits/channel images to RGB colour 16 bits/channel images. Converting the radiographs into colour images permits the introduction of coloured pixels into the image; however no colour was added to the image at this stage. Prior to gradient mapping, the original radiographs were desaturated to eliminate any premapping colour from the images.

Although the radiographs could be studied at this stage, it became clear that finding definable patterns in monochromatic data was difficult. To solve this problem, a previously published method of gradient mapping was adopted and enhanced (Cunningham and Black, 2009b).

Gradient Mapping

Gradient mapping is the process whereby a range of consecutive grey values are converted into arbitrary colour groups so that areas of similar radio-opacity could be matched. Although these arbitrary colour groups could number as many or as few as the observer required, a four-colour gradient fill was selected to maintain consistency with previous studies (Cunningham and Black, 2009b), although slightly different thresholds were applied. Altering the thresholds from those used in Cunningham and Black (2009b) was required to take account of the differences in radiopacity between the ilium and the scapula.

Gradient mapping was employed so the observer could identify patterns in the radiographs with greater ease than if the original radiograph was analysed. The recognition and definition of patterns in an image comprising four arbitrary contrasting colours was considered more reliable and consistent than in traditional radiographs, which involve 256 different shades of grey.

The digital radiographs were processed in Adobe Photoshop CS3 v10.0 using an automated script, which was designed to facilitate batch processing of the images. The automated script instructed the application to open an image, apply the gradient mapping command then save a copy of the resulting image. This process was applied to all digital radiographs.

The colour thresholds selected for gradient mapping were:

- Areas of 0-30% opacity, corresponding to the most radiolucent areas of bone and background film, were recoloured yellow.
- Areas of 30-50% opacity were recoloured violet,
- Areas of 50-70% opacity were recoloured orange,
- Areas of 70-100% opacity, corresponding to the areas of greatest radio-opacity, were recoloured dark blue.

These gradient thresholds were consistent between scans and proved to be the most useful across the entire ontogenetic range, by providing a consistent range of colours and patterns despite large variations in radio-opacity. This process produced a series of images consisting of four contrasting colours, compared to 256 shades of grey (Figure 3.1), and allows easier detection of qualitative patterns.

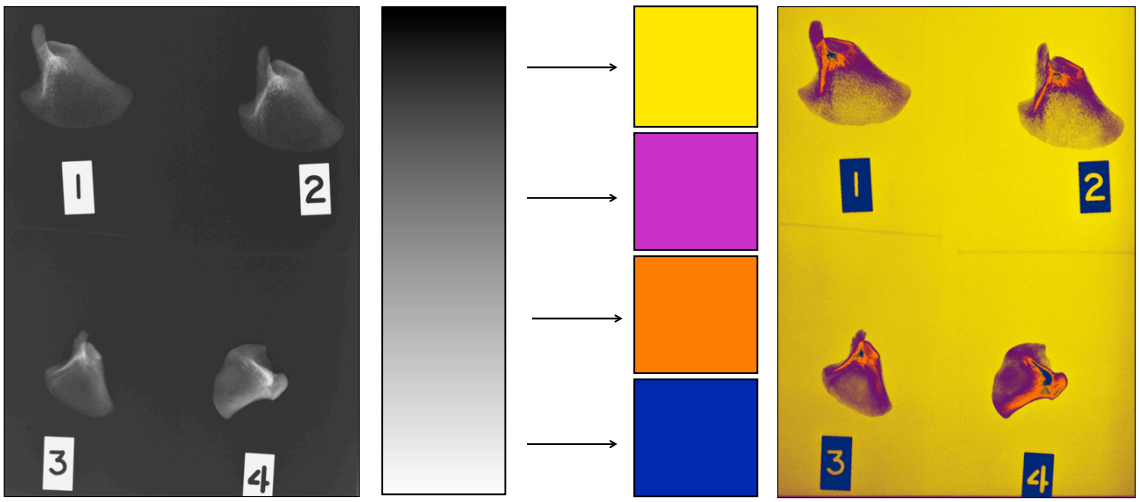

Figure 3.1: Graphic depiction of how greyscale values map to one of four colours. Black/yellow = radiolucent; white/blue = radiopaque.

The gradient mapped radiographs were printed onto sheets of A4 paper and patterns were identified and described. Skeletal ages of the specimens were not considered at this stage, only morphological features and patterns. Based on these perceived patterns, specimens were grouped into appropriate descriptive groups.

Colleagues familiar with radiography, gradient mapping and morphology of the scapula repeated the process of pattern identification and specimen grouping and produced similar results. It this therefore considered that this process is sufficiently objective and precise.

Eight groups were identified *post hoc* based on the distinct appearances of the infraspinous fossa, glenoid, spine and lateral border. The gross morphology of the scapula was also considered as it appeared either as broad and round, or narrow and angular. Some structures (e.g. the spine and supraspinous fossa) exhibited clear superimposition due to the nature of two-dimensional radiography, but, since this study does not aim to **quantify** regions of bone, superimposition did not deleteriously influence how the images interpreted during analysis.

3.2. Results

Group 1

This group contained 2 specimens; the youngest specimen in this group was 25 gestational weeks and the oldest was 28 gestational weeks (Table 3.2). A typical specimen from Group 1 is presented in Figure 3.2.

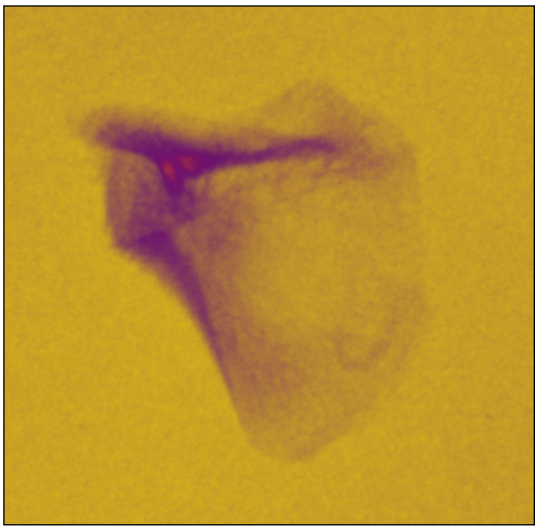

Figure 3.2: A typical specimen from Group 1

Specimen	Age
SC-371	25 G.W.
SC-089	28 G.W.
n	**2**

Table 3.2: Specimens Comprising Group 1

Group 1 consisted of pre-term fetal specimens from the Scheuer Collection. In these specimens, the **lateral border** appeared largely purple, while in the **glenoid** purple areas were also visible, but much less prevalent. The **infraspinous fossa** and supraspinous fossa were mostly yellow.

Perhaps the most characteristic features of this group were the two distinct areas of orange in the lateral area of the **spinous process** in the region of the spinoglenoid notch, whose proximity to the invasion site of the nutrient foramen suggests that they were separated by an area of reduced thickness which might be occupied by a neurovascular bundle in the living.

Group 2

This group contained 11 specimens; the youngest specimen in this group was 32 gestational weeks and the oldest was aged between 0 and 6 months (Table 3.3). A typical specimen from Group 2 is presented in Figure 3.3.

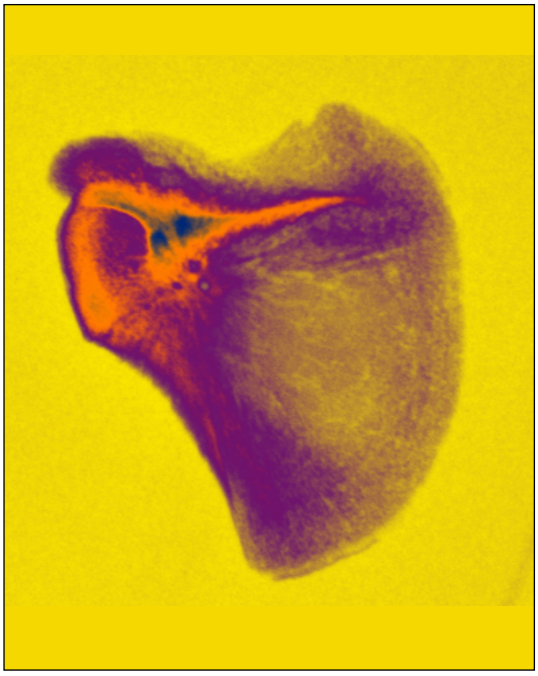

Figure 3.3: A typical specimen from Group 2

Specimen	Age
SC-096	32 G.W.
SC-017	"perinate"
SC-097	
SC-092	
SC-082	
SC-020	
SC-170	
SC-161	
SC-370	
SC-086	
SC-158	0-6 months
n	**11**

Table 3.3: Specimens comprising Group 2

This group consisted mostly of perinatal specimens. The estimated age range of this group varied from 32 gestational weeks to six months postpartum. In these specimens, the **glenoid** region began to exhibit an orange plate parallel to the articular surface.

In Group 2 the **lateral border**, which appeared as purple in Group 1, began to appear as orange as an area of increased thickness radiated from the location of the ossification centre towards the inferior angle.

Another 'spike' of orange also appeared in the region of the **spine**, radiating from the ossification centre in a medial direction. The two distinct areas of orange at the lateral end of the spinous process, as described in Group 1, appeared as two distinct areas of blue.

The **infraspinous fossa** and supraspinous fossa began to appear as light purple. In the infraspinous fossa the region of lighter colouration was encapsulated into a well-defined area that was medial to the lateral border and inferior to the medial border.

Group 3

This group contained 8 specimens; all specimens in this group were determined to be perinates (Table 3.4). A typical specimen from Group 3 is presented in Figure 3.4.

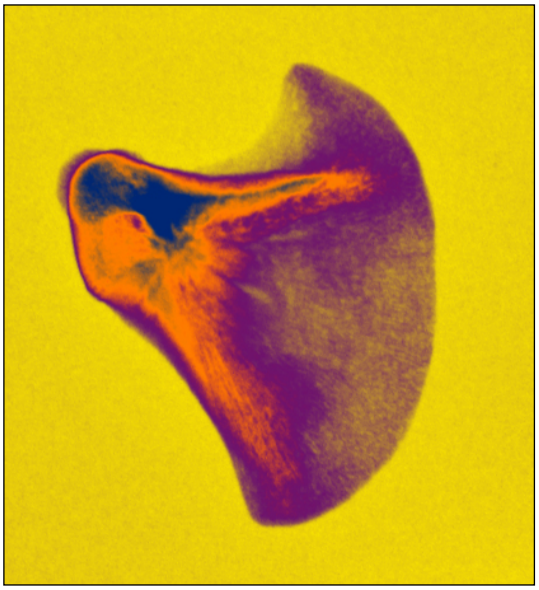

Figure 3.4: A typical specimen from Group 3

Specimen	Age
SC-083	"perinate"
SC-085	
SC-157	
SC-016	
SC-088	
SC-084	
SC-087	
SC-369	
n	**8**

Table 3.4: Specimens comprising Group 3

This group appeared as a further progression of the characteristics observed in Groups 1 and 2. An orange trajectory appeared along almost the entire length of the **lateral border**.

The **infraspinous fossa** increased in thickness resulting in it appearing entirely purple in all but the most mature specimens in this group. There was a gradient based decrease visible passing medially from the lateral border towards the medial border and also inferiorly from the spinous process in the more medial aspect of the fossa.

In this group, the two distinct areas of increased thickness that were observed at the lateral end of the **spinous process** in less mature specimens now appeared as a single area of blue. The orange 'spike' seen along the length of the spine in the previous group is observed as a blue 'spike' in this group.

The **glenoid** appeared as largely orange, however in the more mature specimens, areas of blue appeared in the glenoid. If areas of blue were present in the glenoid, they tended to exist as two trajectories:

1. one running from the area of the nutrient artery to the inferior region of the glenoid,
2. the other running almost horizontally from superior to inferior. This trajectory appeared more dense at its inferior extremity.

These two trajectories met at the inferior glenoid to from an 'L' shaped blue area.

Group 4

This group contained 8 specimens; the youngest specimen in this group was 5 months old and the oldest was aged between 2 and 5 years (Table 3.5). A typical specimen from Group 4 is presented in Figure 3.5.

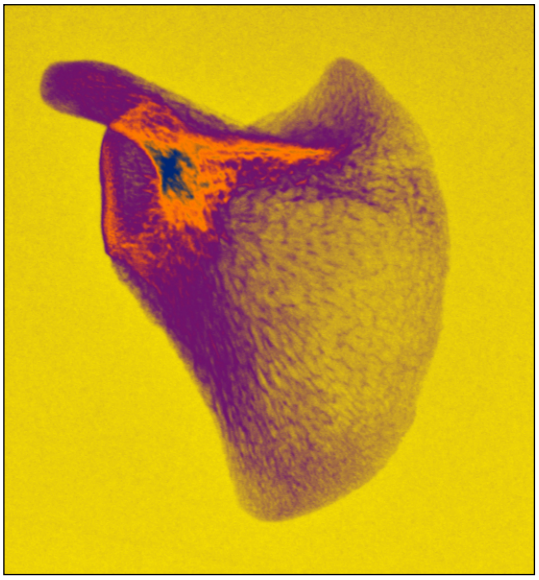

Figure 3.5: A typical specimen from Group 4

Specimen	Age
SC-021	5 months
SC-091	4-6 months
SC-023	1 year
SC-147	1-2 years
SC-141	1.5-2 years
SC-024	2 years
SC-025	3 years
SC-172	2-5 years
n	**8**

Table 3.5: Specimens comprising Group 4

Observations of the first three groups appeared to show progressive development, as bone was laid down on top of the structural attributes that already existed in the fetal period. Bones from the first three groups did not appear to differ a great deal in radiographic appearance but showed a gradual maturation and increasing thickness; in Group 4, however, the progressive deposition of bone observed in less mature groups appeared to falter and showed an uneven morphological appearance to the bone. Incidentally, this group contained the greatest number of damaged specimens.

This group is characterised by an absence of blue (and in some cases orange) in the **glenoid**.

In this group, an orange trajectory did not travel the entire length of the **lateral border**, and in some cases orange areas were entirely absent.

Bone in the **infraspinous fossa** appeared as yellow, rather than the purple expanse observed in less mature specimens.

The area of blue observed at the lateral extent of the **spinous process** remains, but the blue projection travelling towards the medial border was absent.

Group 5

This group contained 13 specimens; the youngest specimen in this group was aged between 2 and 4 years and the oldest was aged between 12 and 15 years (Table 3.6). A typical specimen from Group 5 is presented in Figure 3.6.

This group showed a return to a form of progressive growth. Unlike less mature groups that developed uniformly across the bone, this group exhibited new bone being laid down in a highly organised fashion.

In this group of specimens, blue made a return to the **glenoid**, parallel to the long axis of the articular surface.

The area of blue in the lateral end of the **spine** remained and extended laterally to resemble the ‘spike’ described in Group 3.

The **lateral border** also showed increased bone deposition: Areas of orange were observed in all specimens in this group, with several exhibiting very limited introduction of blue pixels.

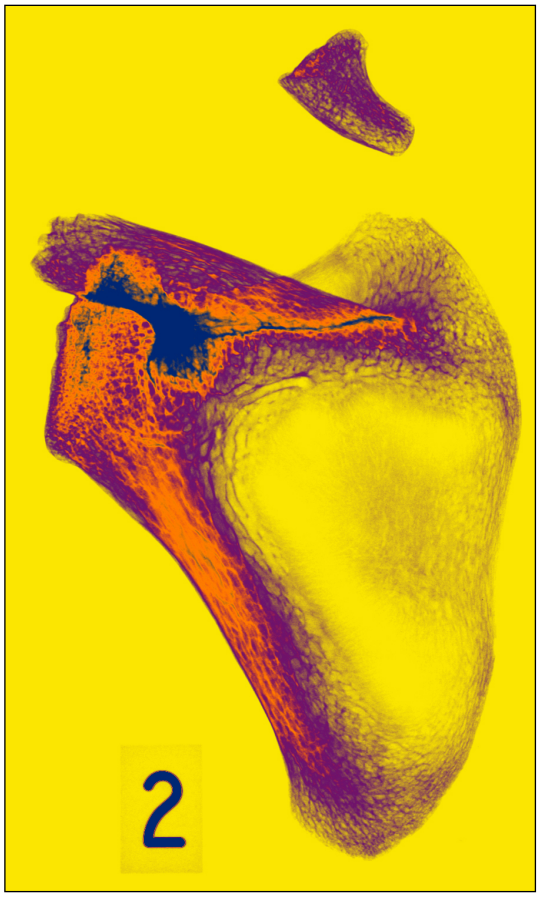

Figure 3.6: A typical specimen from Group 5

Specimen	Age
SC-257	2-4 years
SC-131	3y 4m
SC-090	3-5 years
SC-029	4 years
SC-026	
SC-159	4-5 years
SC-027	
SC-258	4-6 years
SC-028	6 years
SC-259	6-8 years
SC-029	8 years
SC-031	12 years
SC-001	12-15 years
n	**13**

Table 3.6: Specimens comprising Group 5

Compared to the progressive pattern observed elsewhere in the scapula, the **infraspinous fossa** and supraspinous fossa appeared somewhat anomalous - the widespread deposition of bone in the aforementioned areas was not replicated here. A solid purple infraspinous fossa was absent in all specimens in this group; in all there was a yellow centre with the majority exhibiting a yellow expanse spanning the gap between the orange buttresses of the spine and the purple and orange boundaries of the lateral border.

In addition to the changing opacity patterns, the morphology of the scapula also appeared to change. In previous groups, the scapulae appeared as round bones that were as long craniocaudally as they were wide mediolaterally; in this group the scapulae adapted a more angular shape that is elongated craniocaudally.

Group 6

This group contained 10 specimens; the youngest specimen in this group was aged between 6 and 8 years and the oldest was described as a late adolescent (Table 3.7). A typical specimen from Group 6 is presented in Figure 3.7.

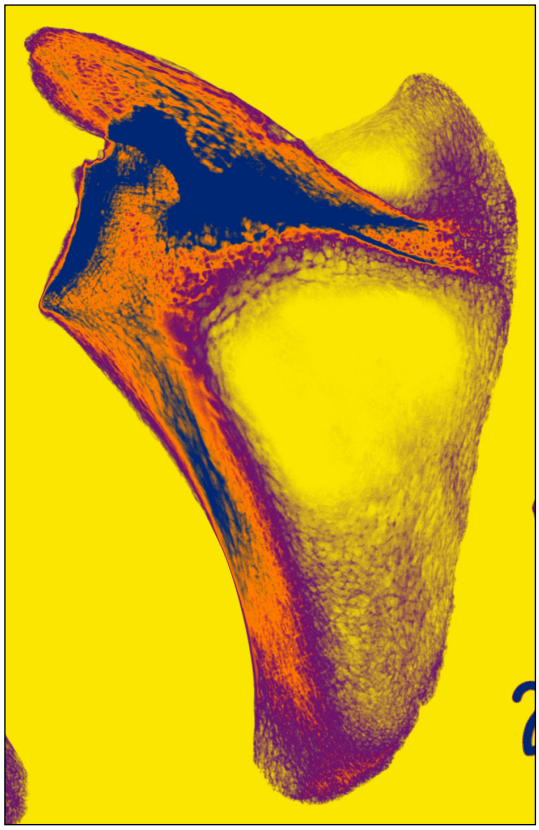

Figure 3.7: A typical speicmen from Group 6

Specimen	Age
SC-260	6-8 years
SC-095	7 years
SC-132	8y 7m
SC-171	9-12 years
SC-175	10-16 years
SC-030	11 years
SC-013	10-14 years
SC-133	12 years
SC-094	“late adolescent”
SC-105	
n	**10**

Table 3.7: Specimens comprising Group 6

The limited infiltration of blue pixels observed in the **lateral border** of Group 5 appeared more extensive in this group. This condensation of blue was localised approximately half way between the glenoid and the inferior angle, with occasional blue pixels extending superiorly towards the position of the primary ossification centre in more mature specimens.

The single blue ‘spike’ of the **spinous process** observed in the previous group bifurcated in these specimens. Two blue ‘spikes’ could clearly be seen heading towards the medial border one along the superior border of the spine and one along the inferior border.

The **glenoid** continued to exhibit a blue ‘plate’ parallel to the position of the articular surface.

Notably, there was no abundance of blue in the area of the nutrient artery (formerly the ossification centre), which remained largely orange despite the surrounding areas (lateral spinous process, glenoid, and lateral border) exhibiting extensive areas of blue. In occasional more mature specimens, limited infiltration of blue pixels could be seen.

Purple pixels in the **infraspinous fossa** were further reduced in this group. Any purple pixels that remained in this region were concentrated around the perimeter of the yellow expanse, with the exception of faint oblique lines, which were observed in the more mature specimens in this group.

Group 7

This group contained 15 specimens; the youngest specimen in this group was aged between 6 and 8 years and the oldest specimens were described as adult (Table 3.8). A typical specimen from Group 7 is presented in Figure 3.8.

The isolated area of blue observed in the **lateral border** of Group 6 appeared to extend superiorly in this group, to the extent that it reached the area immediately inferior to the location of the nutrient artery.

The blue twin ‘spike’ at the medial end of the **spinous process** observed in the previous group persisted in these specimens. Similarly, the **glenoid** continued to exhibit a blue ‘plate’ parallel to the position of the articular surface.

The area of the nutrient artery now appeared as a mix of blue and orange pixels, as opposed to the paucity of blue observed in Group 6. This infiltration of blue in the area of the nutrient artery resulted in incomplete communication between the blue areas of the glenoid, lateral border and spine.

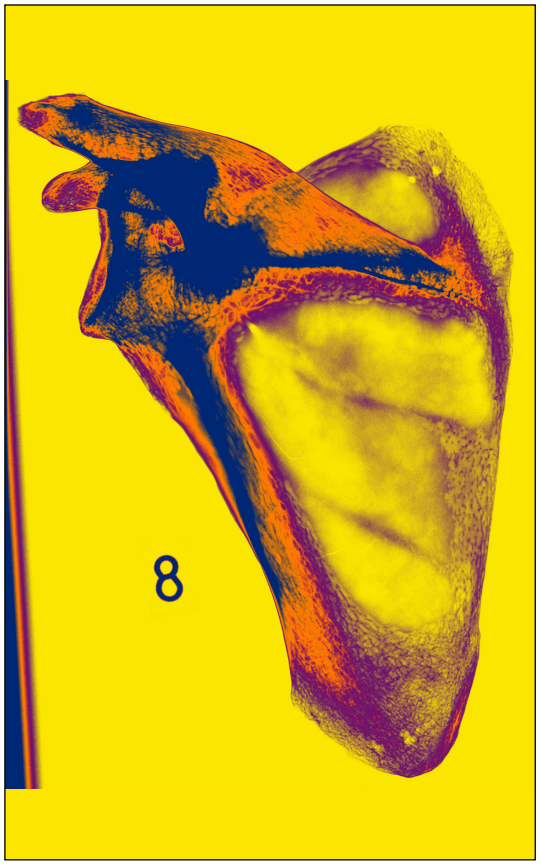

Figure 3.8: A typical specimen from Group 7

Specimen	Age
SC-255	6-8 years
SC-014	9 years
SC-098	10-12 years
SC-032	12 years
SC-018	13-14 years
SC-033	14 years
SC-038	19 years
SC-099	“late adolescent”
SC-100	
SC-102	
SC-104	
SC-106	
F	“adult”
G	
H	
n	**15**

Table 3.8: Specimens comprising Group 7

The **infraspinous fossa** and supraspinous fossae in Group 7 appeared similar to those in Group 6. In the infraspinous fossa, a largely yellow expanse was framed by a purple perimeter medially and inferiorly and by the blue trajectories of the spine superiorly and the lateral border laterally. Oblique purple lines were also visible in this group.

Group 8

This group contained 14 specimens; the youngest specimen in this group was aged 17 years and the oldest specimens were described as adults (Table 3.9). A typical specimen from Group 8 is presented in Figure 3.9.

In this group the blue trajectory of the **lateral border** occupied the same area as in Group 7. In addition, the blue of the lateral border in this group appeared much more robust.

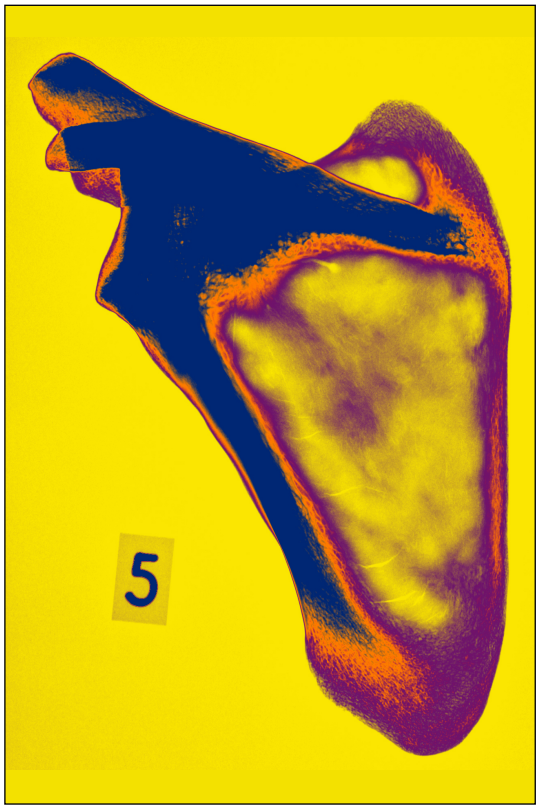

Figure 3.9: A typical specimen from Group 8

Specimen	Age
SC-034	17 years
SC-134	18 years
SC-375	18-22 years
SC-036	19 years
SC-037	
SC-035	
SC-101	19y 6m
SC-138	“late adolescent”
SC-103	
A	“adult”
B	
C	
D	
E	
n	**14**

Table 3.9: Specimens comprising Group 8

The blue twin ‘spike’ at the medial end of the **spinous process** observed in previous groups was only visible in one specimen of this group. Similar to the lateral border, the blue trajectory of the spine had become much more robust in this group and extended close to the root of the spine on the medial border.

The area of the nutrient artery became progressively blue in this group. The incomplete communication between the blue areas of the glenoid, lateral border and spine that was observed in Group 7 was complete in Group 8. The contact between

these blue areas lead to the blue ‘plate’ of the **glenoid** becoming indistinguishable in many specimens, although evidence of it was visible in specimens where the area of communication was less extensive.

The **infraspinous fossae** in Group 8 appeared similar to those observed in Groups 6 and 7.

3.3. Discussion

To facilitate discussion of the eight developmental groups, they have been arranged into three descriptive phases. Interpretation of the gradient mapped radiographs revealed two distinct progressive phases of development separated by a period of resorption. These eight developmental groups and three descriptive phases are summarised in Table 3.10 and Figure 3.10 respectively. The transient period identified between the two phases of growth is termed the ‘Reboot’ and is discussed on Page 70.

The Pre-Reboot phase consists of Groups 1, 2 and 3 (generally fetal and perinatal specimens, and individuals younger than six months postpartum). The Reboot phase consists only of Group 4 (the youngest individual in this group is 5 months, the oldest is defined as 2-5 years old). The third Descriptive Phase, Post-Reboot, comprises of Groups 5-8, and contains only specimens over three years of age.

Examples of the least and most mature specimens in each Descriptive Phase are shown in Figure 3.10 to illustrate the ranges of maturity present. Examples of ‘typical’, or average, configuration are provided for the Pre-Reboot and Post-Reboot phases. In the Reboot phase, the assignment of a ‘typical’ arrangement in The Reboot phase was not deemed useful, due to the limited sample size.

When interpreting results it is essential to consider the role of structural superimposition of structures (for example, the spine and acromion are superimposed on the superior portion of the glenoid) and there is an inability to distinguish between cortical and trabecular bone in two-dimensional radiography.

Descriptive Summary of Groups

Group	Glenoid	Lateral Border	Spinous Process	Infraspinous Fossa
1	Purple, but less than the lateral border.	Purple	Purple, with two distinct areas of orange in the lateral extremity.	Mostly yellow.
2	An orange plate exists parallel to the articular surface.	An orange ‘spike’ radiates from the location of the nutrient foramen in the direction of the inferior angle.	An orange 'spike' radiates medially from the location of the nutrient artery. The two distinct areas of orange in Group 1 become blue.	Yellow speckled with purple.
3	Orange (with limited blue in mature specimens).	An orange trajectory along the whole length of the lateral border.	The two distinct areas of blue in Group 2 become a single area of blue. The orange 'spike' in Group 2 becomes blue.	Mostly purple.
4	No blue (or orange, in some specimens).	The length of the lateral border is not entirely orange, and orange is totally absent in some cases.	Blue in the lateral extent of the spinous process remains, but the ‘spike’ of Group 3 is absent.	Yellow
5	A blue plate exists parallel to the articular surface.	Orange (with limited blue in mature specimens)	Blue in the lateral extent of the spine, with the return of the blue ‘spike’ of Group 3.	Yellow
6	A blue plate exists parallel to the articular surface.	A condensation of blue exists half way between the glenoid and the inferior border (with occasional blue pixels extending superiorly in more mature specimens)	A bifurcated blue ‘spike’ is visible.	Yellow (with faint oblique lines which in some specimens).
7	A blue plate exists parallel to the articular surface.	The blue condensation extends superiorly to reach the area inferior to the nutrient artery.	A bifurcated blue ‘spike’ is visible.	Yellow (with faint oblique lines in some specimens).
8	The blue plate becomes indistinguishable as it meets the blue areas of the spine and lateral border. The plate remains visible in less robust specimens.	The blue condensation extends superiorly to meet blue areas of the glenoid and spine.	The blue of the spine extends medially to meet the blue areas of the glenoid and lateral border. The blue spike becomes invisible in most specimens.	Yellow (with faint oblique lines in some specimens).

Table 3.10: A summary of patterns observed by group.

Phase	Groups	Maturity		
		Least	Average	Most
Pre-Reboot (<0.5y)	1, 2, 3	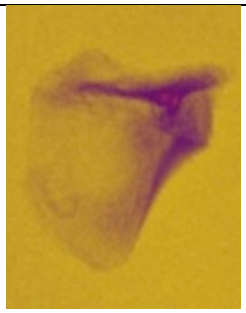	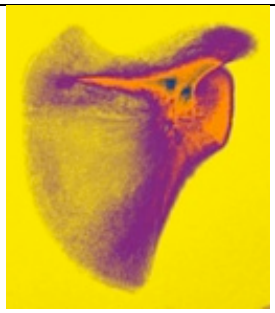	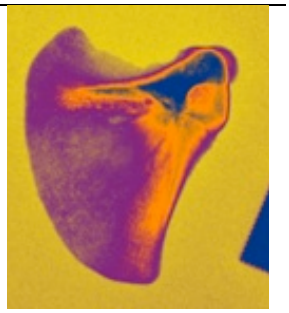
Reboot (0.5 – 5y)	4	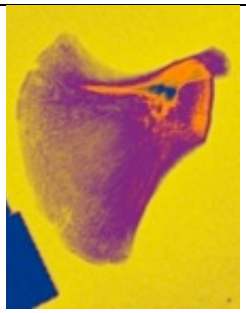	n/a	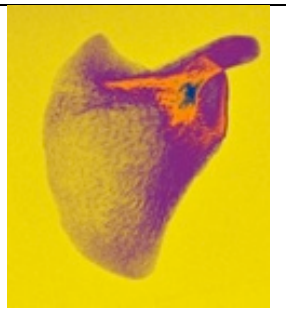
Post-Reboot (>3y)	5, 6, 7, 8		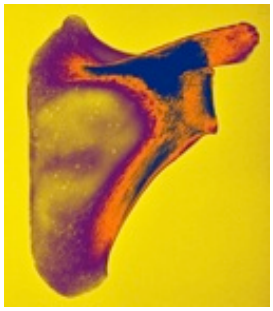	

Figure 3.10: Summary of developmental phases in the juvenile scapula.

Pre-Reboot

Precocious Trajectories

During the first phase of development, two trajectories of increased radio-opacity were apparent. Both originated from the region of the spinoglenoid notch and projected to either the medial border (along the long axis of the spine) or to the inferior angle (along the lateral border). These structural trajectories represent regions of increased thickness or density; they could be of structural significance as they were observed from the earliest stages of development through to full skeletal maturity.

In addition to these two trajectories, the glenoid also appeared relatively radio-opaque in the Pre-Reboot phase. These three regions, which were visible in the gradient mapped radiographs of Groups 1-3, endured to into the adult scapula and so are clearly necessary accumulations of increasing bone thickness or density to withstand or transfer biomechanical stresses.

Anetzberger & Putz (1996) have shown that the lateral border and spine constitute ‘supporting pillars’, to accommodate forces associated with movement. Gupta and van der Helm (2004) used finite element technology to model the stresses passing through the adult scapula: they concluded that the thickened structures of the scapula, which have now been shown to exist at the earliest stages of development, are subjected to significant bending stresses. From this they deduced that the role of the fossae in the adult is to act as a muscle attachment site, rather than to transmit load forces.

They attributed the thickened, lateral border to ‘the most important force of the scapula’: the glenohumeral joint reaction force during humeral abduction. Similarly, they attribute thickening of the spine to high tensile stresses across the cranial and caudal surfaces of the spine. Both these observations could be of relevance in the development of the fetal scapula, since the areas of increased stress - and morphological change - correspond with the areas of increased densities observed in this study.

It follows that, given the absence of significant load, these trajectories should be absent in the fetus and neonate. This study demonstrates that this is not the case. The existence of these trajectories in the fetus and neonate suggests that the “form follows function” principle, originally described by Wolff (1892), may be somewhat irrelevant at the earliest stages of development, and an alternative influence may play a much larger role.

Such alternative influences could include those of a genetic nature. Also the effect of *in utero* muscle movements, which begin after 11 fetal weeks (Reissis and Abel, 2012), could mimic the biomechanical load the scapula will be subjected to in later life, resulting in the appearance of similar trajectories. It is also possible that both scenarios, genetic and *in utero* movement, could produce these precocious anatomical characteristics. Whatever the case, it is clear that the "form follow function" principle cannot be attributed as the cause of these trajectories at this early stage of development.

Central Locus

Several radiolucent striations can be seen radiating from, or converging on, a central point. The most obvious manifestation of one such striation is the separation of the two blue areas of the spine in Group 2. The central radiolucency remains until the final Group when it becomes obscured by the convergence of the blue areas of the spine, lateral border and glenoid.

The location of the central radiolucency corresponds with the approximate location of the primary nutrient foramen, which indicates the likely invasion site of the nutrient artery, and associated vein.

At an early age, it is likely that this radiating vascular distribution, also observed in the juvenile ilium (Cunningham and Black, 2009a), has involvement in the development of the bone. This likelihood is corroborated by the observations of Crock (1996), which show that the distribution of the nutrient artery corresponds closely with the areas of increased opacity observed in individuals below 3 years old and the subsequent regression of the fossae in older individuals (Figure 3.11).

Although the distribution of the nutrient artery within the bone closely mirrors areas of increased opacity, it is unlikely that vasculature is the causative factor. However, it is possible that the radiating vasculature may influence the directional arrangement of the trabeculae as it enters the medullary cavity.

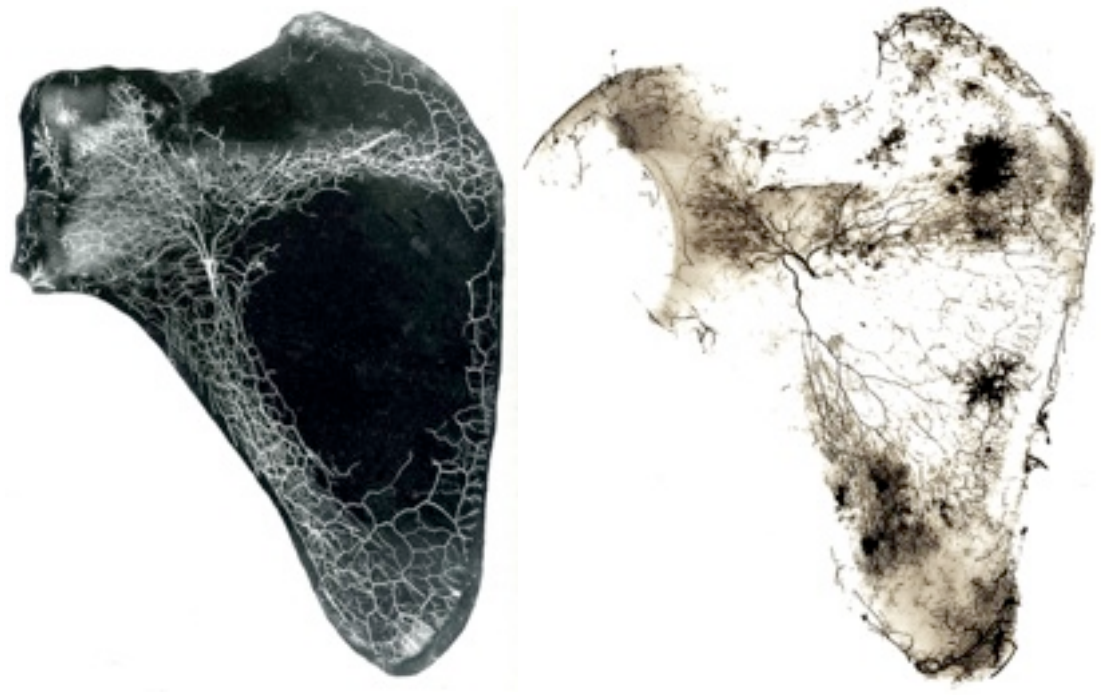

Figure 3.11: Distributions of nutrient arteries in the juvenile scapula. From (Crock, 1996).
LEFT: The body of the scapula in a girl aged 8 weeks. The main nutrient artery is visible at the neck of the scapula, the nutrient artery to the spine of the scapula enters its base from the suprascapular fossa, but its origin is obscured.
RIGHT: The scapula of an 11-year-old boy, with the coracoid, spine and acromion 'removed at their bases'. Supply to the 'transparent bone of the infraspinous fossa' is from the periosteal arteries surrounding the bone.

Although the location of the primary nutrient artery invasion site (on the ventral neck), and the resulting ossification centre (deep to the spinoglenoid notch), is well documented, it is not entirely clear why invasion of the nutrient artery occurs precisely where it does. It has been reported that the intersection of two trajectories represents the area under greatest stress, which results in thickening of the cartilaginous anlage and subsequently the ossified bone (Carter and Beaupré, 2001; Cunningham and Black, 2009a; Dalstra and Huiskes, 1995). As the perichondrium around the region of greatest stress begins to ossify, chondrocytes within the thickened anlage would cease to receive nutrients by diffusion through the water-based matrix; as the chondrocytes become ischaemic, they send out the angiogenic signals causing invasion of the nutrient artery (Scheuer and Black, 2000). It stands to reason that the thickest part of the anlage would contain the greatest prevalence of chondrocytes, and thus would be the most likely nutrient artery invasion site in response to the

angiogenic signals, effectively meaning that the region of the anlage that endures the greatest strain becomes the primary attractor of the nutrient artery and eventual ossification centre.

It is generally accepted that the scapula ossifies from its cartilaginous anlage in week 8 initially around the ventral aspect of the surgical neck. It is reported that this ossification is initially perichondral in nature, before invasion of the nutrient artery triggers endochondral ossification of the anlage itself (Breathnach, 1965; Scheuer and Black, 2000).

The beginnings of scapular endochondral ossification are well documented. Scheuer and Black (2000) note that the largest nutrient foramen is found on the lateral aspect of the supraspinous fossa as it meets the ventral aspect of the spine. This is thought to be the primary ossification centre – triggered possibly by invasion of the suprascapular artery at the lateral aspect of the supraspinous fossa before extending bidirectionally to the proximal (vertebral) and distal (glenoid) borders (Figure 2.5).

The Ogden and Phillips' (1983) ossification model is not based solely on endochondral ossification; they also suggest that intramembranous ossification takes place between the endochondral cones. However, since Ogden and Phillips observed no instances of intramembranous ossification it seems unlikely that the scapula develops via dermal intramembranous ossification, with the exception of the initial perichondral ossification.

Furthermore, when considering other bones that are known to be part dermal, part endochondral (e.g. temporal, occipital) it becomes clear that each component develops separately before eventually fusing after substantial independent ossification via differing modes. This is certainly not seen in the scapula, which develops as a single bone.

Reboot

When comparing Group 4 to the pre- and post- reboot phases, it becomes clear that significant changes occur in the scapula at this time, both micro- and macro-morphologically.

In Group 4, the progression observed in the pre-reboot phase ceases and appears to almost reverse through resorption of bone. This resorption results in non-uniform decreased ‘density’ throughout the bone. It appears that this phase takes place before the age of three, but is never observed in perinates. After this phase the scapulae return to progressive growth, but obvious differences exist between pre- and post-reboot development. In the post-reboot phase, new bone is laid down in a discriminatory fashion and the fossae fail to thicken. This is in contrast to the Pre-Reboot phase, which exhibits relatively uniform development across the bone.

Morphological changes, on a larger scale, also occur. The typical rounded shape of specimens in Groups 1-3 begins to change during the reboot phase where the scapula transforms from a curved bone, which is as wide (mediolaterally) as it is long (craniocaudally), to an angular bone, which is craniocaudally elongated.

These almost age prescriptive micro- and macro- morphological adaptations may have a common trigger although this phenomenon has not previously been described. Between the ages of six months and a year, as children begin to leave the transient quadrupedal phase and become bipedal, the scapula begins its reboot and remodels to accommodate to its new role.

The reboot phase is perhaps a result of a conflict between modern and ancient. While habitual bipedalism causes the modern scapula to bear tensile stresses as it carries the weight of the upper limb, the ancient scapula would be expected to do the opposite. The ancient, quadrupedal, scapula acts as the most proximal extension to the column of long bones that comprise the forelimb. The entire column habitually

bears part of the organism's entire mass, and is thus under largely compressive stresses.

This shift represents a complete directional and mechanical role reversal, from transmitting the weight of the individual in one direction, to transmitting the load of the limb in the opposite direction. This transformation is unique to the modern human scapula**.** As the juvenile scapula rapidly undergoes complete reversal of its biomechanical role, the bone is forced to redress its genetic template.

The mismatch between ancient genetic template and modern bipedal behaviour and the resulting resorption and resumption of (modified) development has parallels with the computing phase "Reboot". Typical dictionary definitions of reboot describe, "to boot again, especially after power failure or malfunction" or "to start (a process, etc.) afresh or with renewed vigour". Both these definitions can comfortably be applied to the process underway in Group 4.

Post-Reboot

In Groups 5-8, the organisation of the scapula is significantly different to that seen in Groups 1-3. Although several key areas (the glenoid, lateral border and spine) remain dense, the infraspinous and supraspinous fossae often differ. These areas, while relatively dense in the neonate appear to become largely resorbed in Groups 5-8.

In addition, the bone also remodels on a macro-morphological scale. By Group 5, the bone adopts a much more craniocaudally elongated and angulated appearance, as opposed to the rounded scapula of the neonate which is almost as wide mediolaterally as it is long craniocaudally. Concurrently, the lateral border of the more mature scapula adopts a more concave shape and oblique ridges, caused by the insertion of the tendinous intersections of the infraspinatus and subscapularis muscles, begin to appear and persist into adulthood. These observations of differential opacity patterns and changing shape are corroborated upon comparison with a series of backlit scapulae (Figure 2.7).

Gradient mapped radiography, backlit photographs, and traditional examination of all juvenile scapulae in the Scheuer Collection shows that the scapula develops as a relatively thick and largely opaque bone before the scapular blade thins later in development. The persistence of thick areas of bone outwith the blade (i.e. the spine, lateral border and glenoid) is thought to be a result of biomechanical factors (Anetzberger and Putz, 1996; Gupta and Dan, 2004).

Conclusion

The presence of three distinct phases of bone maturation in the scapula within the space of 3 years appears to be unique in the human skeleton. The pre-reboot phase shares some similarities with the development of the juvenile ilium where both display precocious trajectories (Cunningham and Black, 2009a; 2009b; 2009c; 2010). In the ilium, these trajectories radiate from a central location near the acetabulum and have been attributed to the absorption and distribution of loads generated during a bipedal gait (Rook et al., 1999; Dalstra and Huiskes, 1995). That these trajectories are well developed in the neonate prior to any direct locomotive influence supports the hypothesis of a predetermined phylogenetic template, perhaps laid down in anticipation of future functional/locomotive demands. The trabecular bone shows little notable alteration in the ilium as it grows other than resorption in a region of the blade where the two cortices eventually come into apposition: this area represents the region where stress on the bone is reportedly at its lowest (Cunningham and Black, 2009a; Dalstra and Huiskes, 1995; Carter and Beaupré, 2001). Therefore the ilium appears to show early phylogenetic and ontogenetic stability, supporting the possibility that it fulfils its original design requirements by being a bone that is ultimately involved in weight transfer, and muscle attachment, for locomotion.

The scapula initially shows similarities with the ilium but very quickly the structural arrangements of the two bones diverge as the scapula responds to alternative

requirements. Three influences can be identified that act on the scapula during this phase, which could influence, enhance or counteract the early phylogenetic directive:

1. Evolutionary, embryological and anatomical evidence supports the fact that the scapula is originally a cervical structure, which descends to its final position on the posterior thoracic wall. At birth the scapula is elevated and full descent is not achieved until approximately four years of age (Scheuer and Black, 2000). During this time it must remodel to accommodate the directional pull of the musculature that is partly responsible for the postnatal migration: this is evidenced through the increased length of the infraspinous fossa prior to six years of age (Scheuer and Black, 2000).
2. Within the first year the child also experiences weaning, which is known to have a deleterious effect on the whole-body calcium reservoir through increased remodelling to release nutrients required to rebalance the dietary shift (Pettifor and Zlotkin, 2004). A bone that is actively remodelling due to migratory pressures may be susceptible to the dietary mineral deficits during this period.
3. It is possible that human scapular morphology is phylogenetically programmed to reflect anticipated locomotive requirements and for a very short period of time in the child's life this is realised by both the upper and lower limbs as the child crawls (Keen, 1993; Haywood and Getchell, 2001). Therefore, during the first year of life, both limbs could be said to fulfil their phylogenetic anticipatory role - assuming that it is programmed for quadrupedal locomotion. However, the crawling mode is transitory (indeed some children never display this phase and go directly from sitting to walking), whereas the habitual mode of locomotion is established early in the child's development towards the end of the first year, perfected throughout the second year before attaining mature gait around 8 years of age (Keen, 1993). During this time, the ilium must accept

its predetermined role in locomotion but the scapula is released to adopt an entirely different functional role.

It is not possible to say which of the three ontogenetic influences (topographical migration, weaning or locomotive emancipation) exerts the greatest influence. Additional factors may be involved, and it seems likely that multiple factors combine to cumulatively affect development (Verhulst and Creeger, 2003). The result is that the micro-architecture of the scapula appears to falter in its development and regresses. Whilst it 'reboots', it meets the demands of its new role in a swift and efficient manner between the ages of 6 months and three years. The scapula does not, and perhaps cannot, significantly alter its external macro-morphology as it is perhaps restricted by rigid phylogenetic constraints, but to ensure that it is fit for its new purpose, it realigns its micro-architecture as the limb becomes a prehensile and non-weight bearing structure designed for direct interaction and engagement with the external environment (Carter and Beaupré, 2001).

The primary directive for initial scapular composition may well be anticipatory of future functional requirements: previous research provides evidence of a phylogenetic signal that is expressed more strongly in the child than in the adult (Young, 2008). Therefore, the infant scapula may represent a challenge to evolutionary dictates, which become less dominant as ontogenetic and more recent evolutionary adaptations assume greater importance. In this sample, both the macro-morphological and micro-architectural appearances of the scapula remain largely unchanged after 4 years of age. This suggests that once it had realigned to its new demands it remains stable with phylogenetic influence and ontogenetic change reaching an accepted equilibrium. Such developmental plasticity has been mentioned in the literature, but rarely in relation to recent human adaptations; most discussions tend to focus on early vertebrates (Starck and Chinsamy, 2002; Donoghue et al., 2006), later amniotes

(Müller et al., 2010) or occasionally hominids (Collard and Wood, 2007; Lycett and Collard, 2005).

Perhaps a two-tier mechanism influences the development of the scapula:

1. A rigid template that controls **macro-morphology** in preparation for phylogenetically **anticipated demands** that may, or may not, materialise.
2. An adaptive **micro-architecture** that initially compliments the phylogenetic template but has the flexibility to respond to shifting **ontogenetic demands**.

The success of such a model depends on the ability of the reboot to provide a structure that is fit for purpose for the lifetime of the individual and does not ultimately fail. Skeletal failure (other than as a result of direct trauma) tends to manifest in the elderly when the structure can no longer withstand the forces applied to it: femoral neck fractures and vertebral crush fractures are examples for this. Indeed, the large number of damaged reboot specimens could suggest that these scapulae may be physically less able to withstand the trauma of handling/inhumation, perhaps through diminished quality and/or quantity of bone. Is structural failure in the human skeleton a result of the compromise between largely unchanging macro-morphological phylogenetic constraints and micro-architectural ontogenetic refinements that achieve transitory successful adaptation? The scapula is a bone that does not have a high failure rate: this may be indicative of its successful rebooting into a bone that is well suited to the stresses of its adopted function. Interestingly, almost all of the damaged specimens included in this study occurred in the reboot phase: they all presented with fragmented fossae with only the triangular remnants of the axillary border, glenoid region and spine remaining intact. Thus, it appears that the scapula is neither constrained by its original anticipated function nor co-opted into a structure for which it will ultimately fail, and could represent a functional and structural success story for osteological adaptation.

Chapter 4: Anthropometric Study

An anthropometric study was performed to best inform and direct the design of the stereoscopic study detailed in Chapter 6: Stereoscopic Study. The main aim of this anthropometric study was to determine the regularity of shape in the perinatal scapula. In ascertaining the stability in shape of the perinatal scapula, a reliable method can be designed to subsequently examine specific parts of the bone. Chapter 6 of this thesis will utilise the findings of this anthropometric study to design volumes of interest (VOIs). A VOI can be defined as a selected subset of samples (in this case, volumes of bone within the scapula) within a dataset (in this case, a micro-CT scan of a juvenile scapula) identified for a particular purpose (in this case, quantitative analysis of trabecular bone).

When superimposing a grid of fixed proportions over multiple specimens to define volumes of interest, it must be the case that particular osteological landmarks appear consistently in specific volumes of interest. If osteological features are not placed consistently in the same volume, then any subsequent comparative analysis is undermined. Reliable and consistent grid positioning validates the practice of forming datasets by combining measurements of a specific volume of interest from multiple specimens. Furthermore, if a static grid performs successfully across the entire bone and all volumes of interest then comparing these combined datasets can be considered scientifically valid.

Ascertaining the strength of the correlation between particular anthropometric measurements will reveal how variable the shape of the scapula is in this sample. High correlation coefficients between two measurements imply that those dimensions are closely related, and that there is minimal shape variation in the sample. Conversely, a low correlation coefficient between two measurements suggests that proportions are more variable and comparison of data should be undertaken with caution.

4.1. Materials & Methods

The sample of fetal, perinatal and infant (0-1y) specimens (Table 4.1) was examined anthropometrically to describe and determine the constancy of the proportions of the juvenile scapula in this restricted age cohort. This restricted age cohort was utilised to due to its use in the final qualitative analysis, detailed in Chapter 6. Metric analysis assisted in the design of the system used define VOIs for use in Chapter 6. In addition, this process also assisted in the detection of outliers, which could be examined in greater detail and excluded from future studies if deemed appropriate.

Age	**n**		
	Left	Right	Total
Fetal (<0y)	2	2	4
Neonatal (~0y)	13	13	26
Infant (0-1y)	4	4	8
Total	**19**	**19**	**38**

Table 4.1: Specimens used in the metric analysis.

Measurements were taken using digital callipers (resolution: 0.01mm; accuracy: 0.03mm; repeatability: 0.01mm) from the specimens using techniques described in the literature (Fazekas and Kósa, 1978; Scheuer and Black, 2000; Rissech and Black, 2007; Saunders et al., 1993). These measurements represent anatomical rather than functional landmarks, and of the developing scapula and do not take account of the associated soft tissues (e.g. cartilage). Since the findings of this anthropometric study are used only to design subsequent methodologies that only utilise dry bone, this was not deemed detrimental to the process. These measurements are represented diagrammatically in Figure 4.1 and definitions are as follows:

1. Maximum length of the glenoid surface: Maximum distance between the superior and inferior borders of the glenoid articular surface, excluding the articular surface for the coracoid process.
2. Middle diameter of the glenoid surface: distance from the middle of the posterior border of the glenoid rim to the middle of the anterior border, perpendicular to the long axis of the glenoid surface.
3. Spine length: Maximum distance between the medial end of the spine on the medial border and the tip of the acromion process.
4. Scapular length (also described as the maximum length): Distance between the superior and inferior angles of the scapula.
5. Scapular width (also described as the maximum width): Distance between the posterior margin of the glenoid fossa and the medial extent of the spine on the medial border.
6. Infrascapular height: Distance between the point at which the long axis of the spine intersects the medial border of the scapula to the inferior angle.
7. Suprascapular height: Distance between the point at which the axis of the spine intersects the medial border of the scapula to the superior angle.
8. Acromial width: Maximum distance between the anterior and posterior borders of the acromion process, perpendicular to the axis of the spine.
9. Length of the glenoidal mass: distance between the superior border of the articulation site for the coracoid process and the inferior border of the glenoid surface.
10. Scapular index: This value was calculated by dividing the maximum width (5) by the maximum length (4), and multiplying by 100.

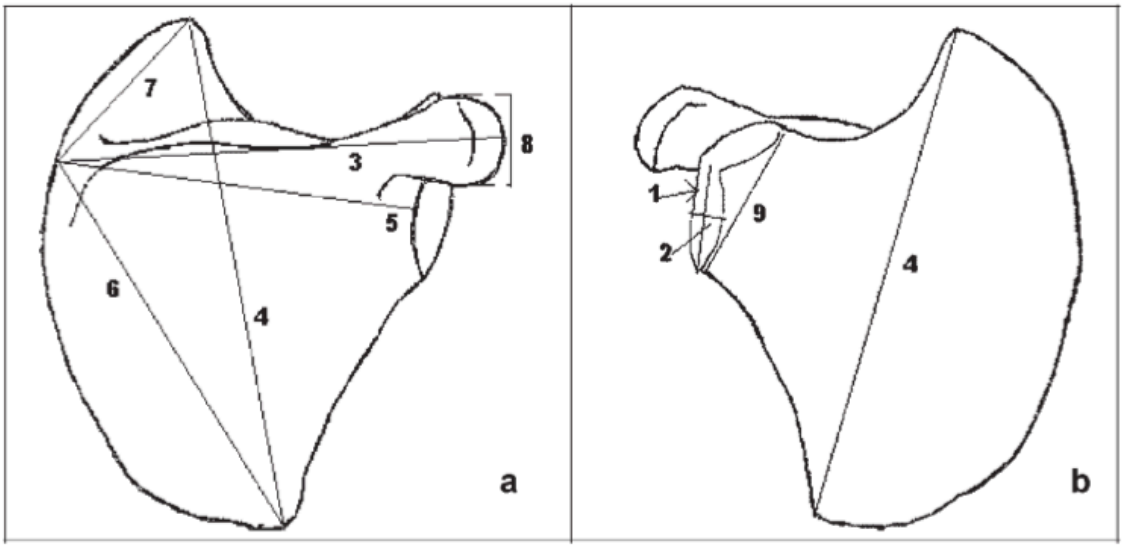

Figure 4.1: Dorsal (a) and ventral (b) view of a juvenile scapula. Maximum length (1) and middle diameter (2) of the glenoid surface; spine length (3); scapular length (4); scapular width (5); infrascapular height (6); supra- scapular height (7); acromial width (8); and maximum length of the glenoidal mass (9), which includes the glenoidal and coracoid articular surfaces. (Rissech and Black, 2007)

4.2. Results

Although all available anthropometric measurements were completed, only results relevant to the subsequent stereoscopic study are presented here. Raw data and additional scatter plots for all anthropometric measurements are included in Appendix B. Three measurement ratios were considered relevant to the stereoscopic study:

1. **Middle diameter of the glenoid : length of the glenoid mass**

   This ratio was considered important to the stereoscopic study as it quantifies the regularity of the proportions of the glenoid mass, which will comprise VOIs 1-4 in the subsequent stereoscopic study (Chapter 6). The 'length of the glenoid mass' was selected rather than the 'maximum length of the glenoid surface' because eventual volume of interest placement in this region is not restricted solely to the articular portion of the glenoid.

2. **Spine length : scapular width.**

   This ratio was considered important to the stereoscopic study as it quantifies the regularity of the proportions of spine of the scapula and the acromion, which will comprise VOIs 5-8 in the subsequent stereoscopic study (Chapter 6).

3. **Scapular length : scapular width.**

   This ratio was considered important to the stereoscopic study as it quantifies the regularity of the proportions of blade of the scapula, which will comprise VOIs 9-23 in the subsequent stereoscopic study (Chapter 6).

These three ratios were considered useful in ascertaining the constancy of the proportions of the glenoid, spine and blade respectively (Table 4.2), which are the three regions that were used to define the VOIs of the stereoscopic study. Descriptive statistics for the selected anthropometric measurements are presented in Table 4.3.

Measurement		Relevance to stereoscopic study	
1	**2**	**Region**	**VOIs**
Middle diameter of the glenoid surface	Length of the glenoid mass	Glenoid	1-4
Spine length	Scapular width	Spine and acromion	5-8
Scapular length	Scapular width	Blade	9-23

Table 4.2: Selected anthropometric measurements and their relevance to the subsequent stereoscopic study of Chapter 6.

Measurement	Range (mm)		Mean (mm)	Standard Deviation (mm)	Coefficient of variation
	Minimum	Maximum			
Middle diameter of the glenoid surface	3.37	9.45	6.04	1.14	18.89%
Length of glenoid mass	6.91	17.08	11.93	2.01	16.82%
Spine length	23.04	43.88	31.89	4.06	12.73%
Scapular width	19.19	35.83	28.11	3.49	12.42%
Scapular length	25.69	48.74	35.40	4.92	13.91%

Table 4.3: Descriptive statistics of relevant anthropometric measurements.

Correlation Coefficients

Pearson Product Moment Correlations were calculated using SigmaPlot 12 (Systat Software Inc.). The output of this test included the correlation coefficient, P-value and the number of samples included in the calculation.

The P-value is the probability of being incorrect in concluding that there is a correlation between the measurements; a smaller P-value indicates a greater probability that the measurements are correlated. Traditionally an acceptable value for P is considered to be < 0.05; in this study P-values were all less than 0.00835.

The correlation coefficient (r) is a measurement of the strength of the association between individual measurements. A correlation coefficient of +1 indicates a perfect positive relationship between the two measurements, with both always increasing

equally. A correlation coefficient of -1 indicates a perfect negative relationship between the two measurements, with one measurement increasing and the other decreasing equally. A correlation coefficient of 0 indicates no relationship between the two measurements.

Pearson's correlation coefficients were calculated for all combinations of measurements, and are presented in Figure 4.2, and the data for the selected anthropometric measurements relevant to the stereoscopic study are shown in a combined scatter plot (Figure 4.3).

	Length of the glenoid surface	Middle diameter of the glenoid	Length of the glenoid mass	Spine length	Scapular width	Scapular length	Infra-scapular height	Supra-scapular height
Middle diameter of the glenoid	0.840							
Length of the glenoid mass	0.939	0.890						
Spine length	0.898	0.855	0.949					
Scapular width	0.882	0.882	0.945	0.948				
Scapular length	0.869	0.865	0.945	0.917	0.960			
Infra-scapular height	0.886	0.922	0.958	0.932	0.968	0.968		
Supra-scapular height	0.712	0.800	0.842	0.848	0.873	0.895	0.857	
Acromial width	0.733	0.600	0.632	0.617	0.685	0.651	0.605	0.552

Figure 4.2: Pearson's correlation coefficients (*r*) of measurements of fetal and perinatal scapulae, colour-coded by strength. Green = high correlation; Red = low correlation. All P-values ≤ 0.00835.

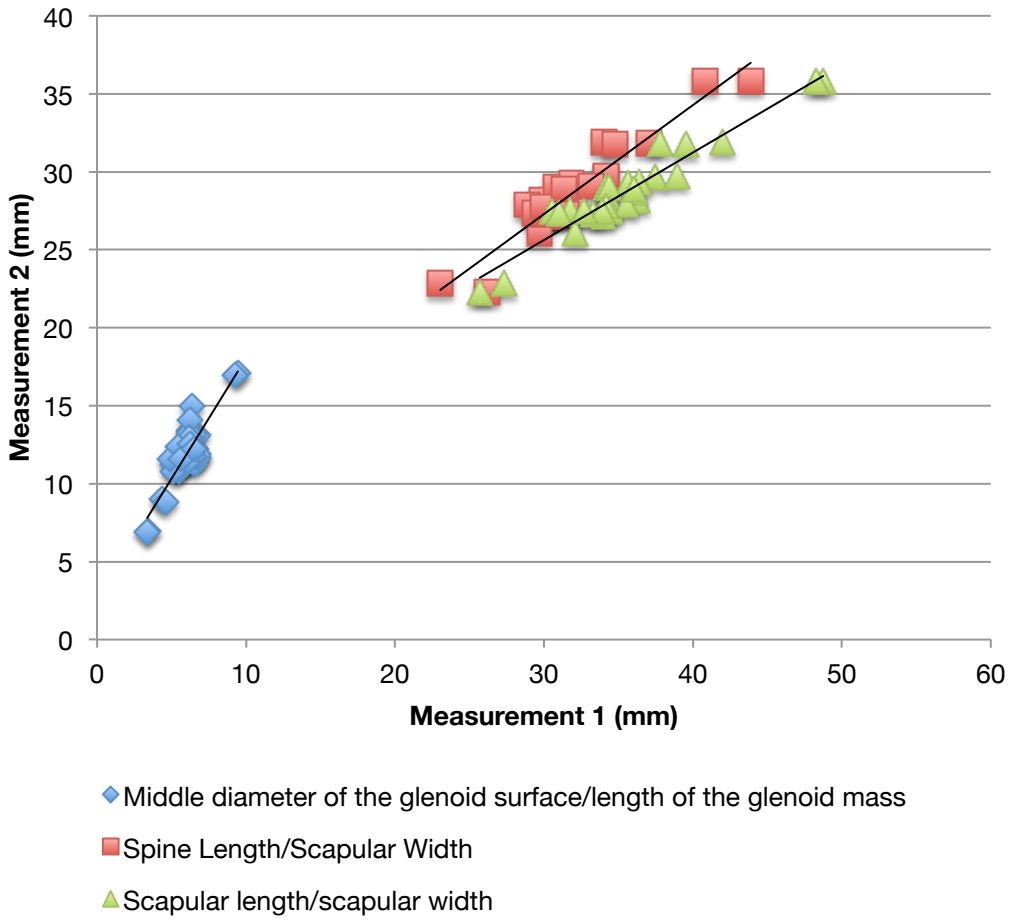

Figure 4.3: Selected anthropometric measurements of fetal and perinatal scapulae.

4.3. Discussion

The results show that the majority of anthropometric measurements are strongly and positively correlated with each other. The clear exception is acromial width, which failed to achieve a correlation coefficient of greater than 0.733 with any other measurement. Suprascapular height and the length of the glenoid surface were also relatively weakly correlated, achieving a correlation coefficient of only 0.712. All other features showed a correlation value in excess of 0.800.

Of the metrics selected as relevant to future studies the correlations were much stronger. Scapular width and scapular length, length of the glenoid mass and middle diameter of the glenoid surface, and spine length to scapular width were all strongly correlated, with Person's *r* values of 0.948, 0.890 and 0.948 respectively.

The descriptive statistics (Table 4.3) suggest that there is a wide range of values in this sample. This should be expected given that the sample includes specimens of varying stages of development. This finding, combined with the strong correlation coefficients suggests that the proportions of the scapula do not change substantially as the bone changes in absolute size in the early stages of growth. It follows that the use of scalable static grids in the glenoid, spine, acromion and blade of the scapula in this developmental group would be appropriate.

Although these data show that the proportions of the scapula are uniform during this period of development, the relative proportions of the bone will, at some point, inevitably change as the bone becomes elongated crandiocaudally. Figure 4.4 is a combination of scapular length and scapular width data from Rissech and Black (2007), showing the relationship between age and scapular length (blue) and the relationship between age and scapular width (red). When considering these two sets of measurements together it is apparent that a divergence between the two occurs which becomes more pronounced with increasing age. This is a result of the disparity

between the constant linear relationship between scapular length and age, and the reported quadratic polynomial relationship between scapular width and age.

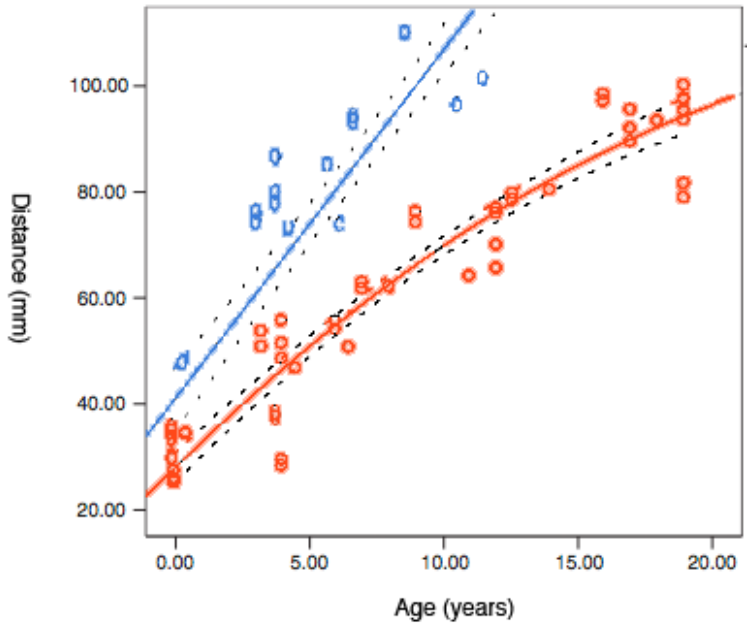

Figure 4.4: Scapular length (blue) and scapular width (red) changes with increasing age. (After (Rissech and Black, 2007))

Given the findings of the previous chapter, the sample examined in this study is contained within the “pre-reboot” phase of development. In Figure 4.4, “post-reboot” specimens are represented in the divergent end of this graph; therefore it seems likely that the reboot itself could also be described mathematically as the transient period in development as scapular width and length diverge to produce a change in gross morphology.

This concept is further supported by observations of the scapular index (effectively the width:length ratio), which suggest that the index significantly decreases between the pre- and post- reboot phases. Figure 4.5 summarises data from the literature with data from this study and demonstrates the transition of the juvenile scapula to a crandiocaudally elongated bone.

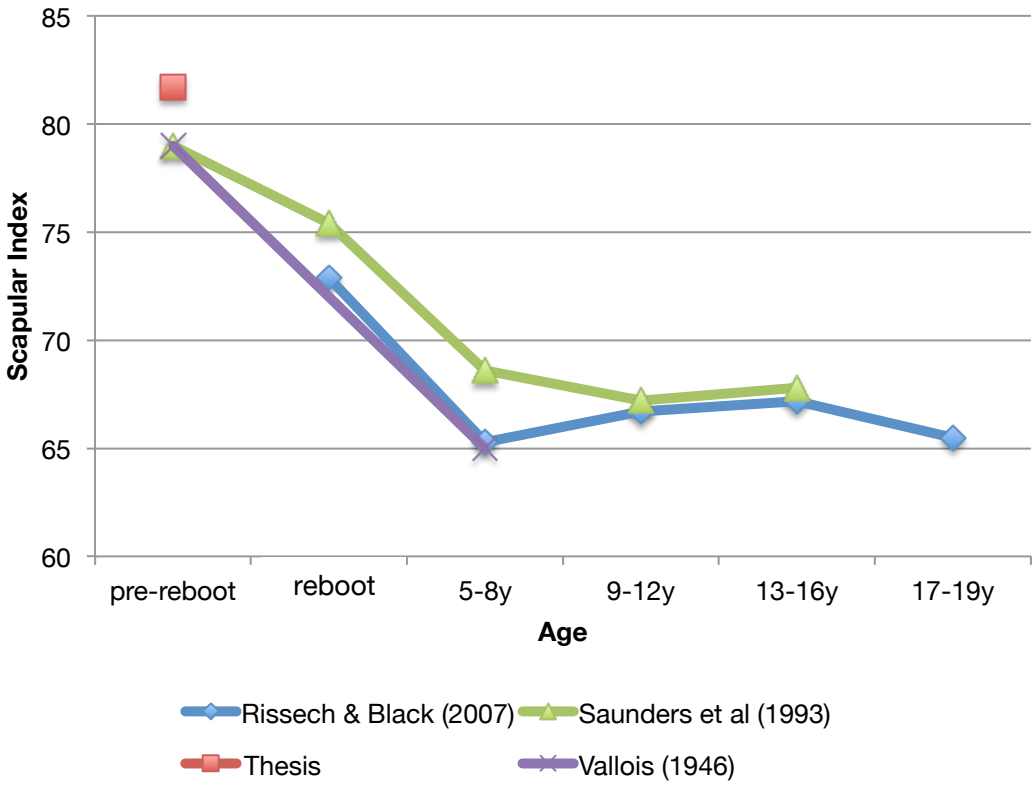

Figure 4.5: Changes to scapular index with age.

Chapter 5: Stereoscopic Error Study

5.1. Introduction

The stereoscopic part of this research (Chapter 6) uses commercially available software (CTAn, SkyScan) to determine a series of calculations on particular volumes of interest (VOIs) of trabecular bone. The software is capable of determining quantifiable trabecular morphology from three-dimensional image stacks, and although it can largely automate the process of counting and measuring trabeculae, the process relies on the user defining a volume of interest (VOI) manually and assigning a threshold level during binarisation.

These two user dependent actions (i.e. spatial definition of VOIs, and threshold variation) as sources of error and have not been discussed in depth in the literature; consequently they were examined to validate the technique. An error study was carried out to determine how unavoidable sources of user error affect measurements of trabecular bone. The information gained assisted in validating the results of the stereoscopic study as a whole, which aimed to quantify and describe trabeculae in the developing scapula by employing this technique.

5.2. Materials & Methods

Five bone volumes were identified from a random selection of three perinatal scapulae. Three individuals were examined to negate the possibility that one individual could be anomalous, and the three anatomical locations were selected to negate the possibility that one volume could be anomalous. These volumes were taken from three individuals (SC-161-L, SC-084-L and SC-016-R) and three anatomical locations (acromion, anterior-superior quadrant of the glenoid, and posterior-superior quadrant of the glenoid) (Table 5.1). These anatomical sites were selected because of their well-defined anatomical boundaries.

Volume of Interest (VOI)	Individual	Volume
A	SC-161-L	Acromion
B	SC-084-L	Acromion
C	SC-084-L	Anterior-superior quadrant of the glenoid
D	SC-016-R	Posterior-superior quadrant of the glenoid
E	SC-016-R	Anterior-superior quadrant of the glenoid

Table 5.1: Summary of volumes of interest used in the error study.

These three specimens were micro-CT scanned at the Centre for Medical Engineering and Technology (CMET) at the University of Hull using an X-Tek HMX 160 scanner (at 60kV, 20μA). Scans were made at resolutions between 37.2μm and 42.4μm, depending on the specimen size. These scans were exported as a series of 2D slices in 16-bit TIFF format, which were each labelled using the specimen number and a sequential number corresponding to the slice number.

The variation in scanning resolution was due to restrictions imposed by the reconstruction method, which could only process a limited volume of data. This resulted in larger specimens being scanned at lower resolutions, while smaller specimens were scanned at higher resolutions. The maximum scanning resolution permitted by the operating system was selected for each specimen. The resolution achieved was deemed sufficient to investigate trabecular bone, and was found to be comparable with, or greater than, similar methodologies elsewhere in the literature (Rincón-Kohli and Zysset, 2009; Bousson et al., 2012; Lim et al., 2010; Cunningham and Black, 2009a).

Scans were transported from the University of Hull on a series of compact disks, and transferred to secure servers at the University of Dundee.

CTAn was operated on a Dell Optiplex 780 desktop computer, with an Intel Core 2 Quad 3.0GHz processor and 4GB of RAM running 64-bit Microsoft Windows 7. Analysis of each volume of interest (VOI) was carried out to calculate the following parameters:

- Bone volume fraction (**BV/TV**)
- Structural model index (**SMI**)
- Trabecular thickness (**Tb.Th**)
- Trabecular number (**Tb.N**)
- Trabecular separation (**Tb.Sp**)
- Degree of anisotropy (**DA**)

Detailed descriptions of these metrics, and how they are calculated, are detailed on Page 115.

To test the effect of **threshold variation** each VOI was identified once, and analysed five times with redefined threshold levels. These five analyses, each of the same VOI but with different threshold levels, were undertaken to determine if threshold variability introduced statistically significant differences between the repeated analyses.

To test the effect of **spatial discrepancies** in VOI placement, the threshold level was fixed before the VOI was defined repeatedly and analysed five times. These five analyses, each of different VOI placement but with a constant threshold level, were undertaken to determine if spatial discrepancies introduced statistically significant differences between the repeated analyses.

This procedure resulted in ten sets of data for each VOI. The results of each analysis were assigned an identifier to enable speedy identification. ‘T’ or ‘S’ was appended to the VOI name (i.e. A, B, C, D, E) depending on whether the dataset was measuring threshold variations (T) or spatial discrepancies (S). A number was added to the ‘T’ or ‘S’ to describe each of the five analyses. For example, the data from the **third** analysis of **threshold** variation from the acromion of specimen SC-084-L (**VOI B**) would be labelled $\mathbf{B_{T3}}$.

Analysis of variance was then performed to detect any statistically significant difference between T1-5 and S1-5 for each of the five VOIs.

5.3. Results

Analysis of variance shows that changes in both threshold and spatial definition do not produce statistically different metrics. This is the case when considering both all the metrics that CTAn is capable of producing (Table 5.2), as well as selected metrics that will be considered in Chapter 6 (Table 5.3).

Overall Effect of Change

VOI	A	B	C	D	E
Difference between T1-5	NSS (P = 1.000)	NSS (P = 0.993)	NSS (P = 1.000)	NSS (P = 1.000)	NSS (P = 998)
Difference between S1-5	NSS (P = 1.000)	NSS (P = 0.971)	NSS (P = 0.999)	NSS (P = 1.000)	NSS (P = 1.000)

Table 5.2: Summary of statistically significant differences between VOIs, using all metrics. NSS = no statistically significant difference.

VOI	A	B	C	D	E
Difference between T1-5	NSS (P = 0.999)	NSS (P = 1.000)	NSS (P = 1.000)	NSS (P = 1.000)	NSS (P = 0.999)
Difference between S1-5	NSS (P = 1.000)	NSS (P = 1.000)	NSS (P = 0.997)	NSS (P = 0.997)	NSS (P = 1.000)

Table 5.3: Summary of statistically significant differences between VOIs, using only selected metrics that will be considered in Chapter 6. NSS = no statistically significant difference.

Specific Effects of Changes in Threshold

Further study into which individual metrics were most affected by changes in threshold was considered by calculating the coefficient of variation for each metric for all analyses (Table 5.4-Table 5.8), and are summarised in Table 5.9.

	BV/TV	SMI	Tb.Th	Tb.N	Tb.Sp	DA
T1	38.80469	1.20626	1.43748	0.26995	1.79646	0.53647
T2	36.06473	1.3741	1.41157	0.25549	1.85126	0.53364
T3	37.45304	1.29206	1.42666	0.26252	1.82053	0.53457
T4	36.04034	1.37125	1.40902	0.25578	1.85106	0.53357
T5	44.37703	0.8396	1.50653	0.29456	1.70688	0.53386
SD	3.45316545	0.221728	0.039885	0.016159	0.059588	0.001211
MEAN	38.547966	1.216654	1.438252	0.26766	1.805238	0.534422
CV	**9%**	**18%**	**3%**	**6%**	**3%**	**0%**

Table 5.4: Effect of threshold (T) variations on selected metrics for VOI A

	BV/TV	SMI	Tb.Th	Tb.N	Tb.Sp	DA
T1	36.13774	1.24896	1.36744	0.26427	2.04074	0.55612
T2	37.47661	1.17475	1.38473	0.27064	2.00851	0.55584
T3	34.80717	1.32359	1.35287	0.25728	2.06152	0.55444
T4	34.80717	1.32359	1.35287	0.25728	2.06152	0.55444
T5	32.20519	1.45332	1.32397	0.24325	2.09485	0.55098
SD	1.95420884	0.103435	0.022367	0.010201	0.031723	0.002045
MEAN	35.086776	1.304842	1.356376	0.258544	2.053428	0.554364
CV	**6%**	**8%**	**2%**	**4%**	**2%**	**0%**

Table 5.5: Effect of threshold (T) variations on selected metrics for VOI B

	BV/TV	SMI	Tb.Th	Tb.N	Tb.Sp	DA
T1	43.73148	1.08227	1.33481	0.32762	1.55072	0.85343
T2	58.45268	-0.01355	1.52542	0.38319	1.38885	0.85991
T3	55.26304	0.26042	1.47728	0.37409	1.42182	0.86131
T4	55.26304	0.26042	1.47728	0.37409	1.42182	0.86131
T5	55.26304	0.26042	1.47728	0.37409	1.42182	0.86131
SD	5.68403803	0.41547	0.072173	0.022153	0.062972	0.003422
MEAN	53.594656	0.369996	1.458414	0.366616	1.441006	0.859454
CV	**11%**	**112%**	**5%**	**6%**	**4%**	**0%**

Table 5.6: Effect of threshold (T) variations of selected metrics for VOI C

	BV/TV	SMI	Tb.Th	Tb.N	Tb.Sp	DA
T1	45.05495	1.15559	1.56831	0.28728	1.70704	0.68426
T2	29.62959	1.9761	1.39154	0.21293	2.00873	0.67885
T3	35.57952	1.66059	1.45646	0.24429	1.87768	0.68495
T4	41.86132	1.34288	1.52579	0.27436	1.75285	0.68352
T5	51.41016	0.73768	1.64341	0.31283	1.60717	0.68505
SD	8.42310544	0.473875	0.097589	0.038739	0.155899	0.002577
MEAN	40.707108	1.374568	1.517102	0.266338	1.790694	0.683326
CV	**21%**	**34%**	**6%**	**15%**	**9%**	**0%**

Table 5.7: Effect of threshold (T) variations on selected metrics for VOI D

	BV/TV	SMI	Tb.Th	Tb.N	Tb.Sp	DA
T1	74.3834	-1.6608	1.9449	0.3825	1.3114	0.657
T2	52.0081	0.6698	1.5356	0.3387	1.5471	0.6949
T3	37.5482	1.5804	1.3737	0.2733	1.7544	0.6977
T4	48.3907	0.9380	1.4958	0.3235	1.5930	0.6966
T5	41.2002	1.3763	1.4153	0.2911	1.6883	0.6973
SD	14.4150	1.3031	0.2282	0.0426	0.1700	0.0178
MEAN	50.7061	0.5807	1.5531	0.3218	1.5788	0.6887
CV	**28%**	**224%**	**15%**	**13%**	**11%**	**3%**

Table 5.8: Effect of threshold (T) variation on selected metrics for VOI E

VOI	BV/TV	SMI	Tb.Th	Tb.N	Tb.Sp	DA
A	9%	18%	3%	6%	3%	0%
B	6%	8%	2%	4%	2%	0%
C	11%	112%	5%	6%	4%	0%
D	21%	34%	6%	15%	9%	0%
E	28%	224%	15%	13%	11%	3%

Table 5.9: Summary of the effect of threshold (T) variations on the coefficient of variation of selected metrics. Highlighted cells are the result of a measurement error caused by extreme threshold variation.

Specific Effects of Spatial Changes

Further study into which individual metrics were most affected by changes in threshold was considered by calculating the coefficient of variation for each metric for all analyses (Table 5.11-Table 5.14), and are summarised in Table 5.15.

	BV/TV	SMI	Tb.Th	Tb.N	Tb.Sp	DA
S1	44.37703	0.8396	1.50653	0.29456	1.70688	0.53386
S2	44.4518	0.77047	1.51156	0.29408	1.75068	0.5483
S3	42.9185	0.78027	1.52556	0.28133	1.86686	0.54767
S4	43.66159	0.57054	1.5585	0.28015	1.97337	0.55231
S5	44.42314	0.56653	1.55306	0.28604	1.902	0.55641
SD	0.671537	0.12779	0.023713	0.006837	0.109604	0.0085
MEAN	43.96641	0.705482	1.531042	0.287232	1.839958	0.54771
CV	**2%**	**18%**	**2%**	**2%**	**6%**	**2%**

Table 5.10: Effect of spatial (S) variations on selected metrics for VOI A

	BV/TV	SMI	Tb.Th	Tb.N	Tb.Sp	DA
S1	32.20519	1.45332	1.32397	0.24325	2.09485	0.55098
S2	32.12958	1.46178	1.37775	0.2332	2.16095	0.57073
S3	32.00582	1.43733	1.3166	0.24309	2.12571	0.58852
S4	33.53593	1.34095	1.4001	0.23952	2.17578	0.54714
S5	34.1848	1.27541	1.41287	0.24195	2.18615	0.60289
SD	0.98647045	0.081957	0.043887	0.004189	0.037796	0.023919
MEAN	32.812264	1.393758	1.366258	0.240202	2.148688	0.572052
CV	**3%**	**6%**	**3%**	**2%**	**2%**	**4%**

Table 5.11: Effect of spatial (S) variations on selected metrics for VOI B

	BV/TV	SMI	Tb.Th	Tb.N	Tb.Sp	DA
S1	55.26304	0.26042	1.47728	0.37409	1.42182	0.86131
S2	55.55269	0.26611	1.47647	0.37625	1.41442	0.86939
S3	56.04444	0.24791	1.4819	0.37819	1.41304	0.86873
S4	56.00214	0.25625	1.48206	0.37787	1.41319	0.82936
S5	56.70821	0.23963	1.48592	0.38164	1.39738	0.85067
SD	0.54996513	0.010446	0.003877	0.002779	0.008924	0.01664
MEAN	55.914104	0.254064	1.480726	0.377608	1.41197	0.855892
CV	**1%**	**4%**	**0%**	**1%**	**1%**	**2%**

Table 5.12: Effect of spatial (S) variations on selected metrics for VOI C

	BV/TV	SMI	Tb.Th	Tb.N	Tb.Sp	DA
S1	51.41016	0.73768	1.64341	0.31283	1.60717	0.68505
S2	51.59904	0.74428	1.66309	0.31026	1.60003	0.66618
S3	51.81933	0.70334	1.6604	0.31209	1.59365	0.70881
S4	49.29056	0.82711	1.53347	0.32143	1.60048	0.66448
S5	48.78024	0.9162	1.49909	0.3254	1.5865	0.67642
SD	1.42875282	0.08595	0.077656	0.00662	0.00782	0.018028
MEAN	50.579866	0.785722	1.599892	0.316402	1.597566	0.680188
CV	**3%**	**11%**	**5%**	**2%**	**0%**	**3%**

Table 5.13: Effect of spatial (S) variations on selected metrics for VOI D

	BV/TV	SMI	Tb.Th	Tb.N	Tb.Sp	DA
S1	41.20015	1.37634	1.41528	0.29111	1.68829	0.6973
S2	42.74501	1.33655	1.45471	0.29384	1.68586	0.74176
S3	35.72507	1.73163	1.39412	0.25626	1.79401	0.73428
S4	36.47697	1.68583	1.42174	0.25657	1.79802	0.75147
S5	34.81854	1.74925	1.33062	0.26167	1.79772	0.74164
SD	3.54210967	0.202175	0.046079	0.018938	0.060007	0.021025
MEAN	38.193148	1.57592	1.403294	0.27189	1.75278	0.73329
CV	**9%**	**13%**	**3%**	**7%**	**3%**	**3%**

Table 5.14: Effect of spatial (S) variations on selected metrics for VOI E

VOI	BV/TV	SMI	Tb.Th	Tb.N	Tb.Sp	DA
A	2%	18%	2%	2%	6%	2%
B	3%	6%	3%	2%	2%	4%
C	1%	4%	0%	1%	1%	2%
D	3%	11%	5%	2%	0%	3%
E	9%	13%	3%	7%	3%	3%

Table 5.15: Summary of the effect of spatial (S) variations on the coefficient of variation of selected metrics.

5.4. Discussion

After repeated measurements and analysis of variance, neither spatial variations nor threshold discrepancies produced significantly different results. Although differences are not statistically significant, analysis of coefficient of variation results shows that there were some metrics that are more affected than others.

Effects of Threshold (T) Variation

Altering the threshold (T), while keeping the volume of interest (S) constant, does not produce statistically significant results (Table 5.2;Table 5.3). Despite this, some particular metrics are affected more than others:

The structural model index (SMI) is most affected by variation in threshold. Repeated measurement of SMI while varying the threshold resulted in a coefficient of variation of 18%, 8%, 112%, 34% and 224% in VOIs A-E respectively. After closer inspection of the raw data, it appears that one of the SMI measurements of VOIs C and E is a negative number. These are likely to be anomalous readings created by too high a threshold. This anomaly was also observed by Hara et al (2002).

Although this type of anomalous measurement contributes a great deal to error, the error is simple to detect after analysis and provides an excellent indication of unsuitable threshold definition. Any analyses that include a negative SMI measurement should be omitted and repeated in future studies.

Bone volume fraction (BV/TV) is also affected by threshold selection. This is to be expected, since threshold selection directs the software to include or omit large numbers of pixels in its definition of bone.

Unlike the structural model index, the degree of anisotropy (DA) appears largely unaffected by variations in threshold. In all VOIs except one (VOI E), the coefficient of variation remained at 0%.

These findings are similar to those of Hara et al (2002), who concluded that "*threshold selection is important for the accurate determination of volume fraction and mechanical properties, especially for low bone volume fractions*" and that "*the architectural directionality is less sensitive to changes in threshold*".

Effects of Spatial (S) Variation

Altering the spatial definition of a VOI, while keeping the threshold constant, does not produce statistically significant results (Table 5.2;Table 5.3). Despite this, some particular metrics are affected more than others:

SMI appears to be most affected by spatial definition; however this effect is less than that observed when altering threshold levels. While degree of anisotropy measurements were unaffected by variations in threshold, some error was observed with the introduction of spatial changes.

Conclusion

In summary, spatial changes to VOIs results in much less error to measurements than alterations in threshold, with the exception of DA (Table 5.16), although neither source of error is statistically significant. The findings of this study suggest that error introduced by the software operator during threshold and VOI placement does not significantly affect the outcome of the analysis. It should be noted that these results do not allow address the possibility that an interaction between these two variables could be underway.

	BV/TV	SMI	Tb.Th	Tb.N	Tb.Sp	DA
T	15%	79.2%	6.2%	8.8%	5.8%	0.6%
S	3.6%	10.4%	2.6%	2.8%	2.4%	2.8%

Table 5.16: The effects of threshold (T) and spatial (S) variation on average CV for selected metrics.

Chapter 6: Stereoscopic Study

The stereoscopic study aimed to expand on the findings of the qualitative gradient mapping investigation to describe the internal trabecular architecture of pre-reboot scapulae from a quantitative perspective. Unlike the radiographic study (Chapter 3), this study does not assess differences with age but differences between regions (VOIs) in the pre-reboot cohort only. Therefore, the aim of this stereoscopic study is to compare between regions (VOIs) within the pre-reboot scapula.

Reboot and post-reboot specimens were excluded from this part of the study for three reasons:

1. There was insufficient time to complete analysis of the entire ontogenetic range.
2. The findings of the anthropometric study and reports in the literature suggested that the shape of the scapula changes during its development and would make placement of homologous VOIs across age groups impossible.
3. Due to the way micro-CT scanners gather data, datasets from larger specimens would be collected at lower resolutions. Scanning the pre-reboot cohort (comprising the smallest specimens) resulted in achieving acceptable scanning resolutions.

Following micro-computed tomographic (micro-CT) imaging of specimens, each specimen scan was reconstructed and a series of multiplanar grids applied to define volumes of interest (VOIs). Following this process, the trabecular bone within each VOI was defined and quantified in terms of the principle histomorphometric parameters that are typically used in trabecular bone analysis.

6.1. Materials & Methods

Thirty-six juvenile scapulae from the Scheuer Collection (Table 6.1) were micro-CT scanned at the Centre for Medical Engineering and Technology (CMET) at the University of Hull using an X-Tek HMX 160 scanner (at 60kV, 20μA). Scans were made at resolutions between 25.4μm and 46.6μm, depending on the specimen size. These scans were exported as a series of 2D slices in 16-bit TIFF format, which were each labelled using the specimen number and a sequential number corresponding to the slice number.

Age		**n**
Juvenile	Fetal (<0y)	5
	Neonatal (~0y)	29
	Infant (0-1y)	2
Total		**36**

Table 6.1: Specimens used in the quantitative micro-CT study.

Variation in scanning resolutions is due to restrictions imposed by the reconstruction method, which can only process a limited volume of data. This results in larger specimens being scanned at lower resolutions, while smaller specimens are scanned at higher resolutions. The maximum scanning resolution permitted by the operating system was selected for each specimen. The resolution achieved was deemed sufficient to investigate trabecular bone, and was found to be comparable with, or greater than, similar methodologies elsewhere in the literature (Rincón-Kohli and Zysset, 2009; Bousson et al., 2012; Lim et al., 2010; Cunningham and Black, 2009a).

Scans were transported from the University of Hull on a series of compact disks, and transferred to secure servers at the University of Dundee.

Volume of Interest Design

Three methods of defining volumes of interest were explored: a static grid, landmark-derived grid and a multiplanar grid were all considered.

METHOD 1: 'Static Grid'

A static grid system was designed to partition each specimen into square VOIs. This involved attempting to position and rescale a rigid grid over digital images of specimens while keeping comparable regions in the same grid squares (Figure 6.1). Similar techniques have already been documented in the literature: Lim *et al* (2010) devised a three-dimensional grid solely for defining regions of the glenoid of the scapula, while Cunningham and Black (2009a; 2009b) also superimposed a two-dimensional fixed grid on neonatal ilia.

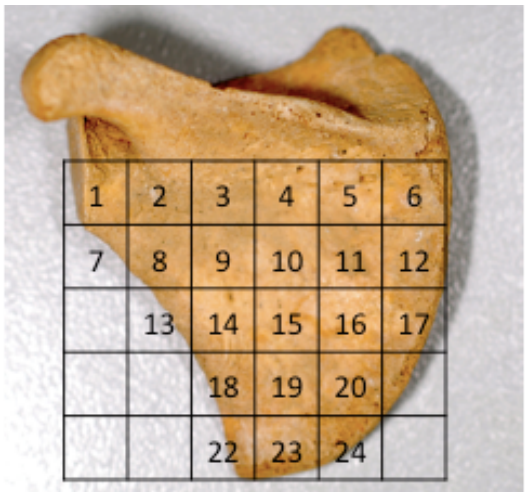

Figure 6.1: An example of the static grid approach to VOI design.

Attempts to apply a static grid to specimens of various ages highlighted the fact that the scapula does not grow uniformly in all directions. Particular inconstancies between VOIs were observed at the inferior angle and glenoid, due to the differential growth of the developing scapula. Specifically, the scapula grows more rapidly caudocranially than it does mediolaterally, which ultimately leads to the cradiocaudally elongated profile observed in more mature specimens. It was envisaged that this problem would escalate as this technique was applied to specimens of increasing age, thus effectively ruling out the 'static grid' approach as a means of comparing the same VOIs consistently across different age ranges.

METHOD 2: 'Landmark-derived' grid

To ensure maximum homology between VOIs, a system was considered which was based on morphological landmarks. Since the specific landmarks vary between specimens, the landmark derived grid system would also vary to encompass a slightly different, but structurally comparable region, in each specimen.

The following points were identified on digital images of the infraspinous fossa for each specimen (Figure 6.2):

A. Most inferior point on the glenoid margin.
B. Lateral extremity of the base of the spine, at the spinoglenoid notch.

C. Interior angle.

D. The root of the spine at the medial border.

E. ¼CD

F. ½CD

G. ¾CD

Lines were then drawn between each point, resulting in the infraspinous fossa being divided into eleven different regions (Figure 6.2).

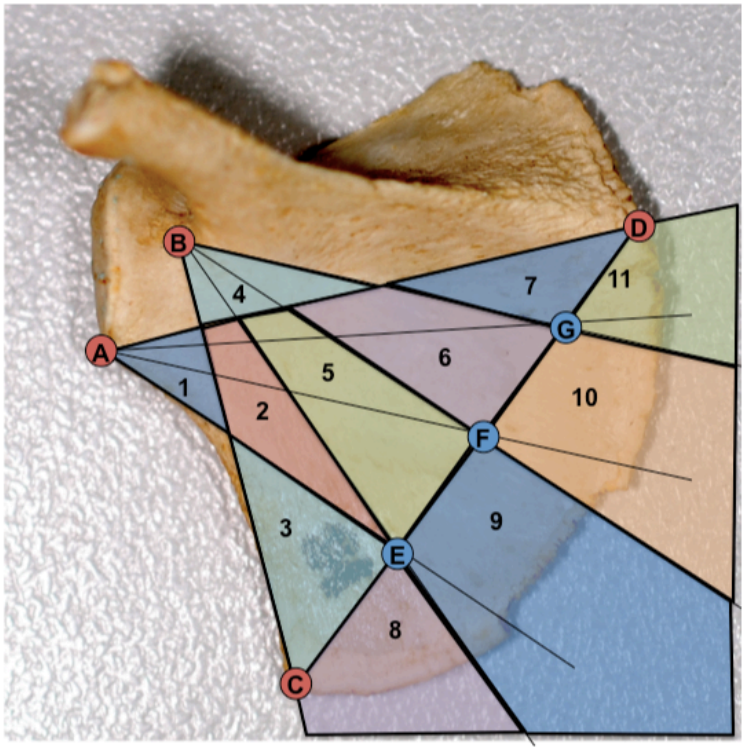

Figure 6.2: VOIs 1 to 11, derived from landmark points A to G.

Although this particular method only applies to the infraspinous fossa, similar methods using different landmarks were devised for the other regions of the scapula.

This approach is based on morphological landmarks and aimed to take account of inherent variations in morphology due to growth. As a result of the varying locations of the landmarks, the lines projected from the landmarks (and the subsequently derived grids) also varied from specimen to specimen. This led to each VOI encompassing a slightly different, but structurally comparable region in each specimen.

This approach was initially favoured due to the potential to compare specimens of different shape and size, including those of differing skeletal ages. However, on closer inspection, it was considered that this technique was unreliable, impractical and likely susceptible to observer error.

The designation of landmarks poses the first major problem with this technique. The use of occasionally ambiguous locations would likely contribute to greater inter-observer error should this method be attempted by others. Furthermore, the extensive damage to some specimens of this age (typically to the extremities, which are used in this technique) would render this technique either unusable or less reliable.

Should a defined landmark be damaged, or missing, the observer would either be unable to locate it (and therefore unable to derive the related VOIs) or they would have to estimate its location from pre-existing anthropometric data. If the latter is selected, a significant degree of inter-observer error could be introduced as an additional source of error in the anthropometric data.

In addition to the primary morphological landmarks, secondary mathematically calculated points were required to ensure there were a sufficient number of points from which to derive a grid. Although these points were based on a line projected between two morphological landmarks, the introduction of geometric locations rather than absolutely definable physical ones further reduces the validity of this technique.

METHOD 3: Multiplanar Grid

Due to the shortcomings of Methods 1 and 2, a third solution was sought. It was decided that the single landmark-based grid would be dismissed, while a series of modified static grids would be employed only to perinatal specimens, which would become the focus of the study. Results of the earlier anthropometric study (Chapter 4) showed that this approach was appropriate and that use of a static grid in this age group allowed reliability of VOI placement, which would positively contribute to the validity of results and subsequent comparisons. Time limitations also favoured this

approach, as analysis of the entire age range would not be possible in the time available.

By attempting various approaches to VOI design, it also became apparent that using one plane to define the various volumes was insufficient, due to anatomical structures (specifically the glenoid and spinous processes) extending in different directions with different orientations. The juvenile scapula is an irregular three-dimensional structure unlike, for example, the juvenile ilium, and defining VOIs requires a three-dimensional approach.

Multiplanar Reconstruction

Multiplanar reconstruction (MPR) is a means of reconstructing a three-dimensional scan in a different (usually orthogonal) plane to that in which it was originally imaged. In clinical imaging, for example, a scan is normally obtained so that each slice is in the axial plane. The entire scan can be reconstructed by stacking each slice in the correct order then reslicing the scan in an alternative plane, usually to obtain a more useful and informative view of a particular structure of interest.

In the clinical setting this technique is used only to view structures in a different plane, however most software capable of MPR is also capable of rebuilding the entire scan in an alternative plane and exporting it as a new stack of images.

In this case, MPR was necessary due to limitations of the analysis software (CTAn) that will ultimately analyse the trabecular morphology; the trabecular analysis software is only capable of defining regions of interest (ROIs) in each two-dimensional slice then extrapolating them into neighbouring slices to create a three-dimensional VOI.

Therefore, MPR is necessary for the following reasons:

1. Static grids can be applied easily to resliced image stacks for faster VOI placement; relying on traditional VOI placement would prevent completion of the analysis before the predefined project deadline. Defining a VOI in an arbitrary oblique plane requires ROIs to be defined in potentially every slice, while defining a VOI in an image stack that is sliced in the same plane as the static grid allows two ROIs to be defined (at the top and bottom of the VOI) followed by automated extrapolation between the two.
2. Defining multiple simple VOIs in the same plane as the static grid that defines them also helps to maximise accuracy and minimize potential overlapping of VOIs, which could create false similarities between VOIs.
3. MPR allows multiple static grids to be employed to different regions of a bone; this is necessary to accommodate analysis of the processes of the scapula.

A CT viewer with MPR capabilities was identified. OsiriX v5.5 (64-bit) was operated on an Apple Mac Mini with 2.3GHz Intel Core i5 processor and 8GB of RAM running 64-bit Mac OS X Lion (10.7).

Three planes were identified whereby the different regions of the scapula could be considered in isolation:

1. Plane 1 was parallel to the articular surface of the glenoid: it facilitated analysis of the glenoid and acromion.
2. Plane 2 was designed to allow study of the blade of the scapula, consisting of both the infra- and supra- spinous processes and the conjoining area ventral to the base of the spine. This plane was in the standard anatomical coronal plane, and identified by two points: the inferior and superior angles.

3. Plane 3 was designed to study the spinous process. Three points define this plane: the spinoglenoid notch, the root of the spine and the truncated lateral extremity of the spine.

Due to this multiplanar approach, it was decided that particular regions of the scapula should be isolated from the scan once they were analysed and prior to further MPR. This would prevent neighbouring VOIs in different planes from overlapping, and so create false positive results on comparison.

The original scan was reconstructed in Plane 1 and the glenoid and acromion were isolated leaving the spine and the blade. The boundary between the glenoid and the rest of the scapula was identified as the point at which the spinoglenoid notch became visible. The remaining portion of the scapula was again reconstructed in Plane 2 and the spine was isolated. It was originally intended to reconstruct the spinous process in Plane 3, however on inspection of the data it became clear this was not necessary to define VOIs, although the spine was still isolated to prevent overlapping of VOIs. This process is summarised in Figure 6.3, and resulted in three constituent scapular components (Figure 6.4).

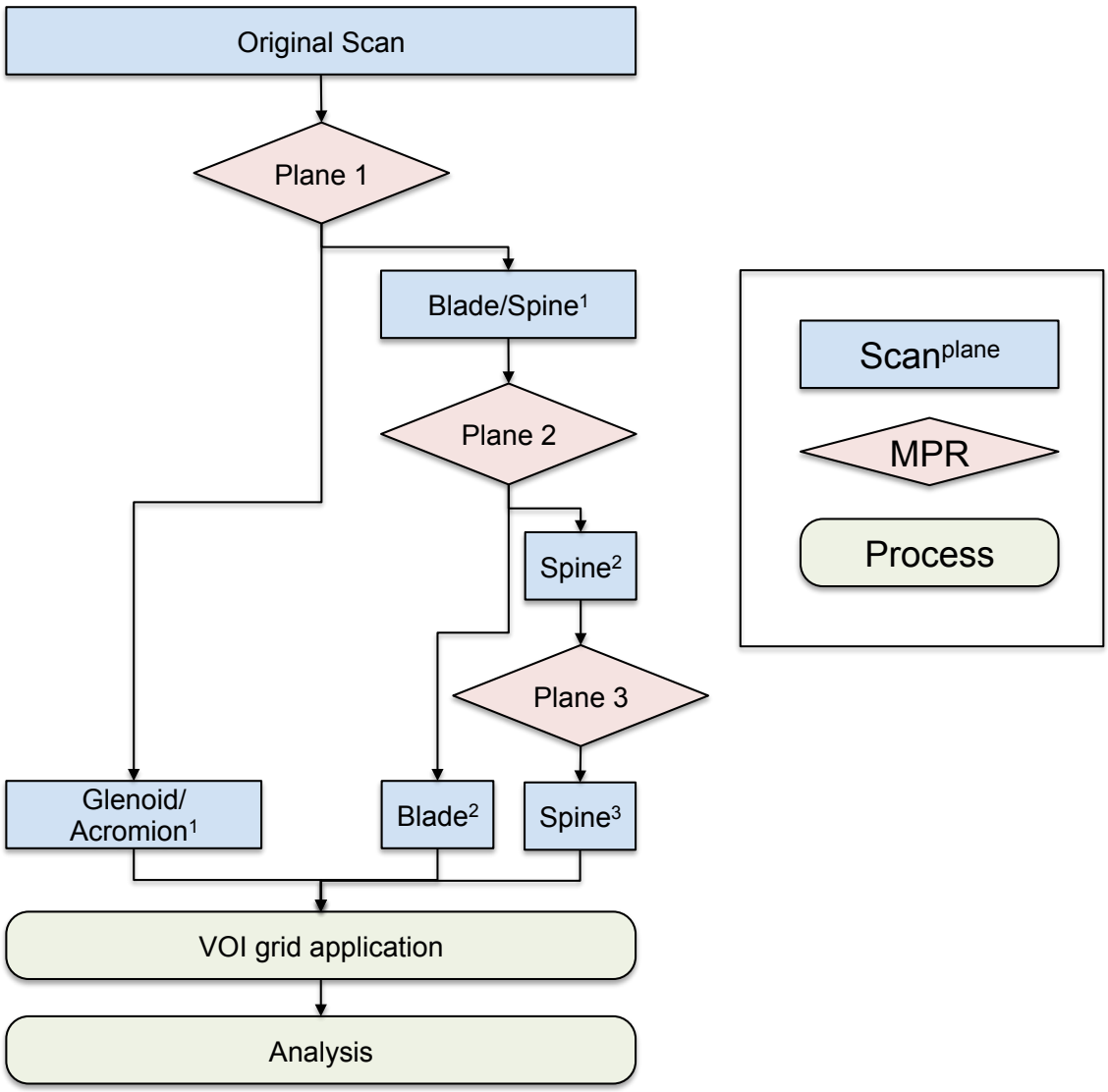

Figure 6.3: Summary of MPR process, including the ultimately rejected Plane 3 reconstruction.

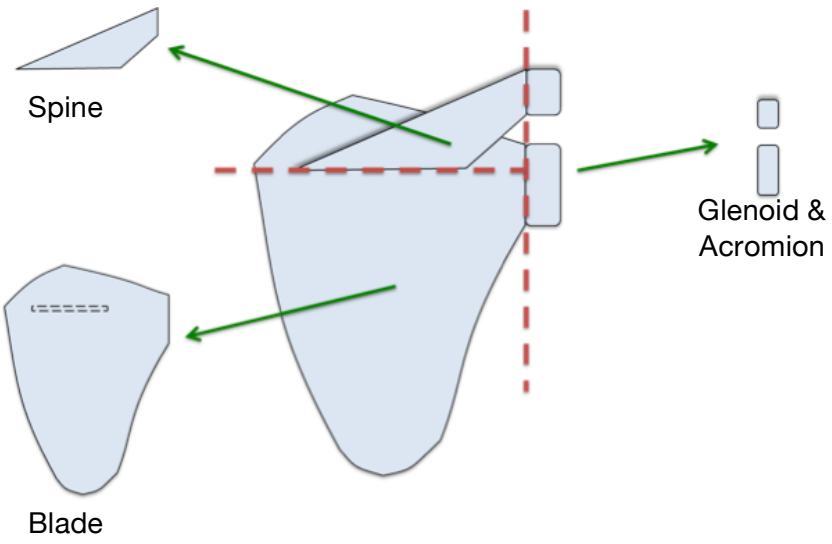

Figure 6.4: The three constituent parts of the scapula: Glenoid & acromion; spine; blade.

During the MPR process a software bug was detected that resulted in the scan resolution being altered during reconstruction. Although assistance from the software developers was sought, time constraints demanded an immediate solution. The following procedure was developed to ensure the scan retained its original resolution during each MPR:

1. The scan was imported into OsiriX and opened in 2D View.
2. The scan was then opened in 3D MPR View, and the resolution calibrated with data from the header file. Three windows appeared: each depicted a perpendicular plane.
3. The ‘Zoom Sync’ setting was activated, to ensure all three MPR views remained at the same zoom level.
4. A TIFF file from the image stack of the original scan was opened and scaled to 100% of original size.
5. The MPR window that depicted the scan in the original plane was resized to match the original TIFF file (from Step 4). It was essential that the contents of this window remained at this magnification during the MPR process.
6. ‘Zoom Sync’ was deactivated.
7. The desired plane was defined by altering the slice axes and zoom levels in the two other MPR windows, then exported as a new image stack in DICOM format.

Before the resulting image stacks could be analysed, they were converted from DICOM files into TIFF format images using Photoshop CS3 v10.0. This conversion was necessary to view and analyse the data in the analysis software, CTAn.

As a result of the MPR process each scan was divided into three constituent parts (Figure 6.4), each in a plane suitable for analysis. A static grid was then applied to each region to define the VOIs. The glenoid and acromion comprised volumes 1-4 and

5 respectively (Figure 6.5); the spine consists of volumes 6-8 (Figure 6.6); the remaining blade (including the infra- and supra- spinous fossae) contained volumes 9-23 (Figure 6.7). 23 VOIs were selected for this study as it was judged this was the minimum number of VOIs that would provide meaningful information about functionally relevant areas; furthermore, greater than 23 VOIs would result in the study becoming too time consuming to complete within the allotted time and could detrimentally effect the reliability of the results, since CTAn calculates an average value across each VOI.

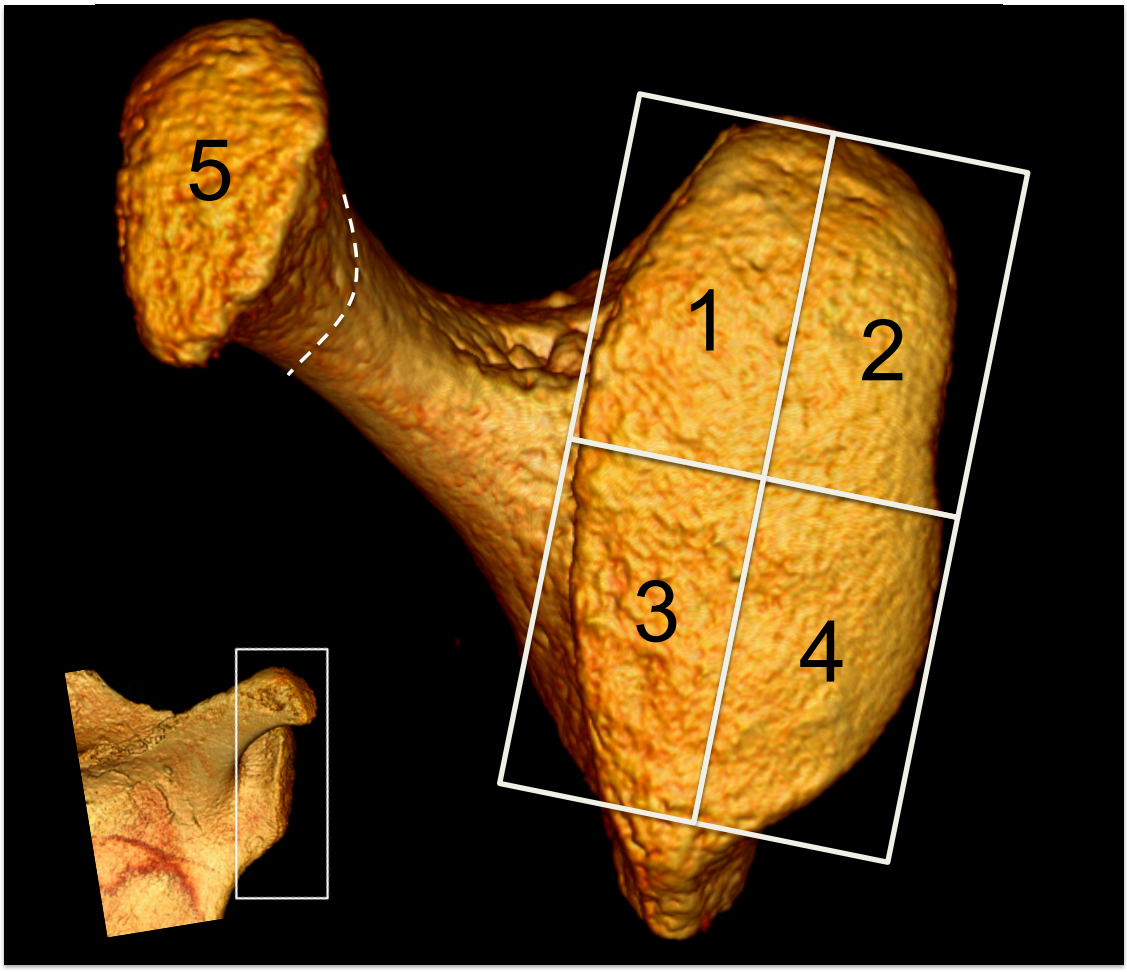

Figure 6.5: Surface rendering of a micro-CT scan depicting VOIs 1-4 (at the glenoid) and VOI 5 (at the acromion).

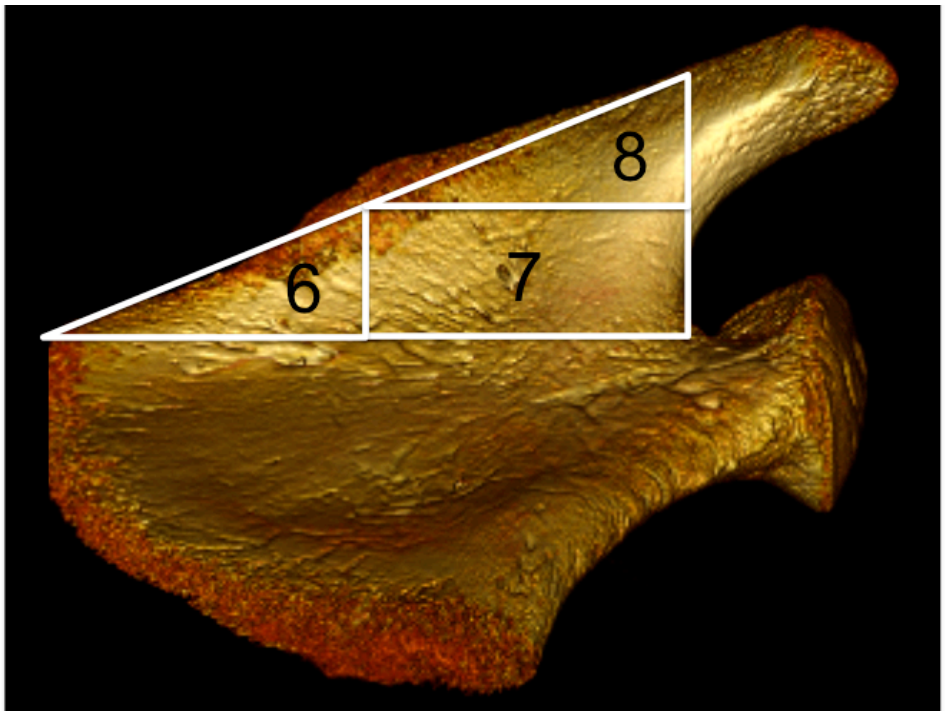

Figure 6.6: Surface rendering of a micro-CT scan depicting VOIs 6, 7 and 8 in the spinous process.

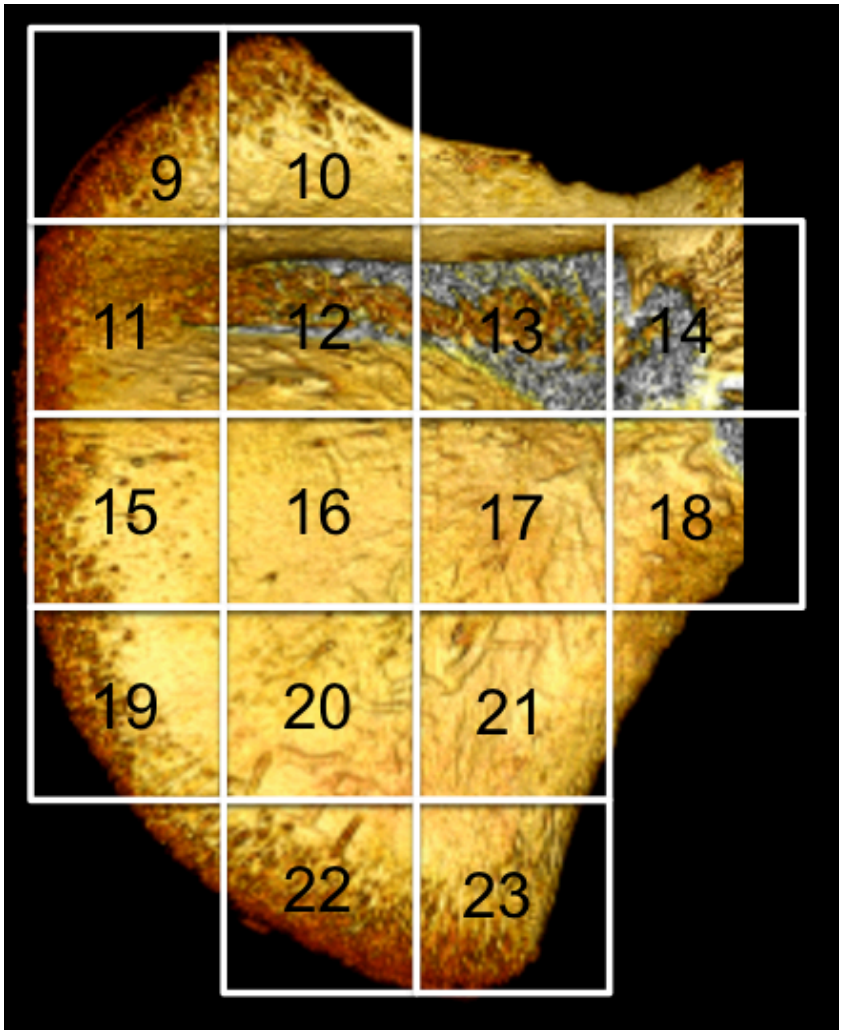

Figure 6.7: Surface rendering of a micro-CT scan, depicting VOIs 9-23 of the blade.

A three-dimensional schematic of how the VOIs interact is presented in Figure 6.8, where the glenoid is coloured green (VOIs 1-4), acromion blue (VOI 5), spine orange (VOIs 6-8) and blade pink (9-23). This style of schematic will be used to summarise the results of the study in Section 6.2: Results. Terminology used to describe specific regions of the blade is presented in Figure 6.9.

This method, combined with the results of the error study (Chapter 5), suggests that there is homology of VOIs between specimens. Despite homologous regions, it is possible that some error might be introduced into the analysis by nature of VOI placement; this would become apparent in results with higher standard deviation (SD) and coefficient of variance (CoV).

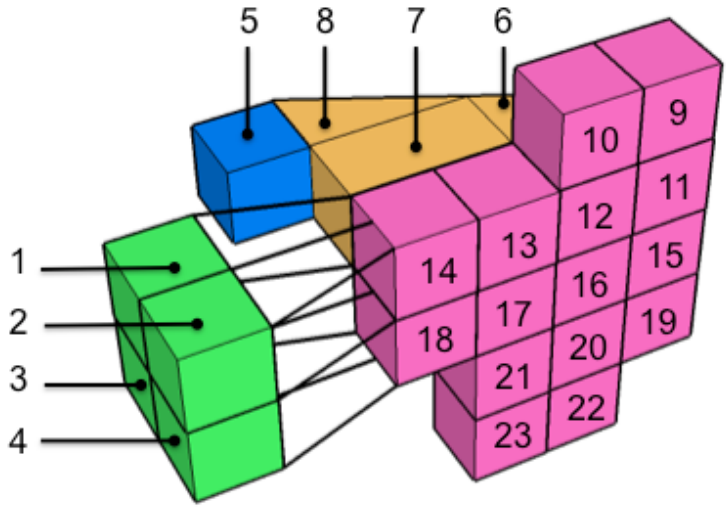

Figure 6.8: A schematic of VOIs, showing VOI interactions in three-dimensions. Glenoid (1-4) = Green; Acromion (5) = Blue; Spine (6-8) = Orange; Blade (9-23) = Pink.

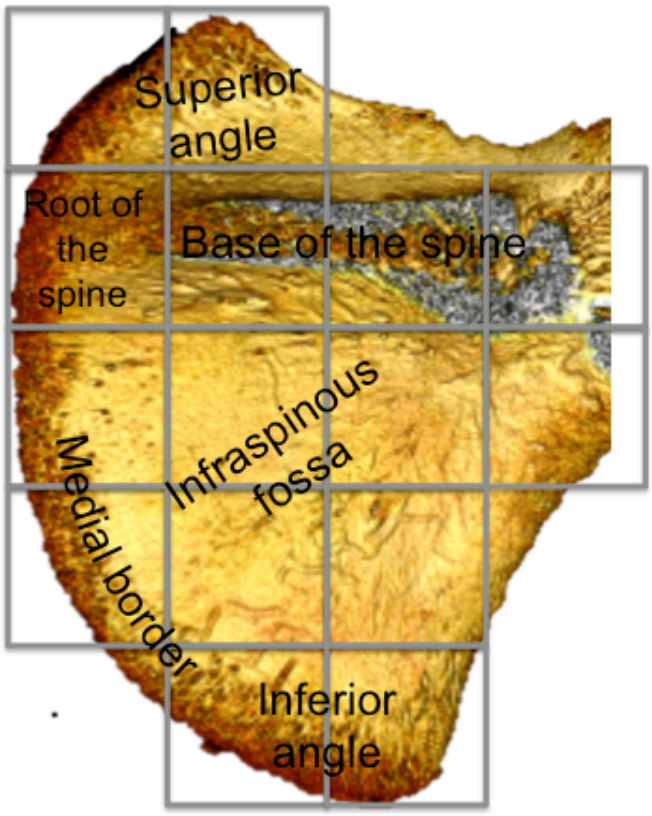

Figure 6.9: Descriptive terminology of the blade in the context of the static grid.

Trabecular Analysis

After undergoing multiplanar reconstruction in OsiriX, the data were suitable for trabecular analysis. An additional software package, CTAn, developed by the micro-CT scanner manufacturer SkyScan, was used to define VOIs and analyse the internal structure.

This software is capable of measuring quantifiable trabecular morphology, as defined by Parfitt et al (1987), from three-dimensional image stacks. CTAn was operated on a Dell Optiplex 780 desktop computer, with an Intel Core 2 Quad 3.0GHz processor and 4GB of RAM running 64-bit Microsoft Windows 7.

After opening a scan in CTAn, the software was calibrated to the resolution of that particular scan: resolution values were taken from the header file that accompanied each scan. This action informs the software of the absolute dimensions of each voxel and ensures that measurements derived from those voxels are accurate.

The appropriate static grid was superimposed onto the monitor to aid in VOI definition. The portion of the image stack that corresponded to a particular VOI was defined by selecting slices as the ‘top of selection’ and ‘bottom of selection’. This action ensured that only slices between (and including) the top and bottom slice would be included in the analysis.

After defining the interslice boundaries of the VOI, the intraslice areas were defined to further isolate the VOI within the scan. A WACOM tablet and pen were used to define all of the medullary space (including trabecular bone) in the region of interest within the top slice. This process was repeated in the bottom slice, and CTAn was instructed to interpolate the area though the rest of the inter-slice selection. Each slice in the interslice selection was then reviewed to ensure that the automated interpolation process had selected the correct region. Any errors in this process were corrected manually by redefining the VOI in any given slice and interpolating again.

Care was taken not to include any cortical bone in the VOI. If cortical bone was included in the VOI, the analysis software would not distinguish between it and 'real' trabecular bone, thus influencing trabecular measurements.

Once the VOI had been defined it was isolated from the rest of the scan and a histogram was produced based on the distribution of grey values. Selecting upper and lower thresholds on the histogram binarised the VOI. This process allows the software to designate whether grey values should be considered bone or medullary space (Figure 6.10). Although the software was capable of automating this process, the results were unreliable; inspection of automatically binarised slices revealed that some trabeculae were often excluded from the analysis during the process. To overcome this issue, the thresholds were defined manually so only solid trabecular bone was included in the analysis. The result of the binary process produces a VOI as a stack of biphasic black and white images, where white represents bone and black represents space. The findings of the error study (Chapter 5) suggest that manual segmentation does not introduce significant error into the analysis.

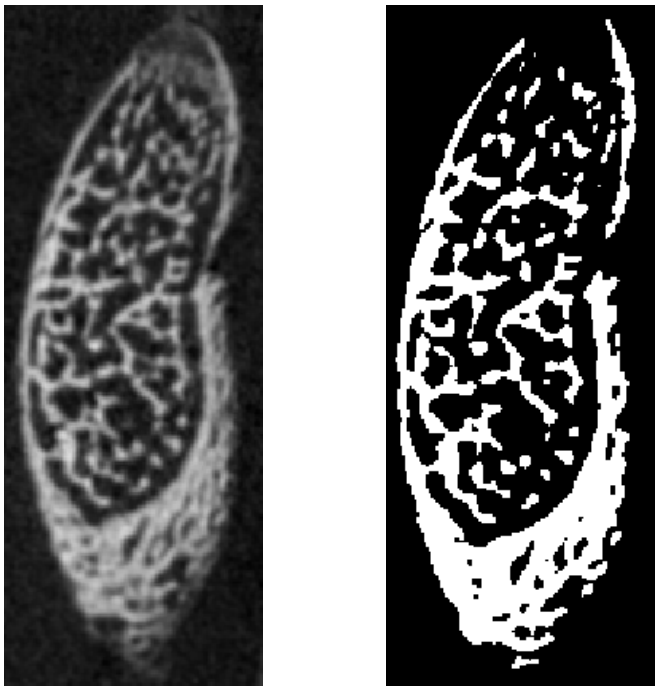

A **B**

Figure 6.10: A: Original grey scale image; B: Binarised Image

Following VOI definition and binarisation, the volume was analysed by the software by selecting the '3D Analysis' tab. This automated process calculated the following parameters:

- Bone volume fraction (**BV/TV**)
- Structural model index (**SMI**)
- Trabecular thickness (**Tb.Th**)
- Trabecular number (**Tb.N**)
- Trabecular separation (**Tb.Sp**)
- Degree of anisotropy (**DA**)

The software outputted the data as a comma-separated value (CSV) file, which was imported into Microsoft Excel where a colour-coded schematic was produced and descriptive statistics were calculated for each metric. The process of VOI definition and binarisation was repeated for each VOI in each specimen.

Bone volume fraction (BV/TV)

Bone volume fraction is a measure of the proportion of a VOI that is occupied by binarised solid objects. In this study it describes the trabecular bone volume (BV) in relation to the total volume of the VOI (TV) represented as a percentage. BV.TV is only useful if calculated from a binarised volume of solid (bone) and (medullary) space, while solid cortical bone must not be included in the analysis. Trabecular bone volume fraction is considered to be the most important metric in analysing juvenile trabecular bone (Aubin et al., 1998); it has been shown to reflect the biomechanical capability of trabecular bone (Pothuaud et al., 2002; Cunningham and Black, 2009a), and is thought to respond to developmental changes to loading before other parameters (Tanck et al., 2001).

Structural model index (SMI)

Structural model index quantifies the relative prevalence of trabecular morphologies. The index describes the surface concavity or convexity of trabeculae, thus indicating whether they more closely resemble plates or rods. A perfect plate, cylinder (rod) and sphere have SMI values of 0, 3 and 4 respectively. Analysis of a volume that contains a mixture of plates and rods will result in a SMI value between 0 and 3 depending on the relative proportion of rods to plates. SMI was devised by Hildebrand and Ruegsegger (1997), and uses an artificially dilated 3D voxel model which is produced by artificially adding one voxel to all binarised object surfaces. SMI is calculated as follows:

$$SMI = 6 \times \left(\frac{S' \times V}{S^2} \right)$$

Where S is the original surface area, S' is the change in surface area caused by artificial dilation and V is the original object volume.

Trabecular thickness (Tb.Th)

Trabecular thickness is calculated as an average of local thickness at each solid voxel, as defined during binarisation. Local thickness calculation was originally defined by Hildebrand and Ruegsegger (1997) as the diameter of the largest sphere that fulfils two conditions:

1. The sphere must enclose the point, but the point may not necessarily be at the centre of the sphere,
2. The sphere must be entirely contained within the solid structure.

Rather than calculate local thickness for all solid pixels in the VOI, CTAn uses a “skeletonisation” technique designed by Remy and Thiel (2002) to identify the medial axis of all structures in the volume before employing the Hildebrand and Ruegsegger

(1997) “sphere-fitting” method only to voxels lying on the axis. Values for trabecular thickness are expressed in mm.

Trabecular separation is thought to be of importance when investigating the degree of remodelling in bone and regions of advanced ossification and growth are proposed to exhibit increased trabecular thickness (Ding and Hvid, 2000; Reissis and Abel, 2012; Cunningham, 2009).

Trabecular separation (Tb.Sp)

Trabecular separation is a measure of the average size of the spacing between solid objects in a VOI. It is calculated in the same way as trabecular thickness, except applied to space rather than solid voxels. Values for trabecular separation are expressed in mm.

Trabecular separation has been shown to be relevant in the study of osteoporosis and increased separation is thought to have biomechanical consequences (Kang et al., 1999).

Trabecular number (Tb.N)

Trabecular number describes the number of traversals across a solid (trabecular) structure made per millimetre on a random linear path through a VOI. It is a secondary morphometric parameter calculated as:

$$Tb.N = \frac{1}{(Tb.Th + Tb.Sp)}$$

Values for trabecular number are expressed in mm^{-1}.

Degree of anisotropy (DA)

Isotropy is a measure of the presence or absence of alignment of structures along a particular directional axis. Trabeculae in isotropic VOIs can be described as exhibiting uniformity in all directions (trabecular organisation), while trabeculae in anisotropic VOIs can be described as exhibiting different values when measured in different directions (trabecular disorganisation). DA is traditionally expressed as the maximum eigenvalue divided by the minimum eigenvalue; eigenvalues are defined as of a set of values of a parameter for which a differential equation has a non-zero solution (an eigenfunction) under given conditions. This scale is considered mathematically difficult to analyse so CTAn produces a more convenient index, which is calculated as:

$$DA = \left(1 - \left[\frac{\min eigenvalue}{\max eigenvalue}\right]\right)$$

Using this calculation method, a value of 0 indicates total isotropy (trabecular organisation) and 1 indicates total anisotropy (trabecular disorganisation).

Alongside BV/TV, DA has been shown to be one of the most important determinants of mechanical strength (Odgaard, 1997), and has also been shown to correlate highly with an increased risk of femoral fractures (Ciarelli et al., 1991).

Data Presentation

Descriptive Statistics

For each metric a table of descriptive statistics, which includes the mean, standard deviation, range and coefficient of variation was prepared for each VOI, was created. Raw data are available in Appendix C: Stereoscopic Data. A graph of the mean measurements with standard deviation error bars for each metric was derived from the raw data.

A schematic representation of all VOIs was prepared for each metric to convey a sense of relative location to the data (Figure 6.11). Each VOI in the schematic was coloured to reflect its relative mean value. Absolute mean values were mapped to a relative colour using a conditional formatting tool in Microsoft Excel. This conditional formatting resulted in the highest mean value being mapped to green, while the lowest mean value was mapped to red. A series of twenty-five arbitrary incremental values were subjected to the same conditional formatting procedure to demonstrate extreme high (green), low (red) and intermediate values are designated the appropriate colour on the spectrum (Figure 6.12).

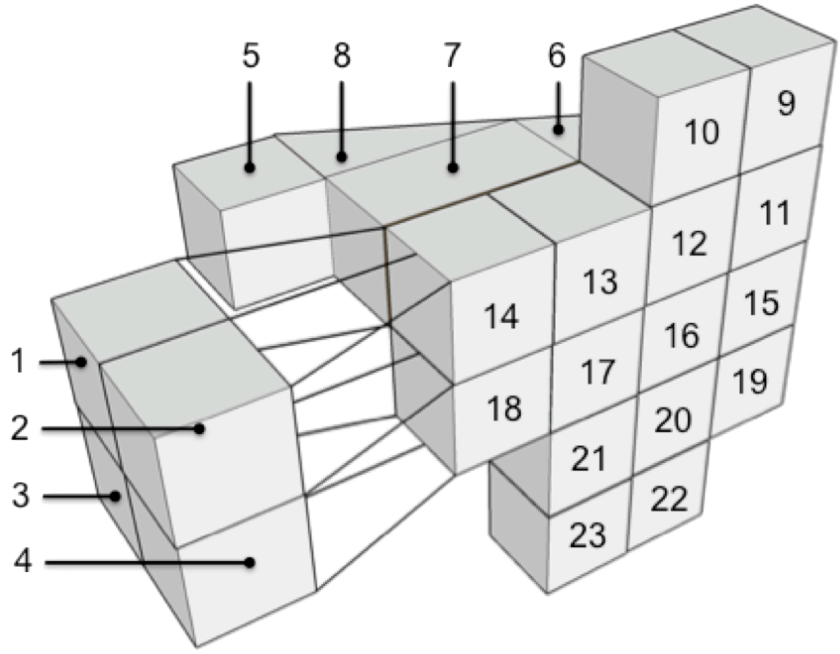

Figure 6.11: Format of the schematic used to present results.

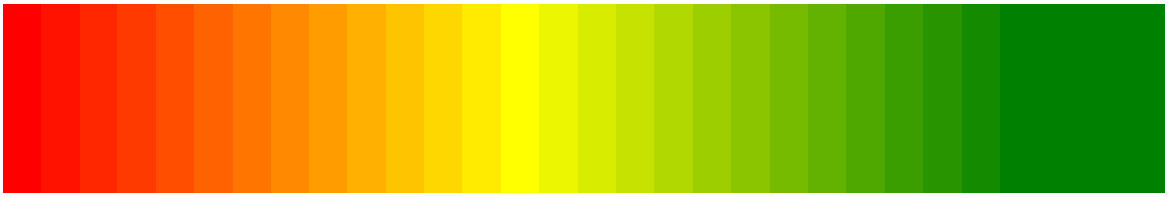

Figure 6.12: A series of twenty-five arbitrary incremental numbers, subjected to the conditional formatting procedure.

Statistical Testing

The data were statistically tested using SigmaPlot 12 (Systat Software Inc.). All metrics failed the Shapiro-Wilk normality test ($P<0.05$), which suggests that the data is non-parametic and not normally distributed. As a result, the data were subjected to Kruskal-Wallis analysis of variance (ANOVA) on ranks, which is designed to handle non-parametric data. For all metrics, the overall differences in the median values among the VOIs were greater than would be expected by chance for all metrics ($P \leq 0.001$). Full statistical analyses are available in Appendix D: Statistical Testing. To isolate which VOIs differed statistically for a given metric, a pairwise multiple comparison procedure was undertaken using Dunn's Method. This test produces the difference of rank means, the Q-value (i.e. power of the result of the statistical test) and whether $P<0.05$ for each combination of VOI.

The output of the test comprises 253 responses of either "YES", "NO" and "DO NOT TEST", one for every combination of VOI. If a VOI is found to be not significantly different to another VOI, all VOIs with p ranks between the p ranks of the two groups that are not different are also assumed not to be significantly different, and a result of "DO NOT TEST" is given.

The outcome of the pairwise comparison procedures for each metric are presented in tabular form where a green cell containing 'Y' indicates a statistically significant difference between VOIs, and a red cell containing 'N' indicates no statistically significant difference between VOIs.

For presentation of these statistical results, the blade is subdivided into distinct regions to facilitate interpretation:

- Superior angle (VOIs 9, 10)
- Spinous base (VOIs 12-14)
- Spinous root (VOI 11)
- Infraspinous fossa (VOIs 15-21), including three subgroups:
    - Medial (VOIs 15, 16)
    - Lateral (VOIs 17, 18)
    - Inferior (VOIs 19, 21)
- Inferior angle (VOIs 22, 23)

Patterns in the statistical results were then sought, and VOIs were separated into groups based on their common statistical differences and lack thereof; thus, separation into groups is not an indication of statistically significant difference *per se*, but an indication of statistical distinctions only. Each of these groups was then attributed a range of median values from the raw data, and assigned a descriptor (e.g. low, moderate or high). Each group of VOIs was also assigned a colour, which was used schematically to convey locational context.

6.2. Results

Bone Volume Fraction (BV/TV)

Table 6.2 contains the descriptive statistics for bone volume fraction (BV/TV) for each volume of interest, and mean measurements with standard deviation error bars are displayed graphically in Figure 6.13.

Bone Volume Fraction (%)					
VOI	Mean	Range		Std. Dev.	CoV
		Min.	Max.		
1	38.898	35.127	43.254	2.308	5.93%
2	38.734	34.204	44.947	2.491	6.43%
3	36.991	30.715	42.939	3.243	8.77%
4	37.435	31.968	43.506	3.121	8.34%
5	33.422	26.680	40.047	3.416	10.22%
6	30.017	22.596	36.897	3.860	12.86%
7	26.927	18.939	32.850	3.027	11.24%
8	29.871	19.477	37.702	4.650	15.57%
9	38.169	28.937	41.454	2.507	6.57%
10	38.448	31.661	42.860	2.799	7.28%
11	31.752	27.118	36.724	1.853	5.84%
12	29.804	27.059	33.701	1.669	5.60%
13	20.979	13.860	28.340	4.014	19.13%
14	31.362	27.122	35.317	2.352	7.50%
15	33.045	28.567	35.946	1.859	5.63%
16	35.372	33.319	37.402	1.404	3.97%
17	30.744	14.357	38.094	5.076	16.51%
18	33.051	21.403	37.910	4.049	12.25%
19	41.348	33.312	45.383	2.151	5.20%
20	41.318	37.075	44.810	2.047	4.95%
21	39.021	34.450	42.466	1.830	4.69%
22	42.315	36.930	46.754	2.736	6.47%
23	43.690	39.493	47.182	2.238	5.12%

Table 6.2: Descriptive statistics for bone volume fraction (BV/TV) at each volume of interest.

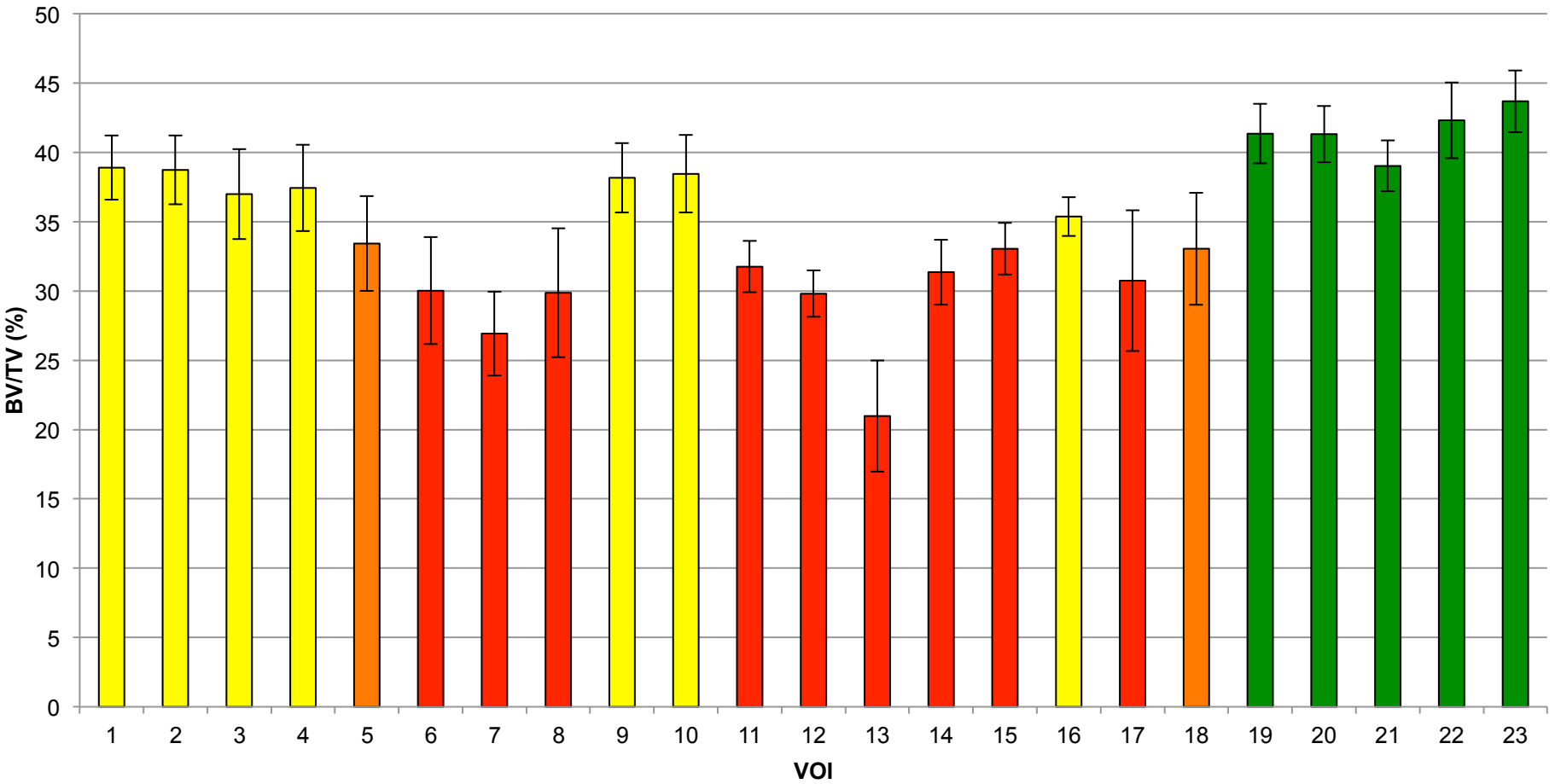

Figure 6.13: Graphic representation of mean (±SD) BV/TV values for each VOI. Bar colours relate to statistical distinctions, which are summarised in Figure 6.15C and Table 6.3.

Regions of lowest BV/TV are located in and around VOI 13, where the spine, glenoid and blade combine. Regions with the highest BV/TV values are found at the inferior half of the blade (VOIs 19-23), superior angle (VOIs 9-10) and glenoid (VOIs 1-4).

The results of statistical testing are summarised in Figure 6.14.

REGION		GLENOID				ACROMION	SPINE			SUPERIOR ANGLE		SPINOUS BASE				INFRA-SPINOUS FOSSA							INFERIOR ANGLE	
	VOI	1	2	3	4	5	6	7	8	9	10	11	12	13	14	15	16	17	18	19	20	21	22	23
GLENOID	1																							
	2	N																						
	3	N	N																					
	4	N	N	N																				
ACROMION	5	Y	N	N	N																			
SPINE	6	Y	Y	Y	Y	N																		
	7	Y	Y	Y	Y	N	N																	
	8	Y	Y	Y	Y	N	N	N																
SUPERIOR ANGLE	9	N	N	N	N	N	Y	Y	Y															
	10	N	N	N	N	N	Y	Y	Y	N														
SPINOUS BASE	11	Y	Y	Y	Y	N	N	N	N	Y	Y													
	12	Y	Y	Y	Y	N	N	N	N	Y	Y	N												
	13	Y	Y	Y	Y	N	N	N	N	Y	Y	N	N											
	14	Y	Y	Y	Y	N	N	N	N	Y	Y	N	N	N										
INFRA-SPINOUS FOSSA	15	Y	Y	Y	N	N	N	N	N	Y	Y	N	N	N	N									
	16	N	N	N	N	N	N	N	N	N	N	N	N	N	N	N								
	17	Y	Y	Y	Y	N	N	N	N	Y	Y	N	N	N	N	N	N							
	18	Y	N	N	N	N	N	N	N	N	N	N	N	N	N	N	N	N						
	19	N	N	N	N	Y	Y	Y	Y	N	N	Y	Y	Y	Y	Y	N	Y	Y					
	20	N	N	N	N	Y	Y	Y	Y	N	N	Y	Y	Y	Y	Y	N	Y	Y	N				
	21	N	N	N	N	Y	Y	Y	Y	N	N	Y	Y	Y	Y	Y	N	Y	Y	N	N			
INFERIOR ANGLE	22	N	N	N	N	Y	Y	Y	Y	N	N	Y	Y	Y	Y	Y	N	Y	Y	N	N	N		
	23	N	N	N	N	Y	Y	Y	Y	N	N	Y	Y	Y	Y	Y	N	Y	Y	N	N	N	N	

Figure 6.14: Summary of multiple pairwise comparisons (Dunn's Method) for BV/TV for all VOIs. Green 'Y' signifies a statistically significant (P<0.05) difference between VOIs; Red 'N' signifies no statistically significant difference.

The spine (VOIs 6-8), its base and root (VOIs 11-14), VOI 15 and VOI 17 have a significantly lower bone volume fraction than the glenoid (VOIs 1-4), superior angle (VOIs 9-10), inferior portion of the infraspinous fossa (VOIs 19-21) and the inferior angle (VOIs 22-23), but not significantly lower than the acromion (VOI 5) or VOI 18.

The acromion and VOI 18 contained a significantly lower proportion of bone than only the inferior portion of the infraspinous fossa and the inferior angle, but not significantly lower than the glenoid and the superior angle.

The glenoid and the superior contained significantly more bone than the spine, its base and root, VOI 15 and VOI 17, but not significantly less than the inferior portion of the glenoid and the inferior angle.

The inferior portion of the glenoid and the inferior angle had a significantly greater proportion of bone than the acromion, spine (including its base and its root) and VOIs 15, 17 and 18.

VOI 16 was not significantly different to any other volume, and can be considered as having moderate bone volume fraction.

The statistical analysis indicates four distinct groups of VOIs with very low (21-32%), low (33%), moderate (37-39%) and high (39-44%) bone volume fraction:

- Very low: the spine (including its base and root) and VOIs 15 and 17.
- Low: the acromion and VOI 18.
- Moderate: the glenoid, superior angle and VOI 16.
- High: the inferior portion of the infraspinous fossa and the inferior angle.

Mean measurements for each VOI are presented schematically in Figure 6.15B. The groups of statistically distinct regions are presented in schematic and tabular forms in Figure 6.15C and Table 6.3 respectively. Additionally, bars in Figure 6.13 have been coloured to reflect the distinct regions.

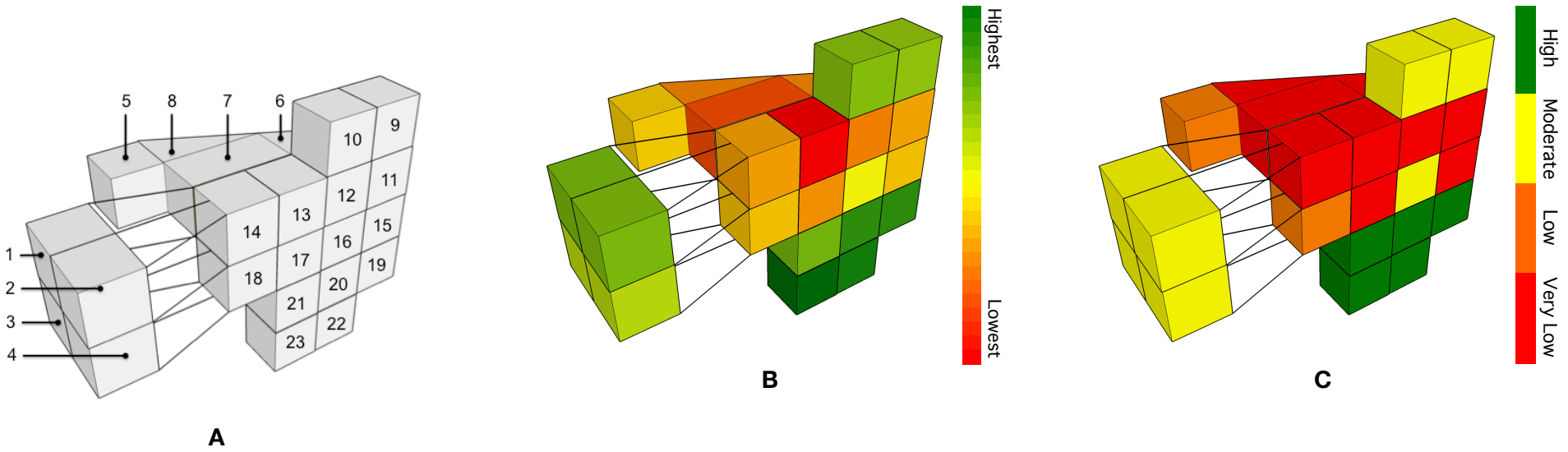

Figure 6.15: BV/TV VOI Schematics.
A: VOI numbers, for reference. B: Mean BV/TV values. C: Statistically distinct groups of VOIs.

Group	BV/TV Range	VOIs	Description
High	39-44%	19-23	Inferior portion of infraspinous fossa and inferior angle
Moderate	37-39%	1-4;9-10; 16	Glenoid, superior angle, VOI 16
Low	33%	5, 18	Acromion, VOI 18
Very Low	21-32%	6-8; 11-15; 17	Spine (including its base and root), VOI 15, VOI 17

Table 6.3: Summary of statistically distinct groups of VOIs for BV/TV.

Structural Model Index (SMI)

Table 6.4 shows the descriptive statistics for structural model index (SMI) for each volume of interest. Mean measurements with standard deviation error bars are presented graphically in Figure 6.16. SMI values relevant to this study can range between 0 and 3, where 0 describes a plate and 3 describes a rod. The SMI values could theoretically also extend between -1 (for concave structures) and 4 (for spheres).

Structural Model Index					
VOI	Mean	Range		Std. Dev.	CoV
		Min.	Max.		
1	1.39	1.03	1.67	0.16	11.23%
2	1.39	0.93	1.72	0.21	14.93%
3	1.42	0.97	1.84	0.23	15.96%
4	1.38	0.99	1.70	0.19	13.78%
5	1.47	0.97	2.02	0.30	20.58%
6	1.99	1.62	2.32	0.18	9.07%
7	2.28	1.99	2.53	0.15	6.43%
8	2.33	1.75	2.83	0.26	11.22%
9	1.68	1.26	2.11	0.21	12.53%
10	1.77	1.25	2.03	0.18	9.92%
11	1.71	0.43	2.33	0.33	19.60%
12	2.02	1.49	2.51	0.20	10.06%
13	2.30	0.95	2.76	0.33	14.30%
14	2.05	1.11	2.37	0.24	11.46%
15	1.90	1.38	2.21	0.20	10.29%
16	1.93	1.59	2.16	0.22	11.39%
17	1.93	1.46	2.43	0.24	12.39%
18	2.07	1.48	2.66	0.24	11.43%
19	1.62	0.99	2.09	0.23	13.89%
20	1.76	1.34	2.14	0.20	11.35%
21	1.61	1.14	2.04	0.20	12.62%
22	1.39	0.97	1.91	0.24	17.15%
23	1.16	0.34	1.71	0.32	27.67%

Table 6.4: Descriptive statistics for structural model index (SMI) at each volume of interest (VOI)

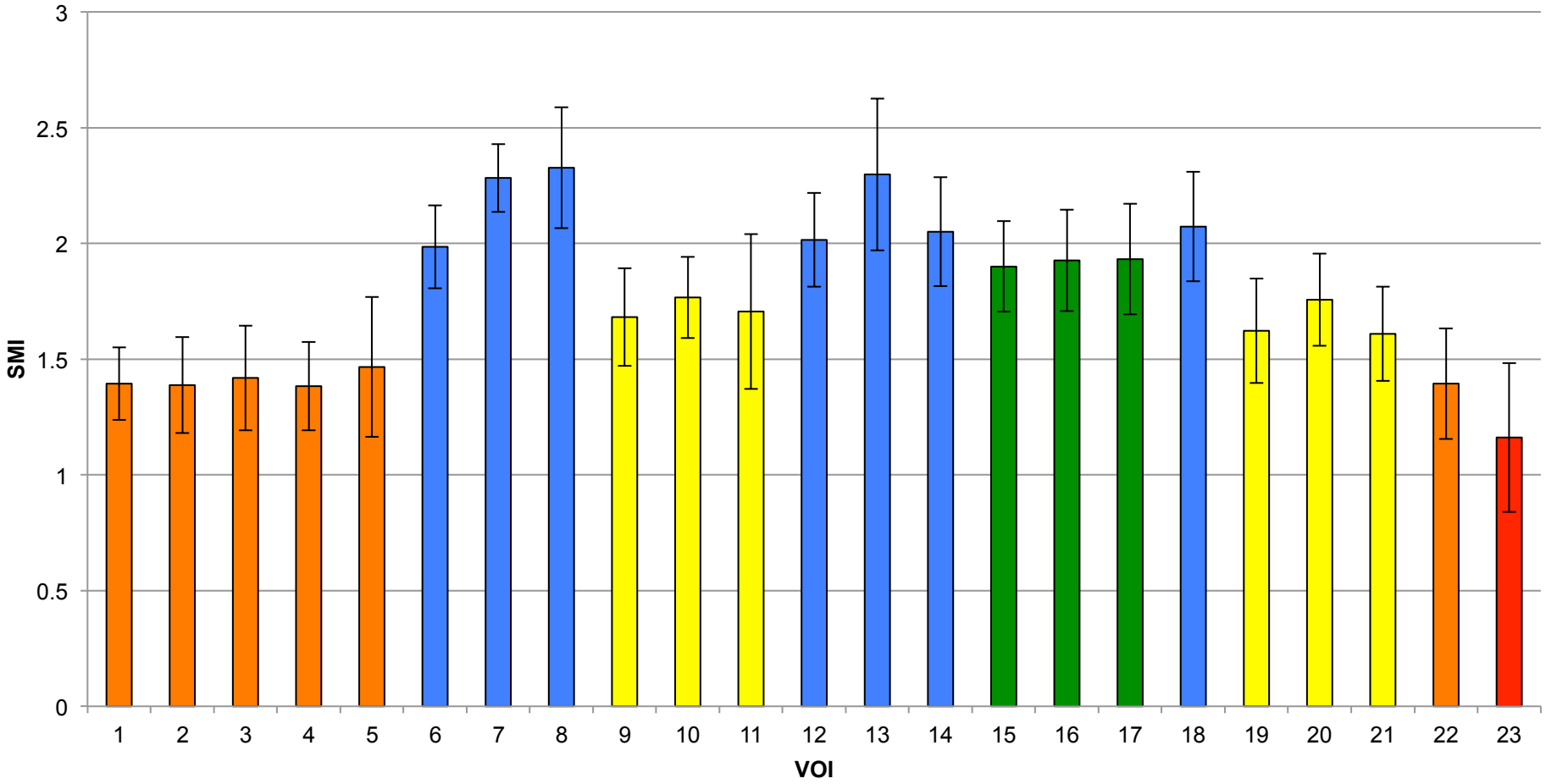

Figure 6.16: Graphic representation of mean (±SD) SMI values for each VOI.
Bar colours relate to statistical distinctions, which are summarised in Figure 6.18C and Table 6.5.

Although a range of SMI results were observed, most VOIs contained trabeculae that were more rod-shaped. Exceptions included the glenoid, acromion and the inferior angle, which possessed the most plate-like trabeculae. VOI 13 and its neighbouring volumes in the spine (VOIs 7, 8) and its base (VOIs 12,14) tended towards rod-like shapes.

The outcome of statistical testing is summarised in Figure 6.17, which highlights the clearest differences between rods and plates.

REGION		GLENOID				ACROMION	SPINE			SUPERIOR ANGLE		SPINOUS ROOT				INFRA-SPINOUS FOSSA							INFERIOR ANGLE	
	VOI	1	2	3	4	5	6	7	8	9	10	11	12	13	14	15	16	17	18	19	20	21	22	23
GLENOID	1																							
	2	N																						
	3	N	N																					
	4	N	N	N																				
ACROMION	5	N	N	N	N																			
SPINE	6	Y	Y	Y	Y	Y																		
	7	Y	Y	Y	Y	Y	N																	
	8	Y	Y	Y	Y	Y	N	N																
SUPERIOR ANGLE	9	N	N	N	N	N	N	Y	Y															
	10	N	N	N	N	N	N	Y	Y	N														
SPINOUS ROOT	11	N	N	N	N	N	N	Y	Y	N	N													
	12	Y	Y	Y	Y	Y	N	N	N	N	N	N												
	13	Y	Y	Y	Y	Y	N	N	N	Y	Y	Y	N											
	14	Y	Y	Y	Y	Y	N	N	N	Y	N	N	N	N										
INFRA-SPINOUS FOSSA	15	N	N	N	N	N	N	Y	N	N	N	N	N	N	N									
	16	N	N	N	N	N	N	N	N	N	N	N	N	N	N	N								
	17	N	N	N	N	N	N	N	N	N	N	N	N	N	N	N	N							
	18	Y	Y	Y	Y	Y	N	N	N	Y	N	N	N	N	N	N	N	N						
	19	N	N	N	N	N	Y	Y	Y	N	N	N	Y	Y	Y	N	N	N	Y					
	20	N	N	N	N	N	N	Y	Y	N	N	N	N	Y	N	N	N	N	N	N				
	21	N	N	N	N	N	Y	Y	Y	N	N	N	Y	Y	Y	N	N	N	Y	N	N			
INFERIOR ANGLE	22	N	N	N	N	N	Y	Y	Y	N	N	N	Y	Y	Y	N	N	N	Y	N	N	N		
	23	N	N	N	N	N	Y	Y	Y	Y	Y	Y	Y	Y	Y	Y	Y	Y	Y	N	Y	N	N	

Figure 6.17: Summary of multiple pairwise comparison (Dunn's Method) results for SMI between all VOIs. Green 'Y' signifies a statistically significant (P<0.05) difference between VOIs; red 'N' signifies no statistically significant difference.

The spine, its base and VOI 18 were significantly more rod-like than the glenoid, acromion, inferior portion of the infraspinous fossa and the inferior angle.

Part of the infraspinous fossa (VOIs 15-17) was not significantly different to any other region, with the exception of VOI 23 at the inferior angle.

The statistical results for the superior angle, root of the spine and the inferior portion of the infraspinous fossa were similar to the results for the glenoid and acromion, although there were exceptions to the overall pattern. Additionally, these regions were statistically different to VOI 23, whereas the glenoid and acromion were not.

The glenoid, acromion and VOI 22 (at the inferior angle) contained trabeculae that were significantly more rod-like than those in the spine, its base and VOI 18, although not significantly different to VOI 23.

Trabeculae in VOI 23 were significantly more rod-like than those in all other regions, with the exception of the glenoid and the acromion.

These data suggest that five distinct regions are statistically distinguishable from the trabecular structural model index:

- Very low (1.2): VOI 23 at the inferior angle
- Low (1.4): the glenoid, acromion and VOI 22 at the inferior angle
- Moderate (1.6-1.8): the superior angle, root of the spine, and inferior portion of the infraspinous fossa.
- High (1.9): VOIs 15-17 of the infraspinous fossa
- Very high (2.0-2.3): the spine, its base and VOI 18.

Mean measurements for each VOI are presented schematically in Figure 6.18B**.** Groups of statistically distinct regions are presented in schematic and tabular forms in Figure 6.18C and Table 6.5 respectively. Additionally, bars in Figure 6.16 have been coloured to reflect the distinct regions.

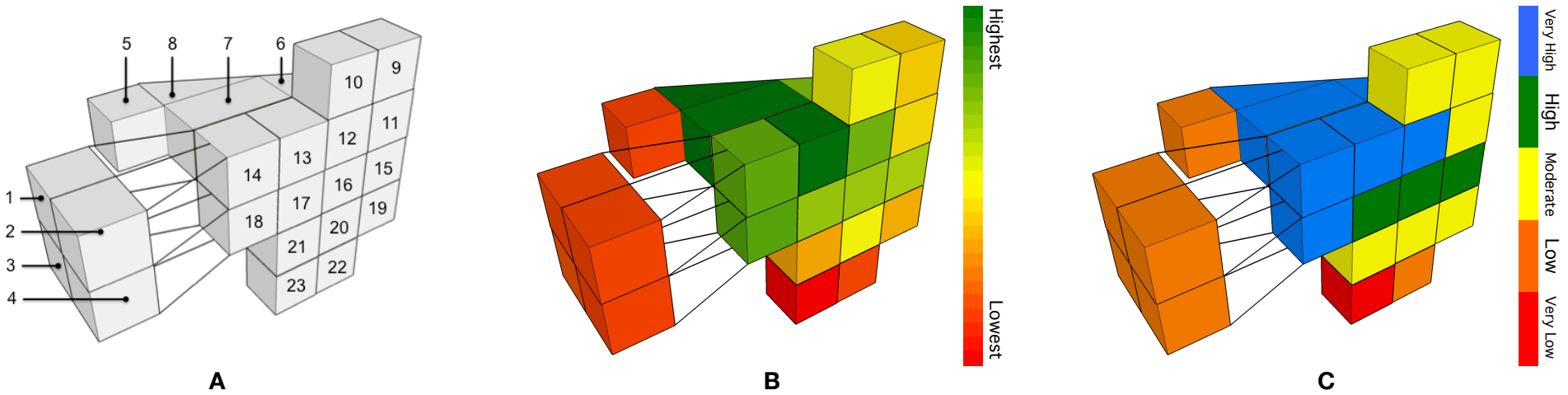

Figure 6.18: SMI VOI Schematics.
A: VOI numbers, for reference. B: Mean values. C: Statistically distinct groups of VOIs.

Group	SMI Range	VOIs	Description
Very High	2.0-2.3	6-8; 12-14; 18	Spine (including its base), VOI 18
High	1.9	15-17	Part of the superior portion of the infraspinous fossa
Moderate	1.6-1.8	9-11; 19-21	Superior angle, root of the spine, inferior portion of the infraspinous fossa
Low	1.4	1-5; 22	Glenoid, acromion, medial side of the inferior angle
Very Low	1.2	23	Lateral side of the inferior angle

Table 6.5: Summary of statistically distinct groups of VOIs for SMI.

Trabecular Thickness (Tb.Th)

Table 6.6 shows the descriptive statistics for trabecular thickness (Tb.Th) for each volume of interest. Mean measurements with standard deviation error bars are presented graphically in Figure 6.19.

Trabecular Thickness (mm)					
VOI	Mean	Range		Std. Dev.	CoV
		Min.	Max.		
1	0.204	0.151	0.244	0.020	9.643%
2	0.203	0.140	0.237	0.022	10.829%
3	0.213	0.159	0.264	0.022	10.493%
4	0.212	0.148	0.255	0.025	11.881%
5	0.235	0.139	0.318	0.034	14.417%
6	0.235	0.196	0.290	0.023	9.978%
7	0.257	0.183	0.353	0.036	14.165%
8	0.250	0.179	0.333	0.039	15.689%
9	0.208	0.122	0.279	0.032	15.248%
10	0.207	0.141	0.256	0.021	10.290%
11	0.214	0.137	0.286	0.031	14.628%
12	0.232	0.146	0.304	0.034	14.778%
13	0.244	0.082	0.340	0.064	26.408%
14	0.284	0.176	0.373	0.045	15.977%
15	0.191	0.120	0.245	0.028	14.635%
16	0.173	0.156	0.210	0.019	11.062%
17	0.210	0.130	0.270	0.032	15.154%
18	0.245	0.166	0.326	0.040	16.296%
19	0.202	0.137	0.246	0.028	14.007%
20	0.195	0.126	0.249	0.029	15.062%
21	0.218	0.144	0.295	0.029	13.496%
22	0.215	0.146	0.264	0.027	12.576%
23	0.226	0.154	0.270	0.026	11.455%

Table 6.6: Descriptive statistics for trabecular thickness (Tb.Th) at each volume of interest (VOI).

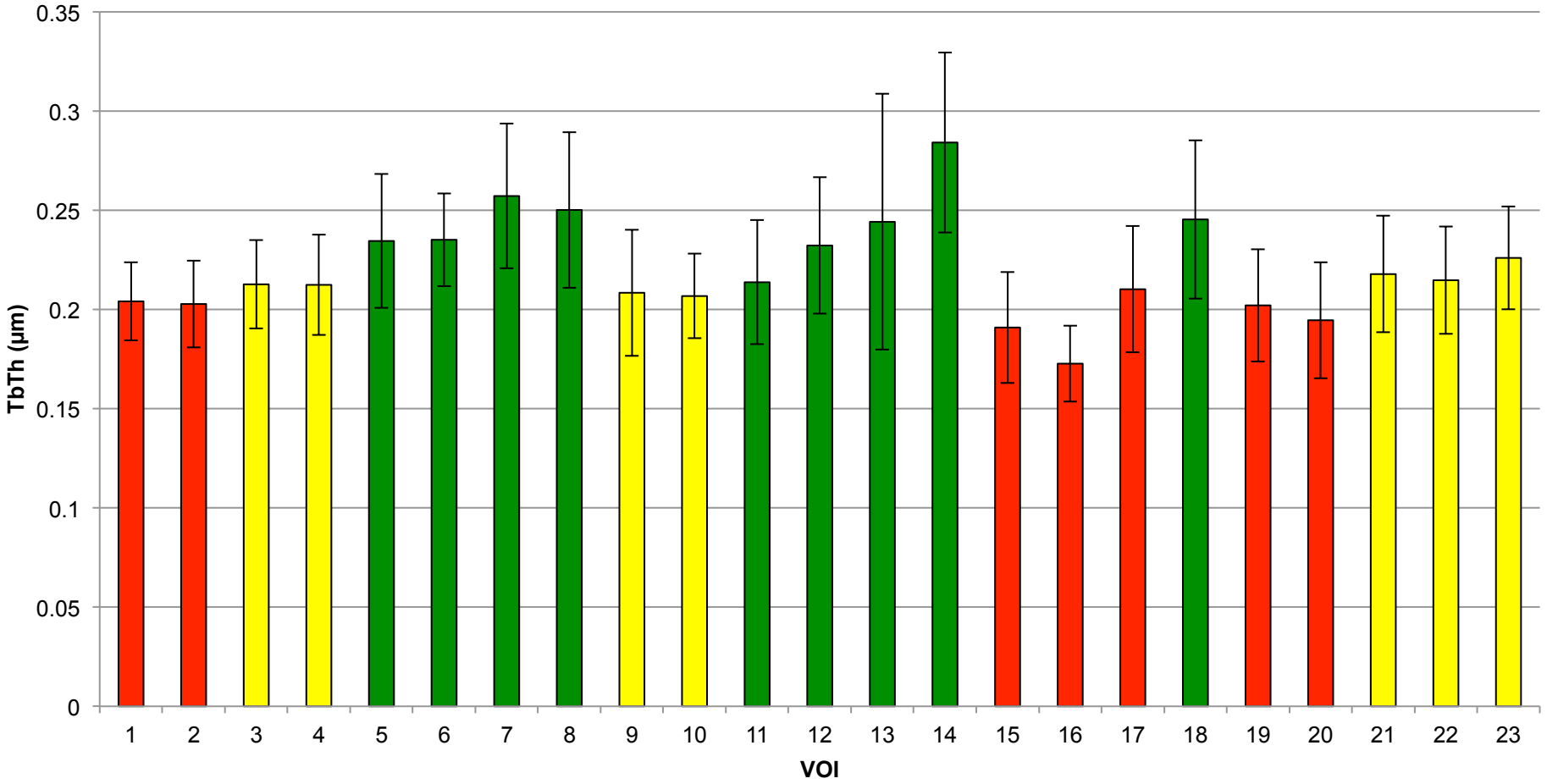

Figure 6.19: Graphic representation of mean (±SD) Tb.Th values for each VOI.
Bar colours relate to statistical distinctions, which are summarised in Figure 6.21C and Table 6.7.

The thickest trabeculae (>0.230mm) were located in the spine and its base and the acromion. Trabeculae were thinner in the glenoid, superior angle, infraspinous fossa and inferior angle. Patterns of statistical differences for Tb.Th were less apparent than for other metrics.

The results of the statistical testing are summarised in Figure 6.20.

REGION		GLENOID				ACROMION	SPINE			SUPERIOR ANGLE		SPINOUS ROOT				INFRA-SPINOUS FOSSA							INFERIOR ANGLE	
	VOI	1	2	3	4	5	6	7	8	9	10	11	12	13	14	15	16	17	18	19	20	21	22	23
GLENOID	1																							
	2	N																						
	3	N	N																					
	4	N	N	N																				
ACROMION	5	Y	Y	N	N																			
SPINE	6	Y	Y	N	N	N																		
	7	Y	Y	Y	Y	N	N																	
	8	Y	Y	N	N	N	N	N																
SUPERIOR ANGLE	9	N	N	N	N	N	N	Y	Y															
	10	N	N	N	N	N	Y	Y	Y	N														
SPINOUS ROOT	11	N	N	N	N	N	N	Y	N	N	N													
	12	Y	Y	N	N	N	N	N	N	N	N	N												
	13	Y	Y	N	N	N	N	N	N	Y	Y	N	N											
	14	Y	Y	Y	Y	N	N	N	N	Y	Y	Y	N	N										
INFRA-SPINOUS FOSSA	15	N	N	N	N	Y	Y	Y	Y	N	N	N	Y	Y	Y									
	16	N	N	N	N	Y	Y	Y	Y	N	N	N	Y	Y	Y	N								
	17	N	N	N	N	N	N	Y	N	N	N	N	N	N	Y	N	N							
	18	Y	Y	N	N	N	N	N	N	N	Y	N	N	N	N	Y	Y	N						
	19	N	N	N	N	N	Y	Y	Y	N	N	N	N	Y	Y	N	N	N	Y					
	20	N	N	N	N	Y	Y	Y	Y	N	N	N	Y	Y	Y	N	N	N	Y	N				
	21	N	N	N	N	N	N	Y	N	N	N	N	N	N	Y	N	N	N	N	N	N			
INFERIOR ANGLE	22	N	N	N	N	N	N	Y	N	N	N	N	N	N	Y	N	N	N	N	N	N	N		
	23	N	N	N	N	N	N	N	N	N	N	N	N	N	Y	N	N	N	N	N	N	N	N	

Figure 6.20: Summary of multiple pairwise comparison (Dunn's Method) results for Tb.Th for all VOIs. Green 'Y' signifies a statistically significant difference (P<0.05) between VOIs, Red 'N' signifies no statistically significant difference.

The spine, its base the acromion and VOI 18 contained significantly thicker trabeculae than VOIs 1 and 2 of the glenoid, the medial portion of the infraspinous fossa and VOIs 19 and 20 of the inferior portion of the infraspinous fossa, which were significantly thinner. This was the only instance in the study where the superior and inferior portions of the glenoid are different.

Isolated differences were detected elsewhere, but no patterns could be readily distinguished. Incidentally, these regions were associated with trabecular thickness measurements that could not be considered especially thick or thin.

These results indicated there were effectively three regions of low (0.173-0.204mm), moderate (0.207-0.226mm) and high (0.232-0.284mm) trabecular thickness:

- Low: The superior portion of the glenoid, VOIs 15-17 of medial portion of the infraspinous fossa and VOIs 19/20 (of the inferior portion of the infraspinous fossa.
- Medium: The inferior portion of the glenoid, superior angle, VOI 21 (of the inferior portion of the infraspinous fossa) and the inferior angle.
- High: The spine, its base and root, the acromion and VOI 18 (of the lateral portion of the infraspinous fossa).

Mean measurements for each VOI are presented schematically in Figure 6.21B. Groups of statistically distinct regions are presented in schematic and tabular forms in Figure 6.21C and Table 6.7 respectively. Additionally, bars in Figure 6.19 have been coloured to reflect the statistically distinct groups.

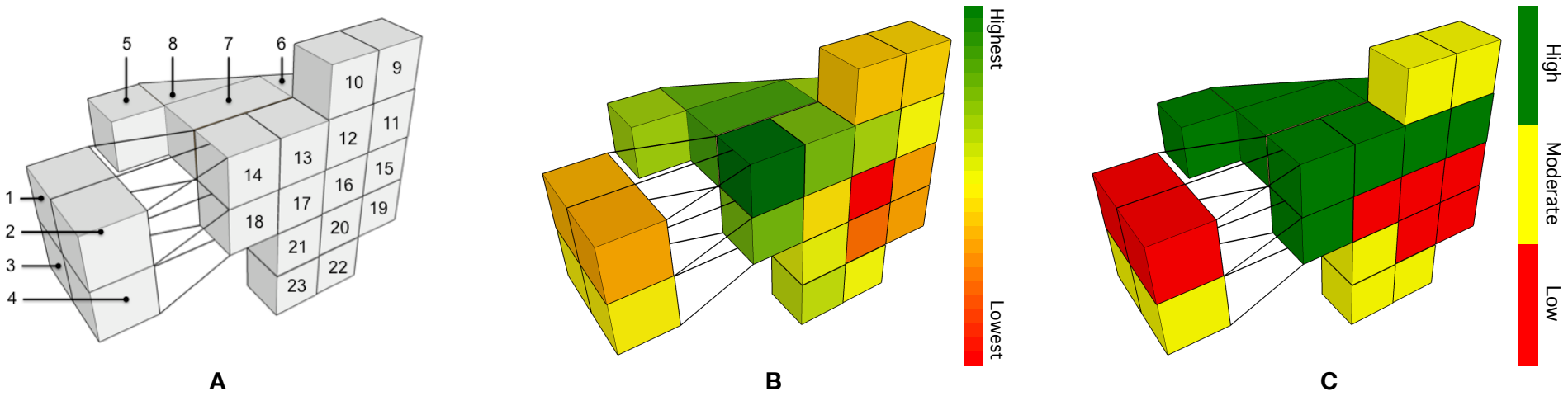

Figure 6.21: Tb.Th VOI Schematics.
A: VOI numbers, for reference. B: Mean values. C: Statistically distinct groups of VOIs.

Group	Tb.Th Range (mm)	VOIs	Description
High	0.232-0.284	5-8; 11-14; 18	Acromion, spine (including its base and root) and part of the lateral portion of the infraspinous fossa
Moderate	0.207-0.226	3-4; 9-10; 21-23	Inferior portion of the glenoid, root of the spine, superior angle, part of the inferior portion of the infraspinous fossa, part of the lateral portion of the infraspinous fossa and the inferior angle
Low	0.173-0.204	1-2; 15-17; 19-20	Superior portion of the glenoid, the medial portion of the infraspinous fossa, VOIs 19 and part of the inferior portion of the infraspinous fossa

Table 6.7: Summary of statistically distinct groups of VOIs for Tb.Th.

Trabecular Number (Tb.N)

Table 6.8 shows the descriptive statistics for trabecular number (Tb.N) for each volume of interest. Mean measurements with standard deviation error bars are presented graphically in Figure 6.22.

Trabecular Number (1/mm)					
VOI	Mean	Range		Std. Dev.	CoV
		Min.	Max.		
1	1.923	1.604	2.825	0.227	11.828%
2	1.936	1.604	3.205	0.297	15.313%
3	1.755	1.430	2.657	0.231	13.168%
4	1.785	1.467	2.773	0.255	14.265%
5	1.451	1.011	2.101	0.238	16.380%
6	1.286	0.898	1.781	0.224	17.404%
7	1.061	0.670	1.450	0.165	15.596%
8	1.217	0.586	1.684	0.252	20.737%
9	1.874	1.416	3.012	0.337	17.959%
10	1.878	1.506	2.745	0.242	12.875%
11	1.520	1.180	2.312	0.271	17.834%
12	1.316	1.000	2.172	0.248	18.863%
13	0.946	0.429	3.191	0.460	48.562%
14	1.133	0.792	1.592	0.204	17.993%
15	1.768	1.396	2.712	0.282	15.970%
16	2.068	1.650	2.311	0.234	11.304%
17	1.473	1.034	1.934	0.239	16.230%
18	1.391	0.656	2.114	0.319	22.934%
19	2.089	1.674	3.089	0.343	16.421%
20	2.169	1.655	3.157	0.334	15.389%
21	1.825	1.406	2.638	0.277	15.189%
22	1.999	1.499	2.740	0.267	13.365%
23	1.958	1.543	2.781	0.246	12.563%

Table 6.8: Descriptive statistics for trabecular number (Tb.N) at each volume of interest (VOI).

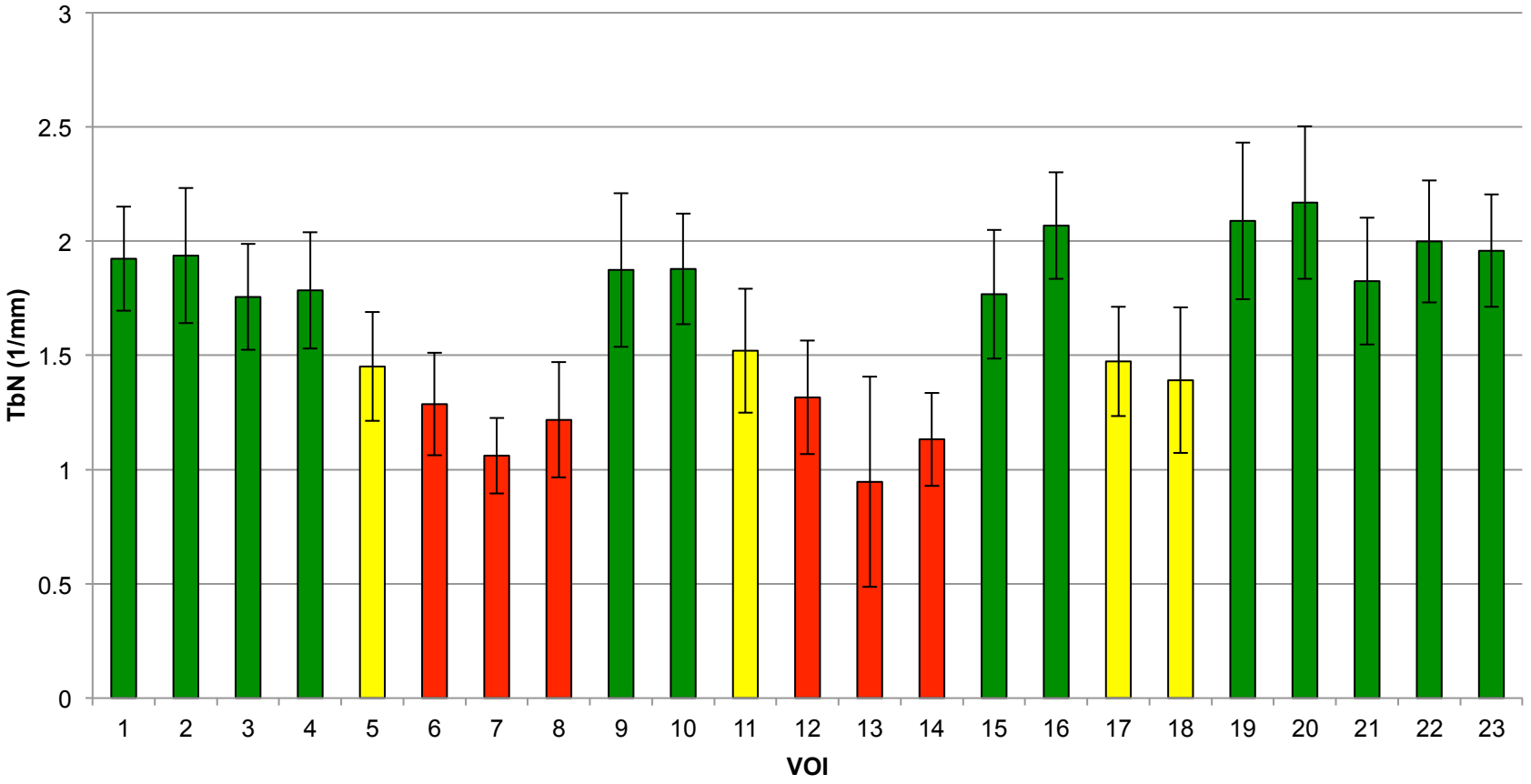

Figure 6.22: Graphic representation of mean (±SD) Tb.N values for each VOI.
Bar colours relate to statistical distinctions, which are summarised in Figure 6.24C and Table 6.9.

The lowest frequency of trabeculae was observed in VOI 13, and to a similar extent in neighbouring regions in the spine and its base. A greater number of trabeculae were present in the superior angle, glenoid and inferior and medial portions of the infraspinous fossa. Trabecular number in the superior portion of the glenoid was greater than in the inferior portion, however this was not be statistically significant (Figure 6.23).

REGION		GLENOID				ACROMION	SPINE			SUPERIOR ANGLE		SPINOUS ROOT				INFRA-SPINOUS FOSSA							INFERIOR ANGLE	
	VOI	1	2	3	4	5	6	7	8	9	10	11	12	13	14	15	16	17	18	19	20	21	22	23
GLENOID	1																							
	2	N																						
	3	N	N																					
	4	N	N	N																				
ACROMION	5	N	N	N	N																			
SPINE	6	Y	Y	Y	Y	N																		
	7	Y	Y	Y	Y	N	N																	
	8	Y	Y	Y	Y	N	N	N																
SUPERIOR ANGLE	9	N	N	N	N	N	Y	Y	Y															
	10	N	N	N	N	N	Y	Y	Y	N														
SPINOUS ROOT	11	N	N	N	N	N	N	Y	N	N	N													
	12	Y	Y	Y	Y	N	N	N	N	Y	Y	N												
	13	Y	Y	Y	Y	N	N	N	N	Y	Y	Y	N											
	14	Y	Y	Y	Y	N	N	N	N	Y	Y	N	N	N										
INFRA-SPINOUS FOSSA	15	N	N	N	N	N	Y	Y	Y	N	N	N	Y	Y	Y									
	16	N	N	N	N	N	Y	Y	Y	N	N	N	Y	Y	Y	N								
	17	N	N	N	N	N	N	N	N	N	N	N	N	N	N	N	N							
	18	Y	Y	N	N	N	N	N	N	Y	Y	N	N	N	N	N	Y	N						
	19	N	N	N	N	N	Y	Y	Y	N	N	N	Y	Y	Y	N	N	N	Y					
	20	N	N	Y	N	Y	Y	Y	Y	N	N	Y	Y	Y	Y	Y	N	Y	Y	N				
	21	N	N	N	N	N	Y	Y	Y	N	N	N	Y	Y	Y	N	N	N	Y	N	N			
INFERIOR ANGLE	22	N	N	N	N	N	Y	Y	Y	N	N	N	Y	Y	Y	N	N	N	Y	N	N	N		
	23	N	N	N	N	N	Y	Y	Y	N	N	N	Y	Y	Y	N	N	N	Y	N	N	N	N	

Figure 6.23: Summary of multiple pairwise comparison (Dunn's Method) results for Tb.N between all VOIs. Green 'Y' signifies a statistically significant difference (P<0.05) between VOIs; Red 'N' signifies no statistically significant difference.

The results of statistical testing are summarised in Figure 6.23, which reveals a clear distinction between regions of high and low trabecular number. The glenoid, superior angle, inferior angle and medial and inferior portions of the infraspinous fossa contain significantly more trabeculae than the regions of the spine and its base.

Regions that were not isolated by the statistical testing include the acromion, root of the spine and the lateral portion of the infraspinous fossa.

These distinctions suggest that there are three regions of low (0.95-1.32/mm), moderate (1.39-1.52/mm) and high (1.76-2.17/mm) trabecular number:

- Low: the spine (VOIs 6-8) and its base (VOIs 12-14)
- Moderate: acromion (VOI 5), root of the spine (VOI 11) and lateral portion of the infraspinous fossa (VOIs 17, 18)
- High: inferior and medial portions of the infraspinous fossa (VOIs 15/16/19-23), glenoid (VOIs 1-4) and superior angle (VOIs 9, 10).

Mean measurements for each VOI are presented schematically in Figure 6.24B. Groups of schematically distinct regions area presented in schematic and tabular forms in Figure 6.24C and Table 6.9 respectively. Additionally, bars in Figure 6.22 to reflect the statistically distinct regions.

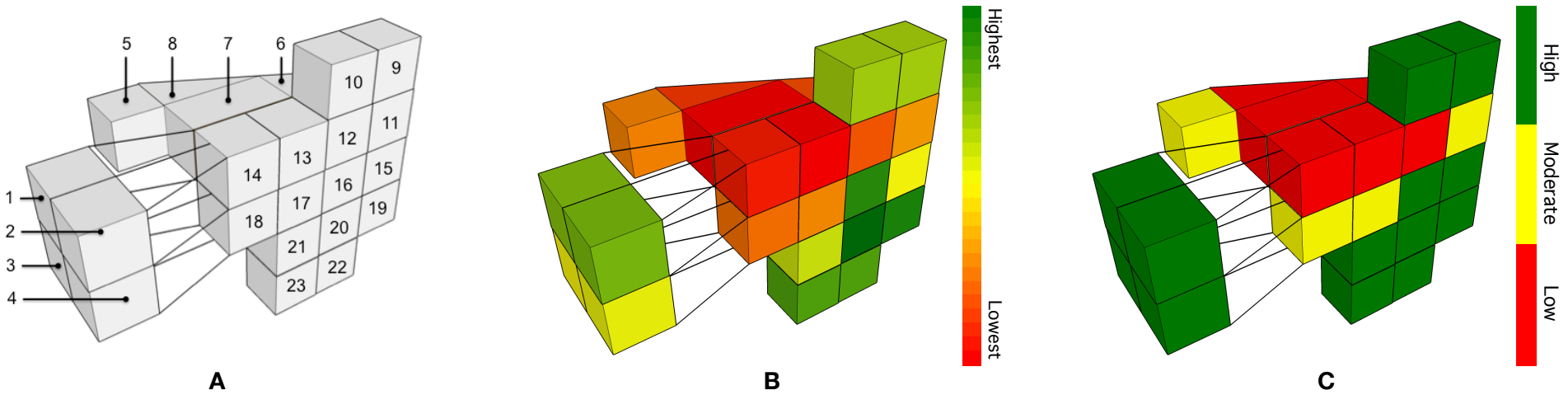

Figure 6.24: Tb.N VOI Schematics.
A: VOI numbers, for reference. B: Mean values. C: Statistically distinct groups of VOIs.

Group	Tb.N Range (1/mm)	VOIs	Description
High	1.76-2.17	1-4; 9-10;15-16; 19-23	Inferior and medial portions of the infraspinous fossa, glenoid and superior angle
Moderate	1.39-1.52	5; 11; 17-18	Acromion, root of the spine and lateral portion of the infraspinous fossa
Low	0.95-1.32	6-8;12-14	Spine and its base

Table 6.9: Summary of statistically distinct groups of VOIs for Tb.N.

Trabecular Separation (Tb.Sp)

Table 6.10 shows the descriptive statistics for trabecular separation (Tb.Sp) for each volume of interest. Mean measurements with standard deviation error bars are presented graphically in Figure 6.25**.**

Trabecular Separation (mm)					
VOI	**Mean**	**Range**		**Std. Dev.**	**CoV**
		Min.	**Max.**		
1	0.270	0.194	0.326	0.024	8.999%
2	0.265	0.177	0.311	0.027	10.309%
3	0.299	0.199	0.377	0.034	11.331%
4	0.291	0.193	0.357	0.034	11.834%
5	0.393	0.232	0.661	0.097	24.680%
6	0.410	0.268	0.638	0.097	23.768%
7	0.430	0.265	0.748	0.112	25.991%
8	0.411	0.269	0.776	0.105	25.561%
9	0.286	0.180	0.433	0.048	16.834%
10	0.283	0.191	0.362	0.036	12.765%
11	0.353	0.179	0.520	0.072	20.490%
12	0.415	0.219	0.631	0.091	21.870%
13	0.526	0.082	0.825	0.167	31.656%
14	0.439	0.279	0.762	0.105	23.963%
15	0.286	0.156	0.362	0.045	15.707%
16	0.228	0.199	0.270	0.025	10.909%
17	0.404	0.274	0.811	0.134	33.062%
18	0.390	0.219	0.643	0.111	28.478%
19	0.259	0.171	0.330	0.038	14.515%
20	0.245	0.151	0.344	0.039	15.882%
21	0.307	0.206	0.426	0.045	14.792%
22	0.268	0.200	0.320	0.031	11.616%
23	0.272	0.191	0.325	0.028	10.356%

Table 6.10: Descriptive statistics for trabecular separation (Tb.Sp) at each volume of interest (VOI).

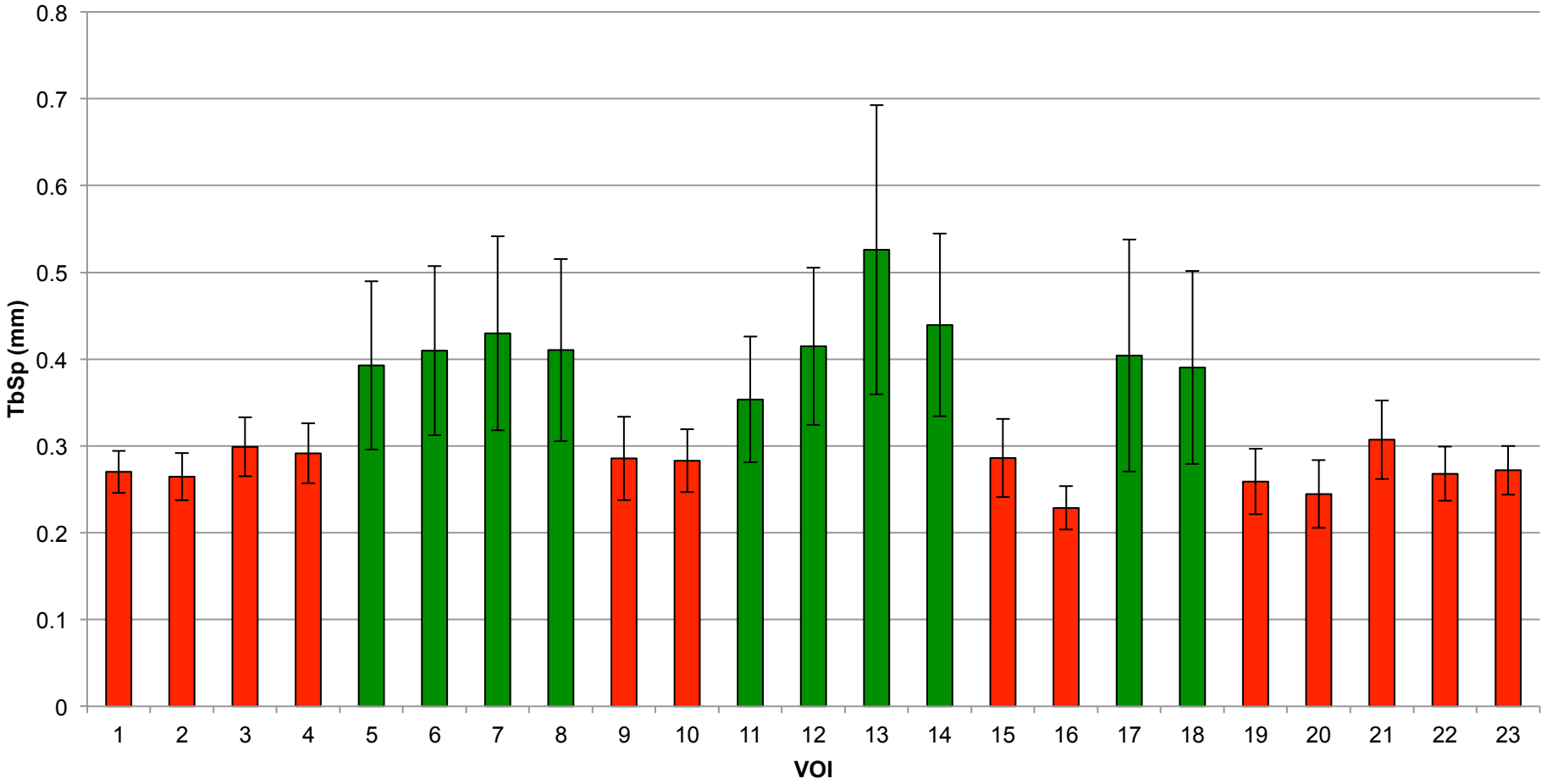

Figure 6.25: Graphic representation of mean (±SD) Tb.Sp values for each VOI.
Colours relate to statistical distinctions, which are summarised in Figure 6.27C and Table 6.11.

VOI 13 has the largest spaces between trabeculae, with neighbouring regions in the spine, its root and base, the acromion and the lateral portion of the infraspinous fossa also having relatively large spaces between trabeculae. The lowest Tb.Sp measurement was in VOI 16, in the medial portion of the infraspinous fossa. The inferior portion of the infraspinous fossa, inferior angle, superior angle and glenoid all had relatively low Tb.Sp.

The results of statistical testing is summarised in Figure 6.26.

REGION		GLENOID				ACROMION	SPINE			SUPERIOR ANGLE		SPINOUS ROOT				INFRA-SPINOUS FOSSA							INFERIOR ANGLE	
	VOI	1	2	3	4	5	6	7	8	9	10	11	12	13	14	15	16	17	18	19	20	21	22	23
GLENOID	1																							
	2	N																						
	3	N	N																					
	4	N	N	N																				
ACROMION	5	Y	Y	N	Y																			
SPINE	6	Y	Y	Y	Y	N																		
	7	Y	Y	Y	Y	N	N																	
	8	Y	Y	Y	Y	N	N	N																
SUPERIOR ANGLE	9	N	N	N	N	Y	Y	Y	Y															
	10	N	N	N	N	Y	Y	Y	Y	N														
SPINOUS ROOT	11	Y	Y	N	N	N	N	N	N	Y	Y													
	12	Y	Y	Y	Y	N	N	N	N	Y	Y	N												
	13	Y	Y	Y	Y	N	N	N	N	Y	Y	N	N											
	14	Y	Y	Y	Y	N	N	N	N	Y	Y	N	N	N										
INFRA-SPINOUS FOSSA	15	N	N	N	N	Y	Y	Y	Y	N	N	N	Y	Y	Y									
	16	N	N	N	N	Y	Y	Y	Y	N	N	Y	Y	Y	Y	N								
	17	Y	Y	N	N	N	N	N	N	Y	Y	N	N	N	N	Y	Y							
	18	Y	Y	N	N	N	N	N	N	Y	Y	N	N	N	N	N	Y	N						
	19	N	N	N	N	Y	Y	Y	Y	N	N	Y	Y	Y	Y	N	N	Y	Y					
	20	N	N	N	N	Y	Y	Y	Y	N	N	Y	Y	Y	Y	N	N	Y	Y	N				
	21	N	N	N	N	N	Y	Y	N	N	N	N	Y	Y	Y	N	N	N	N	N	N			
INFERIOR ANGLE	22	N	N	N	N	Y	Y	Y	Y	N	N	Y	Y	Y	Y	N	N	Y	Y	N	N	N		
	23	N	N	N	N	Y	Y	Y	Y	N	N	Y	Y	Y	Y	N	N	Y	Y	N	N	N	N	

Figure 6.26: Summary of multiple pairwise comparison (Dunn's Method) results for Tb.Sp between all VOIs. Green 'Y' signifies a statistically significant difference (P<0.05) between VOIs; Red 'N' signified no statistically significant difference.

The acromion, spine (including its root and base) and the lateral portion of the infraspinous fossa had significantly higher trabecular separation than the regions of the glenoid, superior angle, the medial and inferior portions of the infraspinous fossa and the inferior angle.

This distinction suggests that there are two regions of low (0.23-0.31mm) or high (0.35-0.53mm) trabecular separation:

- Low: the glenoid (VOIs 1-4), superior angle (VOIs 9, 10), medial and inferior portions of the infraspinous fossa (VOIs 15-16/19-21), and the inferior angle (VOIs 22, 23).
- High: the acromion (VOI 5), spine (VOIs 6-8), its root and base (VOIs 11-14), and the lateral portion of the infraspinous fossa (VOI 17, 18).

Mean measurements for each VOI are presented schematically in Figure 6.27B. Groups of statistically distinct regions are presented in schematic and tabular forms in Figure 6.27C and Table 6.11 respectively. Additionally, bars in Figure 6.19 have been coloured to reflect the distinct groups.

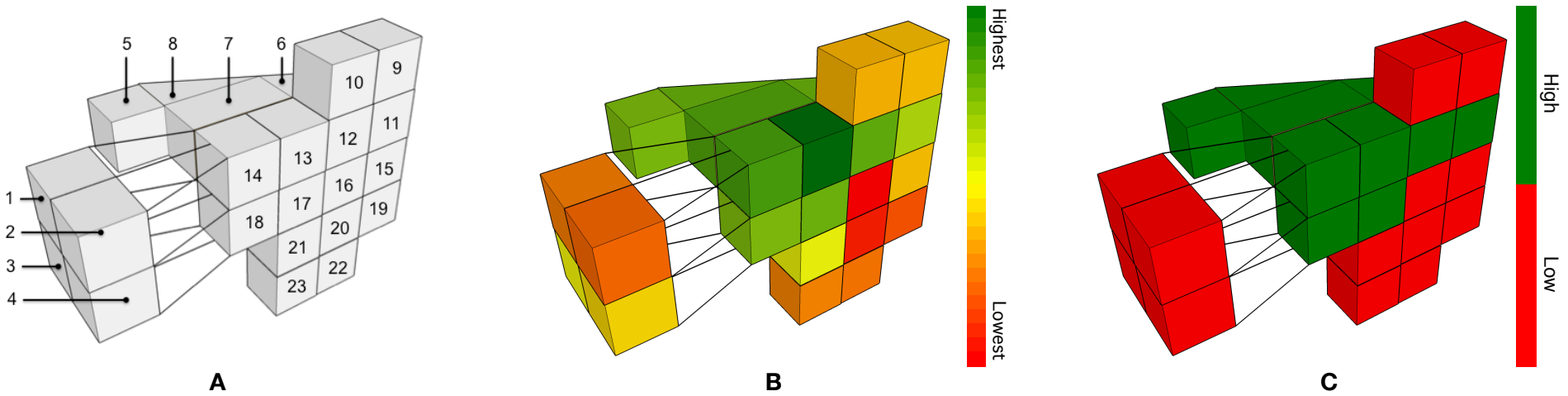

Figure 6.27: Tb.Sp VOI Schematics.
A: VOI numbers, for reference. B: Mean values. C: Statistically distinct groups of VOIs.

Group	Tb.Sp Range (mm)	VOIs	Description
High	0.35-0.53	5-8; 11-14; 17-18	Acromion, spine (including its root and base) and lateral portion of the infraspinous fossa.
Low	0.23-0.31	1-4; 9-10; 15-16; 19-23	Glenoid, superior angle, medial and inferior portions of the infraspinous fossa and inferior angle.

Table 6.11: Summary of statistically distinct groups of VOIs for Tb.Sp.

Degree of Anisotropy (DA)

Table 6.12 shows the descriptive statistics for degree of anisotropy (DA) for each volume of interest. Mean measurements with standard deviation error bars are presented graphically in Figure 6.28.

Degree of Anisotropy					
VOI	Mean	Range		Std. Dev.	CoV
		Min.	Max.		
1	0.547	0.343	0.724	0.095	17.447%
2	0.649	0.501	0.851	0.092	14.228%
3	0.587	0.401	0.780	0.104	17.727%
4	0.533	0.331	0.736	0.104	19.552%
5	0.503	0.380	0.660	0.075	14.938%
6	0.813	0.435	0.999	0.131	16.073%
7	0.759	0.434	0.999	0.166	21.844%
8	0.825	0.612	0.989	0.099	11.993%
9	0.583	0.319	0.792	0.121	20.833%
10	0.630	0.490	0.840	0.091	14.375%
11	0.546	0.391	0.798	0.100	18.238%
12	0.658	0.453	0.950	0.107	16.214%
13	0.831	0.475	1.000	0.136	16.388%
14	0.488	0.205	0.621	0.099	20.369%
15	0.650	0.360	0.915	0.118	18.174%
16	0.768	0.630	0.861	0.091	11.907%
17	0.809	0.696	0.912	0.059	7.287%
18	0.686	0.394	0.843	0.104	15.169%
19	0.625	0.381	0.846	0.120	19.206%
20	0.819	0.521	0.989	0.100	12.257%
21	0.728	0.602	0.846	0.057	7.771%
22	0.680	0.539	0.929	0.095	13.968%
23	0.649	0.565	0.862	0.066	10.162%

Table 6.12: Descriptive statistics for degree of anisotropy (DA) at each volume of interest (VOI).

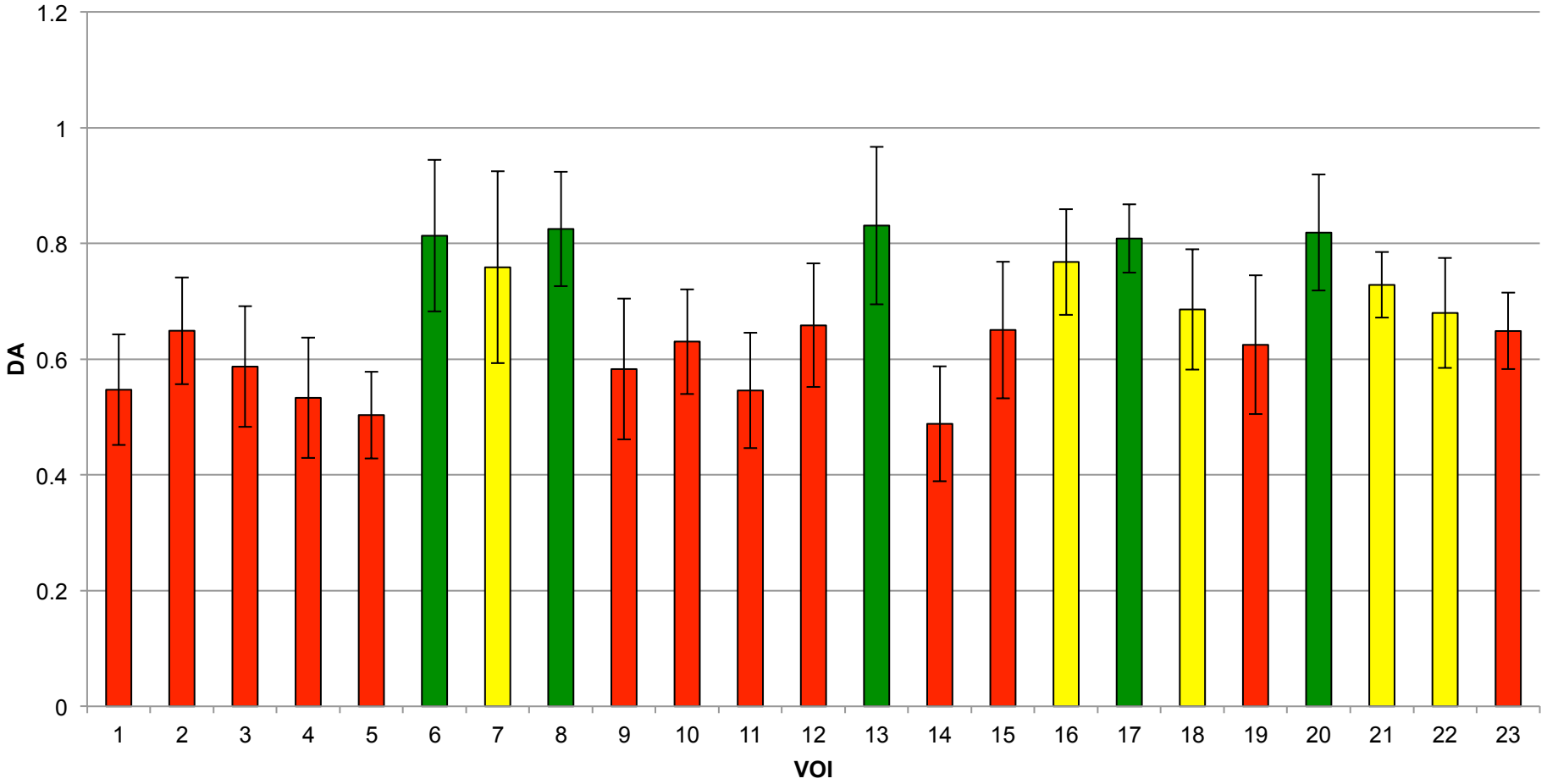

Figure 6.28: Graphic representation of mean (±SD) DA values for each VOI.
Bar colours relate to statistical distinctions, which are summarised in Figure 6.30C and Table 6.13.

The data suggest that trabeculae were most disorganised in VOI 13, central areas of the infraspinous fossa (VOIs 16,17/20, 21) and the spine (VOIs 6-8), while more peripheral regions, such as the glenoid, acromion, medial border and inferior angle tended to contain more aligned and organised trabeculae.

The results of statistical testing are summarised in Figure 6.29.

REGION		GLENOID				ACROMION	SPINE			SUPERIOR ANGLE		SPINOUS ROOT				INFRA-SPINOUS FOSSA							INFERIOR ANGLE	
	VOI	1	2	3	4	5	6	7	8	9	10	11	12	13	14	15	16	17	18	19	20	21	22	23
GLENOID	1																							
	2	N																						
	3	N	N																					
	4	N	N	N																				
ACROMION	5	N	Y	N	N																			
SPINE	6	Y	Y	Y	Y	Y																		
	7	N	N	N	Y	Y	N																	
	8	Y	Y	Y	Y	Y	N	N																
SUPERIOR ANGLE	9	N	N	N	N	N	Y	N	Y															
	10	N	N	N	N	N	Y	N	Y	N														
SPINOUS ROOT	11	N	N	N	N	N	Y	Y	Y	N	N													
	12	N	N	N	N	Y	Y	N	Y	N	N	N												
	13	Y	Y	Y	Y	Y	N	N	N	Y	Y	Y	Y											
	14	N	Y	N	N	N	Y	Y	Y	N	N	N	Y	Y										
INFRA-SPINOUS FOSSA	15	N	N	N	N	Y	Y	N	Y	N	N	N	N	Y	Y									
	16	N	N	N	Y	Y	N	N	N	N	N	Y	N	N	Y	N								
	17	Y	Y	Y	Y	Y	N	N	N	Y	Y	Y	Y	N	Y	Y	N							
	18	N	N	N	Y	Y	N	N	N	N	N	Y	N	N	Y	N	N	N						
	19	N	N	N	N	N	Y	N	Y	N	N	N	N	Y	Y	N	N	Y	N					
	20	Y	Y	Y	Y	Y	N	N	N	Y	Y	Y	Y	N	Y	Y	N	N	N	Y				
	21	N	N	N	Y	Y	N	N	N	N	N	Y	N	N	Y	N	N	N	N	N	N			
INFERIOR ANGLE	22	N	N	N	Y	Y	N	N	Y	N	N	Y	N	N	Y	N	N	N	N	N	N	N		
	23	N	N	N	N	Y	Y	N	Y	N	N	N	N	Y	Y	N	N	Y	N	N	Y	N	N	

Figure 6.29: Summary of multiple pairwise comparison (Dunn's Method) results for DA between all VOIs. Green 'Y' signifies a statistically significant difference (P<0.05) between VOIs; Red 'N' signifies no statistically significant difference.

Unlike the other metrics, no clearly distinguishable regional pattern could be identified. Despite this, several VOIs consistently appeared to differ; VOIs 5, 6, 8, 14, 17 and 20 exhibited most statistical differences. Returning to the raw data it appears that the statistics were unable to isolate differences between the majority of VOIs, with the exception of the VOIs above that displayed extremes of isotropy or anisotropy.

This distinction suggests that there are two groups of low (0.49-0.66) and high (0.81-0.83) anisotropy, separated by one large group of intermediate regions (0.68-0.77):

- Low: Acromion (VOI 5), glenoid (VOIs 1-4), superior angle (VOIs 9, 10), the base of the spine (excluding VOI 13; VOIs 11/12/14) and VOIs 15, 19 and 23.
- Medium: VOIs 7, 16, 18, 21 and 22.
- High: VOIs 6, 8, 13, 17 and 20.

Mean measurements for each VOI are presented schematically in Figure 6.30B. Groups of statistically distinct VOIs are presented in schematic and tabular forms in in Figure 6.30C and Table 6.13 respectively. Additionally, bars in Figure 6.28 have been coloured to reflect the distinct regions.

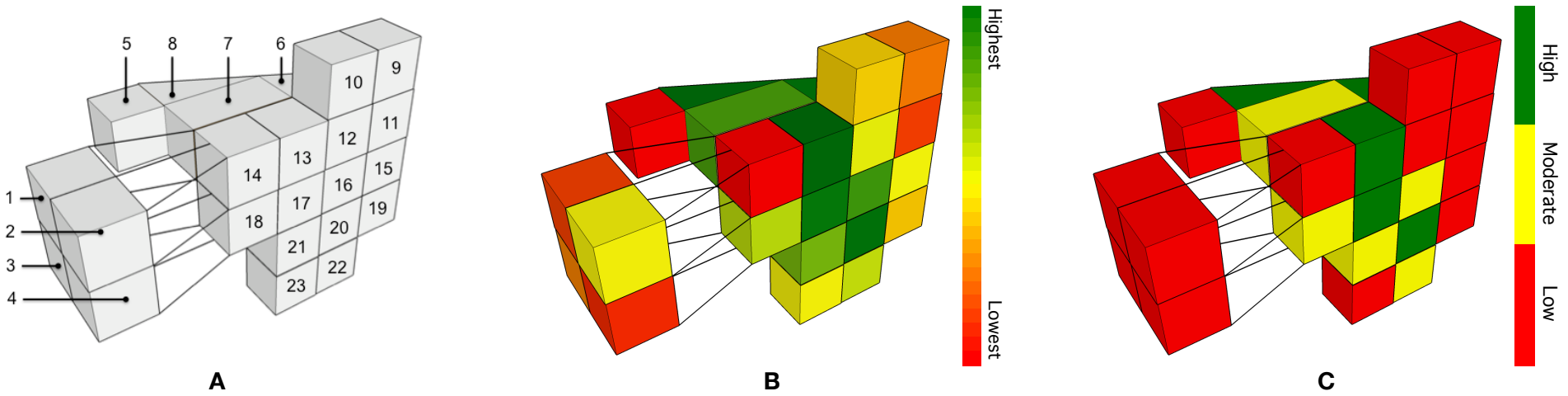

Figure 6.30: DA VOI Schematics.
A: VOI numbers, for reference. B: Mean values. C: Statistically distinct groups of VOIs.

Group	DA Range	VOIs	Description
High	0.81-0.83	6, 8, 13, 17, 20	Part of the spine and its base, VOIs 17 and 20.
Moderate	0.68-0.77	7, 16, 18, 21, 22	
Low	0.49-0.66	1-5; 9-12; 13-14; 19; 23	Acromion, glenoid, superior angle, part of the base and root of the spine, and VOIs 15, 19 and 23

Table 6.13: Summary of statistically distinct groups of VOIs for DA.

6.3. Discussion

Regional Descriptions

Base of the Spine (VOIs 12-14)

The base of the spinous process consists of three VOIs, which exhibited varying trabecular morphology.

VOI 13

The most notable VOI in the spinous base was VOI 13, which corresponds to the position of the primary ossification centre of the scapula, and the likely associated invasion site of nutrient vasculature (Scheuer and Black, 2000; Cigtay and Mascatello, 1979; Brookes, 1971; Crock, 1996). VOI 13 was characterised by a very low bone volume fraction with sparse trabeculae (low Tb.N; high Tb.Sp), which were typically thick unaligned rods. It visibly contained trabeculae of specialised morphology (Figure 6.31). This region also closely resembled the central origin of the radiating trajectories observed in Chapter 3: Radiographic Study

It is highly likely that the low bone volume fraction and trabecular number reflected the large vascular presence in the region, which resulted in remaining trabeculae becoming highly specialised in response to the persisting load.

This region closely resembled the ‘trabecular chiasma’ of the ilium, which was first described by Macchiarelli et al (1999) and subsequently observed by Volpato (2008) and Cunningham & Black (2009a). The distinctiveness of the sparse, central region and its dissimilarity to peripheral regions is also thought to be closely linked to vasculature and growth (Cunningham and Black, 2010). The presence of such a distinctive morphology close to the primary ossification centre and nutrient vessel invasion site, in both the scapula and the ilium, supports this theory, which is discussed in more detail on Page 173.

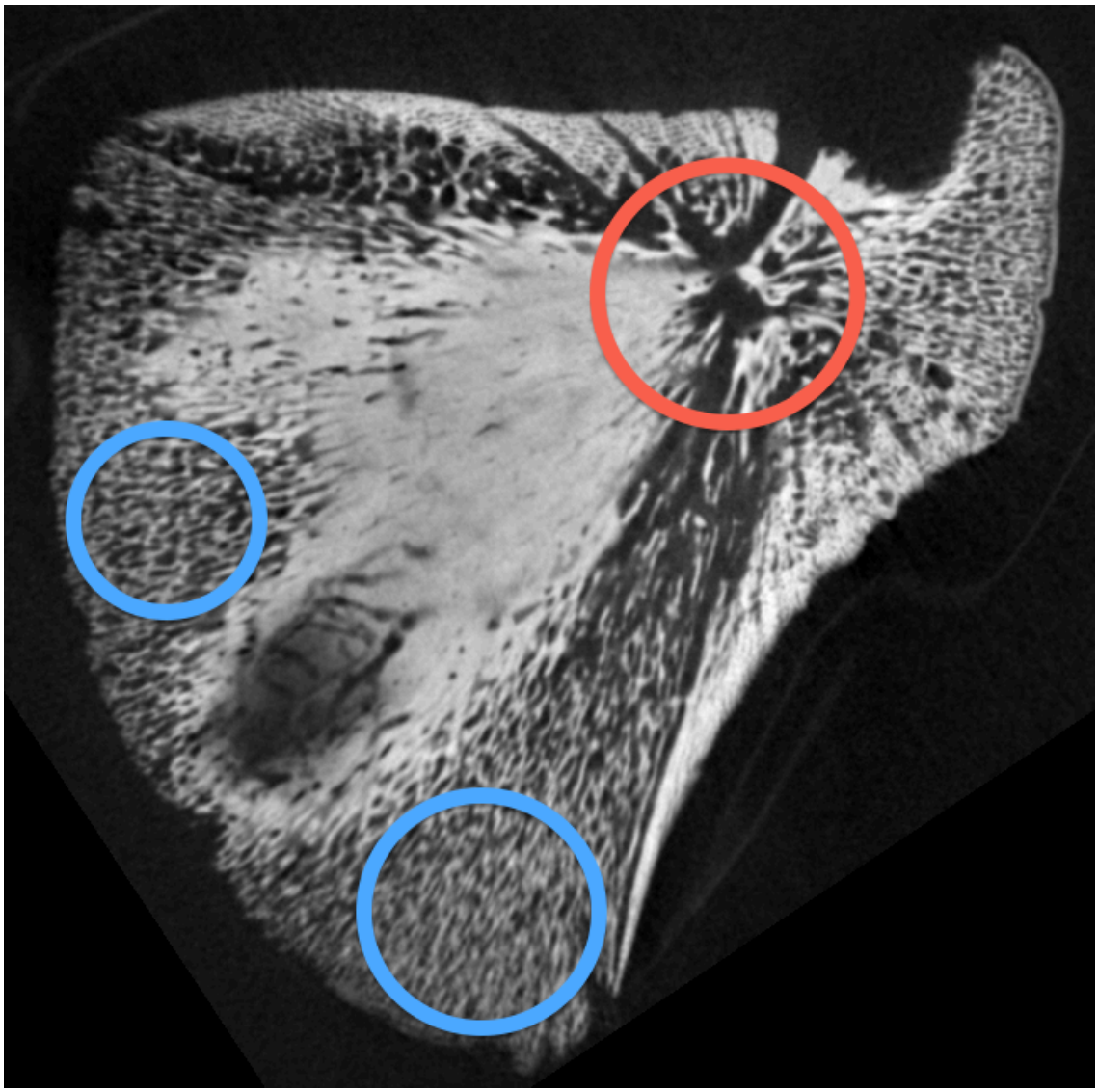

Figure 6.31: A micro-CT slice through a perinatal scapula illustrating the differences between central (VOI 13; red circled) and distal (blue circle) areas. This slice was not made in a typical anatomical plane in an attempt to avoid the natural curvature of the scapula.

Although there were fewer trabeculae and larger spaces in VOI 13, the bone that was present did appear to be structurally more robust than elsewhere in the bone; trabeculae in VOI 13 were generally thicker than those around the inferior angle and had a higher structural model index (i.e. more rod-like) than those around the inferior angle. This suggests that trabeculae in this area were more rod-shaped than in the VOIs that contained newer areas of bone (such as the superior angle, inferior angle and glenoid), where trabeculae were more plate-like.

The presence of thick rods suggested that the trabecular bone in VOI 13 had begun to remodel, perhaps in an attempt to distribute load, and was consistent with indications that as prenatal development progresses trabeculae become thicker and less numerous (Gupta and van der Helm, 2004; Reissis and Abel, 2012). This was in contrast to trabecular bone at the inferior angle, for example, which was diffuse but unspecialised and consistent with regions of new bone growth (Liu et al., 2006; Dalstra and Huiskes, 1995; Byers et al., 2000).

VOIs 12 & 14

The regions immediately medial and lateral to the central region (VOI 13) were VOIs 12 and 14 respectively. They were of similar morphology to each other, according to all of the metric and statistical results. They had a low proportion of trabecular bone that was low in number and high in separation. Trabeculae were thick and rod-like.

Although distinctive, the morphology of these VOIs is less extreme than that observed in VOI 13, which further supports the reasoning that VOI 13 represents a central focal region. Specifically, the reduction in trabecular separation in these areas relative to VOI 13 suggests that medullary vasculature is involved; this is borne out by gross inspection of the micro CT and the radiographic gradient map study,

Root of the Spinous Process (VOI 11)

Although the root of the spinous process has proportionally more bone than its lateral neighbour (VOI 12) and the central region (VOI 13), it still has a low proportion of bone relative to all other VOIs. The volume has a greater number of trabeculae than the base of the spine, although fewer than occurred at the superior and inferior angles. It also had a higher SMI than the base of the spine, indicating more rod-like trabeculae, though again not as rod-like as in the inferior angle and glenoid. Despite these dissimilarities to the base, it did not have significantly reduced trabecular separation or reduced trabecular thickness than found in the base of the spine.

These similarities and distinctions suggest that VOI 11 may be a transitional region between the central highly vascularised region and the more peripheral growing regions. Based on the high bone volume fraction, trabecular number and rod-like model of the trabeculae this VOI may be considered a region of growth, however increased trabecular separation suggests that significant vascular structures may be present.

Spine (VOIs 6-8)

The region of the spine (VOIs 6-8) shared similarities with the regions of the base of the spinous process, particularly VOIs 12 and 14. It could also be described as a region of low bone volume fraction, which was low in trabecular number and high in trabecular separation. Trabeculae in this region tended to be thick, rod-like and relatively disorganised.

The trabecular morphology of the spine was similar to that of its base, although not as extreme as in the central region, VOI 13. It was similar to the spinous base in all metrics, indicating that it may be subjected to similar functional requirements and could have similar vascular content. Like its base, the spine appeared highly vascularised with specialised trabeculae that have a thick rod-like morphology. These features are unsurprising, considering its close proximity to the site of initial ossification at VOI 13.

Although subsequent results suggest that the acromion itself cannot be considered a region of extensive growth at this stage of development, the spine represents a transitional region between the acromion and the central region of VOI 13. Despite being described as ‘transitional’ it is morphologically distinct from the root of the spine (VOI 11), which appeared as a communication been the central region and peripheral regions of growth.

Acromion (VOI 5)

The acromion contained a low proportion of trabecular bone, of intermediate trabecular number and large trabecular separation. Trabeculae in this VOI are thick aligned plates.

This region shared some features with the spine and its base, specifically the thickness and separation of trabeculae. There were also some similarities between the acromion and the glenoid, specifically the plate-like morphology of trabeculae. The bone volume fraction in this region was greater than in the spine and its base, but less than in the glenoid.

This region is similar to the root of the spine (VOI 11) in that it appears to act as a transitional volume between a central, vascularised region and a peripheral growth front. However, this is clearly not possible in the case of the acromion since it is a terminal structure without two neighbouring regions with which to communicate. It should be noted, however, that the acromion does communicate with VOI 11 via soft tissues, such as cartilage and muscle.

The low bone volume fraction, low trabecular number and high trabecular thickness suggest that this region is not consistent with new growth regions (Byers et al., 2000). The acromion appears to be morphologically more consistent with the specialised developmentally “older” bone of the central volumes. Thus, it is more likely that, at this stage of development at least, the acromion is subjected to significant stress and is the site of minimal growth.

Considering the functions of the clavicle, it seems reasonable to identify the acromioclavicular joint as the potential origin of some aspects of stress. The acromion exists as the lateral free extremity of the spine and articulates with the lateral extremity of the clavicle, albeit cartilaginous at this stage of development, at the acromioclavicular joint (Drake et al., 2005). The clavicle acts as a strut to maintain the lateral position of the glenohumeral joint and to transmit stresses between the

pectoral girdle (and upper limb) and the axial skeleton. The joint itself is considered to have a relatively small articular surface relative to the high axial loads it transmits (Terry and Chopp, 2000), and possesses extensive ligamentous support(Palastanga et al., 2007; Prescher, 2000; Debski et al., 2000).

The role of the acromioclavicular joint facilitating movement of the pectoral girdle, particularly in the terminal phases of arm abduction (Inman et al., 1944) and in children (Dayanidhi et al., 2005), is well documented in the literature (Palastanga et al., 2007).

This region is likely to be subjected to additional stresses during the perinatal period of development as the scapula descends from its cervical origin to its final thoracic position (Scheuer and Black, 2000; O'Rahilly and Gardner, 1972); as a result of this migration the clavicle transitions from an oblique position to a horizontal one. (Noback, 1944; McClure and Raney, 1975). In Sprengel's Deformity, where the scapula fails to descend, it maintains a more medial position as a result of not moving inferiorly while being forced laterally by the clavicle (Aydinli et al., 2005). The movement of the scapula inferiorly, causing the lateral extremity of the clavicle to relocate while its medial extremity is fixed, could introduce tensile stress across the acromioclavicular joint. The presence of plate-like trabeculae in this region could suggest that this region maintains a degree of functional elasticity (Liu et al., 2006), perhaps to accommodate load focussed across the joint.

Glenoid (VOIs 1-4)

Moderate volumes of densely packed trabeculae distinguish the trabecular morphology of the glenoid region. Trabeculae are less rod-like here than in the rest of the bone (with the exception of the inferior angle) and are relatively well organised.

These morphological characteristics are considered consistent with recently ossified trabeculae, particularly around the hypertrophic zone of the cartilaginous anlage (Byers et al., 2000). The presence of large amounts of unspecialised trabeculae are synonymous with juvenile bone, and are known to remodel as the individual matures

(Gosman and Ketcham, 2009). The presence of non-remodelled bone in regions of new growth has also been observed in the neonatal ilium (Cunningham and Black, 2009a) and proximal femur (Ryan and Krovitz, 2006).

Some parameters showed differences between the superior and inferior potions of the glenoid, however it seems most likely that differences in measurements between the superior and inferior portions of the perinatal glenoid are due to functional differences between the two regions; a significant proportion of the superior portion of the glenoid mass does not contribute to the articular surface at this stage of development, while in the inferior portion the majority of the trabecular bone lies deep to the articular component of the glenoid (Scheuer and Black, 2000). Although no statistically significant differences between the superior and inferior portions of the glenoid were found, trabeculae in the superior non-articular portion of the glenoid were more numerous, thinner and densely packed than in the inferior portion; these findings suggest that trabeculae in the inferior articular portion of the glenoid more closely resemble load-bearing structures than their counterparts in the superior portion.

These findings could also suggest that the inferior articular portion of the glenoid is a less significant growth region than the superior component, which will ultimately facilitate the coracoid process. The coracoid process, considered a primary centre of ossification in its own right, usually appears during the first year and is known to possess an epiphyseal growth plate (Ogden and Phillips, 1983; Scheuer and Black, 2000). It is also important to note that the coracoid process exists as a cartilaginous anlage at this stage of development.

Differences between the specific regions of the glenoid have been observed elsewhere in the literature. Anglin et al (1999) reported that the posterosuperior region of the adult glenoid (equivalent to VOI 1) was found to be the strongest region in their study. Lim et al (2006; 2010) also showed that the posterior portion of the glenoid fossa also receives predominant loading, particularly during shoulder movement.

These studies considered the adult glenoid, which would have undoubtedly undergone more remodelling in response to movements and load being transmitted across the shoulder joint than would be expected in the neonate.

The differences between the perinate and adult are further highlighted when considering the differences between the measurements in this study and those of adult glenoids reported in the literature. Mimar et al (2008) reported an average BV/TV of 23%, compared to 38% in this study. Similarly, Fritch et al (1998) found that trabeculae in the adult glenoid were much thicker and more plate-like than those observed in this study. Increased remodelling in the adult compared to the neonate could account for these discrepancies.

Superior Angle (VOIs 9, 10)

The region of the superior angle contains a moderate proportion of densely packed trabecular bone. Trabeculae here are not as rod-like as elsewhere in the scapula, and are of moderate thickness. VOI 9, which neighbours the root of the spine, tends to be less well organised than VOI 10.

Attempts to compare these metrics with reports in the literature have proven fruitless, however it seems plausible that similarities between trabecular morphology in this region and that of the glenoid suggests that the superior angle is also a site of modest growth in the neonatal scapula rather than enduring significant loads.

Trabeculae in the superior angle also resemble those in the inferior portion of the infraspinous fossa and the inferior angle, which will be discussed later in this section.

Infraspinous Fossa (VOIs 15-21)

The infraspinous fossa was subdivided into three portions:

- Medial (VOIs 15, 16)
- Lateral (VOIs 17, 18)
- Inferior (VOIs 19-21), which shares similarities with the regions of the inferior and superior angles.

Medial Portion

The medial portion contains a relatively low bone volume fraction, although trabeculae are frequent in number and densely packed. The trabeculae are best described as thin rods, which are aligned perpendicular to the medial border. This type of alignment as part of a radial pattern has been previously referred to in the literature (Noback, 1943), and is consistent with the reported growth front that promotes significant increases in scapular width early in the fetal period (Kedzia et al., 2009).

Lateral Portion

The superior portion of the infraspinous fossa contains a relatively low proportion of trabecular bone, which comprises a moderate frequency of highly spaced rod-like trabeculae.

These volumes correspond to the lateral trajectory, reported in 0

Radiographic Study, and not surprisingly appear to possess structural similarities to the base of the spine, which corresponds to the horizontal trajectory referred to in the same Chapter. It follows that both this region and the spine may be functionally important regions for transmission of load, particularly during humeral abduction, with sparse remodelled trabeculae and a large vascular presence. The importance of these regions has been reported in the literature (Gupta and van der Helm, 2004; Anetzberger and Putz, 1996).

Inferior Portion

The inferior portion of the infraspinous fossa contains a greater proportion of trabecular bone than the volumes superior to it. Trabeculae here are frequent in number and separated by small spaces. The trabeculae themselves are thin and are less rod-like.

This region is most similar to the superior angle, although it contains slightly higher bone volume fraction. This region is again consistent with an area of growth, and, reflecting its location, exhibits morphology between the medial portion of the infraspinous fossa and the inferior angle.

Inferior Angle (VOIs 22, 23)

The inferior angle contains a high proportion of densely packed trabecular bone. Trabeculae in the inferior angle are the most plate-like in the perinatal scapula. They are also more aligned than central regions of the scapula.

The very high bone volume fraction, low trabecular number and plate-like trabecular morphology suggest that this region is a major growth centre and was identified as a ‘major zone’ of growth by Noback (1943)

Upon visual inspection, this region of bone appears visibly dense and with aligned trabeculae, in contrast to the central region of VOI 13 (Figure 6.31). The lateral trajectory, observed in 0

Radiographic Study, terminates at the inferior angle and reflects both the transmission of load down the lateral border of the scapula and the delivery of medullary vasculature to this important growth front.

Regions of Distinct Morphology

To highlight similarities and differences in all pairwise comparison data, results have been combined into one table and reorganised based common on statistical differences, or lack thereof (Figure 6.32).

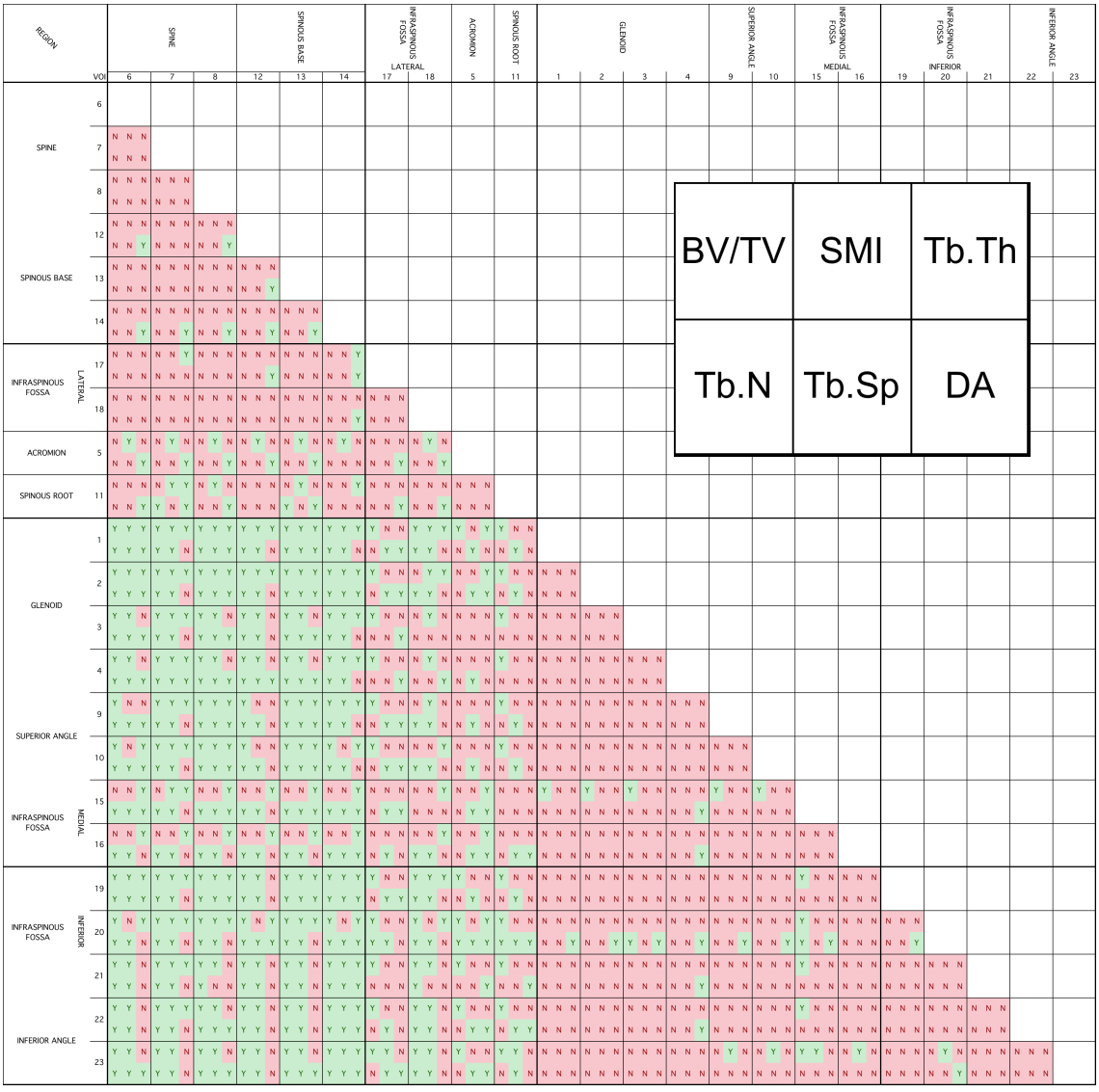

Figure 6.32: Combination of all pairwise comparison data, reorganised by statistical similarities. To represent all six metrics, cells are subdivided into six subunits.
Red 'N' = No statistically significant difference; Green 'Y' = Statistically significant difference (P<0.05)

To arrange the data in this way, some regions, including the infraspinous fossa and the spinous base, were split due to constituent VOIs exhibiting different statistical results to their neighbours. For example, it became apparent that the infraspinous fossa should be split into medial, lateral and inferior components based on their differing outcomes of the statistical analysis. A clear example of this is shown in Figure 6.26, where the VOIs 15-16, 17-18 and 9-21 demonstrate statistically different values. Additionally, VOI 11 often shared more statistical commonalties with the medial portion of the infraspinous fossa and the acromion than with VOIs that contribute to the base of the spine. A summary of VOIs and their regions is presented in Table 6.14.

Region		**VOIs**
Glenoid		1-4
Acromion		5
Spine		6-8
Superior angle		9, 10
Root of the spine		11
Base of the spine		12-14
Infraspinous fossa	Medial Portion	15, 16
	Lateral Portion	17, 18
	Inferior Portion	19-21
Inferior Angle		22, 23

Table 6.14: Descriptive terms and their corresponding VOIs

With the data organised in this format, rather than a separate table for each metric, and arranged by VOI, statistical patterns begin to emerge and groups of VOIs that present similar outcomes across all statistical testing can be isolated:

- VOIs in the **spine,** its **base** and **root,** and the **lateral portion of the infraspinous fossa** show marked similarities to each other although some differences are present between the spine and its base, and the acromion and the root of the spine. The spine and its base are significantly different to the

glenoid, superior angle, medial and inferior portions of the infraspinous fossa and the inferior angle. The **lateral portion of the infraspinous fossa** is not significantly different to the spine or its base, but does show some differences to the acromion, glenoid, superior angle, medial and inferior portions of the infraspinous fossa and the inferior angle.

- The **medial portion of the infraspinous fossa** and the **acromion** are not consistently similar to any other region, as there are some differences to all other VOIs in the scapula. However, the majority of these differences are with the glenoid, superior angle, inferior portion of the infraspinous fossa and inferior angle.
- The **glenoid**, **superior angle**, **inferior portion of the infraspinous fossa**, and **inferior angle** exhibit extensive differences to the spine and its base. There are also clear differences to the lateral portion of the infraspinous fossa, the acromion and the root of the spine. There are no consistent widespread statistical differences amongst these regions themselves.

Combining this statistical interpretation with the original metric data allows the VOIs to be grouped into distinct morphological regions.

The spine and its base contain relatively little trabecular bone that tends to be generally thick and rod-like. Although the statistical analyses did not detect a difference between VOI 13 and the other VOIs in this region, the metrics and interpretations suggest that this region is different to its neighbours. VOI 13 possesses a much lower bone volume than any other region and contains very sparsely distributed thick rods. VOI 13 corresponds to the original site of primary ossification and the associated nutrient vessel invasion; data suggest that a graduated radiating pattern originates from this region. Therefore, when designating regions of distinct morphology in the perinatal scapula, VOI 13 can be described as **central**.

The surrounding VOIs, which exhibit less extreme morphology but exhibit similar outcomes of statistical testing, can be described as **paracentral** regions. The spinous process, its base and root, and the lateral portion of the infraspinous fossa comprise these paracentral regions.

The distinctly different group of VOIs that is statistically similar to each other, and different to the central and paracentral regions, also exhibit different morphology to the central region (VOI 13). These areas include the superior angle, glenoid, inferior portion of the infraspinous fossa and the inferior angle. Trabeculae in these regions are thin, densely packed, frequent and more plate-like and have been categorised as **peripheral** regions.

The **inferior angle** exhibits the most extreme trabecular morphology of the peripheral regions, and is distinct from the other VOIs in the peripheral group, just as the central region is distinct from the paracentral regions. Closer examination of the raw data shows that a greater proportion of the medullary cavity is occupied by trabeculae in the inferior angle, and that trabeculae here resemble the classic definition of plates here more than in any other region.

The acromion and medial portion of the infraspinous fossa do not behave consistently with either the paracentral or the peripheral regions and have been classified as '**transitional**' regions. Despite both being different to the paracentral and peripheral regions, they are not morphologically similar to each other. The medial portion of the infraspinous fossa more closely resembles the peripheral regions, while the acromion has more in common with the paracentral regions. However, the medial portion of the infraspinous fossa and the acromion are distinct enough from the peripheral and peracentral regions respectively to merit being classified separately.

These distinct regions can also be visualised by studying the data for each metric in schematic format. A composite schematic, with the aforementioned statistical distinctions, can be used to describe these specific regions (central, paracentral, transitional and peripheral) and is summarised in Table 6.15 and Figure 6.33.

The central region (Region A) can be described as having extremely sparse, thick, rod-like trabeculae. The paracentral volumes (Region B) possess similar morphology, but not to the extreme level of the central region.

Two transitional regions were identified (Regions C), the medial portion of the infraspinous fossa and the acromion, each with their own distinct morphology. The acromion contains a low proportion of trabecular bone (although greater than the central and paracentral regions), comprises thick plate-like trabeculae that are intermediate in number and separated by large spaces. The medial portion of the infraspinous fossa contains a relatively low volume fraction, where trabeculae are frequent in number, densely packed and relatively thin.

A peripheral region was also identified, which contained a high proportion of trabecular bone. Trabeculae in these volumes can be described as densely packed thin plates. This morphology is most extreme at the inferior angle (Region E) and less extreme in the glenoid, superior angle and inferior portion of the infraspinous fossa (Region D).

The distinct trabecular morphology of these regions is summarised in Table 6.16.

This method of distinguishing differences between volumes produces a limited number of statistically distinct regions, however in doing so subtle differences between the original volumes are lost; this obscures the presence of radial trajectories, first described in the radiographic study.

	Region	Anatomical Locations	VOI(s)
A	Central	Deep to the spinoglenoid notch, corresponding to the location of the primary ossification centre and associated nutrient vessel invasion.	13
B	Paracentral	Spinous process (not including acromion), base and root of the spine, and the lateral portion of the infraspinous fossa.	6-8; 11,12,14; 17,18.
C	Transitional	Acromion	5
		Medial portion of the infraspinous fossa	15,16
D	Peripheral	Glenoid, superior angle and inferior portion of the infraspinous fossa.	1-4, 9,10, 19-21
E		Inferior angle	22,23

Table 6.15: A summary of regions of distinct trabecular morphology.

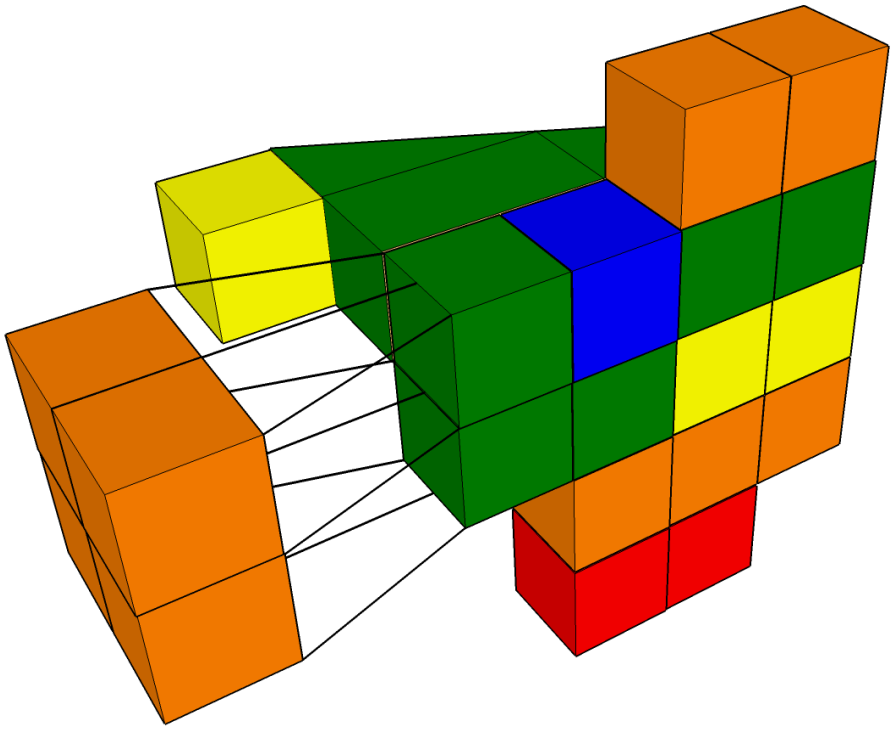

Figure 6.33: Distinct developmental regions of the perinatal scapula. Region A: Central (blue), Region B: Paracentral (green), Region C: Transitional (yellow) and Region D: Inferior blade (red).

Region			VOI(s)	BV/TV (%)	SMI	Tb.Th (mm)	Tb.N (1/mm)	Tb.Sp (mm)	DA
A	**Central**		13	Very low (21.0%)	Very High (2.3)	High (0.224)	Low (0.429)	Very High (0.526)	High (0.831)
B	**Paracentral**		6-8; 11,12,14; 17,18.	Low (26.9-33.05%)	Very High (1.93-2.33)	Moderate/High (0.210-0.284)	Low/Moderate (1.061-1.520)	High (0.353-0.430)	Variable (0.488-0.825)
C	**Transitional**	**Acromion**	5	Moderate (33.4%)	Moderate (1.47)	High (0.235)	Moderate (1.451)	High (0.393)	Low (0.503)
		Medial portion of the infraspinous fossa	15,16	Moderate (33.4-35.4%)	High (1.90-1.93)	Low (0.173-0.191)	High (1.768-2.068)	Low (0.228-0.286)	Moderate/High (0.650-0.768)
D	**Peripheral**		1-4, 9,10, 19-21	High (37.0-41.3%)	Moderate (1.38-1.77)	Low/Moderate (0.195-0.218)	High (1.755-2.169)	Low (0.245-0.307)	Variable 0.533-0.819
E			22,23	Very High (42.3-43.7%)	Low (1.16-1.39)	Moderate (0.215-0.226)	High (1.958-1.999)	Low (0.268-0.272)	Moderate 0.649-0.680

Table 6.16: A summary of trabecular morphology in each distinct region.

Radiating Trajectories

Although a radiating pattern is visible from the raw data and descriptive statistics, the pairwise comparison procedure failed to detect the subtle graduations between neighbouring VOIs and only detected clear statistical differences in the context of the whole scapula. When considering morphology of all the regions in the context of the whole scapula, a graduated radiating pattern is apparent.

The origin of the radiating pattern corresponds to VOI 13, which exhibits a unique morphology of very low bone volume fraction, where trabeculae are sparse, thick and rod-shaped. The radiating pattern terminates at peripheral areas of the bone, which exhibit a markedly different morphology, particularly in terms of bone volume fraction, which is high in peripheral regions. Differences can also be observed in the other measurements, where the number of trabeculae per millimetre is very low centrally and increases peripherally. Similarly, there are larger spaces between trabeculae in more central locations, which are not seen peripherally. Trabeculae are thicker and more rod-like centrally and become thinner and more plate-like distally. A transition appears to occur in VOIs between the central and peripheral regions, which tends to progress along the trajectories that were identified in Chapter 3: Radiographic study.

The stereoscopic analysis suggested that additional trajectories were also apparent, which could not be observed in gradient-mapped radiographs due to the effects of superimposition. Four trajectories were identified in total, all of which originated in the proximity of VOI 13 and extended:

- Dorsally, towards the acromion via the spine
- Inferiorly, to the inferior angle via the lateral border
- Medially, to the root of the spine, before diffusing into the superior angle and down the medial border
- Laterally, towards the glenoid

Two of these trajectories (heading in the inferior and medial directions) are visible in a perinatal gradient mapped radiograph (see Figure 3.4). All four are presented diagrammatically in Figure 6.34.

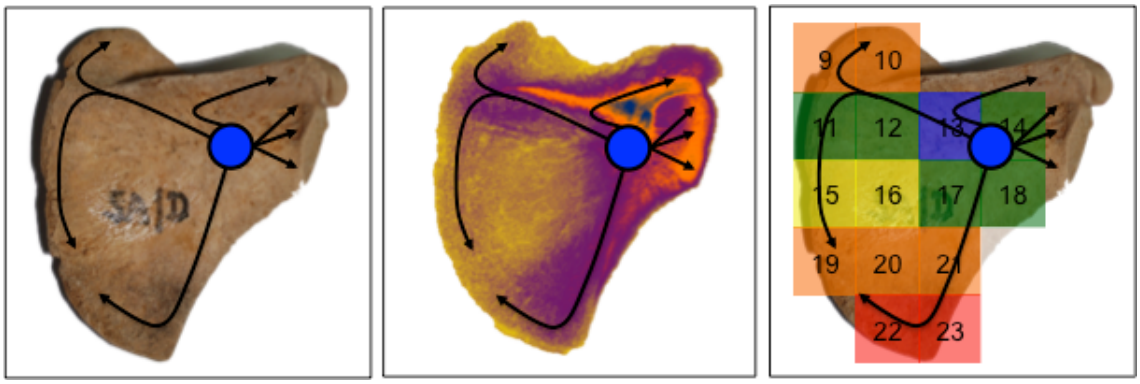

Figure 6.34: Radiating trajectories, originating from a central region (blue circle), and progressing to peripheral regions (arrows). Photograph (left), gradient mapped radiograph (centre) and superimposed micro-CT analysis (right).

The lateral portion of the infraspinous fossa, base of the spine and spine proper possess similar morphological characteristics and correspond to the inferior, medial and dorsal trajectories respectively. With the absence of large volumes of trabecular bone in these regions, it suggests that increased cortical thickness could be responsible for the increased radio-opacity visible radiographically. This description of mature central regions and immature peripheral bone has also been reported in vertebral bodies (Nuzzo et al., 2003) and the ilium (Cunningham and Black, 2010), and previously described in the scapula (Noback, 1943). In the case of the scapula, Noback (1943) described that "*the trabeculae of the scapula radiate from a centre*" while "*peripheral bands*" were observed in the medial border, glenoid and acromion.

Although bone close to the centre appears "older", remodelled and biomechanically less primative, one metric consistently fails to fit the pattern. The theory that the inferior angle is packed with new, unspecialised, bone appears to be contradicted by measurements of the degree of anisotropy. Trabecular bone around the inferior angle exhibits a more isotropic arrangement than around the origin at VOI 13, which implies a greater degree of organisational remodelling in the areas of the periphery. Despite

this, it is possible that increased isotropy in the region of the inferior angle is more likely to be caused by a combination of the distance from the primary centre of ossification (VOI 13) and the way DA is calculated.

DA describes the organisation of medullary bone by quantifying how oriented trabeculae are in a given volume. The scapula is a flat bone that essentially ossifies radially from a central location towards growing fronts (Ogden and Phillips, 1983; Scheuer and Black, 2000). Primary endochondral ossification is triggered by the invasion of vasculature, which then radiates from a central location to supply the bone's medullary cavity. This configuration can be simplified and depicted diagrammatically (Figure 6.35) and compared with visual inspection of a single micro-CT slice (Figure 6.31); calculation of DA at the extremities could result in the appearance of more uniform trabeculae. Conversely, regions more proximal to the centre contain radiating vascular structures, and thus trabeculae, which could result in trabeculae appearing less aligned. Although not an artefact, trabecular alignment in these regions of growth may not imply mechanical remodelling. It may simply be the consequence of radiating structures appearing more aligned the further they are located from an origin.

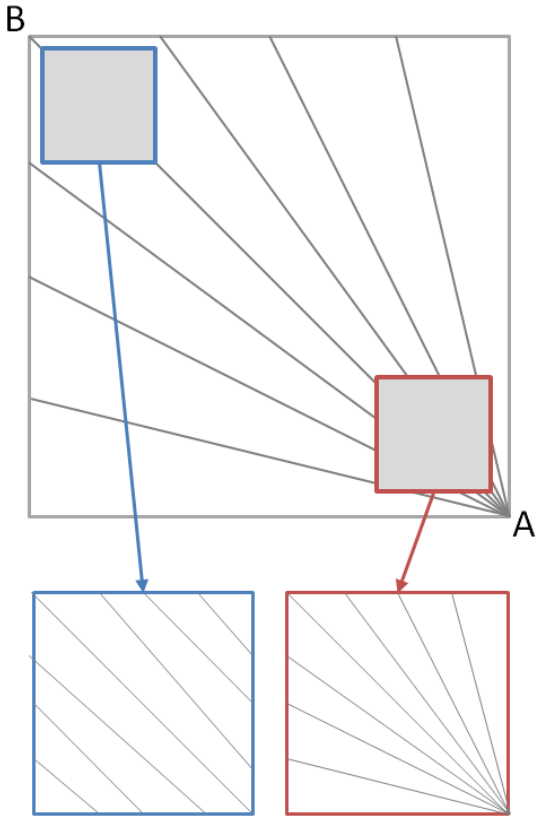

Figure 6.35: A diagrammatic representation of the orientation of trabeculae (grey lines) proximal (A) and distal (B) to an arbitrary origin. Examination of a VOI in each region would result in the appearance of organised trabeculae in distal locations (blue box) rather than proximal ones.

Growth

It is significant that the radiating trajectories project towards terminal growth regions of the bone, specifically the glenoid, acromion, and the medial border (between the associated superior and inferior angles). These regions can be thought of as epiphyseal growth fronts due the presence of secondary epiphyses during development (Scheuer and Black, 2000).

It is often reported in the literature that the scapula can be considered developmentally to be a modified long bone, with proximal and distal epiphyseal growth fronts (Ogden and Phillips, 1983). This study suggests that the medial border (including its inferior and superior terminal angles) and glenoid could correspond to the proximal and distal epiphyses respectively. In this model of growth, the medial border would correspond to the ‘growing’ end of the bone, while the glenoid could be considered the ‘non-growing’ extremity.

It is also widely documented that as secondary ossification centres appear and facilitate longitudinal growth, the epiphyses of the growing ends of the bone fuse last, while the epiphyses on non-growing ends fuse first. The situation in the scapula also complies with this rule, as the epiphysis of the medial border fuses to the body by 23 years of age. Conversely, the epiphyses around the glenoid fuse earlier at around 15-20 years of age. Although there is known to be much variation in the time of appearance, development and fusion of scapular secondary epiphyses (Scheuer and Black, 2000), those that correspond to the proximal growing end do not commence fusion until all other distal non-growing epiphyses have fused (Stewart, 1934).

Although these regions of growth have been identified by their involvement in the radiating trajectories, regional descriptions of these growth fronts suggest that the termini do not behave in the same way. The trabecular morphology of the superior and inferior angles suggests more active growth than occurs at the glenoid and acromion.

In the fetal period, the scapula has been shown to increase its width faster than its length (Kedzia et al., 2009), however as the bone specialises and grows this situation evidently changes as the bone becomes elongated craniocaudally (Rissech and Black, 2007). At the perinatal stage, these results suggest that the inferior angle is the predominant region of growth, while growth at the acromion and glenoid appears somewhat restricted, which could signal the beginning of crandiocaudal elongation of this bone.

The descent of the scapula *in utero* and *post-partum* could also affect the growth and morphology of the bone (Scheuer and Black, 2000; O'Rahilly and Gardner, 1972). The action of muscles pulling in an inferior direction (e.g. latissimus dorsi, serratus posterior, inferior fibres of trapezius) may encourage extensive growth at their attachment sites at the inferior angle.

The trabecular morphology of the acromion suggests that it is subjected to stresses during this period of development. It is suggested that this could also be due to the process of scapular descent, and increased strain across the acromioclavicular joint as a result of the clavicle transitioning from an oblique to horizontal position (Noback, 1944; McClure and Raney, 1975).

The fixed length of the clavicle during descent of the scapula suggests that the acromioclavicular joint would be forced laterally as the scapula descends Figure 6.36, a process that could contribute additional stress on the joint.

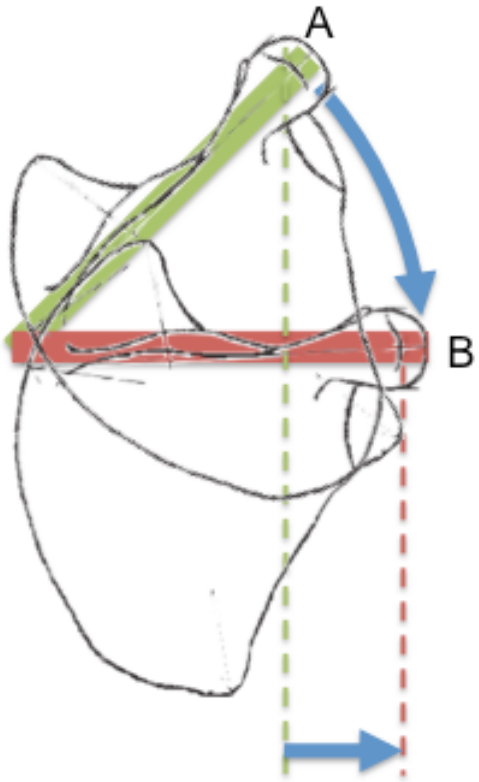

Figure 6.36: Relative positions of the acromioclavicular joint before (A) and after (B) scapular descent.

In Sprengel's deformity, where the scapula fails to descend, the scapula has been shown to maintain a more medial location as a result of not moving inferiorly and being forced laterally by the clavicle (Aydinli et al., 2005). The movement of the scapula inferiorly, causing the lateral extremity of the clavicle to relocate while its medial extremity is fixed, could introduce additional stresses across the

acromioclavicular joint. The presence of plate-like trabeculae in this region could suggest that this region maintains a degree of functional elasticity (Liu et al., 2006), perhaps to accommodate load across the joint.

In addition to the stereoscopic data, the anthropometric analysis also showed that the acromion was somewhat unusual. Of all recorded measurements, the width of the acromion was shown to have the weakest correlation to other anthropometric measurements. This suggests that while the proportions of the bone as a whole are highly restricted during development, the developmental morphology of the acromion appears to be less constrained.

Vasculature

In addition to the qualitative trabecular data, an additional clear and consistent structural arrangement was also observed. This structural arrangement presented itself during the MPR procedure and was visualised by producing surface renderings of the micro-CT data.

All nutrient foramina observed on the external cortical surface were continuous with their associated canals, which converged on a single, central cavernous region located at the approximate site of original primary endochondral ossification (Figure 6.37). In every case, the nutrient canals travelled from the nutrient foramen obliquely through the cortex to a central space, corresponding to VOI 13, which is largely devoid of trabeculae. This location is located at the root of the glenoid, at the approximate site of the primary ossification centre corresponding to VOI 13.

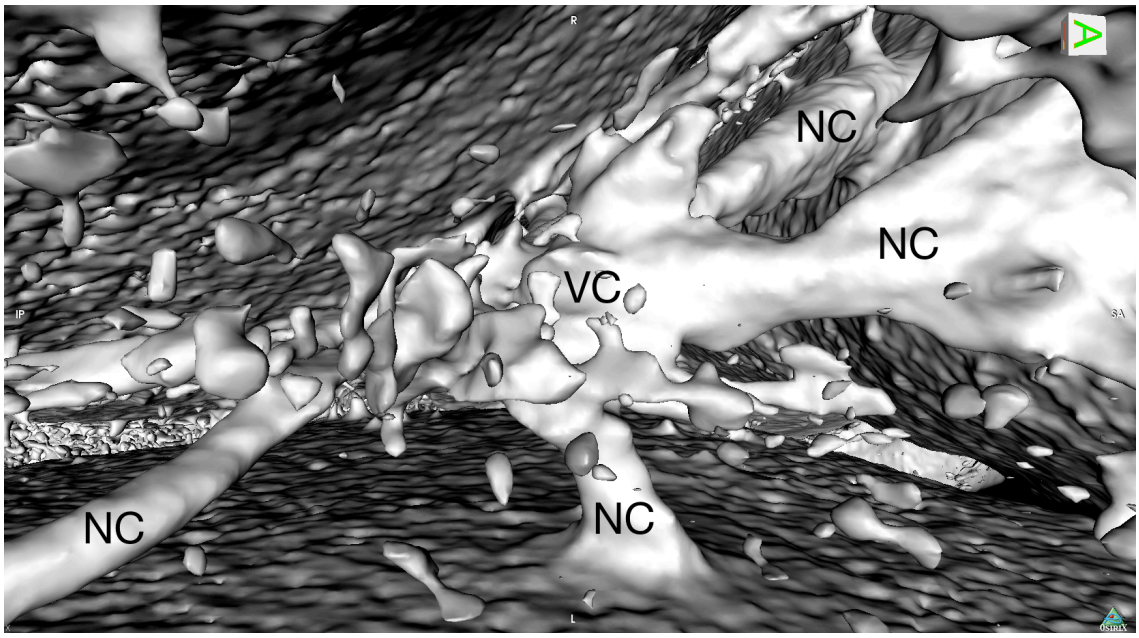

Figure 6.37: Nutrient canals (NC) converging on a vascular centre (VC) in the juvenile scapula.

Vascular channels were also observed inside the medullary cavity radiating from the central expanse in the direction of the extremities of the bone, i.e. the glenoid, acromion (via the spine), the medial border (via the root of the spine) and the inferior angle (via the lateral border). These vascular tracts mirror the radio-opaque areas identified on the gradient mapped radiographs (Figure 3.4). This central expanse represents the only conduit between the nutrient canal and the internal vascular supply of the medulla. Due to the three-dimensional nature of this vascular arrangement, two short videos of a surface rendering and a volume rendering have been included on a supplementary compact disc, labelled Appendix E, which is stored on the inside back cover of the thesis.

These observations compliment regional trabecular measurements, notably the sparse trabeculae described in the region of VOI 13 and the radiating pattern emerging from it. It follows that trabeculae can be described generally according to their position along a theoretical vascular-growth axis.

Trabeculae proximal to the vascular centre are older, and as a result more sparse and structurally robust. Conversely, structures distal to the vascular centre (and proximal to a growth front) are newer, and as a result more numerous and unspecialised. Comparison of this idea to the representation in Figure 6.33 supports this theory.

The specialisation of trabeculae close to the vascular centre could be due two factors:

1. Wolff's Law states that bone remodels and adapts to the stresses to which it is subjected, and it is understood that the primary ossification centre corresponds to the site of greatest stress in the cartilaginous anlage (Carter and Beaupré, 2001). The fact that there are fewer trabeculae in the region of the vascular/ossfication centre could result in those trabeculae adapting biomechanically more than peripheral trabeculae, which are more numerous due to diffuse vasculature and new ossification.
2. The region of the vascular centre also represents the initial site of ossification; therefore the few trabeculae that do exist in this region are among the "oldest" in the scapula. These trabeculae have had more time than their peripheral counterparts to remodel and adapt to stresses passing through the bone. 'New' trabeculae in the periphery have simply not existed long enough to remodel.

Invasion of the nutrient vessels into the cartilaginous anlage is triggered when angiogenic signals are released, as chondrocytes become ischaemic and hypertrophy. This is normally the result of ossification of the perichondrium due to *in utero* muscle attachments, as the deposition of a non-water based mineral matrix effectively severs the anlage from its nutrient supply. The invasion of blood vessels brings osteoblasts that begin to convert the anlage into bone. As the anlage (now with an ossified centre and dedicated vascular supply) rapidly begins to grow (Kedzia et al., 2009), rather than attracting additional nutrient vessels from distant sites outside the bone, the growth fronts draw on the existing vascular centre for their blood supply.

As development continues, the central vascular region becomes more significant while peripherally the vasculature diverges and spreads, resulting in smaller and more diffuse vessels. This idea is also supported this by study's findings, as peripheral growth regions contain large amounts of small, thin, trabecular plates with potentially small, vascular spaces in between.

These observations contradict current thinking, which proposes that the nutrient vessels enter the cortical shell then immediately branch and radiate towards the extremities of the bone to supply the medulla and growth fronts Figure 6.38A (Brookes, 1971; Mysorekar, 1967). Rather, the observations of this study suggest that arterial supply to the medulla is delivered from the systemic circulation to the vascular centre by nutrient arteries through the nutrient foramina and canals; arterial supply is then distributed from the central expanse to the living cells present throughout the medullary cavity via secondary channels that radiate from the centre Figure 6.38B. There is no reason to believe that the venous side of this vascular arrangement is structurally different, other than its reversal of flow.

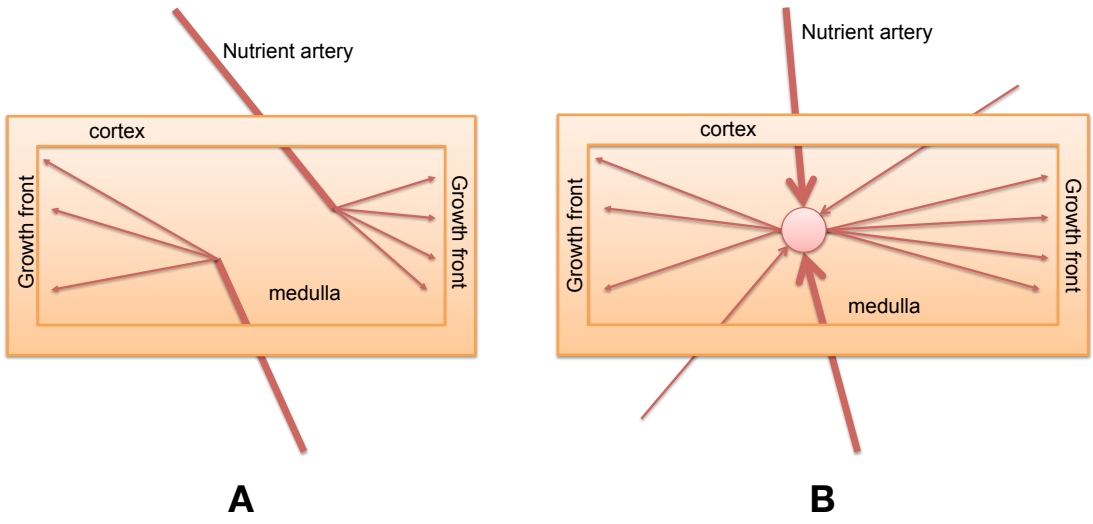

Figure 6.38: Generally accepted (A) and newly proposed (B) configurations of medullary vascular.

There are only fleeting references to such an arrangement in the literature. Digby (1916) mentioned of the long bones:

"The canal points towards the site which the oldest part of the bone would occupy were it not that the osseous tissue first formed is subsequently absorbed in providing the medullary cavity."

It may be that the "medullary cavity" Digby describes is homologous to the vascular centre that has been observed in the scapula.

A more comprehensive study was undertaken by Sirang (1973) in an investigation of 330 ilia, including adult, perinatal and fetal specimens. Sirang showed that nutrient vessels entered the bone from both the pelvic and gluteal sides of the blade, and that these vessels anastomosed inside the bone.

Furthermore, Sirang found that 100% of nutrient canals contained veins while only 43% contained arteries. Sirang claimed that describing these structures as 'nutrient' foramina, canals and vessels is misleading, since the structures chiefly facilitate the removal of material from the medullary space rather than the supply. This could suggest that the medullary vasculature is important in the export of haemopoietic products to the systemic circulation – this would be particularly important during periods of development.

These observations could also shed light on a classic, but as yet unexplained, anatomical adage. "From elbow I go, to the knee I flee" refers to the direction of the nutrient canal in long bones, and describes how in all instances (except, for unknown reasons, the fibula) the nutrient canal is directed towards the non-growing end of the bone (Scheuer and Black, 2000). Although frequently observed and referred to in the literature, no clear explanation for this can be found.

Previously discussed results support suggestions that the scapula can be developmentally considered as a modified long bone (Ogden and Phillips, 1983), with proximal and distal growth fronts. This study suggests that the medial border (including the inferior and superior angles) and glenoid correspond to the proximal and distal epiphyses, respectively. In this model of development, the medial border (equating to the proximal epiphysis) would correspond to the 'growing' end of the bone, while the glenoid (equating to the distal end) could be considered the 'non-growing' extremity.

Observations of the nutrient canals in perinatal escapula during this study suggest that that the classic rhyme could be extended to include the girdles. In both bones, the nutrient canals are directed towards a central cavernous region. This results in the appearance of canals being directed towards the joint, and simultaneously away from the 'growing end'. Similar observations have been made in the neonatal ilium, where nutrient foramina are oriented towards the vascular centre and away from the iliac crest (Aydinli et al., 2005; Cunningham and Black, 2010; 2013).

In addition to simply adding to the rhyme, the situation in the girdles could help to explain the underlying developmental anatomy. Rather than the directional arrangement of the nutrient canal being directly related to the non-growing end of a bone, it is more likely that it is directed at the vascular centre, which appears to remain at the non-growing end as the growing end extends away from the centre at a faster rate.

Without knowledge of the internal structures of bone, and specifically the vascular centre, it would appear as though the nutrient canal was directed towards the non-growing end when in fact it is directed towards the vascular centre. As an example, (Henderson, 1978) hypothesised that the direction of obliquity of the nutrient canal was caused by "the periostium sliding over the surface of the bone" towards the

growing end during growth. Attempts to find further references to this hypothesis in the literature have been fruitless.

In addition to growth and development, the presence of such a vascular conduit could have considerable clinical implications, particularly in the field of orthopaedic surgery and when considering the growth and development of bone. Some publications do not take this vascular centre into account and advise drilling deeper into the central column to avoid loosening or failure of prosthetic glenoids (Anglin et al., 1999), however others have recorded substantial reductions in the strength of subchondral bone as drilling depth is increased (Frich et al., 1997). No instances in the literature attribute failure of shoulder arthroplasty to the presence of a vascular centre.

Chapter 7: Conclusion

7.1. Summary of Findings

The aim of this research was to describe the trabecular morphology of the juvenile scapula and relate it to the functional requirements placed on the bone at different times in the life of the individual. Two studies were employed; one a qualitative radiographic investigation of scapulae from the full developmental range, and the other was a quantitative micro-CT investigation of scapulae aimed at the child of less than one year of age.

The complex shape of the scapula demanded that previously established methodologies be adapted for use on this unique bone: Multiplanar reconstruction (MPR) was used to analyse the separate regions (i.e. glenoid, acromion, spine and blade) of the scapula in isolation, perinatal scapulae were analysed anthropometrically to validate the use of a series of static grids to define volumes of interest (VOIs) and an intraobserver error study was conducted to ensure the histomorphometric analysis was repeatable and reliable.

The error study showed that the error introduced by an observer during threshold definition or VOI placement does not impact significantly on the results of the analysis.

Three distinct developmental phases were identified from the radiographic and the anthropometric review studies: pre-reboot (<0.5y), reboot (0.5-3y) and post-reboot (>3y). The pre-reboot specimens were analysed in detail in the quantitative investigation.

Pre-reboot (<0.5y)

The radiographic study showed that two trajectories of increased radio-opacity are apparent in the earliest stages of development, which persist to skeletal maturity. In addition to these two trajectories, the glenoid also appeared relatively radio-opaque in the pre-reboot phase. These regions, which were visible in the gradient mapped radiographs of developmental groups 1-3, persist to become crucial biomechanical features of the adult scapula.

The radiographic study also revealed a number of radiolucent striations radiating from or converging on a central locus, which persists until skeletal maturity. The location of the central radiolucency corresponds with the approximate location of the primary nutrient foramen, which indicates the probable invasion site of the nutrient artery and associated vein.

The quantitative study revealed regions of distinct morphology in the pre-reboot scapula: the observed radiating trajectories of the radiographic study were visible again in the raw data and descriptive statistics. From both the qualitative and quantitative studies a total of four trajectories were identified, all of which originated in close proximity to the vascular/ossification centre (VOI 13) and extended:

- Dorsally, towards the acromion via the spine
- Inferiorly, to the inferior angle via the lateral border
- Medially, to the root of the spine, before diffusing to the superior angle and down the medial border
- Laterally, towards the glenoid

The radiating pattern observed in pre-reboot specimens has been discussed in relation to growth and vasculature. A clear and consistent structural arrangement, which involved nutrient canals and vascular distribution, was also observed.

The anthropometric study showed that the proportions of the scapula are relatively constant in pre-reboot specimens, with changes in absolute size in the early stages of development not resulting in changes in shape. It follows that the use of scalable static grids in the glenoid, spine, acromion and blade of the scapula in this developmental group are appropriate.

Reboot (0.5-5y)

The radiographic study identified a developmental phase in the scapula during which significant micro- and macro- morphological changes occurred. During the reboot phase the progressive development observed in the pre-reboot phase ceased and indeed reversed. Bone resorption causes decreased ‘density’ throughout the bone, following which the scapulae appears to return to progressive and specialised growth.

Morphological changes also occurred on a larger scale: the typical rounded shape of pre-reboot specimens began to change during the reboot. During the reboot phase, the scapulae transformed from a curved bone, which was as wide (mediolaterally) as it was long (craniocaudally), to an angular bone, which was craniocaudally elongated. A review of the literature as part of the anthropometric study also corroborated these findings.

Post-reboot (>3y)

The radiographic study revealed clear differences between pre- and post- reboot specimens. In post-reboot specimens new bone was laid down in a discriminatory fashion, as the fossae failed to thicken after they thinned during the reboot phase. This was in contrast to the pre-reboot phase, which exhibited uniform development across the bone. The radiographic study and the anthropometric review also revealed that post-reboot the scapula also remodels on a macro-morphological scale, adopting a craniocaudally elongated and angulated appearance, rather than the rounded scapula of the pre-reboot specimens. Concurrently, the lateral border adopts a more concave

shape and oblique ridges, caused by the insertion of tendinous intersections of infraspinatus and subscapularis, begin to appear and persist into adulthood.

7.2. Application of Findings

Anthropology & Evolutionary Theory

This research examined human juvenile scapulae and revealed an unexpected and previously unreported episode when the organisation of bone seemingly falters and then remodels (‘reboots’) to result in an alternative structural template that appears to be ontogenetically stable by 3-4 years of age. Whilst the external shape of the scapula may be highly constrained by its phylogenetic commitment to potential modes of locomotion, the micro-architecture appears to adjust to more immediate demands and does so in a fairly swift and responsive manner within a narrow window of opportunity. Although the external morphology of the human skeleton has been the primary source of evidence for the evolution of bipedality in the past, this research suggests that the answers from inside our bones may be equally enlightening.

It is suggested that the reboot represents a phase in development where the scapula is released from its developmental constraints, while the pelvic girdle remains committed to its phylogenetically predetermined role. During the first year of life, both limbs could be said to fulfil their phylogenetic anticipatory role - assuming that they are programmed for quadrupedal locomotion. However, crawling behaviour is transitory (or absent), whereas the habitual mode of locomotion is established towards the end of the first year, perfected throughout the second year before attaining a mature gait around 8 years of age (Cunningham and Black, 2010). During this time, the ilium must accept its predetermined role in locomotion, but the scapula is released to adopt an entirely different functional role.

It appears that the scapula is neither constrained by its original anticipated function nor co-opted into a configuration that will eventually prove unsuitable. It is suggested

that the scapula could be further analysed to reveal evidence for adaptive variation in the primate (or other mammals) in relation to types of locomotion - quadrupedal, suspensory or knuckle walking.

Forensic Science & Identification

The findings of this study could be utilised in the forensic arena as an additional aging technique; the radiographic, anthropometric and micro-CT investigations could all potentially contribute to this field.

Figure 7.1 correlates the developmental groups established in the radiographic study (Chapter 3) with skeletal age. A radiograph of a scapula could be provided to an observer, which would be gradient-mapped and the image analysed. Successfully placing a specimen in the correct developmental group could suggest a skeletal age and could thus contribute to the formation of a complete biological profile. Further understanding of trabecular morphology, particularly its uniqueness, could also result in the stereoscopic findings becoming forensically useful, perhaps in the analysis of fragmented remains. In isolation, the juvenile scapula is easily confused with the squamous part of the temporal bone. Analysis of trabecular morphology could assist in successfully identifying ambiguous bone fragments in a forensic or archaeological context.

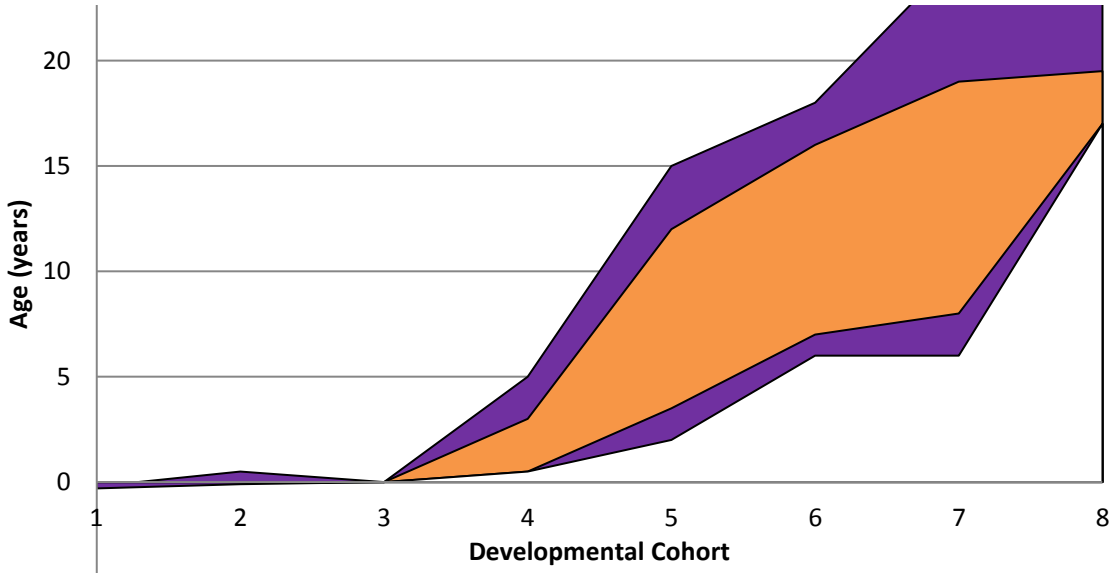

Figure 7.1: Age ranges for each Developmental Group.
Orange = minimum age range; Purple = maximum age range.

These suggested techniques that rely on interpretation of secondary radiographic data could be particularly beneficial in scenarios where observers do not have direct access to forensically relevant material, such as hostile conflict zones or environments subjected to chemical, biological, radiological or nuclear (CBRN) events. Further study is needed to clarify and verify the aging potential of the findings of this thesis.

Clinical Relevance

The quantitative and qualitative observations of this study may contribute to the significant clinical problem of glenoid component revision in total shoulder arthroplasty. Failure of the glenoid component is the most common complication of total shoulder arthroplasty (Matsen et al., 2008), and loosening has been shown to occur in 96% of implanted glenoids (Strauss et al., 2009). A review by Fox et al (2009) showed that 13% of glenoid replacements fail and require further revision, while a similar study by Fevang et al (2009) suggested that 22% of glenoids components fail.

Several risk factors that contribute to glenoid component failure have been identified in the literature; it is understood that minimal bone stock (Schrumpf et al., 2011) and avascular necrosis of the glenoid (Fox et al., 2009) can both contribute to these high

failure rates. The findings of the quantitative study (Chapter 6) show that particularly low bone volume fraction and high trabecular separation were typical in the region of the glenoid neck and spinoglenoid notch (VOIs 13/14). Should this situation persist into adulthood, the potential contribution to glenoid component failure seems assured.

Observations of the nutrient canals converging to a central locus before radiating to the growing ends of the bone (including the glenoid) could also prove relevant. Pathological changes associated with vascular disruption do not occur in the glenoid while they are underway in the humerus (Catto in Nixon, 1983); this suggests interruption of the medullary supply (from nutrient vessels) is responsible for avascular necrosis rather than the external vessels that supply the soft tissues and cortical bone.

With the exception of the glenoid labrum, nutrient vessels have been shown to be numerous and are considered an important vascular supply of the scapular neck and surrounding bone (Cooper et al., 1992; Abrassart et al., 2006; Hamel et al., 2012). Trauma has been cited as a potential cause of avascular necrosis in the glenoid and, although exceptionally rare, one case of glenoid avascular necrosis secondary to traumatic injury has been located in the literature (Nixon, 1983). Dzioba and Quinlan (1984) also reported avascular necrosis of the glenoid after trauma; in this case no surgical intervention was employed. A rare case of total glenoid dislocation secondary to a traumatic fracture has also been reported after a motorcyclist was thrown from his bike, which had collided with an articulated truck. Surgical repair of the fracture less than 24 hours after the injury successfully prevented avascular necrosis of the glenoid (Limb and McMurray, 2005).

Smith et al (2006) reported osteonecrosis of the glenoid secondary to disruption of the blood supply after placement of multiple suture anchors in the body and neck of the scapula. The authors suggested that the vascular supply to the glenoid was disrupted by implantation of multiple surgical devices in the glenoid neck and body, which correspond to VOIs 13 and 14 in this thesis. Smith et al (2006) reported that these

implants had a negative effect on the blood supply of the subchondral bone of the glenoid, and recommend that surgeons avoid extensive dissection of the glenoid architecture.

Osteochondritis dessicans (OCD) describes pathological changes to articular cartilage and subchondral bone and is caused by vascular disruption and is considered a consequence of avascular necrosis. Recent studies have shown that the symptoms of OCD improve after encouraging revascularisation by drilling small holes into the subchondral bone, which encourages angiogenesis (Chu et al., 2009). This also highlights the importance of the medullary vasculature to the healthy maintenance of subchondral bone in the glenoid.

Considering the observations of this thesis, as well as the aforementioned reports in the literature, it seems possible that osteonecrosis, perhaps secondary to vascular disruption, of the glenoid is common in patients who have undergone shoulder arthroplasty, but is treated as ‘normal’ postoperative pain and inflammation. Indeed, pain relief medications and corticosteroid injections are often used to good effect in managing these postoperative symptoms. It may be that avascular osteonecrosis of the glenoid is a common sequela that is iatrogenic in nature and directly attributable to disruption of the vascular centre observed in this study. This vascular disruption and subsequent avascular osteonecrosis could be the cause of the high loosening and total failure rates associated with shoulder arthroplasty.

7.3. Study Limitations

The main limitations associated with this thesis are related to the number and provenance of juvenile skeletal remains examined; concerns regarding small sample sizes and remains of unknown or limited provenance have been raised previously in the literature (Liu et al., 2006; Cunningham, 2009; Ryan and Krovitz, 2006; Gosman and Ketcham, 2009).

This study examined 83 specimens in the qualitative radiographic study, 38 specimens in the anthropometric study and 36 specimens in the quantitative stereoscopic study, all from the Scheuer Collection, which is considered one of the largest repositories of juvenile remains in the world. While a large sample size is always desirable, the nature of juvenile remains means that limited numbers are an unavoidable reality. It should also be noted that statistical analyses of the resulting data considers sample size when calculating the significance of findings. A related consequence of working with rare skeletal material is an uneven spread of ages being available for study: only 3 fetal and 4 infant specimens, compared to 28 adolescents.

A further limiting factor of human, and especially juvenile, remains is associated with sample mortality. Most specimens in the Scheuer Collection are of archaeological provenance and their causes of death are unknown; the possibility that their terminal condition could affect bone morphology in general, or the scapula specifically, cannot be excluded. Gross inspection and anthropometric analysis of the bones was carried out with the aim of identifying possible anomalous or pathological specimens, but no such specimens were found. While other pathologies may have been present at the time of death it is considered unlikely that they had an effect on the scapulae.

7.4. Study Strengths

Although there are some unavoidable limitations relating to the nature of the specimens used in this study, there are also strengths associated with the sample and recent advances in three-dimensional imaging. While the material contained in the Scheuer Collection is often undocumented, its use here is still considered as strength of this study; juvenile skeletal remains are difficult to access, with the material itself being generally well preserved and largely representative of the entire developmental range.

Micro-CT allows for non-destructive quantification of microarchitecture that would not have been possible previously due to the irreplaceable nature of the specimens. The maximum scanning resolutions available have also improved; in the last five years the maximum resolution has increased from 34.5μm in some studies (Cunningham, 2009) to 25.4μm in this study. The introduction of MPR and an intraobserver error study have further advanced this methodology and improved the reliability of the method and results.

7.5. Recommendations for Improvement

Recent advances in imaging technology have resulted in further improvements to the maximum achievable scanning resolution; in recent (Oct 2012) testing of a new micro-CT detector a neonatal scapula was scanned and a resolution of 16.4527μm was achieved. To further increase the accuracy of the results of this type of study, specimens should be periodically reimaged as new technologies emerge.

It is also possible that advances in micro-CT imaging could lead to the possibility of larger specimens being imaged at higher resolutions; this possibility creates opportunities to perform studies of larger bones, perhaps across all developmental ranges.

While the introduction of MPR to this study improved previously established methodologies by improving accuracy and decreasing the potential for false positive statistical results, there are still improvements to be made to the VOI placement technique. The ability to define multiple VOIs at once would help eliminate the possibility of including borderline trabeculae in more than one VOI.

While MPR has made the manual placement of VOIs less labour intensive and time consuming than was reported in previous studies (Cunningham, 2009), an automation of this process would further increase observer efficiency and could result in studies of greater scope being attempted in similar timeframes. However, the design of automated algorithms to identify specific volumes of bone correctly could be extremely complicated; indeed, algorithms that automatically distinguish between bone and non-bone currently exist, but require a large amount of user contribution. Stradwin, a software package developed by the Department of Engineering, University of Cambridge, has been employed primarily to acquire 3D ultrasound data, but has also been used to automatically quantify cortical thickness from CT data (Treece et al., 2010). Although this software has provided promising results from clinical CT data, the software is unable to process the large datasets associated with micro-CT scans and

fails to distinguish between juvenile cortical and trabecular bone (Treece and Gee, 2012).

Although MPR is a relatively simple and widely used technique, it would be prudent to establish conclusively whether the procedure introduces significant error into the study. A statistical comparison of the results of trabecular analysis of the same VOI before and after being subjected to MPR would establish what affect, if any, MPR has on the outcome of trabecular analyses.

7.6. Suggestions for Further Research

While this thesis describes in detail the developmental morphology of the human scapula, there are additional areas of research that could expand and compliment the findings.

With advances in imaging technology and computing power it will become possible to scan larger specimens without a decrease in scanning resolution. It will become viable to repeat the quantitative micro-CT section of this thesis on scapulae from other developmental groups, while particular attention should be focussed on skeletal material in the reboot phase of development.

It should be considered that this thesis also identified challenges associated with developing a method that identifies comparable VOIs across a bone that exhibits allometric growth; the most appropriate course for future studies of other developmental groups would be to establish firstly the consistency of scapular shape of the group in question, then design a series of static grids. If the results of any future study were to be compared with the results of this investigation, care would have to be taken to ensure that VOIs from each study correspond to structurally/functionally homologous regions.

With improvements to VOI placement techniques it would also become possible to extend the scope of this investigation to include neighbouring bones, namely the clavicle and humerus. A description of trabecular morphology across the entire pectoral girdle would allow observers to further hypothesise on the involvement of load transmission across joints. The presence of a reboot phase in the clavicle, for example, would contribute further evidence for the theory proposed in this thesis; a resorption phase would perhaps also be expected in the clavicle as the upper limb becomes free from the preordained locomotive fate. Furthermore, the relevance of a reboot phase in a phylogenetic context could also be discussed more fully by investigating the development of different species, particularly primates, in a similar manner as this thesis.

Measurement and analysis of cortical thickness could also compliment the findings of this thesis. While previous studies have measured cortical thickness at limited specific locations across a bone (Cunningham and Black, 2009c; Warner et al., 2006), advancing imaging resolution and computing power now allows more extensive data collection and high-resolution visualisation of the cortical shell (Treece et al., 2010). Although not specifically designed for use on high resolution CT or juvenile bone, these more modern techniques could be adapted for use on the sample that was used in this thesis.

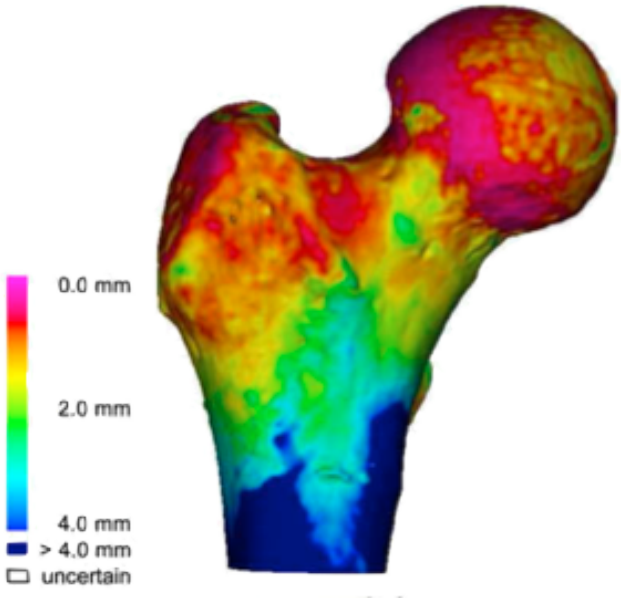

Figure 7.2: Automated cortical thickness data mapped to a surface rendering of the original scan. (Treece et al., 2010)

Further study of configuration of vascular distribution in the medullary space is also desirable. It would be useful to qualitatively describe and to quantitatively measure the vascular distribution in the same sample that was analysed in this study. It would also be useful to establish whether the arrangement observed here persists into skeletal maturity and subsequent degeneration with associated old age, and if a similar arrangement is present at other sites in the human skeleton. The clinical implications of the outcomes of such studies could be significant, particularly for orthopaedic research focussed on the design and testing of shoulder arthroplasty techniques.

It may also be possible to map the vascular channels in the micro-CT scans that were gathered for this study and establish whether the arrangement of the channels is unique to each individual. With the vascular centre defined as the origin, the length and direction of each nutrient canal could be measured to define a series of three-dimensional vectors. These vector profiles could be subjected to directional statistical testing which could establish whether they are unique to the individual, and longitudinal studies could establish the permanence of the deep vascular profile. Personal observations, as well as reports in the literature, suggest that nutrient canals

are visible in clinical CT scans (Richardson and Montana, 1985; Ebraheim et al., 1997; Lee et al., 2000), and with an estimated 72 million clinical CT scans performed in the United States annually the forensic human identification potential of deep vascular profiling could be significant (Berrington de Gonzalez et al., 2009). Personal observations also suggest that converging nutrient canals may also be present at other sites in the juvenile skeleton, such as the pubis, ilium and femora.

While the scope of this thesis was primarily to describe the developmental morphology of the human scapula, it is not possible to definitively test any proposed form-function relationships between biomechanical loading and observed morphology. It is suggested that a complex computer model of the neonatal pectoral girdle could be designed to investigate the relationships between trabecular morphology and load. Finite element (FE) modelling would be of use in establishing a force-function relationship between function and structure at the earliest stages of development, although due to limitations computing power it is unlikely that complex FE models could make use of the data from this thesis in the near future.

7.7. Conclusion

This thesis presents a radiographic description of developmental morphology of the human scapula and a comprehensive morphological description of trabecular bone in the perinatal scapula. While the aim was originally to describe the changing trabecular morphology in the developing scapula, considerable thought has gone into the design, advancement and validity of the methodologies presented in this thesis. The work of previous studies has been considered and improved upon to take into account recent advances in software and hardware. Specifically, the introduction of MPR to the methodology has resulted in a more efficient and reliable technique that could allow future researchers to examine larger datasets in shorter periods of time. Additional anthropometric data were also gathered on the perinatal scapula, which was used to assist in the design of the multiplanar stereoscopic analysis. User error associated with threshold definition and VOI placement was also investigated and found to be negligible.

With respect to development of the juvenile scapula, three distinct developmental phases, comprising eight separate groups, were identified from the radiographic study and anthropometric review study: pre-reboot (<0.5y), reboot (0.5-3y) and post-reboot (>3y). A clear pattern of regional organisation was visible at the earliest stages of development, echoing the findings of Cunningham and Black (2009a). It was suggested that the reboot represents a developmental period in which the scapula undergoes functional change under a two-tier mechanism, which influences its overall development.

On one level the scapula appears constrained by a rigid template that controls macro-morphology in preparation for phylogenetically anticipated demands, which may, or may not, materialise; on a second tier is the adaptive micro-architecture that initially compliments the phylogenetic template, but retains the flexibility to respond to shifting ontogenetic demands.

The trabecular architecture of the pre-reboot specimens was subsequently analysed in quantitative detail. A progressive radiating pattern, which originated from the approximate location of the primary ossification centre, was identified; it is suggested that a combination of radiating growth and internal vascular distribution are significant contributors to this pattern.

This thesis provides a detailed account of the developmental morphology of the human scapula and contributes new elements to the evolving methodologies used in this field. The findings of this study also lay the foundation for further investigation of the radiating pattern of ossification and the potential for micro-architecture in developing bone to adapt to ontogenetic demands despite gross morphology that is phylogenetically constrained.

References

Abrassart, S. et al. (2006) Arterial supply of the glenoid: An anatomic study. *Journal of Shoulder and Elbow Surgery*. [Online] 15 (2), 232–238.

Anetzberger, H. & Putz, R. (1996) The scapula: principles of construction and stress. *Acta anatomica*. 156 (1), 70–80.

Anglin, C. et al. (1999) Glenoid cancellous bone strength and modulus. *Journal of Biomchanics*. 32 (10), 1091–1097.

Aubin, J. et al. (1998) Transcriptional interferences at the Hoxa4/Hoxa5 locus: importance of correct Hoxa5 expression for the proper specification of the axial skeleton. *Developmental Dynamics*. [Online] 212 (1), 141–156.

Aydinli, U. et al. (2005) Surgical treatment of sprengel's deformity: a modified Green procedure. *Acta orthopaedica Belgica*. 71 (3), 264–268.

Berman, D. S. et al. (2000) Redescription of Seymouria sanjuanensis (Seymouriamorpha) from the Lower Permian of Germany based on complete, mature specimens with a discussion of paleoecology of the Bromacker locality assemblage. *Journal of Vertebrate Paleontology*. [Online] 20 (2), 253–268.

Berrington de Gonzalez, A. et al. (2009) Projected cancer risks from computed tomographic scans performed in the United States in 2007. *Archives of internal medicine*. 169 (22), 2071.

Bialek, P. et al. (2000) Characterization of a novel insertional mouse mutation, kkt: A closely linked modifier of Pax1. *Developmental Biology*. [Online] 218 (2), 354–366.

Bousson, V. et al. (2012) Trabecular bone score (TBS): available knowledge, clinical relevance, and future prospects. *Osteoporosis International*. [Online] 23 (5), 1489–1501.

Breathnach, A. S. (1965) *Frazer's Anatomy of the Human Skeleton*. 6 edition. London: Churchill.

Brookes, M. (1971) *The blood supply of bone*. Butterworth-Heinemann.

Byers, S. et al. (2000) Quantitative histomorphometric analysis of the human growth plate from birth to adolescence. *Bone*. 27 (4), 495–501.

Carter, D. R. & Beaupré, G. S. (2001) *Skeletal Function and Form*. Cambridge University Press.

Carter, D. R. et al. (1989) Relationships between loading history and femoral cancellous bone architecture. *Journal of Biomchanics*. 22 (3), 231–244.

Chu, P.-J. et al. (2009) Osteochondritis Dissecans of the Glenoid: A Rare Injury Secondary to Repetitive Microtrauma. *The Journal of Trauma: Injury, Infection, and Critical Care*. [Online] 67 (3), E62–E64.

Ciarelli, M. J. et al. (1991) Evaluation of orthogonal mechanical properties and density of human trabecular bone from the major metaphyseal regions with materials testing and computed tomography. *Journal of Orthopaedic Research*. [Online] 9

(5), 674–682.

Cigtay, O. S. & Mascatello, V. J. (1979) Scapular defects: a normal variation. *American Journal of Roentgenology*. [Online] 132 (2), 239–241.

Coates, M. I. et al. (2002) Fins to limbs: what the fossils say. *Evolution and Development*. 4 (5), 390–401.

Collard, M. & Wood, B. (2007) Hominin homoiology: an assessment of the impact of phenotypic plasticity on phylogenetic analyses of humans and their fossil relatives. *Journal of Human Evolution*. [Online] 52 (5), 573–584.

Cooper, D. E. et al. (1992) Anatomy, histology, and vascularity of the glenoid labrum. An anatomical study. *Journal of Bone and Joint Surgery*. 74 (1), 46–52.

Crock, H. V. (1996) *An atlas of vascular anatomy of the skeleton and spinal cord*. London: Dunitz Martin Ltd.

Culham, E. & Peat, M. (1993) Functional anatomy of the shoulder complex. *The Journal of orthopaedic and sports physical therapy*. 18 (1), 342–350.

Cunningham, C. A. (2009) *A qualative and quantitave investigation of the structural morphology in the neonatal ilium*. University of Dundee.

Cunningham, C. A. & Black, S. M. (2009a) Anticipating bipedalism: trabecular organization in the newborn ilium. *Journal of Anatomy*. [Online] 214 (6), 817–829.

Cunningham, C. A. & Black, S. M. (2009b) Development of the fetal ilium--challenging concepts of bipedality. *Journal of Anatomy*. [Online] 214 (1), 91–99.

Cunningham, C. A. & Black, S. M. (2009c) Iliac cortical thickness in the neonate - the gradient effect. *Journal of Anatomy*. [Online] 215 (3), 364–370.

Cunningham, C. A. & Black, S. M. (2010) The neonatal ilium-metaphyseal drivers and vascular passengers. *Anatomical record*. [Online] 293 (8), 1297–1309.

Cunningham, C. A. & Black, S. M. (2013) The vascular collar of the ilium- three-dimensional evaluation of the dominant nutrient foramen. *Clinical Anatomy*. [Online] 26 (4), 502–508.

Dalstra, M. & Huiskes, R. (1995) Load transfer across the pelvic bone. *Journal of Biomchanics*. 28 (6), 715–724.

Dayanidhi, S. et al. (2005) Scapular kinematics during humeral elevation in adults and children. *Clinical Biomechanics*. [Online] 20 (6), 600–606.

Debski, R. E. et al. (2000) Ligament Mechanics During Three Degree-of-Freedom Motion at the Acromioclavicular Joint. *Annals of Biomedical Engineering*. [Online] 28 (6), 612–618.

Digby, K. H. (1916) The Measurement of Diaphysial Growth in Proximal and Distal Directions. *Journal of Anatomy and Physiology*. 50 (Pt 2), 187–188.

Ding, M. & Hvid, I. (2000) Quantification of age-related changes in the structure model type and trabecular thickness of human tibial cancellous bone. *Bone*. [Online] 26 (3), 291–295.

Donoghue, P. C. J. et al. (2006) Early evolution of vertebrate skeletal tissues and cellular interactions, and the canalization of skeletal development. *Journal of Experimental Zoology Part B: Molecular and Developmental Evolution*. [Online] 306B (3), 278–294.

Drake, R. et al. (2005) *Gray's Anatomy for Students Deluxe Package*. Philadelphia: Churchill Livingstone.

Dzioba, R. B. & Quinlan, W. J. (1984) Avascular Necrosis of the Glenoid. *Journal of Trauma and Acute Care Surgery*. 24 (5), 448.

Ebraheim, N. A. et al. (1997) Anatomic considerations of the principal nutrient foramen and artery on internal surface of the ilium. *Surgical and Radiologic Anatomy*. 19 (4), 237–239.

Edwards, J. L. (1989) Two perspectives on the evolution of the tetrapod limb. *American zoologist*. 29 (1), 235–254.

Fajardo, R. J. & M ller, R. (2001) Three-dimensional analysis of nonhuman primate trabecular architecture using micro-computed tomography. *American Journal of Physical Anthropology*. [Online] 115 (4), 327–336.

Fazekas, I. G. & Kósa, F. (1978) *Forensic fetal osteology*. Budapest: Akadémiai Kiadó.

Fevang, B.-T. S. et al. (2009) Risk factors for revision after shoulder arthroplasty. *Acta Orthopaedica*. [Online] 80 (1), 83–91.

Fox, T. J. et al. (2009) Survival of the glenoid component in shoulder arthroplasty. *Journal of Shoulder and Elbow Surgery*. [Online] 18 (6), 859–863.

Frich, L. H. et al. (1997) Bone strength and material properties of the glenoid. *Journal of Shoulder and Elbow Surgery*. [Online] 6 (2), 97–104.

Frich, L. H. et al. (1998) Glenoid bone architecture. *Journal of Shoulder and Elbow Surgery*. 7 (4), 356–361.

Gardner, E. & Gray, D. J. (1953a) Prenatal development of the human shoulder and acromioclavicular joints. *American Journal of Anatomy*. [Online] 92 (2), 219–276.

Gardner, E. & Gray, D. J. (1953b) Prenatal development of the human shoulder and acromioclavicular joints. *The American journal of anatomy*. 92219–276.

Gosman, J. H. & Ketcham, R. A. (2009) Patterns in ontogeny of human trabecular bone from SunWatch Village in the Prehistoric Ohio Valley: general features of microarchitectural change. *American Journal of Physical Anthropology*. [Online] 138 (3), 318–332.

Graham, A. (2005) Vertebrate evolution: turning heads. *Current biology*. [Online] 15 (18), R764–R766.

Gupta, S. & Dan, P. (2004) Bone Geometry and Mechanical Properties of The Human Scapula Using Computed Tomography Data. *Trends in Biomaterials and Artificial Organs*. 17 (2).

Gupta, S. & van der Helm, F. C. T. (2004) Load transfer across the scapula during humeral abduction. *Journal of Biomchanics*. [Online] 37 (7), 1001–1009.

Hamel, A. et al. (2012) The arterial supply of the coracoid process. *Surgical and Radiologic Anatomy*. [Online] 34 (7), 599–607.

Hara, T. et al. (2002) The influence of microcomputed tomography threshold variations on the assessment of structural and mechanical trabecular bone properties. *Bone*. 31 (1), 107–109.

Haywood, K. & Getchell, N. (2001) *Life span motor development*. Champaign, IL, USA: Human Kinetics Publishers.

Henderson, R. G. (1978) The position of the nutrient foramen in the growing tibia and femur of the rat. *Journal of Anatomy*. 125 (Pt 3), 593–599.

Hildebrand, T. & Ruegsegger, P. (1997) A new method for the model-independent assessment of thickness in three-dimensional images. *Journal of microscopy*. [Online] 185 (1), 67–75.

Hildebrand, T. & Rüegsegger, P. (1997) Quantification of Bone Microarchitecture with the Structure Model Index. *Computer methods in biomechanics and biomedical engineering*. [Online] 1 (1), 15–23.

Huang, R. et al. (2000) Dual origin and segmental organisation of the avian scapula. *Development*. 127 (17), 3789–3794.

Huang, R. et al. (2006) Regulation of scapula development. *Anatomy and Embryology*. [Online] 211 Suppl 165–71.

Inman, V. T. et al. (1944) *Observations on the Function of the Shoulder Joint*. 26 (1), 1–30.

Kang, C. et al. (1999) R'2 measured in trabecular bone in vitro: relationship to trabecular separation. *Magnetic resonance imaging*. 17 (7), 989–995.

Kedzia, A. et al. (2009) Analysis of Human Scapula Morphometry in the Fetal Period. *Advances in Clinical and Experimental Medicine*. 18 (3), 197–204.

Keen, M. (1993) Early Development and Attainment of Normal Mature Gait. *Journal of Prosthetics and Orthotics*. 5 (2), 35/23.

Kuijper, S. et al. (2005) Genetics of shoulder girdle formation: roles of Tbx15 and aristaless-like genes. *Development*. [Online] 132 (7), 1601–1610.

Laurenson, R. D. (1964) The Primary Ossification of the Human Ilium. *Anatomical record*. 148209–217.

Lee, J. H. et al. (2000) Nutrient canal of the fibula. *Skeletal radiology*. [Online] 29 (1), 22–26.

Lewis, W. H. (ed.) (n.d.) *Gray's Anatomy of the Human Body* [online]. Available from: http://www.bartleby.com/107 (Accessed September 2012).

Li, G. & Luo, Z.-X. (2006) A Cretaceous symmetrodont therian with some monotreme-like postcranial features. *Nature*. [Online] 439 (7073), 195–200.

Lim, D. et al. (2010) Mapping of the morphological and the material characteristics on the glenoid and estimation of predominant loading condition on the glenoid

through the mapping. *Journal of Mechanical Science and Technology*. [Online] 23 (2), 409–419.

Lim, D. et al. (2006) The effect of the loading condition corresponding to functional shoulder activities on trabecular architecture of glenoid. *Journal of biomechanical engineering*. [Online] 128 (2), 250–258.

Limb, D. & McMurray, D. (2005) Dislocation of the glenoid fossa. *Journal of Shoulder and Elbow Surgery*. [Online] 14 (3), 338–339.

Liu, X. S. et al. (2006) Quantification of the roles of trabecular microarchitecture and trabecular type in determining the elastic modulus of human trabecular bone. *Journal of Bone and Mineral Research*. [Online] 21 (10), 1608–1617.

Lycett, S. J. & Collard, M. (2005) Do homoiologies impede phylogenetic analyses of the fossil hominids? An assessment based on extant papionin craniodental morphology. *Journal of Human Evolution*. [Online] 49 (5), 618–642.

Macchiarelli, R. et al. (1999) Hip bone trabecular architecture shows uniquely distinctive locomotor behaviour in South African australopithecines. *Journal of Human Evolution*. [Online] 36 (2), 211–232.

Matsen, F. A. et al. (2008) Glenoid component failure in total shoulder arthroplasty. *Journal of Bone and Joint Surgery*. [Online] 90 (4), 885–896.

Matsuoka, T. et al. (2005) Neural crest origins of the neck and shoulder. *Nature*. [Online] 436 (7049), 347–355.

McClure, J. G. & Raney, R. B. (1975) Anomalies of the scapula. *Clinical Orthopaedics and Related Research*. (110), 22–31.

McGonnell, I. M. (2001) The evolution of the pectoral girdle. *Journal of Anatomy*. 199 (Pt 1-2), 189–194.

Mimar, R. et al. (2008) Evaluation of the mechanical and architectural properties of glenoid bone. *Journal of Shoulder and Elbow Surgery*. [Online] 17 (2), 336–341.

Moore, K. L. & Persaud, T. (1998) *Essentials of Embryology and Birth Defects*. 5 edition. Philadelphia: W.B. Saunders Company.

Müller, J. et al. (2010) Homeotic effects, somitogenesis and the evolution of vertebral numbers in recent and fossil amniotes. *Proceedings of the National Academy of Sciences of the United States of America*. [Online] 107 (5), 2118–2123.

Mysorekar, V. R. (1967) Diaphysial nutrient foramina in human long bones. *Journal of Anatomy*. 101 (Pt 4), 813–822.

Nixon, J. E. (1983) Avascular necrosis of bone: a review. *Journal of the Royal Society of Medicine*. 76 (8), 681.

Noback, C. R. (1943) Some gross structural and quantitative aspects of the developmental anatomy of the human embryonic, fetal and circumnatal skeleton. *The Anatomical Record*. [Online] 87 (1), 29–51.

Noback, C. R. (1944) The developmental anatomy of the human osseous skeleton during the embryonic, fetal and circumnatal periods. *The Anatomical Record*.

[Online] 88 (1), 91–125.

Nuzzo, S. et al. (2003) Microarchitectural and physical changes during fetal growth in human vertebral bone. *Journal of Bone and Mineral Reseach*. [Online] 18 (4), 760–768.

O'Rahilly, R. & Gardner, E. (1972) The initial appearance of ossification in staged human embryos. *The American journal of anatomy*. [Online] 134 (3), 291–301.

Odgaard, A. (1997) Three-dimensional methods for quantification of cancellous bone architecture. *Bone*. 20 (4), 315–328.

Ogden, J. A. & Phillips, S. B. (1983) Radiology of postnatal skeletal development. VII. The scapula. *Skeletal radiology*. 9 (3), 157–169.

Oxnard, C. E. (1968) The architecture of the shoulder in some mammals. *Journal of Morphology*. [Online] 126 (3), 249–290.

Palastanga, N. et al. (2007) *Anatomy and human movement*. 5 edition. London: Elsevier.

Parfitt, A. M. et al. (1987) Bone histomorphometry: standardization of nomenclature, symbols, and units. *Jounral of Bone and Mineral Research*. [Online] 2 (6), 595–610.

Pettifor, J. M. & Zlotkin, S. (2004) *Micronutrient Deficiencies During the Weaning Period and the First Years of Life*. Vol. 54. Basel: Karger.

Pothuaud, L. et al. (2002) Combination of topological parameters and bone volume fraction better predicts the mechanical properties of trabecular bone. *Journal of Biomchanics*. 35 (8), 1091–1099.

Prescher, A. (2000) Anatomical basics, variations, and degenerative changes of the shoulder joint and shoulder girdle. *European journal of radiology*. 35 (2), 88–102.

Reissis, D. & Abel, R. L. (2012) Development of fetal trabecular micro-architecture in the humerus and femur. *Journal of Anatomy*. [Online] 220 (5), 496–503.

Remy, É. & Thiel, É. (2002) Medial axis for chamfer distances: computing look-up tables and neighbourhoods in 2D or 3D. *Pattern Recognition Letters*. 23649–661.

Richardson, M. L. & Montana, M. A. (1985) Nutrient canals of the ilium: A normal variant simulating disease on computed tomography. *Skeletal radiology*. [Online] 14 (2), 117–120.

Rincón-Kohli, L. & Zysset, P. K. (2009) Multi-axial mechanical properties of human trabecular bone. *Biomechanics and Modeling in Mechanobiology*. [Online] 8 (3), 195–208.

Rissech, C. & Black, S. (2007) Scapular development from the neonatal period to skeletal maturity: A preliminary study. *International Journal of Osteoarchaeology*. [Online] 17 (5), 451–464.

Romer, A. S. (1956) *The Osteology of the Reptiles*. Malabar, FL, USA: Krieger Publishing Company.

Romer, A. S. & Parsons, T. S. (1977) *The Vertebrate Body*. 5 edition. Philidelphia: W.B.

Saunders.

Rook, L. et al. (1999) Oreopithecus was a bipedal ape after all: evidence from the iliac cancellous architecture. *Proceedings of the National Academy of Sciences of the United States of America*. 96 (15), 8795–8799.

Ryan, T. M. & Ketcham, R. A. (2002) Femoral head trabecular bone structure in two omomyid primates. *Journal of Human Evolution*. 43 (2), 241–263.

Ryan, T. M. & Krovitz, G. E. (2006) Trabecular bone ontogeny in the human proximal femur. *Journal of Human Evolution*. [Online] 51 (6), 591–602.

Saunders, S. et al. (1993) Diaphyseal growth in a nineteenth century skeletal sample of subadults from St Thomas' church, Belleville, Ontario. *International Journal of Osteoarchaeology*. [Online] 3 (4), 265–281.

Sánchez-Villagra, M. R. & Maier, W. (2006) Homologies of the mammalian shoulder girdle: a response to Matsuoka et al. (2005). *Evolution and Development*. [Online] 8 (2), 113–115.

Scheuer, L. & Black, S. M. (2000) *Developmental Juvenile Osteology*. 1st edition. London: Elsevier Academic Press.

Schrumpf, M. et al. (2011) The glenoid in total shoulder arthroplasty. *Current Reviews in Musculoskeletal Medicine*. [Online] 4 (4), 191–199.

Singh, M. K. et al. (2005) The T-box transcription factor Tbx15 is required for skeletal development. *Mechanisms of development*. [Online] 122 (2), 131–144.

Sirang, H. (1973) [Canalis alae ossis ilii and its significance]. *Anatomischer Anzeiger*. 133 (3), 225–238.

Smith, M. J. et al. (2006) Osteonecrosis of the glenoid. A case report. *The journal of bone and joint surgery*. [Online] 88 (8), 1836–1839.

Starck, J. M. & Chinsamy, A. (2002) Bone microstructure and developmental plasticity in birds and other dinosaurs. *J Morphol*. [Online] 254 (3), 232–246.

Stewart, T. D. (1934) Sequence of epiphyseal union, third molar eruption and suture closure in Eskimos and American Indians. *American Journal of Physical Anthropology*. [Online] 19 (3), 433–452.

Strauss, E. J. et al. (2009) The glenoid in shoulder arthroplasty. *Journal of Shoulder and Elbow Surgery*. [Online] 18 (5), 819–833.

Tamura, K. et al. (2001) Evolutionary aspects of positioning and identification of vertebrate limbs. *Journal of Anatomy*. 199 (Pt 1-2), 195–204.

Tanck, E. et al. (2001) Increase in bone volume fraction precedes architectural adaptation in growing bone. *Bone*. 28 (6), 650–654.

Terry, G. C. & Chopp, T. M. (2000) Functional anatomy of the shoulder. *Journal of athletic training*. 35 (3), 248–255.

Thomason, J. J. (1985) JSTOR: Paleobiology, Vol. 11, No. 3 (Summer, 1985), pp. 323-335. *Paleobiology*.

Treece, G. M. & Gee, A. H. (2012) *Stradwin*.

Treece, G. M. et al. (2010) High resolution cortical bone thickness measurement from clinical CT data. *Medical Image Analysis*. [Online] 14 (3), 276–290.

Verhulst, J. & Creeger, C. E. (2003) *Developmental dynamics in humans and other primates*. New York: Adonis Press.

Vickaryous, M. K. & Hall, B. K. (2006) Homology of the reptilian coracoid and a reappraisal of the evolution and development of the amniote pectoral apparatus. *Journal of Anatomy*. [Online] 208 (3), 263–285.

Volpato, V. (2008) Morphogenèse de l'endostructure osseuse de l'ilion humain. *Comptes Rendus Palevol*. [Online] 7 (7), 463–471.

Wake, M. H. (1992) *Hyman's Comparative Vertebrate Anatomy*. Chicago: University of Chicago Press.

Warner, S. E. et al. (2006) Adaptations in cortical and trabecular bone in response to mechanical loading with and without weight bearing. *Calcified Tissue International*. [Online] 79 (6), 395–403.

Weichert, C. K. & Presh, W. (1975) *Elements of Chordate Anatomy*. 4 edition. New York: McGraw-Hill Book Company.

Young, N. M. (2008) A comparison of the ontogeny of shape variation in the anthropoid scapula: functional and phylogenetic signal. *American Journal of Physical Anthropology*. [Online] 136 (3), 247–264.

Appendix A: Gradient Mapped Radiographs

Group 1

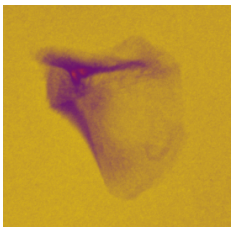
SC-371

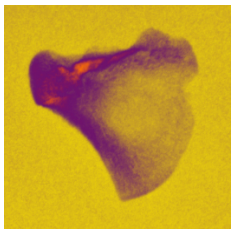
SC-089

Group 2

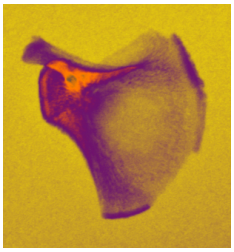
SC-096

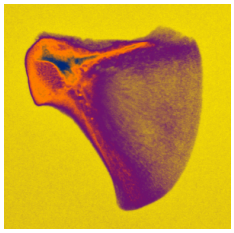
SC-017

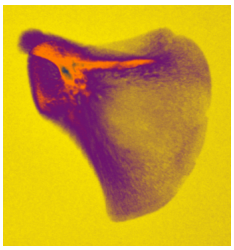
SC-097

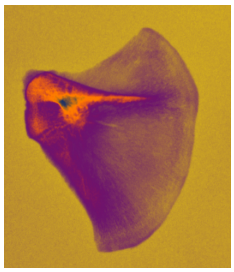
SC-082

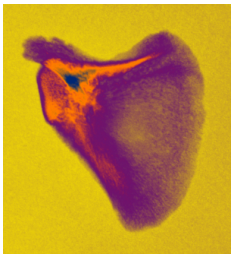
SC-020

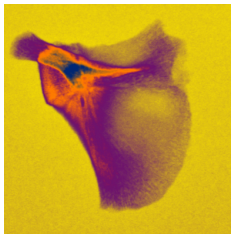
SC-170

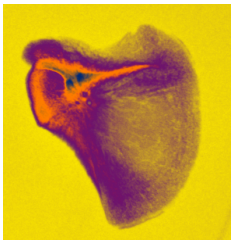
SC-161

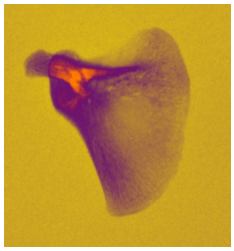
SC-370

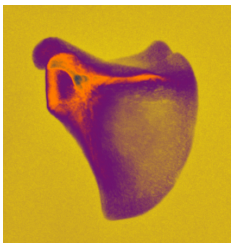
SC-086

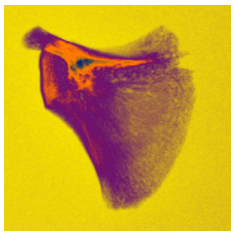
SC-158

Group 3

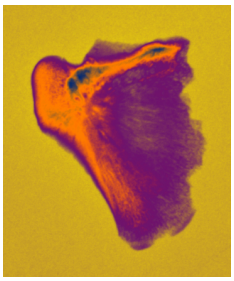
SC-083

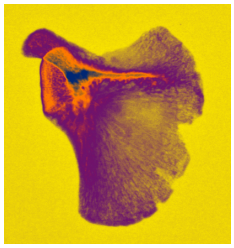
SC-085

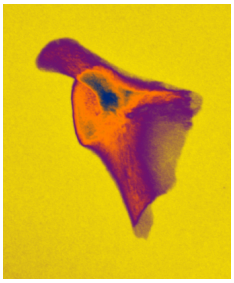
SC-157

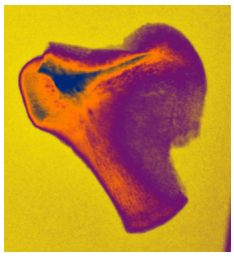
SC-016

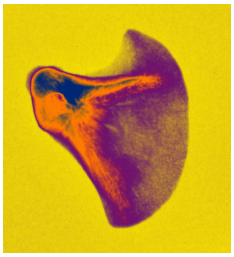
SC-088

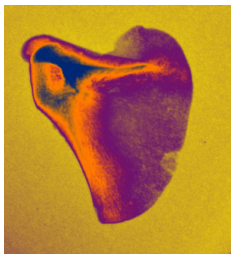
SC-084

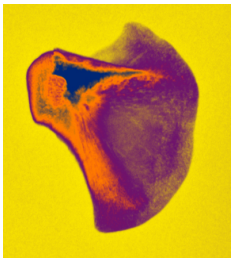
SC-087

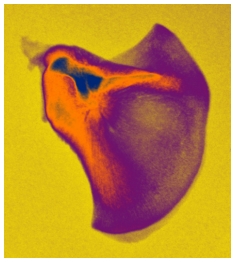
SC-369

Group 4

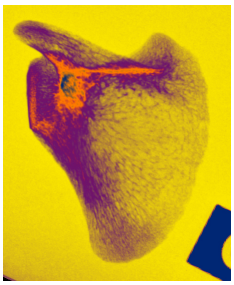
SC-021

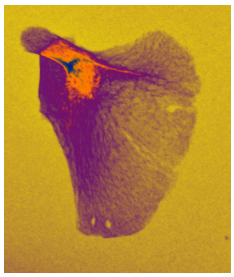
SC-091

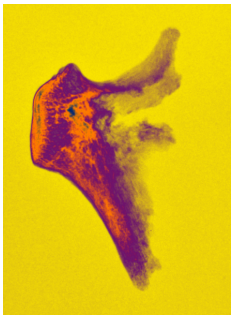
SC-023

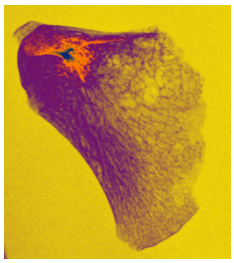
SC-147

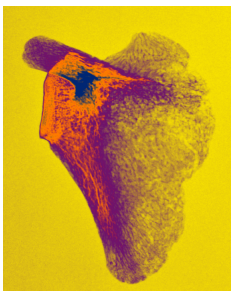
SC-141

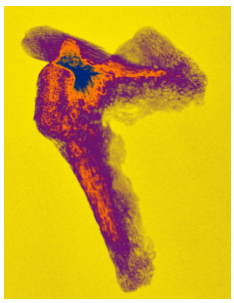
SC-024

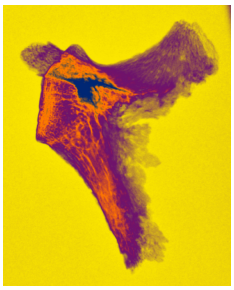
SC-024

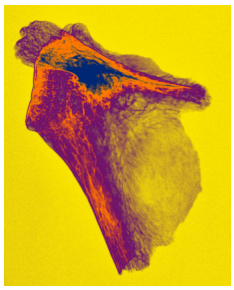
SC-172

Group 5

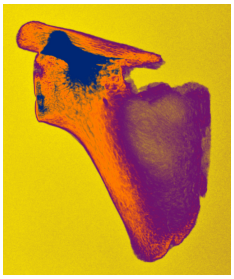
SC-257

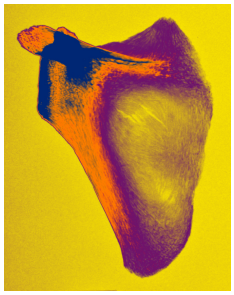
SC-131

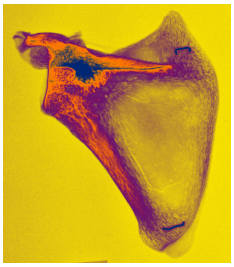
SC-090

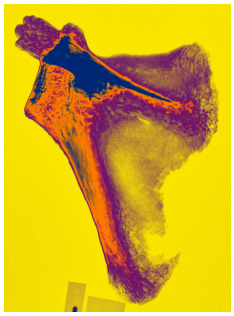
SC-029

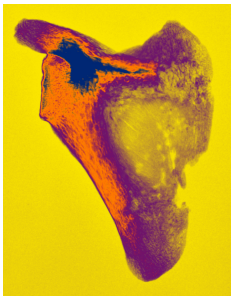
SC-026

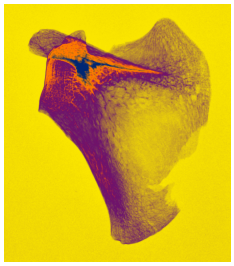
SC-159

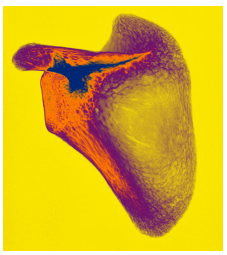
SC-027

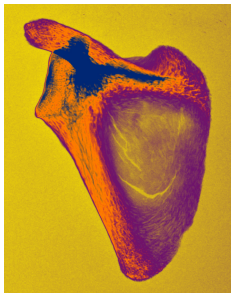
SC-258

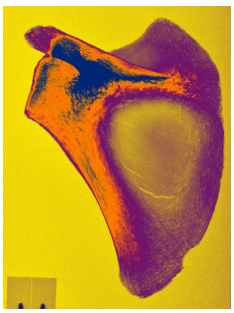
SC-259

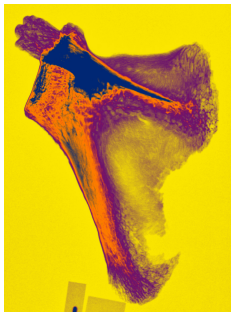
SC-029

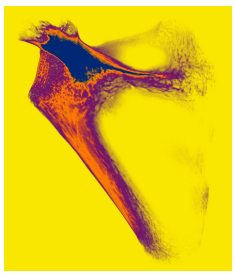
SC-031

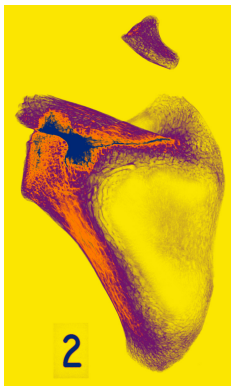

SC-001

Group 6

SC-260

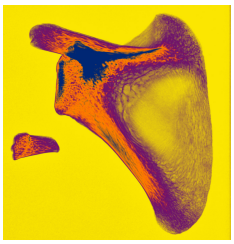

SC-095

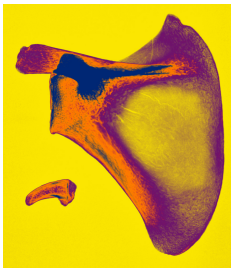

SC-132

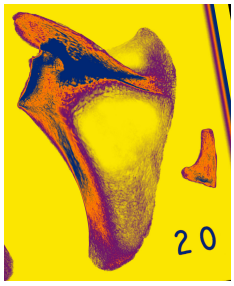

SC-171

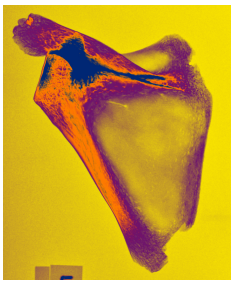

SC-175

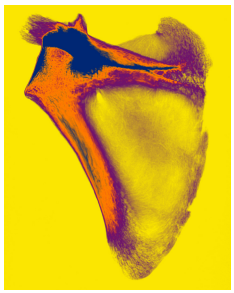

SC-030

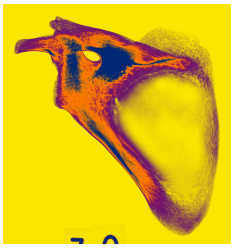

SC-013

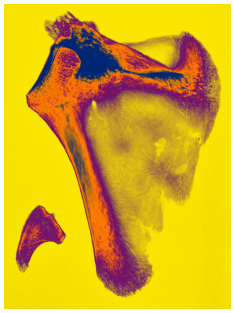

SC-133

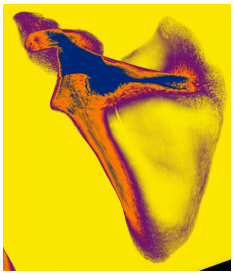

SC-094

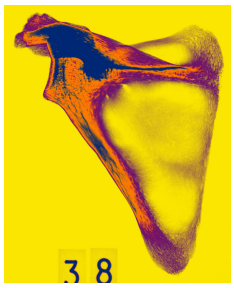

SC-105

Group 7

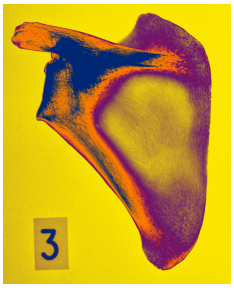

SC-255

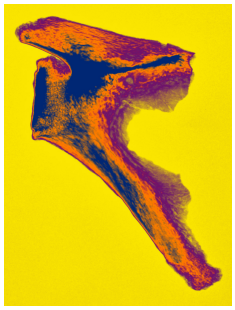
SC-014

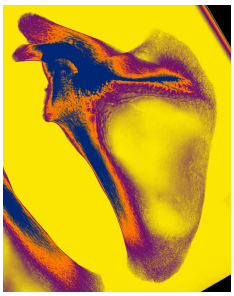
SC-098

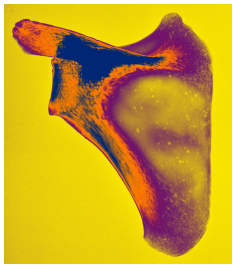
SC-032

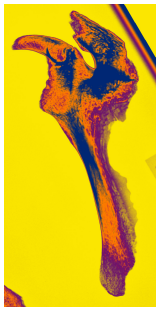
SC-018

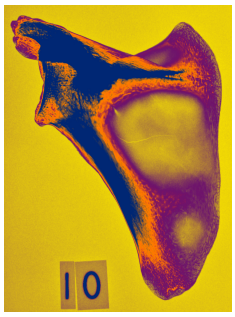

SC-033

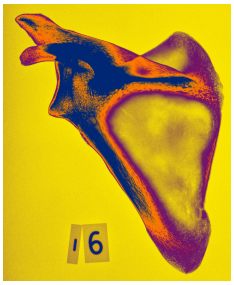

SC-038

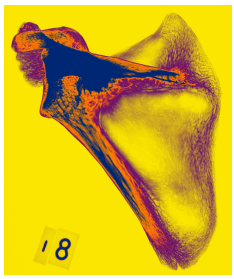

SC-099

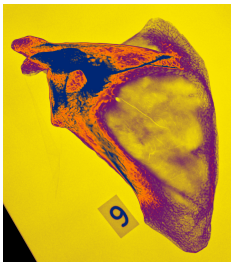

SC-100

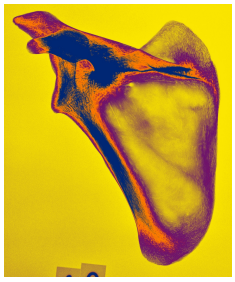
SC-102

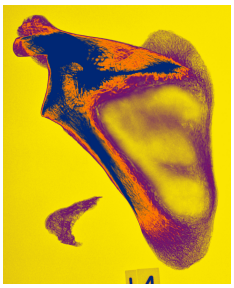
SC-104

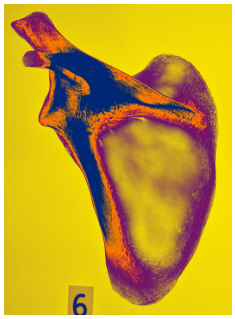

SC-106

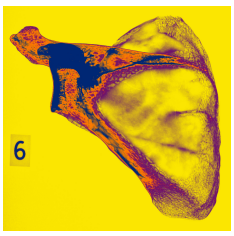

F

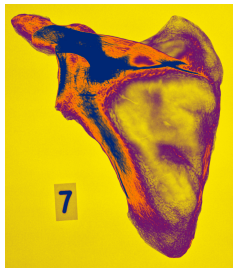

G

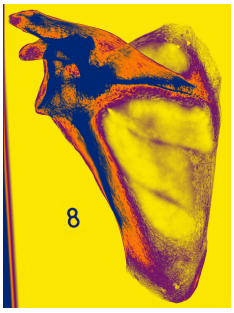

H

Group 8

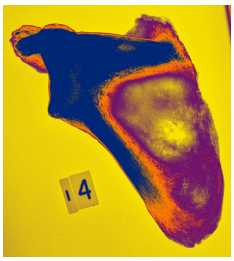

SC-034

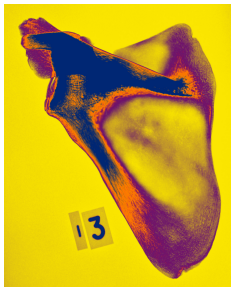

SC-134

SC-375

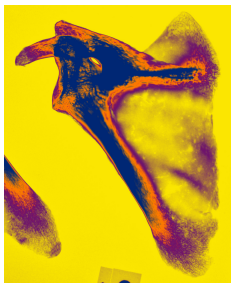

SC-036

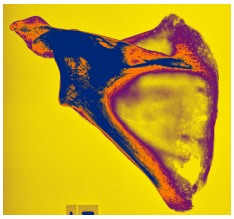

SC-037

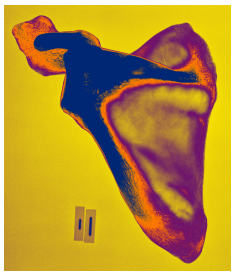

SC-035

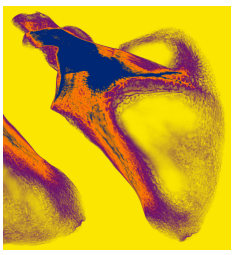

SC-101

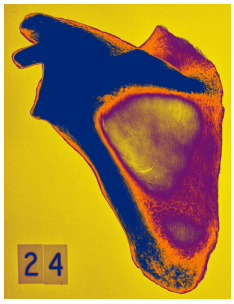

SC-138

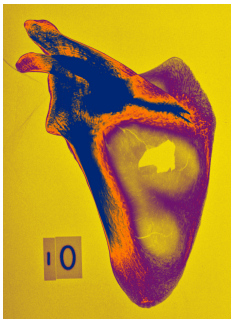

SC-103

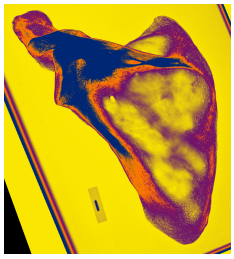

A

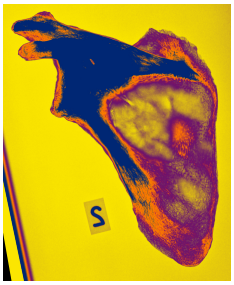

B

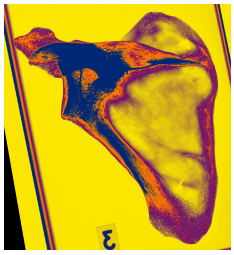

C

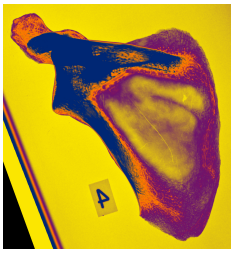

D

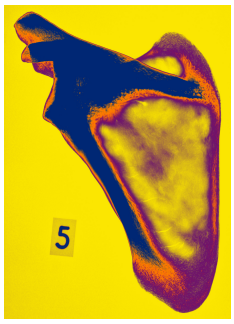

E

Appendix B: Anthropometric Data

SPECIMEN	SIDE	AGE	CONDITION (according to database)	Measurements (mm)								
				Length of glenoid surface	Middle diameter of the glenoid surface	Length of glenoidal mass	Spine length	Scapular width	Scapular length	Infra-scapular height	Supra-scapular height	Acromial width	Scapular index
SC-086	L	PERINATE	COMPLETE	8.41	6.43	12	31.58	27.94	34.5	29.45	13.79	2.74	80.99
SC-021	L	5 MONTHS	COMPLETE	13.11	9.45	17.08	40.77	35.81	48.74	38.92	21.89	3.72	73.47
SC-082	L	PERINATE	PARTIAL/FRAGMENTED	9.07	6.6	11.28			33.9				
SC-083	L	PERINATE	PARTIAL/FRAGMENTED	8.62	6.72	11.84							
SC-084	L	PERINATE	COMPLETE	7.53	6.81	11.62	30.55	27.16	33.99	29.53	13.3	3.24	79.91
SC-085	L	PERINATE	COMPLETE	9.78	6.74	13.09	34.15	29.67	37.46	31.55	15.78	3.51	79.20
SC-087	L	PERINATE	COMPLETE	9.11	6.54	13.2		29.34	36.39	30.77	17.01		80.63
SC-088	L	PERINATE	COMPLETE	8.74	6.26	12.06	29.88	28.19	36.26	30.16	15	3.36	77.74
SC-015	L	PERINATE	PARTIAL/FRAGMENTED	7.68	5.51	10.83							
SC-017	L	PERINATE	COMPLETE	9.37	6.22	11.66		29.43		29.7			
SC-097	L	PERINATE	COMPLETE	8.72	5.13	11.21	29.96	27.47	30.55	25.93	12.46	3.64	89.92
SC-020	L	NEONATE	COMPLETE	7.95	5.51	10.97	30.8	29.06	34.15	29.91	12.85	3.25	85.10
SC-091	L	4-6 MONTHS	COMPLETE	11.42	6.38	14.94	34.17	29.76	38.92	32.97	14.53	3.27	76.46
SC-092	L	PERINATE	COMPLETE	9.88	6.15	13.39	34.02	31.91	42	33.54	16.89	3.49	75.98
SC-170	L	PERINATE	COMPLETE	9.17	5.81							3.3	
SC-158	L	0-6 MONTHS	COMPLETE	8.45	5.45	11.33	29.72	26.08	32.1	26.56	11.02	3.02	81.25
SC-161	L	PERINATE	COMPLETE	8.53	6.69	12.21	31.86	29.25	35.61	29.75	14.51	3.67	82.14
SC-021	R	5 MONTHS	COMPLETE	14.89	9.27	16.95	43.88	35.83	48.25	39.9	18.09	4.46	74.26
SC-082	R	PERINATE	COMPLETE	8.89	5.87	11.38	29.96	27.27		27.14		3.09	
SC-083	R	PERINATE	PARTIAL/FRAGMENTED	9.44	6.8	11.87		29.01	34.35	31.96	12.45		84.45
SC-084	R	PERINATE	COMPLETE	8.68	6.47	11.75	30.08	27.29	33.29	28.19	12.36	2.98	81.98
SC-085	R	PERINATE	COMPLETE	10.52	6.19	13.24		28.21		30.6			
SC-086	R	PERINATE	PARTIAL/FRAGMENTED	8.89	6.41	11.99	31.72	27.5	34.52	28.99	14.25	3.08	79.66
SC-087	R	PERINATE	COMPLETE	10.2	6.31	12.84		28.68	36.09	29.77	15.91		79.47
SC-088	R	PERINATE	COMPLETE	9.08	5.97	11.35	28.87	27.9	35.56	29.51	15.07	3.42	78.46
SC-016	R	PERINATE	COMPLETE	8.9	5.76	11.88	30.88	27.57	31.78	28.46	12.95	3.31	86.75
SC-017	R	PERINATE	COMPLETE	9.32	5.9	11.8	33.12	29.08		29.05		2.76	
SC-097	R	PERINATE	COMPLETE	8.21	5.14	10.77	29.39	27.37	30.98	26.66	12.55	3.58	88.35
SC-020	R	NEONATE	COMPLETE	9.18	4.89	11.56	29.9	27.78	34.15	28.24	12.56	3.34	81.35
SC-091	R	4-6 MONTHS	COMPLETE	10.73	6.24	14.08	37.06	31.84	37.77	32.55	15.66	3.48	84.30
SC-092	R	PERINATE	COMPLETE	8.3	6.21	12.93	34.77	31.74	39.56	32.51	17.51	3.07	80.23
SC-166	R	0-6 MONTHS	COMPLETE										
SC-170	R	PERINATE	COMPLETE	9.54	5.43	12.37	31.87	27.5	33.93	28.03	12.32	3.07	81.05
SC-157	R	PERINATE	PARTIAL/FRAGMENTED	9.3	6.24	12.55						3.26	
SC-158	R	0-6 MONTHS	COMPLETE	8.65	5.65	11.54	31.47	27.48	32.7	27.18	12.51	3.18	84.04
SC-161	R	PERINATE	COMPLETE	10.65	6.51	12.22	31.34	28.89	36	28.09	14.22	4.16	80.25
SC-089	L	28 G.W.	PARTIAL/FRAGMENTED	5.22	3.44	6.95		19.26		18.88			
SC-089	R	28 G.W.	PARTIAL/FRAGMENTED	5.32	3.37	6.91		19.19		18.73			
SC-096	L	32 G.W.	COMPLETE	6.23	4.41	9.02	23.04	22.83	27.35	23.73	8.83	2.67	
SC-096	R	32 G.W.	COMPLETE	6.3	4.62	8.8	26.19	22.32	25.69	23.27	11.87	2.38	86.88

Figure A1: Raw anthropometric data

Specimen	Old Number	Side	Condition	Age (years)									
				via glenoidal surface	via glenoidal surface	via glenoidal mass	via scapular length	via infra-scapular height	via spine length	via scapular width	via supra-scapular height	via acromial width	Average
SC-083	SAB	L	COMPLETE	-1.07	0.36	-1.08							-0.60
SC-084	SAD	L	COMPLETE	-1.76	0.44	-1.18	-0.28	-0.15	-0.76	-0.37	0.22	-1.74	-0.62
SC-085	SAE	L	COMPLETE	-0.34	0.38	-0.53	0.20	0.24	-0.24	0.29	1.53	-1.47	0.01
SC-087	SAG	L	COMPLETE	-0.76	0.20	-0.48	0.05	0.09		0.20	2.18		0.21
SC-088	SAJ	L	COMPLETE	-1.00	-0.03	-0.99	0.03	-0.03	-0.86	-0.10	1.12	-1.62	-0.38
SC-015	LTHE	L	PARTIAL/FRAGMENTED	-1.67	-0.68	-1.53							-1.29
SC-017	LTHG	L	COMPLETE	-0.60	-0.07	-1.16		-0.11		0.22			-0.34
SC-097	STHB2	L	COMPLETE	-1.01	-1.00	-1.36	-0.77	-0.83	-0.84	-0.29	-0.23	-1.34	-0.85
SC-020	P1	L	COMPLETE	-1.50	-0.68	-1.47	-0.26	-0.07	-0.72	0.13	-0.02	-1.73	-0.70
SC-092	SS3	L	COMPLETE	-0.27	-0.13	-0.40	0.84	0.62	-0.26	0.87	2.12	-1.49	0.21
SC-170	"POPPY"	L	COMPLETE	-0.72	-0.42							-1.68	-0.94
SC-161	L1978	L	COMPLETE	-1.13	0.33	-0.92	-0.06	-0.10	-0.57	0.18	0.86	-1.31	-0.30
SC-082	SAA	R	COMPLETE	-0.90	-0.37	-1.29		-0.60	-0.84	-0.34		-1.88	-0.89
SC-083	SAB	R	PARTIAL/FRAGMENTED	-0.55	0.43	-1.07	-0.23	0.32		0.11	-0.23		-0.18
SC-084	SAD	R	COMPLETE	-1.03	0.15	-1.12	-0.38	-0.40	-0.83	-0.34	-0.28	-1.99	-0.69
SC-085	SAE	R	COMPLETE	0.13	-0.09	-0.47		0.06		-0.10			-0.09
SC-086	SAF	R	PARTIAL/FRAGMENTED	-0.90	0.09	-1.02	-0.21	-0.25	-0.59	-0.28	0.72	-1.89	-0.48
SC-087	SAG	R	COMPLETE	-0.07	0.01	-0.64	0.01	-0.10		0.03	1.60		0.12
SC-088	SAJ	R	COMPLETE	-0.78	-0.28	-1.30	-0.06	-0.15	-1.00	-0.18	1.15	-1.56	-0.46
SC-015	LTHE	R	PARTIAL/FRAGMENTED										
SC-016	LTHF	R	COMPLETE	-0.90	-0.46	-1.06	-0.59	-0.35	-0.71	-0.26	0.03	-1.67	-0.66
SC-017	LTHG	R	COMPLETE	-0.63	-0.34	-1.10		-0.24	-0.39	0.13		-2.21	-0.68
SC-097	STH/B2	R	COMPLETE	-1.33	-0.99	-1.55	-0.71	-0.69	-0.93	-0.32	-0.18	-1.40	-0.90
SC-020	P1	R	COMPLETE	-0.72	-1.21	-1.21	-0.26	-0.39	-0.85	-0.21	-0.17	-1.64	-0.74
SC-092	SS3	R	COMPLETE	-1.28	-0.08	-0.60	0.50	0.42	-0.15	0.83		-1.90	-0.28
SC-170	"POPPY"	R	COMPLETE	-0.49	-0.74	-0.85	-0.29	-0.43	-0.57	-0.28	-0.30	-1.90	-0.65
SC-157	E3Z/82	R	PARTIAL/FRAGMENTED	-0.64	-0.05	-0.77						-1.72	-0.79
SC-161	L1978	R	COMPLETE	0.22	0.18	-0.92	0.00	-0.42	-0.64	0.08	0.71	-0.84	-0.18

Figure A2: Age regression data based on anthropometric measurements.

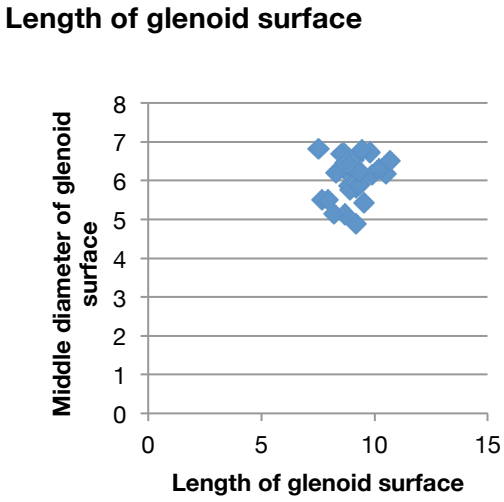

Figure A3: Length of the glenoid surface/middle diameter of the glenoid surface

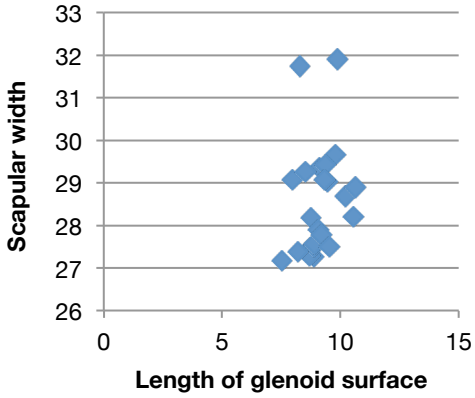

Figure A4: Length of the glenoid surface/scapular width

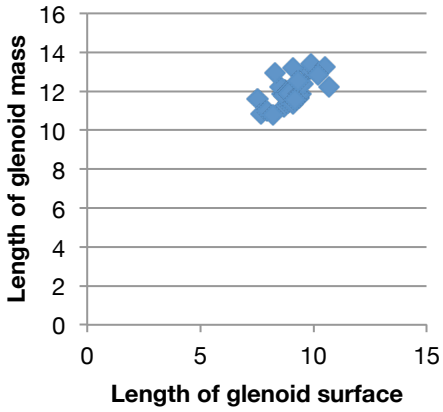

Figure A5: Length of the glenoid surface/length of the glenoid mass

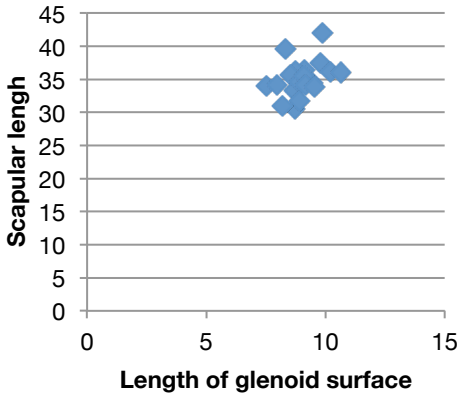

Figure A6: Length of the glenoid surface/scapular length

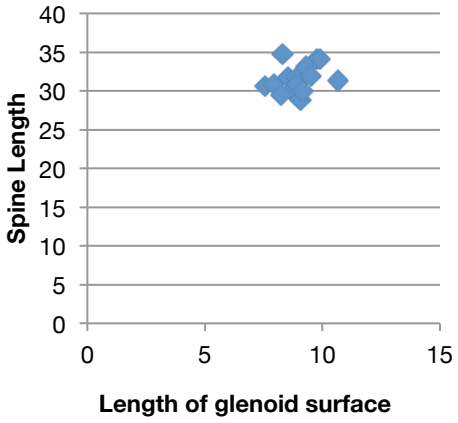

Figure A7: Length of the glenoid surface/spine length

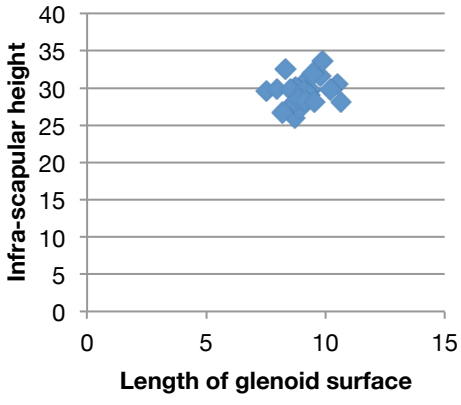

Figure A8: Length of the glenoid surface/infrascapular height

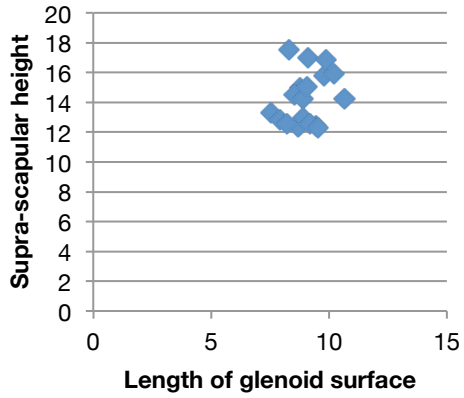

Figure A9: Length of the glenoid surface/suprascapular height

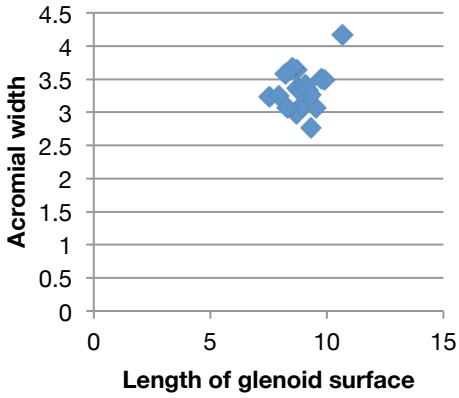

Figure A10: Length of the glenoid surface/acromial width.

Middle Diameter of the glenoid

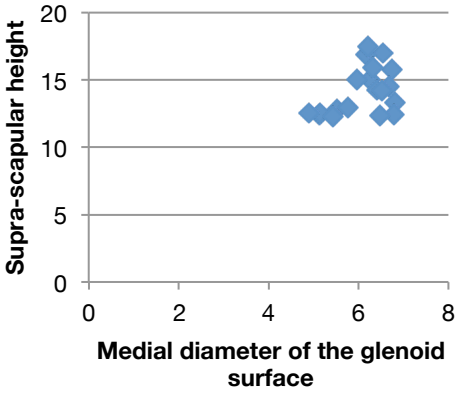

Figure A11: Medial diameter of the glenoid surface/suprascapular height

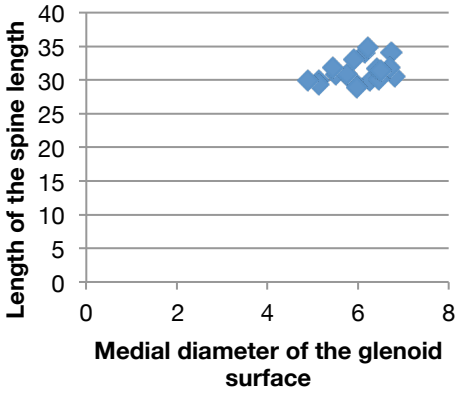

Figure A12: Medial diameter of the glenoid surface/spine length

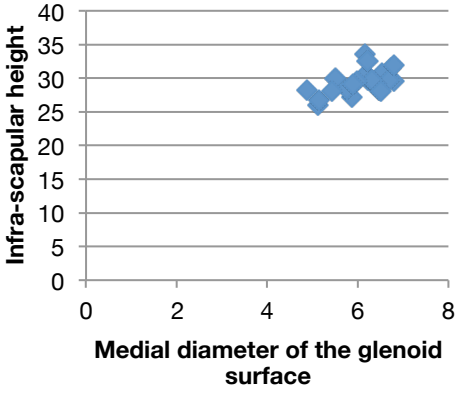

Figure A13: Medial diameter of the glenoid surface/infrascapular height

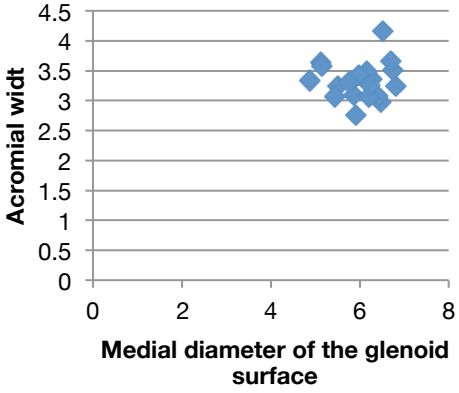

Figure A14: Medial diameter of the glenoid surface/acromial width

Figure A15: Length of the glenoid mass/spine length

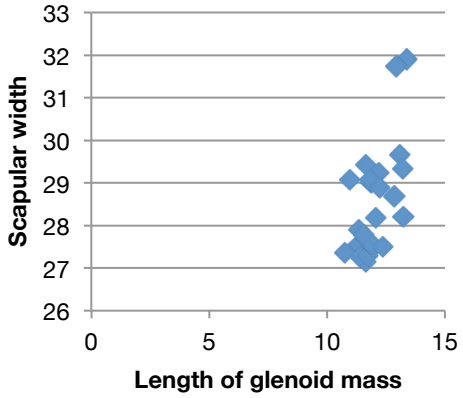

Figure A16: Length of glenoid mass/scapular width

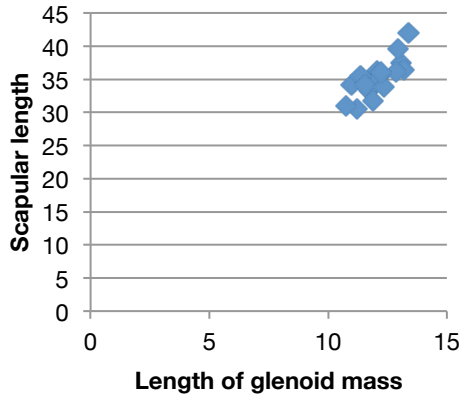

Figure A17: Length of the glenoid mass/scapular length

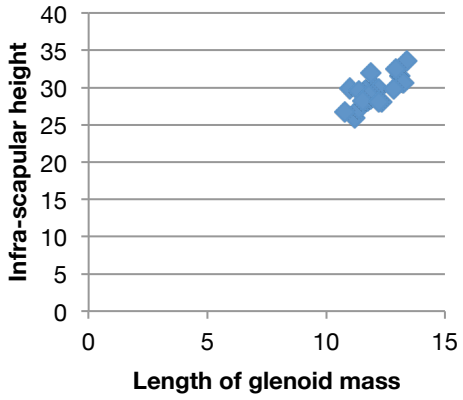

Figure A18: Length of the glenoid mass/infrascapular height

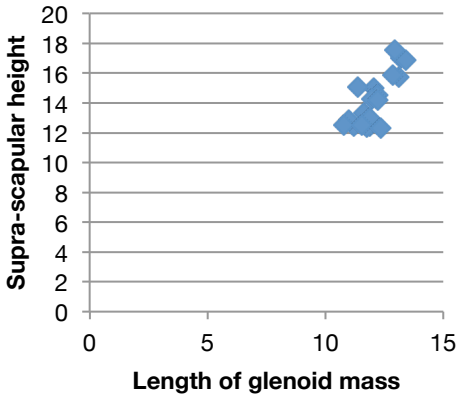

Figure A19: Length of the glenoid mass/qsuprascapular height

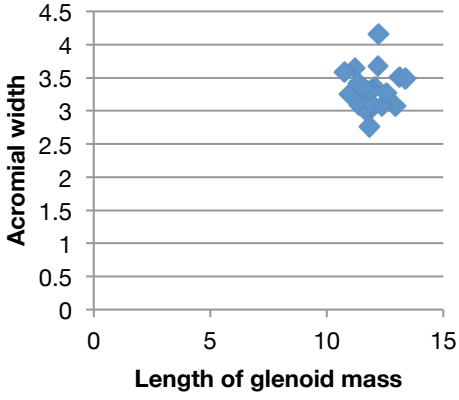

Figure A20: Length of the glenoid mass/acromial width

Spine length

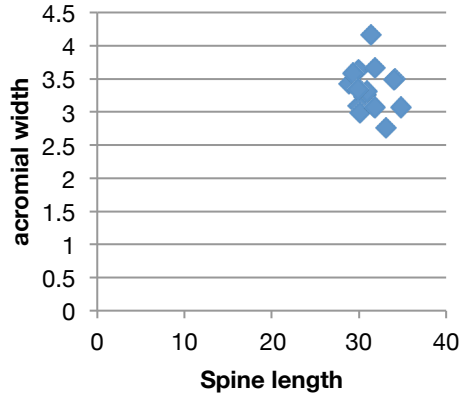

Figure A21: Spine length/acromial width

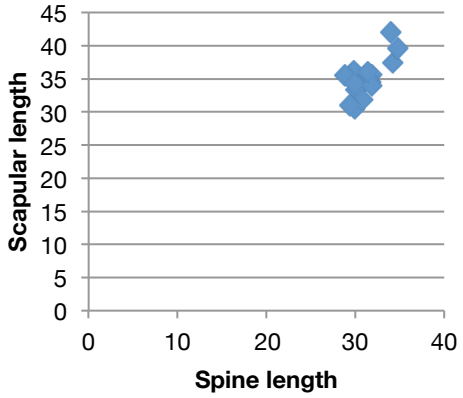

Figure A22: Spine length/scapular length

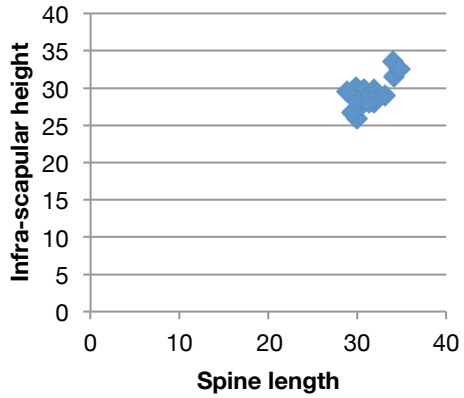

Figure A23: Spine length/infrascapular height

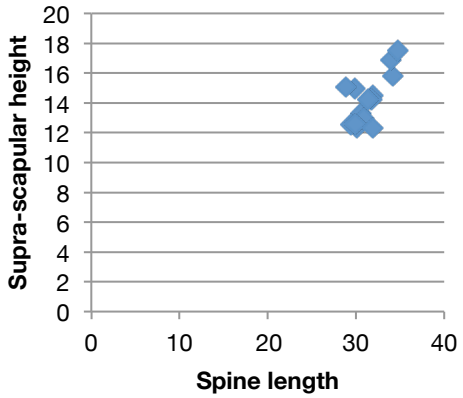

Figure A24: Spine length/suprascapular height

Scapular width

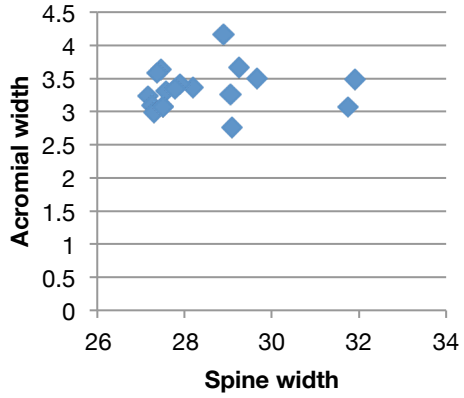

Figure A25: Scapular width/acromial width

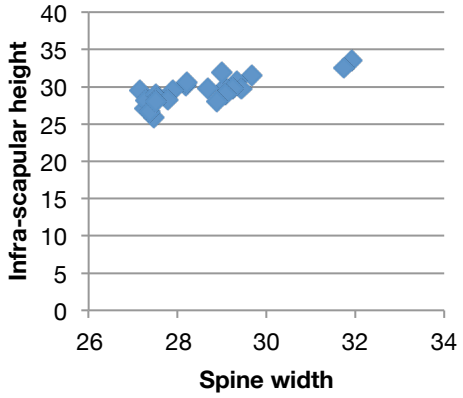

Figure A26: Scapular width/infrascapular height

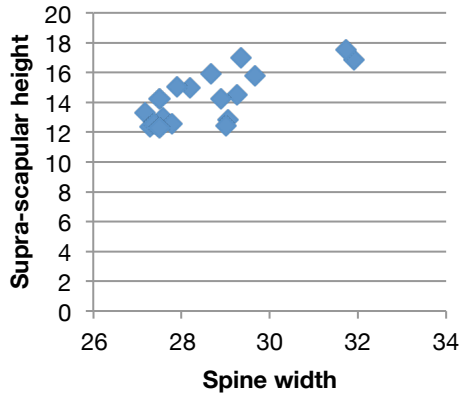

Figure A27: Spine width/suprascapular height

Scapular length

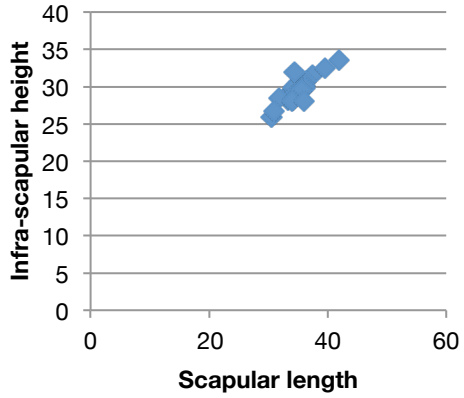

Figure A28: Scapular length/infrascapular height

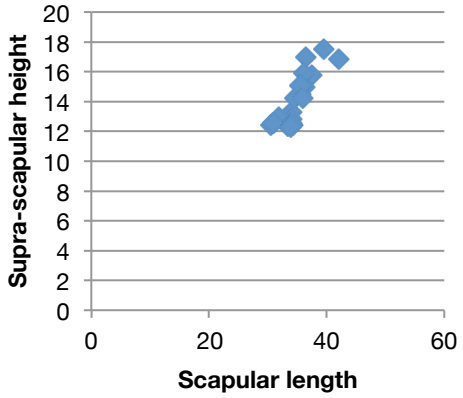

Figure A29: Scapular length/suprascapular height

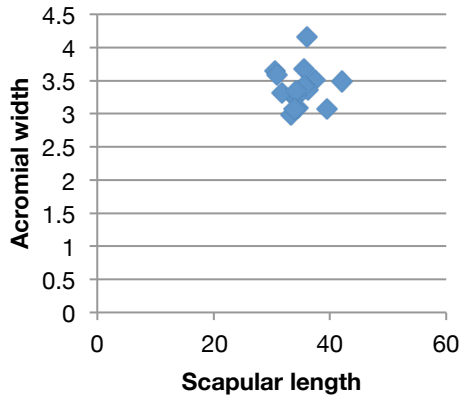

Figure A30: Scapular length/acromial width

Infrascapular height

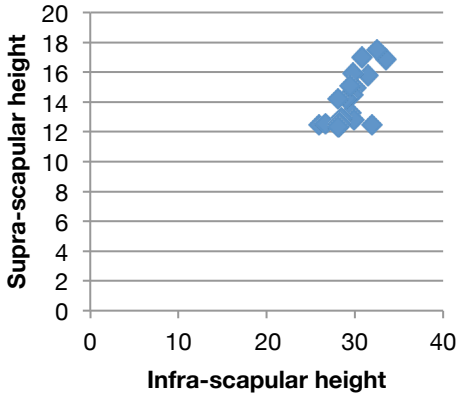

Figure A31: Infrascapular height/supra-scapulr height

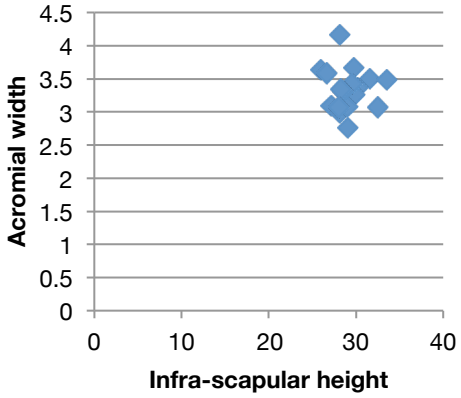

Figure A32: Infrascapular height/acromial width

Suprascapular height

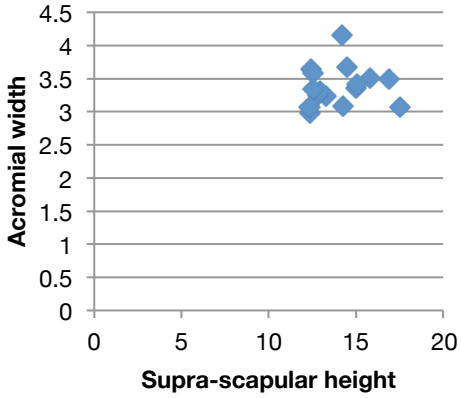

Figure A33: Suprascapular height/acromial width

Appendix C: Stereoscopic Data

Bone Volume Fraction (BV/TV)

	1	2	3	4	5	6	7	8	9	10	11	12
SC-016-R	41.41782	40.61249	34.7208	36.28277		36.89725	32.35796	33.98899	28.93692	37.71755	27.11755	30.08725
SC-017-L	38.76325	37.47025	40.01865	42.72568	33.79975	31.32413	27.4318	23.39412			30.07442	29.86789
SC-017-R	38.86588	37.86516	41.39252	35.70861	30.02656	22.72311	19.64287	22.14638	41.45443	31.66063	36.7236	31.53231
SC-020-L	38.59519	39.92212	37.6981	38.96082	33.96138	25.0693	27.68594	26.79381	38.59756	34.29138	29.76817	29.60732
SC-020-R	41.44227	37.61763	41.50573	41.28478	34.25995	22.80443	31.61421	31.04942	39.26068	35.25673	31.03682	28.9099
SC-082-L	36.76875	39.19939	33.51334	36.14874		30.95853	27.23622		38.34694	38.89108	31.13853	28.79113
SC-082-R	37.29755	42.45315	35.60131	31.96764	32.99916	23.00638	28.7615	28.62742	40.99041	38.6856	32.48595	28.64692
SC-083-L	35.14798	37.387	34.62388	39.62192		23.00062	29.26058		40.75231	34.77309	30.64129	27.18221
SC-083-R	35.27681	37.57051	38.29464	38.84386		22.59573	23.62878	19.51137	41.02587	41.6455	32.3231	29.95218
SC-084-L	41.02277	42.81534	39.69725	41.30737	38.28546	27.91617	29.21117	31.22855	39.88131	41.8733	31.49377	29.6049
SC-084-R	42.69178	37.7723	42.93891	40.43304	39.2781	30.41396	28.02758	28.43962	39.82664	42.86039	33.69362	30.85216
SC-085-L	40.88084	40.05901	37.9228	35.18891	36.03076	31.2021	23.1644	29.64751	39.47734	37.13255	30.68319	30.37539
SC-085-R	35.1266	35.47036	34.09908	32.63545	32.74028	26.80793	28.44363	33.59761	37.29235		33.76613	27.4037
SC-086-L	42.00135	35.55336	34.37951	41.20861	28.08894	29.69039	32.84987	32.91116	38.60557	41.24227	33.36331	30.13621
SC-087-L	39.05624	37.36928	35.38179	36.84297	32.11086	26.85897	28.98318	19.47716	34.20207	37.27534	34.4464	28.01346
SC-087-L	39.28588	39.20793	39.08434	35.3887		28.6723	24.8262	37.70152	35.44962	34.5517	30.53021	30.62453
SC-089-L	43.25409	44.94739	42.26088	41.05132							33.09937	30.94242
SC-089-R	38.06027	36.26481	34.49927	36.52818					40.71099		31.08413	31.65716
SC-369-R						32.01674	27.24961		39.64778	38.58825	30.37347	28.31154
SC-370-L	37.95877	41.13502	35.18384	35.6119	36.59398	31.93808	27.5296	24.59617	36.37888	38.91593	30.66382	29.98131
SC-370-R	38.48982	38.91813	31.27669	33.88586	29.27423	31.44996	23.73788	30.23899	36.06122	39.60833	31.195	29.52366
SC-371-L	37.48297	38.32691	34.70629	36.7583	29.28799	33.86832	18.93885	21.23334	36.80341	38.79492	32.44471	27.80168
SC-086-R	39.7678	40.03881	37.26183	38.22511	34.16319	32.42414	26.4832	34.73638	41.14823	37.58264	34.13932	27.11195
SC-088-L	42.62611	41.84445	41.84995	42.03868	34.74534	32.33226	26.76454	33.85008	39.35122	39.26079	30.25096	27.05928
SC-088-R	42.47345	37.7624	38.80374	43.50591	32.64487	32.63996	24.10762	32.46918	36.62811	38.07043	33.60469	27.75696
SC-092-L	40.5116	36.34934	34.24431	36.61142	29.16444	29.80407	28.46772	31.20208	38.74792		34.09877	33.21749
SC-092-R	38.7897	38.92531	34.40823	39.37039	33.84153	34.48941	27.65418	28.60469	38.29741		32.77903	31.35036
SC-096-L	36.30061	38.58095	30.715	34.30472	35.70271	31.14952	24.96943	31.21876	36.90545	41.33373	31.22045	33.7006
SC-096-R	36.73967	34.20434	33.02999	33.67521	32.90734			33.00769	37.65802		31.4608	32.24034
SC-097-L	38.91718	36.92155	39.36921	39.32964	40.0467	31.62042	26.82379	32.90289	36.30926	34.8093	30.79551	29.68228
SC-097-R	36.90176	42.65697	40.89141	40.37453	38.94837	33.69752	28.4792	33.868	37.69347	37.34277	30.26013	29.60455
SC-157-R	36.76503	37.56469	32.92977	32.10684	32.67117	32.72246	24.74068	32.63978				
SC-158-L	37.70016	41.10599	37.26726	36.12885	32.33157	31.83655	26.03681	31.1194		40.99678	29.98782	30.98575
SC-158-R	35.52514	40.9608	39.23568	34.9616		33.04161	28.35019	31.21261	37.888	41.77104	29.15404	29.71659
SC-161-L	39.827	34.60846	37.57006	35.42234	26.68001	33.04161	28.35019	31.21261	36.78623	41.68451	31.94948	31.63129
SC-161-R	39.68402	36.24523	38.31292	35.79895	31.82894	32.56068	26.78376	33.36983	40.27686	39.91919	33.46894	29.28036
MEAN	38.897603	38.734481	36.991114	37.435418	33.422725	30.017412	26.927065	29.870875	38.168515	38.447704	31.7519	29.804087
STD DEV	2.3078377	2.4914123	3.2429582	3.1205496	3.4161581	3.8596667	3.0267876	4.6504977	2.5070657	2.7992502	1.8530991	1.668639
CoV	6%	6%	9%	8%	10%	13%	11%	16%	7%	7%	6%	6%

Table B1: Raw BV/TV measurements for VOIs 1-12. Individual measurements that are greater than two standard deviations (>2σ) from the mean are highlighted in red.

	13	14	15	16	17	18	19	20	21	22	23
SC-016-R	23.26623	27.61797	32.93605	37.40204		37.61436	45.38312	44.59048	39.29918	39.51492	40.9644
SC-017-L	24.35306	27.12374	32.98032	34.79743	38.09376	36.96586	40.37769	43.56545	36.51418	36.92986	39.49324
SC-017-R	26.0356	30.26971	31.17078	33.31916		37.76406	42.41141	42.42983	36.41346	38.27463	40.63135
SC-020-L	26.56118	30.20982	35.61922	34.72862	34.01384	32.83124	41.0371	44.80957	36.86668	37.43848	40.23156
SC-020-R	25.52183	28.82055	33.8965	36.02571	34.10068	35.96866	42.12101	40.90488	39.21455	40.01773	41.47753
SC-082-L	18.3603	31.90627				33.21118			39.02483		42.1644
SC-082-R	18.13146	32.56657	34.55168		33.14381	32.93307	43.8667	43.28621	42.46561	45.21004	47.00364
SC-083-L	19.00686	29.33339	30.93666		27.71258	34.65816	38.3935	39.99425	40.24095	40.46795	43.88116
SC-083-R	22.578	31.34957	33.8835		27.91599	32.41165	40.90851	43.037	41.29946	42.56304	45.99601
SC-084-L	28.33975	31.00194	31.00757		34.36779	37.36144	43.62787	37.30244	36.62546	46.75434	40.78417
SC-084-R	21.89473	35.31705	33.02972		32.49338	33.43343	41.22827	39.68222	40.88895	45.10762	47.18194
SC-085-L	14.6143	30.4402				21.40259	42.05634	43.77281	37.18164	45.89101	45.24549
SC-085-R	24.89732	34.43114	32.32114		31.22056		40.17337	41.14087	41.51361	44.93712	45.36181
SC-086-L	25.46393	34.01084	34.44957				41.36912		39.0079	41.74078	42.75097
SC-087-L	17.00019	31.7173	35.0276				42.57225	39.72793	40.73811	44.52487	39.6453
SC-087-L	23.5889	31.40049	32.7971			32.43123	41.06476	39.03802	39.40113	41.75564	44.30472
SC-089-L	16.29605	27.45621					40.85126	39.83326	37.91219	39.67365	42.71611
SC-089-R	17.20143	31.20118					43.86319	40.70737	40.07754	39.66221	44.41708
SC-369-R	20.88694	30.22087	34.19905		34.81124		41.91462	39.8812	39.57406	41.39246	42.52306
SC-370-L		33.15699	30.84268		27.28322	31.68435	42.95119	37.07499	38.53449	41.52753	44.49944
SC-370-R	14.99093	32.76042	33.3446		30.97275	34.77085	39.32975	41.95595	39.17998	40.80287	41.57098
SC-371-L	16.24887	27.12188	32.56189			32.54037	41.55152	42.04728	39.19832	43.18045	42.09596
SC-086-R	23.48201	34.22231				31.33196			38.56555		45.27789
SC-088-L	20.52777	34.52806	34.6878	35.96333	35.85872	37.9101	38.75749	43.10673	36.27707	44.95264	43.03505
SC-088-R	13.86047	35.01948	35.46043		26.59144		43.22122	40.3987	39.0416	45.0874	45.30241
SC-092-L	20.83262	30.21235	31.15686			28.31275			37.40304	40.97473	43.15075
SC-092-R	18.00324	29.53573	35.9458		28.85857	24.30927			39.0393	39.53347	46.95175
SC-096-L	17.73906	34.72632	28.56693			33.84271	33.31219	37.67883	38.14001	39.53925	43.1549
SC-096-R	14.98986	32.45054	32.55331			32.00812	40.68793	41.6806	38.7884	45.86701	46.27195
SC-097-L	23.52097	31.67728	31.437		30.1741	35.61187	41.73967	41.37331	41.66528	45.39433	46.96594
SC-097-R	18.91333	31.05453	32.88686			36.05507	41.73225	41.11426	40.24926	44.85773	46.27195
SC-157-R											
SC-158-L	23.59582	31.96265	32.74405		14.35662	25.78023	41.23903	42.81437	34.44976	43.41802	43.50651
SC-158-R	22.37458	33.2648	35.72655		29.71866	34.26885	39.30599	42.58949	38.15824	45.40205	45.92428
SC-161-L	24.08816		34.87022		32.44659	36.63339	42.83077	42.69467	41.41426	43.21194	44.4022
SC-161-R	26.13107	28.2098	29.76958			31.36982	41.91942		41.37592	40.79113	43.99289
MEAN	20.979318	31.361704	33.045367	35.372715	30.743911	33.050594	41.348339	41.318378	39.021142	42.315058	43.689965
STD DEV	4.0135911	2.3523196	1.8588429	1.4040148	5.075516	4.0486695	2.1510026	2.046973	1.8298736	2.7364031	2.2384801
CoV	19%	8%	6%	4%	17%	12%	5%	5%	5%	6%	5%

Table B2: Raw BV/TV measurements for VOIs 13-23. Individual measurements that are greater than two standard deviations (>2σ) from the mean are highlighted in red.

Structural Model Index (SMI)

	1	2	3	4	5	6	7	8	9	10	11	12
SC-016-R	1.36676	1.44013	1.76287	1.57311		1.74262	2.15741	2.24882	1.88081	1.41524	1.90197	1.73671
SC-017-L	1.60888	1.71526	1.39148	1.16691	1.98176	1.68825	2.15529	2.49839			1.82276	1.96683
SC-017-R	1.45933	1.52513	1.1669	1.66197	1.71363	2.0349	2.37208	2.38597	1.55471	1.89315	1.41216	1.49019
SC-020-L	1.49139	1.38204	1.79228	1.40418	1.23467	2.18637	2.25255	2.59016	1.60333	1.75008	1.65777	2.00447
SC-020-R	1.24009	1.67551	1.38106	1.25164	1.38055	2.22036	2.30515	2.17261	1.58057	1.85902	1.67263	2.03478
SC-082-L	1.33491	1.15378	1.45518	1.28171		1.84819	2.31159		1.98509	1.79892	1.75846	2.15179
SC-082-R	1.35737	1.09682	1.46236	1.49663	1.35825	2.20044	2.31137	2.06562	1.41402	1.90172	1.67085	2.29466
SC-083-L	1.40152	1.15857	1.45389	1.19468		2.01059	2.37003		1.38898	1.85619	1.71698	1.76622
SC-083-R	1.6526	1.551	1.33726	1.3626		2.02225	2.36993	2.6969	1.26405	1.65184	1.57781	1.65438
SC-084-L	1.32747	1.08944	1.28182	1.17348	1.06557	2.04337	2.41987	2.43167	1.4626	1.74623	1.77254	2.01948
SC-084-R	1.20261	1.43144	0.96711	1.23866	0.9939	2.01664	2.44596	2.8306	1.52376	1.74782	1.59421	2.03222
SC-085-L	1.2693	1.37596	1.39747	1.45797	1.45661	2.06393	2.28506	2.27823	1.56633	1.61794	1.72756	2.19498
SC-085-R	1.5455	1.58615	1.52386	1.69828	1.91603	2.28985	2.31665	2.54432	1.83171		1.80314	2.25095
SC-086-L	1.12865	1.47543	1.1931	1.39673	1.61228	2.17363	2.30827	2.50709	1.861	1.6963	1.70581	1.80475
SC-087-L	1.44599	1.38505	1.44627	1.35615	2.0213	1.91804	2.4364	2.60469	2.11263	1.25404	0.99681	2.20009
SC-087-L	1.5634	1.52956	1.38182	1.56027		2.01753	2.10512	1.9819	1.60463	2.01472	0.4267	1.72266
SC-089-L	1.21437	0.93487	1.16748	0.99053							1.16621	2.51018
SC-089-R	1.62964	1.60738	1.6268	1.34835					2.01785		2.32951	2.27815
SC-369-R						2.02661	2.53294		1.55297	1.43562	1.66713	2.0753
SC-370-L	1.61095	1.28048	1.6516	1.47939	1.48376	2.11059	2.00338	2.32475	1.90271	1.689	1.85924	1.91678
SC-370-R	1.54695	1.45049	1.84395	1.6653	1.55745	1.99901	2.49333	2.63383	1.77338	1.84257	1.90889	1.90487
SC-371-L	1.6701	1.70402	1.67818	1.65339	1.68843	1.84864	2.49606	2.65751	1.92897	1.80154	1.9447	2.01749
SC-086-R	1.24748	1.17601	1.28044	1.12195	1.14441	1.84394	2.11289	2.1227	1.44837	1.84333	1.60264	2.05464
SC-088-L	1.03112	1.13713	1.16535	1.07994	1.2538	1.72058	2.50284	2.16952	1.42827	1.83359	1.76662	2.07618
SC-088-R	1.32629	1.45123	1.58697	1.1885	1.47311	1.76886	2.29853	2.30584	1.50047	1.74205	1.51192	2.09292
SC-092-L	1.37341	1.56055	1.54841	1.55896	1.31783	2.32096	2.3451	2.45102	1.65291		1.79599	2.16476
SC-092-R	1.4371	1.47047	1.70684	1.4671	1.36419	2.06782	1.99444	2.48104	1.64147		1.84859	1.97325
SC-096-L	1.53284	1.66196	1.77828	1.53836	1.83209	2.21283	2.13275	1.77275	1.52391	1.94391	1.80044	1.8402
SC-096-R	1.45431	1.5865	1.49489	1.62733	1.77641			2.1037	1.83493		2.04445	2.13471
SC-097-L	1.39193	1.36455	1.18818	1.21696	1.03282	2.0512	2.17915	2.12224	1.87072	1.94672	1.8927	2.12236
SC-097-R	1.37632	1.08646	1.1051	1.09439	0.96692	1.82095	2.16198	2.38594	1.72593	2.03411	1.73683	2.02261
SC-157-R	1.33338	1.32652	1.54735	1.50392	1.42752							
SC-158-L	1.3285	1.11682	1.25124	1.30785	1.57992	1.88708	2.40279	2.13943		1.80345	2.2416	2.10842
SC-158-R	1.44766	1.15956	1.09099	1.38559		1.82151	2.11685	1.74884	1.79453	1.88393	2.06414	2.05939
SC-161-L	1.28974	1.52639	1.38743	1.54782	1.73101	1.93808	2.21187	2.35191	1.90062	1.70892	1.72552	1.78345
SC-161-R	1.15641	1.40312	1.17094	1.36313	1.21985	1.61842	2.15237	2.19929	1.68367	1.75154	1.58137	2.06936
MEAN	1.394122	1.38787943	1.41900429	1.38324943	1.46607667	1.98543875	2.283125	2.32690933	1.68174688	1.76655321	1.70590429	2.015148
STD DEV	0.15656087	0.20724728	0.22642397	0.19060466	0.30170676	0.18012195	0.1467314	0.26118646	0.21077063	0.1751754	0.3344351	0.2026315
CoV	11%	15%	16%	14%	21%	9%	6%	11%	13%	10%	20%	10%

Table B3: Raw SMI measurements for VOIs 1-12. Individual measurements that are greater than two standard deviations (>2σ) from the mean are highlighted in red.

	13	14	15	16	17	18	19	20	21	22	23
SC-016-R	2.31434	2.11149	1.79595	1.7503		1.76491	1.25059	1.40227	1.41987	1.39902	1.23418
SC-017-L	2.02559	2.07725	1.85561	1.58783	1.46003	2.08243	1.60385	1.60828	1.62693	1.90437	1.54173
SC-017-R	0.95097	2.17652	1.89162	2.09314		1.72197	1.52203	1.80765	1.71475	1.31807	1.29258
SC-020-L	2.11831	2.05189	1.69492	2.15774	1.69349	2.05653	1.55741	1.34036	1.65061	1.31963	1.27405
SC-020-R	2.12614	2.01771	1.92765	1.92698	1.71182	1.64555	1.45667	1.59485	1.51064	1.51575	1.38592
SC-082-L	2.39753	2.12092				2.07116			1.51888		1.1324
SC-082-R	2.56176	2.16164	1.89608		1.96387	2.06756	1.8429	1.58396	1.54192	0.97003	1.13123
SC-083-L	2.24799	2.08246	1.91556		1.75757	1.48405	1.77982	2.02231	1.30287	1.53478	0.8672
SC-083-R	2.35634	1.92579	1.93962		1.73586	1.96864	1.85354	1.70067	1.29775	1.26434	0.90194
SC-084-L	2.57702	2.31092	2.09981		1.95192	2.11143	1.78529	2.02594	1.71855	1.10439	1.17083
SC-084-R	2.40878	1.96222	2.12053		1.75042	2.06525	1.73635	1.87454	1.41099	1.22213	0.81067
SC-085-L	2.6778	2.21029				2.66179	1.65246	1.94002	2.03903	1.29704	1.32187
SC-085-R	2.71561										
SC-086-L	2.16272	1.10926	1.39191				1.53848		1.80152	1.01111	0.55478
SC-087-L	2.07796	2.30322	1.78425				0.98639	1.49055	1.8555	1.1342	0.34359
SC-087-L	2.08446	2.0644	1.38128			2.15786	1.38109	1.58861	1.14369	1.62146	0.59058
SC-089-L	2.31517	1.56284					1.52669	1.63167	1.72929	1.68671	1.64739
SC-089-R	2.293	1.90965					1.88085	1.96378	1.54378	1.90823	1.54028
SC-369-R	2.41323	2.08069	1.82074		1.79612		1.32738	1.72267	1.42247	1.33314	1.23332
SC-370-L		2.12331	1.76668		2.08434	2.53158	1.74002	2.13867	1.82524	1.53105	1.35013
SC-370-R	2.46499	2.02245	1.89183		1.98004	2.28418	1.78483	1.94316	1.71611	1.54978	1.70622
SC-371-L	1.80453	2.00581	2.20713			2.09793	1.68062	1.865	1.68364	1.68435	1.57616
SC-086-R	2.10946	1.80235				2.15056			1.94958		0.84864
SC-088-L	2.74567	2.05512	1.89424	2.04337	2.16935	2.11182	1.56571	1.79072	1.56828	1.12967	0.91429
SC-088-R	2.70509	2.24098	1.76946		2.43293		1.39944	1.76806	1.42876	1.28934	0.93752
SC-092-L	2.54652	2.21896	2.14943			1.92688			1.69561	1.54145	1.45366
SC-092-R	2.76228	2.14713	1.97892		2.00672	2.19753			1.59609	1.48991	1.05534
SC-096-L	2.22199	1.75849	1.81374			2.16773	2.0861	1.58255	1.64193	1.79355	1.40651
SC-096-R	2.27617	2.04905	1.87776			1.84885	1.61368	1.92062	1.37521	1.40743	1.37221
SC-097-L	2.33316	2.07444	2.11126		2.3165	2.16882	1.69302	1.82558	1.58899	1.27359	1.01476
SC-097-R	2.29594	2.20777	2.03002			2.11993	1.85282	2.01571	1.83552	1.37069	1.37221
SC-157-R											
SC-158-L	2.16166	2.3744	2.13713		1.86547	2.17011	1.8448	1.71776	1.76682	1.35794	1.24849
SC-158-R	2.29912	2.2542	1.97204		1.99458	2.2	1.78476	1.66375	1.83444	1.15509	1.34486
SC-161-L	2.19794		1.86524		2.10513	2.14275	1.51276	1.66192	1.31112	1.16451	0.8532
SC-161-R	2.3883	2.0906	2.11691			2.05417	1.43589		1.64774	1.33708	1.0636
MEAN	2.29816294	2.05043091	1.89990759	1.92656	1.93200889	2.07257036	1.62254133	1.75684393	1.60923882	1.39436969	1.16153941
STD DEV	0.32870261	0.23500363	0.19546806	0.21938252	0.23940943	0.23693125	0.2253511	0.19943467	0.20307573	0.23920107	0.32139263
CoV	14%	11%	10%	11%	12%	11%	14%	11%	13%	17%	28%

Table B4: Raw BV/TV measurements for VOIs 13-23. Individual measurements that are greater than two standard deviations (>2σ) from the mean are highlighted in red.

Trabecular Thickness (Tb.Th)

	1	2	3	4	5	6	7	8	9	10	11	12
SC-016-R	0.21902	0.21255	0.21444	0.20791		0.2072	0.22319	0.22809	0.17395	0.20128	0.19553	0.18752
SC-017-L	0.21422	0.21785	0.21947	0.22456	0.30331	0.26339	0.3014	0.24437			0.21638	0.25649
SC-017-R	0.21259	0.21201	0.21898	0.20662	0.23061	0.24718	0.26479	0.24656	0.22203	0.19478	0.22257	0.24926
SC-020-L	0.21465	0.2272	0.2636	0.23459	0.24592	0.24085	0.25428	0.26747	0.22151	0.20092	0.23202	0.28485
SC-020-R	0.21721	0.22767	0.23707	0.23359	0.24148	0.22103	0.2538	0.28859	0.21244	0.23183	0.21478	0.26401
SC-082-L	0.1879	0.19384	0.20342	0.20943		0.21045	0.22813		0.2003	0.19898	0.21036	0.23175
SC-082-R	0.20324	0.21756	0.20284	0.2004	0.20738	0.21685	0.23208	0.24511	0.22973	0.18633	0.23973	0.25279
SC-083-L	0.19611	0.19895	0.19468	0.20323		0.22175	0.28363		0.22904	0.22403	0.24754	0.26384
SC-083-R	0.21991	0.21514	0.23401	0.24363		0.25165	0.35289	0.33286	0.25953	0.23823	0.22584	0.28985
SC-084-L	0.21093	0.20906	0.22187	0.22633	0.22102	0.20993	0.24865	0.21787	0.20993	0.20093	0.22717	0.22807
SC-084-R	0.2029	0.19421	0.21422	0.21483	0.23457	0.20723	0.2343	0.21166	0.21546	0.20703	0.20026	0.22454
SC-085-L	0.24386	0.23709	0.2441	0.23929	0.24176	0.28747	0.271	0.28465	0.27878	0.22828	0.25288	0.30361
SC-085-R	0.20982	0.21033	0.2086	0.21544	0.24221	0.28954	0.30923	0.29476	0.24807		0.28621	0.25286
SC-086-L	0.20853	0.18896	0.21784	0.23907	0.2197	0.24486	0.27044	0.24774	0.19416	0.20617	0.21624	0.25361
SC-087-L	0.22577	0.23294	0.23984	0.23575	0.31756	0.25822	0.28804	0.20836	0.21353	0.18433	0.26415	0.23701
SC-087-L	0.22569	0.22399	0.23851	0.22258		0.26255	0.25373	0.24834	0.19703	0.19707	0.21772	0.23421
SC-089-L	0.15313	0.14024	0.15904	0.14804							0.1509	0.17484
SC-089-R	0.17919	0.16208	0.18213	0.16567					0.13716		0.13719	0.14578
SC-369-R						0.24329	0.28386		0.25056	0.25627	0.24546	0.2387
SC-370-L	0.20308	0.19717	0.21368	0.19644	0.24814	0.24293	0.27664	0.22174	0.20136	0.20497	0.18667	0.18791
SC-370-R	0.2048	0.20207	0.20492	0.21194	0.2198	0.22743	0.23645	0.28868	0.19733	0.21246	0.21218	0.23193
SC-371-L	0.15058	0.14547	0.1587	0.15943	0.1394	0.2002	0.18833	0.17882	0.12217	0.14132	0.14036	0.15846
SC-086-R	0.20665	0.20657	0.22852	0.23944	0.2128	0.2308	0.22162	0.26731	0.20873	0.20822	0.20516	0.23002
SC-088-L	0.19992	0.20494	0.21471	0.20749	0.21891	0.21902	0.23183	0.21308	0.19886	0.20333	0.20258	0.20487
SC-088-R	0.21364	0.21124	0.22549	0.23911	0.2375	0.22844	0.22379	0.19286	0.20193	0.19658	0.20737	0.21328
SC-092-L	0.23738	0.21989	0.22791	0.24949	0.26743	0.21873	0.33327	0.30556	0.24		0.23539	0.2469
SC-092-R	0.22401	0.22418	0.23611	0.25463	0.29637	0.25216	0.27986	0.30859	0.2085		0.22218	0.22963
SC-096-L	0.18065	0.18675	0.18364	0.17903	0.23412	0.19587	0.18299	0.2262	0.17162	0.19645	0.172	0.19342
SC-096-R	0.178	0.16918	0.18135	0.18066	0.21051			0.23783	0.1821		0.21767	0.23925
SC-097-L	0.20307	0.19596	0.20902	0.2117	0.23525	0.22494	0.23327	0.22222	0.19008	0.19339	0.19275	0.22985
SC-097-R	0.2006	0.21027	0.21225	0.22007	0.22487	0.22789	0.26412	0.26032	0.18909	0.19921	0.19123	0.21631
SC-157-R	0.19567	0.18932	0.1999	0.19301	0.2135							
SC-158-L	0.20127	0.20509	0.21208	0.20745	0.21776	0.23272	0.24676	0.21929		0.23718	0.2221	0.2592
SC-158-R	0.18993	0.20537	0.20906	0.20511		0.22603	0.24847	0.21326	0.20648	0.22458	0.22024	0.25172
SC-161-L	0.21146	0.20106	0.21388	0.21625	0.22175	0.26611	0.24845	0.32208	0.2322	0.21352	0.22602	0.23946
SC-161-R	0.19963	0.20198	0.19935	0.19365	0.22969	0.24903	0.26202	0.26204	0.22703	0.20303	0.22492	0.22436
MEAN	0.20414314	0.20280514	0.21272086	0.21245314	0.23456741	0.23517938	0.25722844	0.25021033	0.20845906	0.20681071	0.21376429	0.23229029
STD DEV	0.01968573	0.02196103	0.02232139	0.02524123	0.03381715	0.02346696	0.03643536	0.03925576	0.03178617	0.0212817	0.03126878	0.03432779
CoV	10%	11%	10%	12%	14%	10%	14%	16%	15%	10%	15%	15%

Table B5: Raw Tb.Th measurements for VOIs 1-12. Individual measurements that are greater than two standard deviations (>2σ) from the mean are highlighted in red.

	13	14	15	16	17	18	19	20	21	22	23
SC-016-R	0.16986	0.24661	0.19759	0.1678		0.17794	0.21029	0.19807	0.16679	0.18387	0.20957
SC-017-L	0.29445	0.33764	0.20577	0.1688	0.19696	0.25871	0.23937	0.20498	0.23505	0.24637	0.25593
SC-017-R	0.0816	0.26482	0.19613	0.16689		0.2894	0.21721	0.20062	0.21664	0.20622	0.21308
SC-020-L	0.32491	0.30026	0.21858	0.21046	0.22309	0.27065	0.22066	0.20358	0.23605	0.20836	0.22109
SC-020-R	0.25532	0.3641	0.19942	0.16687	0.22522	0.23508	0.20392	0.20306	0.22845	0.20912	0.21888
SC-082-L	0.23581	0.27743				0.24243			0.20166		0.21654
SC-082-R	0.29413	0.31444	0.20154		0.25727	0.24169	0.21471	0.22017	0.23196	0.23817	0.25436
SC-083-L	0.29732	0.2806	0.19256		0.2225	0.28446	0.22671	0.2006	0.2454	0.22769	0.23664
SC-083-R	0.31716	0.33462	0.22329		0.27	0.27535	0.22104	0.2285	0.25022	0.24211	0.26124
SC-084-L	0.32117	0.28168	0.19036		0.2194	0.28908	0.21713	0.17948	0.25387	0.22279	0.21157
SC-084-R	0.23026	0.29056	0.18176		0.18911	0.24897	0.1845	0.18329	0.2278	0.21624	0.23021
SC-085-L	0.34032	0.37328				0.32613	0.2362	0.24369	0.26447	0.26363	0.27001
SC-085-R	0.22035	0.29771	0.21293		0.24954		0.24003	0.24865	0.29477	0.25322	0.25391
SC-086-L	0.24711	0.2711	0.19966				0.20977		0.21685	0.19658	0.20848
SC-087-L	0.27329	0.294	0.20783				0.22024	0.19203	0.21239	0.23021	0.23514
SC-087-L	0.25524	0.30162	0.1985			0.20966	0.21315	0.18762	0.20043	0.22077	0.2364
SC-089-L	0.14581	0.17567					0.13722	0.12619	0.14374	0.14644	0.15361
SC-089-R	0.14994	0.19598					0.142	0.14876	0.15943	0.1729	0.17796
SC-369-R	0.26791	0.26391	0.24503		0.21602		0.24564	0.23734	0.21917	0.2547	0.25743
SC-370-L		0.23596	0.14108		0.16451	0.22188	0.18412	0.17321	0.21016	0.19335	0.20568
SC-370-R	0.22704	0.26919	0.16399		0.18069	0.21075	0.19267	0.21181	0.2317	0.20976	0.21438
SC-371-L	0.10638	0.19613	0.12007			0.16587	0.14841	0.15882	0.17378	0.15759	0.17119
SC-086-R	0.24333	0.2766				0.24337			0.19548		0.21348
SC-088-L	0.27802	0.2707	0.19746	0.15559	0.19782	0.20882	0.19518	0.19017	0.20542	0.22611	0.22967
SC-088-R	0.25856	0.29759	0.19376		0.20725		0.22043	0.18655	0.2111	0.24218	0.22137
SC-092-L	0.30883	0.32476	0.204			0.29564			0.239	0.22733	0.2421
SC-092-R	0.29551	0.32231	0.1952		0.21338	0.26548			0.22377	0.22249	0.24776
SC-096-L	0.15118	0.2205	0.12893			0.18554	0.16036	0.13169	0.18946	0.17162	0.19501
SC-096-R	0.15405	0.26379	0.13977			0.18512	0.16721	0.21317	0.23503	0.20782	0.24605
SC-097-L	0.23652	0.30071	0.16838		0.20769	0.28324	0.18278	0.19898	0.2181	0.20708	0.22105
SC-097-R	0.22527	0.31242	0.18488			0.26531	0.19701	0.18593	0.21272	0.20127	0.24605
SC-157-R											
SC-158-L	0.29285	0.34649	0.20318		0.12967	0.23823	0.19626	0.17058	0.19935	0.21921	0.23081
SC-158-R	0.2674	0.30494	0.19614		0.20902	0.28766	0.1919	0.20101	0.22758	0.22159	0.23067
SC-161-L	0.24952		0.21458		0.21546	0.22663	0.21873	0.21526	0.21931	0.22748	0.2544
SC-161-R	0.28666	0.25497	0.20606			0.23906	0.21057		0.22829	0.2134	0.2194
MEAN	0.24420824	0.28420853	0.19094767	0.172735	0.21024211	0.24543393	0.20211032	0.19461414	0.21786829	0.21477788	0.226032
STD DEV	0.06449096	0.04540857	0.02794607	0.01910773	0.03186064	0.03999629	0.02831005	0.0293126	0.02940355	0.02701121	0.02589181
CoV	26%	16%	15%	11%	15%	16%	14%	15%	13%	13%	11%

Table B6: Raw Tb.Th measurements for VOIs 13-23. Individual measurements that are greater than two standard deviations (>2σ) from the mean are highlighted in red.

Trabecular Number (Tb.N)

	1	2	3	4	5	6	7	8	9	10	11	12
SC-016-R	1.89103	1.91072	1.61914	1.74514		1.78074	1.44979	1.49012	1.66352	1.87391	1.3869	1.60445
SC-017-L	1.80952	1.72002	1.82339	1.90265	1.11436	1.18929	0.91014	0.95734			1.38987	1.16447
SC-017-R	1.82817	1.78603	1.89028	1.7282	1.30207	0.91929	0.74182	0.89823	1.86707	1.62547	1.65	1.26504
SC-020-L	1.79805	1.75717	1.43015	1.66078	1.381	1.04087	1.08881	1.00176	1.74245	1.70674	1.28301	1.03938
SC-020-R	1.9079	1.6523	1.75081	1.76743	1.41875	1.03175	1.24564	1.07589	1.84806	1.52079	1.44505	1.09504
SC-082-L	1.95684	2.02223	1.64753	1.72607		1.47108	1.19389		1.91443	1.95456	1.48027	1.24235
SC-082-R	1.83512	1.95134	1.75516	1.59519	1.59124	1.06091	1.2393	1.16796	1.78426	2.07619	1.35511	1.13324
SC-083-L	1.79224	1.87925	1.77847	1.94963		1.03722	1.03165		1.77925	1.55217	1.23785	1.03024
SC-083-R	1.60415	1.74637	1.63646	1.59436		0.8979	0.66957	0.58617	1.58077	1.74815	1.43122	1.03338
SC-084-L	1.94485	2.04797	1.78917	1.82511	1.73223	1.32979	1.17478	1.43335	1.89973	2.08398	1.38633	1.29805
SC-084-R	2.10407	1.94495	2.00447	1.88209	1.67444	1.46766	1.19625	1.34366	1.84842	2.07022	1.68248	1.37403
SC-085-L	1.67637	1.68964	1.55361	1.47053	1.49036	1.08542	0.85476	1.04155	1.41607	1.62661	1.21335	1.00049
SC-085-R	1.67416	1.68645	1.6347	1.51483	1.35172	0.92586	0.91984	1.13985	1.50331		1.17978	1.08375
SC-086-L	2.01417	1.88155	1.57821	1.72369	1.27849	1.21256	1.21467	1.32846	1.98834	2.00041	1.54285	1.18828
SC-087-L	1.72988	1.60428	1.4752	1.5628	1.01117	1.04016	1.00622	0.93477	1.60178	2.02221	1.30405	1.18196
SC-087-L	1.74071	1.75043	1.63866	1.58995		1.09206	0.97846	1.51814	1.79915	1.75325	1.40226	1.30757
SC-089-L	2.82461	3.20505	2.65723	2.77301							2.19344	1.76973
SC-089-R	2.12403	2.23744	1.89424	2.20492					2.96816		2.26582	2.1716
SC-369-R						1.31601	0.95996		1.58236	1.50579	1.23742	1.18607
SC-370-L	1.86915	2.08632	1.64653	1.81288	1.47475	1.31473	0.99514	1.10922	1.80662	1.8986	1.64269	1.59551
SC-370-R	1.87938	1.92601	1.52632	1.59888	1.33188	1.38287	1.00394	1.0475	1.82743	1.8643	1.47024	1.27294
SC-371-L	2.4892	2.63476	2.18697	2.30565	2.10093	1.69169	1.00561	1.18743	3.01235	2.74512	2.3116	1.75453
SC-086-R	1.92439	1.93822	1.6306	1.59645	1.60541	1.40489	1.19498	1.29949	1.97133	1.80497	1.66404	1.17868
SC-088-L	2.13212	2.04175	1.94914	2.02605	1.58721	1.47625	1.1545	1.58862	1.97884	1.9309	1.49326	1.32083
SC-088-R	1.98811	1.78765	1.72084	1.8195	1.37449	1.4288	1.07725	1.68352	1.81393	1.93665	1.62052	1.30146
SC-092-L	1.7066	1.65309	1.50254	1.46746	1.09056	1.36259	0.8542	1.02114	1.61449		1.4486	1.34536
SC-092-R	1.73159	1.73634	1.45728	1.54615	1.14188	1.36775	0.98815	0.92694	1.83679		1.47535	1.36527
SC-096-L	2.00949	2.06597	1.67258	1.91617	1.52498	1.5903	1.36454	1.38014	2.15038	2.10404	1.81513	1.74236
SC-096-R	2.06398	2.02176	1.82131	1.86405	1.56319			1.38789	2.068		1.44533	1.34757
SC-097-L	1.91643	1.88412	1.8835	1.85784	1.70228	1.40575	1.14988	1.48065	1.91022	1.79994	1.59767	1.29139
SC-097-R	1.83954	2.02867	1.92655	1.83466	1.73206	1.47871	1.07828	1.30104	1.99343	1.87453	1.58241	1.36861
SC-157-R	1.87891	1.98422	1.64732	1.66348	1.53028							
SC-158-L	1.87308	2.00429	1.75723	1.74154	1.48473	1.4061	1.00262	1.48843		1.72853	1.35018	1.19546
SC-158-R	1.87047	1.99445	1.87677	1.70454		1.4085	1.04788	1.45919	1.83497	1.85999	1.32373	1.18054
SC-161-L	1.8834	1.72133	1.7566	1.63804	1.20316	1.24166	1.14109	0.96911	1.58425	1.95221	1.41358	1.32092
SC-161-R	1.98789	1.79446	1.92185	1.84861	1.38575	1.30748	1.02222	1.27349	1.77411	1.9662	1.48805	1.30507
MEAN	1.9228457	1.9364743	1.7554517	1.7845237	1.4510878	1.2864575	1.0611197	1.2173683	1.8738834	1.8780868	1.5202697	1.3158749
STD DEV	0.2274338	0.2965276	0.2311613	0.2545554	0.2376917	0.2238914	0.1654952	0.2524497	0.3365302	0.2417967	0.2711309	0.2482076
CoV	12%	15%	13%	14%	16%	17%	16%	21%	18%	13%	18%	19%

Table B7: Raw Tb.N measurements for VOIs 1-12. Individual measurements that are greater than two standard deviations (>2σ) from the mean are highlighted in red.

	13	14	15	16	17	18	19	20	21	22	23
SC-016-R	1.36972	1.11993	1.66686	2.22892		2.1139	2.15811	2.25119	2.35617	2.14911	1.95472
SC-017-L	0.82708	0.80333	1.60276	2.06141	1.93408	1.42887	1.68681	2.12534	1.55343	1.49898	1.54313
SC-017-R	3.19064	1.14302	1.58926	1.99642		1.30491	1.95257	2.11495	1.68081	1.85597	1.9069
SC-020-L	0.81748	1.00613	1.62957	1.65016	1.52469	1.21305	1.85973	2.20111	1.56182	1.7968	1.81967
SC-020-R	0.99959	0.79156	1.69978	2.15885	1.5141	1.53004	2.06555	2.01442	1.71652	1.91359	1.89502
SC-082-L	0.77862	1.15005				1.36996			1.93513		1.94718
SC-082-R	0.61644	1.03571	1.7144		1.28827	1.3626	2.04303	1.96603	1.83072	1.89821	1.84794
SC-083-L	0.63927	1.04537	1.6066		1.24552	1.2184	1.69347	1.99372	1.63981	1.77729	1.85433
SC-083-R	0.71189	0.93687	1.51747		1.03394	1.17712	1.8507	1.88345	1.65056	1.75802	1.76065
SC-084-L	0.88239	1.1006	1.62892		1.56642	1.29243	2.00925	2.0784	1.44268	2.09861	1.92765
SC-084-R	0.95089	1.21549	1.81722		1.71823	1.34286	2.23462	2.16502	1.79497	2.08597	2.04954
SC-085-L	0.42943	0.81547				0.65625	1.78056	1.79628	1.40588	1.74075	1.67572
SC-085-R	1.12988	1.15654	1.51792		1.2511		1.67366	1.65457	1.40835	1.77461	1.78654
SC-086-L	1.03047	1.25457	1.72539				1.97215		1.79882	2.12333	2.05056
SC-087-L	0.62206	1.07882	1.68543				1.93303	2.06888	1.91805	1.93409	1.686
SC-087-L	0.92418	1.04105	1.65225			1.54682	1.92658	2.08068	1.96585	1.89136	1.87418
SC-089-L	1.11761	1.56296					2.97712	3.15661	2.63757	2.70926	2.78078
SC-089-R	1.14719	1.59206					3.08903	2.73636	2.51381	2.29391	2.49584
SC-369-R	0.77962	1.14511	1.39572		1.6115		1.70633	1.68035	1.80565	1.62514	1.65185
SC-370-L		1.4052	2.18616		1.65845	1.42801	2.33275	2.14041	1.83354	2.14779	2.16351
SC-370-R	0.66028	1.217	2.03338		1.71414	1.64989	2.0413	1.98084	1.69096	1.94519	1.93911
SC-371-L	1.52749	1.38282	2.71196			1.96176	2.79971	2.6475	2.25561	2.74009	2.45897
SC-086-R	0.96501	1.23723				1.2874			1.97291		2.12097
SC-088-L	0.73835	1.27553	1.7567	2.31146	1.81271	1.81545	1.98573	2.2667	1.76598	1.98809	1.87377
SC-088-R	0.53607	1.17678	1.8301		1.28305		1.96077	2.16552	1.84944	1.86172	2.04648
SC-092-L	0.67456	0.9303	1.52727			0.95767			1.56497	1.80242	1.78236
SC-092-R	0.60923	0.91638	1.84149		1.35246	0.91566			1.7446	1.77688	1.89506
SC-096-L	1.17335	1.57487	2.21569			1.82404	2.07733	2.86121	2.01304	2.30392	2.21294
SC-096-R	0.97307	1.23015	2.329			1.72909	2.43338	1.95525	1.65039	2.20706	1.8806
SC-097-L	0.99444	1.05343	1.86699		1.45282	1.2573	2.28364	2.07926	1.91033	2.19212	2.12464
SC-097-R	0.83958	0.99399	1.77879			1.35897	2.11827	2.21124	1.89214	2.22872	1.8806
SC-157-R											
SC-158-L	0.80572	0.92247	1.61155		1.10714	1.08218	2.10125	2.50998	1.7281	1.98063	1.88497
SC-158-R	0.83675	1.09087	1.82144		1.42183	1.19131	2.0483	2.11874	1.67673	2.04893	1.99095
SC-161-L	0.96539		1.62507		1.50591	1.61645	1.95816	1.98336	1.88837	1.89956	1.74538
SC-161-R	0.91156	1.10642	1.44468			1.31222	1.99078		1.81245	1.91145	2.00514
MEAN	0.9463324	1.1325906	1.7676607	2.06787	1.4734926	1.3908789	2.0885055	2.16853	1.8247474	1.9987748	1.9575329
STD DEV	0.4595626	0.2037892	0.2822907	0.233743	0.239142	0.318978	0.3429467	0.333718	0.2771652	0.2671308	0.2459156
CoV	49%	18%	16%	11%	16%	23%	16%	15%	15%	13%	13%

Table B8: Raw Tb.Th measurements for VOIs 13-23. Individual measurements that are greater than two standard deviations (>2σ) from the mean are highlighted in red.

Trabecular Separation (Tb.Sp)

	1	2	3	4	5	6	7	8	9	10	11	12
SC-016-R	0.25598	0.25265	0.28899	0.27977		0.27459	0.26508	0.35482	0.27169	0.2688	0.34071	0.33052
SC-017-L	0.27361	0.2831	0.28528	0.27353	0.54911	0.57487	0.47902	0.5283			0.37249	0.52497
SC-017-R	0.27405	0.27824	0.28729	0.28272	0.36315	0.56762	0.65386	0.5025	0.27587	0.28246	0.32491	0.54469
SC-020-L	0.26839	0.2725	0.32266	0.30015	0.46425	0.45772	0.37988	0.47817	0.27737	0.30102	0.43201	0.49332
SC-020-R	0.25592	0.27173	0.28281	0.30507	0.39124	0.46514	0.34833	0.5144	0.27839	0.36218	0.34121	0.46866
SC-082-L	0.27788	0.26747	0.32468	0.32763		0.3615	0.30204		0.27482	0.26247	0.35289	0.42758
SC-082-R	0.29699	0.27314	0.30472	0.33822	0.35821	0.37177	0.33453	0.44652	0.33413	0.28875	0.41578	0.46641
SC-083-L	0.27573	0.26111	0.28426	0.26457		0.51913	0.34938		0.30483	0.29042	0.52043	0.6314
SC-083-R	0.29479	0.27595	0.30669	0.30233		0.63772	0.74759	0.77615	0.40143	0.3285	0.39473	0.63132
SC-084-L	0.26169	0.25278	0.30914	0.29869	0.31937	0.35674	0.30942	0.27777	0.27104	0.25603	0.36552	0.45395
SC-084-R	0.25838	0.26086	0.27854	0.28306	0.33666	0.32303	0.29744	0.27052	0.27559	0.28223	0.3	0.3948
SC-085-L	0.32626	0.3022	0.34893	0.34809	0.33934	0.45827	0.47686	0.45481	0.43347	0.33924	0.47092	0.4581
SC-085-R	0.30491	0.30216	0.31964	0.3311	0.33146	0.61192	0.58003	0.3781	0.33404		0.43943	0.40412
SC-086-L	0.26427	0.2652	0.37728	0.30654	0.47891	0.37251	0.35699	0.32882	0.25928	0.27105	0.3657	0.37528
SC-087-L	0.28436	0.31065	0.32864	0.32087	0.57126	0.50337	0.41854	0.46932	0.30564	0.24451	0.44757	0.48624
SC-087-L	0.29309	0.27783	0.31448	0.31186		0.48612	0.45578	0.34372	0.2852	0.32165	0.52035	0.50314
SC-089-L	0.1944	0.17677	0.19852	0.19309							0.24115	0.34601
SC-089-R	0.23042	0.21734	0.24961	0.22553					0.18218		0.17906	0.2186
SC-369-R						0.32659	0.3807		0.30052	0.32314	0.41786	0.40007
SC-370-L	0.26342	0.2452	0.29038	0.27394	0.33208	0.38366	0.66218	0.44099	0.26644	0.29199	0.29709	0.27407
SC-370-R	0.26711	0.26798	0.30433	0.29426	0.35311	0.3502	0.46983	0.42876	0.30432	0.28948	0.32139	0.39016
SC-371-L	0.21788	0.18774	0.2289	0.23045	0.23152	0.28977	0.38805	0.32406	0.18001	0.19053	0.24526	0.28019
SC-086-R	0.26029	0.26531	0.35968	0.35688	0.36296	0.36467	0.40645	0.44501	0.26225	0.28869	0.31063	0.41749
SC-088-L	0.24836	0.25107	0.27208	0.25768	0.35868	0.31638	0.30226	0.28881	0.26519	0.26743	0.3285	0.37327
SC-088-R	0.25835	0.28203	0.29691	0.28001	0.42058	0.36086	0.38174	0.2694	0.27924	0.25973	0.31657	0.35953
SC-092-L	0.29612	0.29409	0.33781	0.3286	0.66129	0.26771	0.50971	0.47085	0.33667		0.33388	0.34858
SC-092-R	0.28526	0.27727	0.32199	0.30997	0.54998	0.39409	0.53573	0.4679	0.28377		0.3307	0.37488
SC-096-L	0.2676	0.24312	0.28977	0.25749	0.31066	0.31767	0.40315	0.36883	0.27205	0.25219	0.2929	0.29706
SC-096-R	0.26153	0.25112	0.27538	0.25491	0.31639			0.34467	0.26407		0.34858	0.39446
SC-097-L	0.27466	0.27097	0.28244	0.28185	0.35888	0.36095	0.4004	0.36716	0.24741	0.29106	0.30056	0.36308
SC-097-R	0.28405	0.26702	0.29622	0.29638	0.32821	0.35234	0.40858	0.3927	0.2561	0.25573	0.31689	0.36271
SC-157-R	0.26713	0.25885	0.29629	0.28508	0.31633							
SC-158-L	0.29431	0.26639	0.3213	0.30842	0.35399	0.38347	0.39992	0.30184		0.34362	0.34517	0.42864
SC-158-R	0.28685	0.26889	0.30853	0.30955		0.37506	0.44739	0.34558	0.28891	0.26063	0.36155	0.49156
SC-161-L	0.2695	0.28382	0.29319	0.30345	0.41369	0.46468	0.42259	0.52367	0.28242	0.26318	0.34032	0.4225
SC-161-R	0.26387	0.27613	0.27538	0.27869	0.43424	0.4632	0.47798	0.41142	0.28673	0.24551	0.33865	0.38154
MEAN	0.27021171	0.26453371	0.29893543	0.29144086	0.39279815	0.40979125	0.42973219	0.410519	0.28565844	0.28293643	0.35346743	0.41482571
STD DEV	0.02431681	0.02727181	0.03387375	0.03448962	0.09694383	0.09740073	0.1116918	0.10493087	0.04808636	0.03611571	0.07242413	0.0907238
CoV	9%	10%	11%	12%	25%	24%	26%	26%	17%	13%	20%	22%

Table B9: Raw Tb.Sp measurements for VOIs 1-12. Individual measurements that are greater than two standard deviations (>2σ) from the mean are highlighted in red.

	13	14	15	16	17	18	19	20	21	22	23
SC-016-R	0.34751	0.42429	0.28462	0.24094		0.25491	0.23723	0.24502	0.23327	0.24306	0.25469
SC-017-L	0.6487	0.7624	0.31838	0.23129	0.37398	0.37241	0.31603	0.25699	0.33871	0.31981	0.30706
SC-017-R	0.0816	0.39815	0.32903	0.19885		0.53248	0.27852	0.24744	0.31606	0.28714	0.26962
SC-020-L	0.64951	0.54451	0.30374	0.26961	0.40891	0.50601	0.27459	0.26423	0.35781	0.3024	0.28553
SC-020-R	0.60781	0.75622	0.29287	0.21231	0.35727	0.41984	0.26823	0.27729	0.32797	0.26601	0.2766
SC-082-L	0.77364	0.40703				0.40613			0.30256		0.26966
SC-082-R	0.62714	0.42811	0.34051		0.43321	0.45654	0.27774	0.28364	0.30513	0.28788	0.28967
SC-083-L	0.74428	0.45948	0.29482		0.69985	0.54402	0.32989	0.24726	0.4264	0.30148	0.29404
SC-083-R	0.82505	0.56844	0.34886		0.81096	0.64295	0.29889	0.28846	0.32986	0.29903	0.29222
SC-084-L	0.44214	0.40032	0.29018		0.43482	0.34802	0.24677	0.2008	0.36472	0.25722	0.27319
SC-084-R	0.52716	0.3911	0.25606		0.40436	0.41253	0.23629	0.22768	0.32267	0.25762	0.25606
SC-085-L	0.7378	0.53427				0.53426	0.31599	0.27917	0.33597	0.31296	0.32532
SC-085-R	0.23736	0.36493	0.32737		0.4313		0.3213	0.29941	0.38281	0.31453	0.31739
SC-086-L	0.42842	0.35616	0.29628				0.25935		0.33905	0.25178	0.27007
SC-087-L	0.68055	0.47756	0.31548				0.2936	0.25258	0.29274	0.27503	0.29639
SC-087-L	0.57542	0.43364	0.29878			0.29307	0.27819	0.24088	0.25619	0.29112	0.29129
SC-089-L	0.43142	0.30676					0.1944	0.15124	0.20567	0.20028	0.191
SC-089-R	0.33834	0.27854					0.17097	0.18035	0.23073	0.21863	0.20358
SC-369-R	0.53976	0.39451	0.36003		0.35162		0.30158	0.34364	0.30355	0.30616	0.2925
SC-370-L		0.3094	0.21838		0.31937	0.34093	0.22477	0.23134	0.31784	0.24465	0.24288
SC-370-R	0.59485	0.41171	0.25692		0.33676	0.29323	0.25848	0.25138	0.30815	0.25721	0.26825
SC-371-L	0.30072	0.39064	0.15648			0.24234	0.22775	0.20791	0.27214	0.2096	0.24259
SC-086-R	0.50517	0.43025				0.34044			0.25528		0.26189
SC-088-L	0.52764	0.35489	0.28427	0.2179	0.32471	0.25564	0.26189	0.23666	0.30257	0.26632	0.28444
SC-088-R	0.69318	0.35537	0.28494		0.3799		0.26016	0.24852	0.28805	0.27507	0.25715
SC-092-L	0.63488	0.45384	0.29743			0.53192			0.34793	0.27346	0.28203
SC-092-R	0.56885	0.4864	0.25118		0.34441	0.5537			0.30637	0.29006	0.28412
SC-096-L	0.26105	0.33384	0.22485			0.21878	0.21635	0.19086	0.2552	0.23112	0.23493
SC-096-R	0.38655	0.48096	0.23634			0.28982	0.23779	0.25411	0.3347	0.23915	0.27174
SC-097-L	0.41871	0.4812	0.23822		0.27499	0.36405	0.21598	0.24229	0.27477	0.22873	0.24363
SC-097-R	0.47919	0.49733	0.25827			0.34138	0.23127	0.22175	0.2672	0.23208	0.27174
SC-157-R											
SC-158-L	0.61028	0.45265	0.29944		0.35202	0.42656	0.23829	0.19706	0.35588	0.27907	0.29414
SC-158-R	0.64529	0.41956	0.26727		0.36631	0.35848	0.2389	0.26496	0.32155	0.27611	0.26353
SC-161-L	0.5383		0.29029		0.27382	0.29918	0.25831	0.25881	0.29738	0.27029	0.30228
SC-161-R	0.47752	0.39242	0.36155			0.35011	0.25773		0.27591	0.27466	0.26041
MEAN	0.52605265	0.43932	0.28609467	0.22848333	0.40413526	0.3903475	0.2589429	0.24454241	0.30722257	0.2678703	0.27204657
STD DEV	0.16652799	0.10527287	0.04493815	0.02492455	0.13361626	0.1111651	0.03758573	0.03883749	0.04544386	0.03111451	0.02817344
CoV	32%	24%	16%	11%	33%	28%	15%	16%	15%	12%	10%

Table B10: Raw Tb.Sp measurements for VOIs 13-23. Individual measurements that are greater than two standard deviations (>2σ) from the mean are highlighted in red.

Degree of Anisotropy (DA)

	1	2	3	4	5	6	7	8	9	10	11	12
SC-016-R	**0.51944**	0.73602	0.71079	0.56241		**0.68207**	**0.699**	**0.98936**	**0.41037**	**0.62504**	**0.43831**	**0.65582**
SC-017-L	0.34322	0.50489	0.7264	0.44568	0.56299	0.59922	0.77916	0.8257			0.52396	0.60542
SC-017-R	0.62709	0.5747	0.53987	0.33144	0.46448	0.6681	0.64597	0.97431	0.6164	0.59458	0.54258	0.67566
SC-020-L	0.51601	0.72548	0.60259	0.48906	**0.45931**	0.84631	0.96559	0.85034	0.63388	0.62528	0.54036	0.52861
SC-020-R	0.6702	0.55504	0.53566	0.60062	**0.50934**	0.82516	0.85493	0.89186	0.61979	0.48961	0.58675	0.57949
SC-082-L	0.57986	0.62837	0.56567	0.5406		0.7726	0.99207		0.56419	0.67029	0.42982	0.55678
SC-082-R	0.3727	0.53482	**0.48101**	0.49625	0.52257	0.82324	0.60814	0.89085	0.65407	0.83222	0.51817	0.57108
SC-083-L	0.5622	0.60564	**0.43401**	0.39108		0.96886	0.82531		0.58181	0.59607	0.41155	0.47999
SC-083-R	0.56565	0.59857	**0.40305**	0.48872		0.94626	0.6843	0.80992	0.38855	0.62845	0.3909	0.45251
SC-084-L	0.53041	0.68646	**0.54784**	0.36413	0.54935	0.93728	0.60753	0.88534	0.58636	0.68691	0.44381	0.69482
SC-084-R	0.45258	0.55633	0.55206	0.58752	0.46052	0.78486	0.63507	0.88516	0.44976	0.5576	0.50864	0.67606
SC-085-L	0.34481	0.58286	0.62964	0.5547	0.50461	0.99897	0.88496	0.95764	0.32178	0.54443	0.52187	0.5365
SC-085-R	0.47739	0.54912	0.66867	0.58944	0.61495	0.98478	0.84966	0.72252	0.76384		0.55294	0.95024
SC-086-L	0.4792	0.66858	0.43871	0.39019	0.51338	0.98948	0.86705	0.68575	0.6187	0.62148	0.52878	0.5311
SC-087-L	0.67821	0.84904	0.77993	0.68652	0.38022	0.43492	0.43371	0.87337	0.57868	0.68491	0.53791	0.66394
SC-087-L	0.53175	0.68647	0.72089	0.68192		0.8252	0.76794	0.89242	0.58023	0.67919	0.54714	0.73185
SC-089-L	0.53205	0.7323	0.6674	0.56168							0.71999	0.7413
SC-089-R	0.49006	0.82247	0.59287	0.49459					0.79187		0.7976	0.79116
SC-369-R						0.89827	0.63528		0.31893	0.63344	0.45287	0.69517
SC-370-L	0.5206	0.72313	0.53007	0.4538	0.59866	0.88726	0.59317	0.82908	0.72466	0.72071	0.72775	0.83122
SC-370-R	0.53391	0.57445	0.53897	0.49884	0.64664	0.76677	0.86449	0.81976	0.79073	0.84005	0.78502	0.78087
SC-371-L	0.68562	0.85139	0.61691	0.47073	0.65975	0.80043	0.68378	0.85334	0.74208	0.72875	0.54851	0.75168
SC-086-R	0.66011	0.76797	0.47719	0.41465	0.50287	0.78189	0.72087	0.64425	0.57154	0.51108	0.57088	0.64759
SC-088-L	0.48234	0.54649	0.48486	0.49556	0.462	0.58647	0.94069	0.61222	0.5742	0.51873	0.50745	0.6681
SC-088-R	0.66415	0.61171	0.46815	0.4692	0.38985	0.68614	0.97947	0.67294	0.49121	0.52742	0.49387	0.60936
SC-092-L	0.57548	0.60648	0.54055	0.53702	0.41235	0.69738	0.65124	0.88361	0.67141		0.60117	0.68377
SC-092-R	0.44886	0.59698	0.67455	0.69125	0.42244	0.91789	0.99913	0.92497	0.71243		0.64186	0.73822
SC-096-L	0.64053	0.61733	0.71075	0.67996	0.53338	0.87372	0.92887	0.82776	0.52915	0.63014	0.60969	0.7381
SC-096-R	0.72432	0.69811	0.68659	0.59883	0.60555			0.76978	0.60985		0.58441	0.67074
SC-097-L	0.48491	0.63567	0.73732	0.6532	0.47629	0.85474	0.95206	0.74051	0.49799	0.64653	0.49667	0.52492
SC-097-R	0.67485	0.6978	0.53426	0.41279	0.51173	0.91817	0.98661	0.74057	0.63638	0.54903	0.64143	0.69937
SC-157-R	0.63681	0.71974	0.40051	0.42968	0.49589							
SC-158-L	0.54541	0.70434	0.59836	0.60712	0.47797	0.7735	0.4554	0.89608		0.68857	0.44823	0.71197
SC-158-R	0.57173	0.5011	0.74187	0.73563		0.93677	0.52881	0.70919	0.55038	0.49313	0.47452	0.66351
SC-161-L	0.51085	0.66167	0.57768	0.60255	0.42908	0.74178	0.69007	0.77074	0.48779	0.71543	0.4332	0.49867
SC-161-R	0.51677	0.60732	0.63371	0.65098	0.4254	0.81722	0.56902	0.92105	0.58075	0.61243	0.54585	0.70602
MEAN	0.5471451	0.6491097	0.5871246	0.5330954	0.5033915	0.8133034	0.7587297	0.825013	0.582805	0.6304107	0.5458417	0.6583317
STD DEV	0.095459	0.0923538	0.1040814	0.1042314	0.0751968	0.1307224	0.165739	0.0989458	0.1214161	0.0906243	0.0995522	0.1067404
CoV	17%	14%	18%	20%	15%	16%	22%	12%	21%	14%	18%	16%

Table B11: Raw DA measurements for VOIs 1-12. Individual measurements that are greater than two standard deviations (>2σ) from the mean are highlighted in red.

	13	14	15	16	17	18	19	20	21	22	23
SC-016-R	0.97214	0.56439	0.35978	0.69272		0.84194	0.47942	0.73075	0.79065	0.53873	0.59142
SC-017-L	0.82379	0.50658	0.57114	0.86145	0.75855	0.68346	0.38077	0.83712	0.66907	0.69039	0.58858
SC-017-R	0.98937	0.61088	0.69702	0.82227		0.61614	0.57119	0.83221	0.64643	0.59029	0.71967
SC-020-L	0.5702	0.53191	0.66855	0.62998	0.8274	0.84312	0.49598	0.80042	0.68303	0.62741	0.58213
SC-020-R	0.98498	0.49607	0.73375	0.76035	0.89388	0.75533	0.6801	0.8334	0.75575	0.64349	0.60129
SC-082-L	0.71051	0.40121				0.71923			0.7323		0.61755
SC-082-R	0.79987	0.35996	0.58956		0.7344	0.64424	0.79473	0.82396	0.79713	0.58188	0.56941
SC-083-L	0.47537	0.48489	0.69339		0.80356	0.57696	0.56125	0.75271	0.68115	0.5458	0.5766
SC-083-R	0.53784	0.45704	0.60742		0.72807	0.6362	0.65624	0.71226	0.60246	0.61229	0.60944
SC-084-L	0.84665	0.58615	0.6129		0.82357	0.39392	0.64011	0.93385	0.71939	0.59868	0.61412
SC-084-R	0.95679	0.34301	0.61337		0.79585	0.69066	0.61899	0.75539	0.68865	0.63995	0.64797
SC-085-L	0.81419	0.53044				0.68883	0.69082	0.80556	0.73634	0.67877	0.86158
SC-085-R	0.9194	0.54982	0.76471		0.74016		0.75341	0.89988	0.631	0.68309	0.59261
SC-086-L	0.82248	0.44898	0.52221				0.68719		0.69438	0.65001	0.59954
SC-087-L	0.71331	0.35389	0.70171				0.68835	0.63858	0.74244	0.84632	0.60392
SC-087-L	0.8938	0.36909	0.58338			0.61973	0.44383	0.52066	0.68638	0.57034	0.62116
SC-089-L	0.72693	0.49944					0.75359	0.93326	0.77077	0.76071	0.72388
SC-089-R	0.81807	0.62099					0.70404	0.86357	0.76136	0.63138	0.61494
SC-369-R	0.86793	0.46636	0.50566		0.88145		0.44355	0.77419	0.78727	0.5961	0.5936
SC-370-L		0.47329	0.91455		0.82165	0.76974	0.73247	0.96636	0.7339	0.71108	0.6526
SC-370-R	0.77085	0.52412	0.70653		0.83963	0.81831	0.72771	0.86911	0.73139	0.8338	0.69589
SC-371-L	0.99962	0.58864	0.81011			0.70551	0.65434	0.87088	0.73702	0.92925	0.69714
SC-086-R	0.94732	0.58514				0.76642			0.78248		0.66934
SC-088-L	0.84787	0.57327	0.58547	0.84121	0.8135	0.73109	0.6308	0.81207	0.74133	0.69047	0.69338
SC-088-R	0.9119	0.51953	0.60366		0.69572		0.46882	0.75472	0.67924	0.6991	0.68743
SC-092-L	0.74615	0.2694	0.56158			0.73483			0.73593	0.65727	0.62628
SC-092-R	0.90012	0.60308	0.71409		0.84591	0.70038			0.79231	0.74893	0.65605
SC-096-L	0.97954	0.53483	0.84709			0.68481	0.72876	0.9894	0.82112	0.83103	0.73122
SC-096-R	0.9335	0.57414	0.8388			0.76681	0.84622	0.89308	0.80527	0.86646	0.75734
SC-097-L	0.811	0.47898	0.6647		0.86205	0.71393	0.50908	0.77548	0.721	0.68771	0.69329
SC-097-R	0.93591	0.576	0.66214			0.6574	0.60552	0.79976	0.74908	0.68431	0.75734
SC-157-R											
SC-158-L	0.72756	0.20496	0.54365		0.91192	0.79442	0.56007	0.90381	0.84619	0.70838	0.6434
SC-158-R	0.9672	0.45878	0.72883		0.80928	0.60272	0.76046	0.92796	0.72239	0.64231	0.64003
SC-161-L	0.61213		0.48376		0.77505	0.60016	0.44397	0.73084	0.65789	0.5984	0.56491
SC-161-R	0.91641	0.45388	0.62415			0.44842	0.65576		0.65869	0.66057	0.60599
MEAN	0.8309029	0.48821	0.6504553	0.7679967	0.8085053	0.6858825	0.6247594	0.8186634	0.7283194	0.6798394	0.6486011
STD DEV	0.1361694	0.0994419	0.1182119	0.0914472	0.0589133	0.1040425	0.1199934	0.1003462	0.056601	0.0949623	0.0659089
CoV	16%	20%	18%	12%	7%	15%	19%	12%	8%	14%	10%

Table B12: Raw DA measurements for VOIs 13-23. Individual measurements that are greater than two standard deviations (>2σ) from the mean are highlighted in red.

Appendix D: Statistical Testing

Bone Volume Fraction (BV/TV)

One Way Analysis of Variance

Normality Test (Shapiro-Wilk) Failed (P < 0.050)

Test execution ended by user request, ANOVA on Ranks begun:

Kruskal-Wallis One Way Analysis of Variance on Ranks

VOI	N	Missing	Median	25%	75%
1	36	1	38.763	36.769	40.881
2	36	1	37.865	36.922	40.059
3	36	1	37.267	34.408	40.019
4	36	1	36.528	35.189	40.375
5	36	9	32.907	30.027	35.703
6	36	3	31.324	27.388	32.600
7	36	3	27.432	24.898	28.473
8	36	5	31.213	28.440	33.008
9	36	4	38.472	36.791	39.868
10	36	8	38.740	37.168	41.181
11	36	1	31.220	30.530	33.363
12	36	1	29.717	28.647	30.942
13	36	2	21.391	17.605	24.154
14	36	2	31.375	30.041	33.184
15	36	6	32.958	31.370	34.586
16	24	18	35.380	34.376	36.370
17	35	16	31.221	27.916	34.101
18	36	8	33.322	31.765	36.033
19	36	5	41.552	40.688	42.572
20	35	6	41.373	39.857	42.926
21	36	1	39.042	37.912	40.249
22	36	3	41.756	39.846	45.020
23	36	1	43.881	42.096	45.362

H = 559.157 with 22 degrees of freedom. (P = <0.001)

The differences in the median values among the treatment groups are greater than would be expected by chance; there is a statistically significant difference (P = <0.001)

Structural Model Index (SMI)

One Way Analysis of Variance

Normality Test (Shapiro-Wilk) Failed (P < 0.050)

Test execution ended by user request, ANOVA on Ranks begun:

Kruskal-Wallis One Way Analysis of Variance on Ranks

VOI	N	Missing	Median	25%	75%
1	36	1	1.376	1.290	1.546
2	36	1	1.440	1.176	1.551
3	36	1	1.397	1.171	1.587
4	36	1	1.363	1.195	1.548
5	36	9	1.457	1.235	1.714
6	36	4	2.017	1.845	2.100
7	36	4	2.307	2.156	2.395
8	36	6	2.338	2.135	2.516
9	36	4	1.647	1.524	1.868
10	36	8	1.800	1.699	1.878
11	36	1	1.737	1.603	1.859
12	36	1	2.035	1.905	2.135
13	36	2	2.307	2.153	2.485
14	36	2	2.079	1.995	2.184
15	36	6	1.893	1.793	2.047
16	24	18	1.985	1.710	2.109
17	35	16	1.952	1.736	2.084
18	36	8	2.105	1.990	2.169
19	36	5	1.614	1.457	1.785
20	35	6	1.723	1.592	1.930
21	36	1	1.627	1.422	1.729
22	36	3	1.337	1.193	1.538
23	36	1	1.233	0.902	1.372

H = 477.698 with 22 degrees of freedom. (P = <0.001)

The differences in the median values among the treatment groups are greater than would be expected by chance; there is a statistically significant difference (P = <0.001)

Trabecular Thickness (Tb.Th)

One Way Analysis of Variance

Normality Test (Shapiro-Wilk) Failed (P < 0.050)

Test execution ended by user request, ANOVA on Ranks begun

Kruskal-Wallis One Way Analysis of Variance on Ranks

VOI	N	Missing	Median	25%	75%
1	36	1	0.205	0.196	0.215
2	36	1	0.205	0.194	0.218
3	36	1	0.214	0.203	0.229
4	36	1	0.212	0.200	0.234
5	36	9	0.231	0.219	0.242
6	36	4	0.230	0.219	0.251
7	36	4	0.254	0.232	0.279
8	36	6	0.246	0.219	0.286
9	36	4	0.209	0.195	0.229
10	36	8	0.203	0.197	0.221
11	36	1	0.218	0.200	0.227
12	36	1	0.234	0.216	0.253
13	36	2	0.255	0.224	0.294
14	36	2	0.286	0.264	0.313
15	36	6	0.198	0.184	0.206
16	24	18	0.167	0.164	0.179
17	35	16	0.213	0.197	0.223
18	36	8	0.243	0.214	0.281
19	36	5	0.210	0.185	0.220
20	35	6	0.199	0.181	0.212
21	36	1	0.219	0.202	0.235
22	36	3	0.219	0.204	0.229
23	36	1	0.230	0.213	0.246

H = 234.309 with 22 degrees of freedom. (P = <0.001)

The differences in the median values among the treatment groups are greater than would be expected by chance; there is a statistically significant difference (P = <0.001)

Trabecular Number (Tb.N)

One Way Analysis of Variance

Normality Test (Shapiro-Wilk) Failed ($P < 0.050$)

Test execution ended by user request, ANOVA on Ranks begun:

Kruskal-Wallis One Way Analysis of Variance on Ranks

VOI	N	Missing	Median	25%	75%
1	36	1	1.879	1.792	1.988
2	36	1	1.884	1.736	2.022
3	36	1	1.751	1.631	1.884
4	36	1	1.745	1.595	1.882
5	36	9	1.475	1.302	1.591
6	36	4	1.323	1.067	1.424
7	36	4	1.040	0.981	1.189
8	36	6	1.230	1.016	1.440
9	36	4	1.831	1.683	1.957
10	36	8	1.874	1.733	1.992
11	36	1	1.449	1.355	1.621
12	36	1	1.291	1.179	1.365
13	36	2	0.861	0.703	1.007
14	36	2	1.113	1.003	1.232
15	36	6	1.693	1.606	1.833
16	24	18	2.110	1.910	2.250
17	35	16	1.506	1.283	1.658
18	36	8	1.351	1.214	1.599
19	36	5	2.009	1.927	2.158
20	35	6	2.115	1.982	2.231
21	36	1	1.799	1.651	1.918
22	36	3	1.934	1.800	2.148
23	36	1	1.895	1.820	2.050

$H = 486.389$ with 22 degrees of freedom. ($P = <0.001$)

The differences in the median values among the treatment groups are greater than would be expected by chance; there is a statistically significant difference ($P = <0.001$)

Trabecular Separation (Tb.Sp)

One Way Analysis of Variance

Normality Test (Shapiro-Wilk) Failed (P < 0.050)

Test execution ended by user request, ANOVA on Ranks begun:

Kruskal-Wallis One Way Analysis of Variance on Ranks

VOI	N	Missing	Median	25%	75%
1	36	1	0.268	0.260	0.287
2	36	1	0.269	0.253	0.278
3	36	1	0.293	0.282	0.321
4	36	1	0.294	0.274	0.312
5	36	9	0.359	0.331	0.434
6	36	4	0.374	0.351	0.465
7	36	4	0.405	0.351	0.478
8	36	6	0.402	0.340	0.470
9	36	4	0.278	0.266	0.303
10	36	8	0.282	0.260	0.299
11	36	1	0.341	0.317	0.395
12	36	1	0.400	0.363	0.469
13	36	2	0.539	0.426	0.646
14	36	2	0.422	0.384	0.481
15	36	6	0.292	0.257	0.316
16	24	18	0.225	0.209	0.248
17	35	16	0.366	0.337	0.431
18	36	8	0.361	0.295	0.494
19	36	5	0.258	0.236	0.279
20	35	6	0.247	0.225	0.265
21	36	1	0.306	0.275	0.336
22	36	3	0.273	0.244	0.291
23	36	1	0.272	0.257	0.292

H = 404.996 with 22 degrees of freedom. (P = <0.001)

The differences in the median values among the treatment groups are greater than would be expected by chance; there is a statistically significant difference (P = <0.001)

Degree of Anisotropy (DA)

One Way Analysis of Variance

Normality Test (Shapiro-Wilk) Failed ($P < 0.050$)

Test execution ended by user request, ANOVA on Ranks begun:

Kruskal-Wallis One Way Analysis of Variance on Ranks

VOI	N	Missing	Median	25%	75%
1	36	1	0.532	0.485	0.641
2	36	1	0.628	0.575	0.720
3	36	1	0.578	0.513	0.675
4	36	1	0.541	0.454	0.603
5	36	9	0.503	0.459	0.539
6	36	4	0.824	0.748	0.918
7	36	4	0.744	0.635	0.918
8	36	6	0.840	0.741	0.892
9	36	4	0.581	0.506	0.650
10	36	8	0.627	0.551	0.686
11	36	1	0.538	0.475	0.587
12	36	1	0.671	0.571	0.732
13	36	2	0.847	0.742	0.939
14	36	2	0.503	0.453	0.573
15	36	6	0.643	0.580	0.718
16	24	18	0.791	0.677	0.846
17	35	16	0.814	0.759	0.846
18	36	8	0.696	0.624	0.764
19	36	5	0.654	0.509	0.728
20	35	6	0.824	0.755	0.896
21	36	1	0.734	0.683	0.771
22	36	3	0.661	0.605	0.710
23	36	1	0.626	0.600	0.693

$H = 361.407$ with 22 degrees of freedom. ($P = <0.001$)

The differences in the median values among the treatment groups are greater than would be expected by chance; there is a statistically significant difference ($P = <0.001$)